Synthesis and Physicochemical Characterisation of Pristine Metal-Organic Frameworks, Thin-Films and Derived Materials

A thesis submitted to the University of Dublin for the degree of Doctor of Philosophy

Mariah O'
Doherty

School of Chemistry

Trinity College Dublin, the University of Dublin

2022

Declaration

I declare that this thesis has not been submitted as an exercise for a degree at this or any other university and that it is entirely my own work, except where otherwise citied, referenced, acknowledged or accredited.

I agree to deposit this thesis in the University's open access institutional repository or allow the Library to do so on my behalf, subject to Irish Copyright Legislation and Trinity College Library conditions of use and acknowledgement.

Mariah O' Doherty

Acknowledgments

I have to start by expressing my deepest gratitude to my academic supervisor Prof. Wolfgang Schmitt for his help and guidance throughout my PhD.

I give great thanks to everybody in the Schmitt group. In particular, I'd like to thank Éadaoin whose brilliant chemical knowledge and top banter was both useful and appreciated, Kevin who always has an answer to any questions I've had, Lua who has been supportive from being by 4th year project supervisor to now, my project students Aviral and Ciara, and the upstairs boys Ximo, Muhamad, Dean and Joe. A special shout out to Mo and Avi for bringing the espresso machine to the office. Thanks to everyone who supported me directly with my research, Ximo for helping me extensively with eletrochem, Friedrich who helped me get my head around crystallography, Debo for analysing topology and Dr. Nian-Yong Zhu and Dr Amal Cherian Kathalikkattil for measuring my crystals structures.

I would like to thank the efforts of the School of Chemistry staff, Dr. John O' Brien and Dr. Manuel Ruether for NMR measurements. Dr. Brendan Twamley for help with difficult PXRD samples, Dermot Daly and Clive Downings for training on electron microscopes, and Dr. Gary Hessman for mass spectrometry measurements. Without their contributions, this work would not be possible. Just as importantly, thanks to the 2019 Werner committee members.

Finally, I give my greatest gratitude to my parents, my sister Bríd, my partner Mac, my friends, the Tallaght house crew and my cats Pinto and Bonzo for their stability and continuous support during my studies. Also, I gratefully acknowledge Science Foundation Ireland (SFI) for their financial support.

Summary

Metal-organic frameworks (MOFs) are a class of inorganic-organic hybrid materials. They are composed of metal centres linked by organic ligands through strong bonds, forming 1-, 2- and 3-dimensional frameworks. The research presented in this thesis concerns the synthesis of MOFs and MOF-derived materials, namely carbon-based metal oxide materials, synthesised from MOF precursors, and their suitability for potential industrial applications. In particular, the affinity of these materials to catalyse the oxygen evolution reaction. The structures of the resulting materials were characterised using a combination of single-crystal and powder X-ray diffraction methods and were further assessed using a diverse set of complimentary analytical techniques.

Chapter 1 gives a general introduction to MOFs, summarises the previous literature that relate to the work described in this thesis, and outlines the specific research undertaken in this thesis. This chapter introduces the structure and synthesis of MOFs, their properties, and the applications of these materials for potential industrial uses in green energy technologies.

Chapter 2 centres on the synthesis of **Co@C-500** and the formation of **Co@C-500** on thin-film electrode surfaces. The tritopic ligand 4,4',4''-(benzene-1,3,5-triyltris(ethyne-2,1- diyl))tribenzoic acid (**H_3BETB**) is employed in the synthesis of **{Co_5}-MOF** and MOF-bound thin films to act as a precursor for the synthesis of **Co@C-500** *via* thermal-treatment. PXRD, FT-IR and Raman characterisation of the resulting materials confirm the presence of a spinel cobalt oxide material and an amorphous carbon framework. Electron microscopy methods give an insight into the structure of the system, revealing a core@shell with spherical nanoparticles within a porous carbon mesh, with nanoparticles aggregating into clusters. The porosity of **Co@C-500** is confirmed using N_2 gas sorption which shows a reversible type-I isotherm at 77 K with a maximum uptake of 191 cm^3/g at 1 P/P_0. This step is consistent with the presence of small pores of *ca.* 2 nm in diameter and confirming **Co@C-500** as a microporous material. Under electrocatalytic conditions **Co@C-500**/FTO and **Co@C-500**/CC reveals overpotentials of 400 and 320 mV to reach 10 mA cm^{-2}, respectively in alkaline medium. Further, these thin films were found to be stable for prolonged periods of time under the applied conditions.

Chapter 3 expands on the use of 4,4',4''-(benzene-1,3,5-triyltris(ethyne-2,1-diyl))tribenzoic acid and the general method detailed in Chapter 1 to synthesise a number of

mixed-metal MOFs, {(**CoNi)$_5$}-MOF**, {(**CoZn)$_3$}-MOF**, {(**MnZn)$_3$}-MOF** and {(**MnCo)$_3$}-MOF**, with {(**CoNi)$_5$}-MOF** also being deposited on conductive electrodes. The fundamental aim is to synthesise materials with applications as OER catalysts. Because of this, focus is shifted to incorporating transition metal ions which have previously been proven as the active components of successful OER catalysts. Earth-abundant metals Co(II), Mn(II) Zn(II) and Ni(II) are incorporated. These MOFs are characterised using a combination of single-crystal X-ray diffraction and EDX, XPS and computational modelling to determine both the structure and the metallic composition of the materials. Electrochemical OER experiments conducted on the MOFs show moderate catalytic activity. In particular {(**CoNi)$_5$}-MOF** demonstrates an onset overpotential of 462 mV at pH7.2, and a Tafel slope of 164 mV dec^{-1}. The catalytic properties of {(**CoNi)$_5$}-MOF** are enhanced by the thermal treatment of the MOF under N_2 at 500 °C to produce **CoNi@C-500** materials. The systems exhibit a decrease in onset overpotential and Tafel slope, to 390 mV and 410 mV dec^{-1}, respectively at pH 7.2. The annealed material was found to be stable in alkaline media, and catalysed the OER reaction, reaching an overpotential of 497 mV at 10mA cm^{-2}.

Chapter 4 details the synthesis of two linearly extended novel ligands, trimethyl-4,4',4"-(((1,3,5-triazine-2,4,6-triyl)tris(benzene-4,1-diyl))tris(ethyne-2,1-diyl))tribenzoate (**H$_3$TAP**), trimethyl-3,3',3"- (((1,3,5-triazine-2,4,6-triyl) tris (benzene-4,1-diyl)) tris(ethyne-2,1-diyl))tribenzoate (**H$_3$TAM**) in the hopes to synthesise highly-augmented MOFs for photo- and electro-catalytic applications. A set of four highly interpenetrated MOFs are reported, ({**Cu$_2$}-MOF-1**, **{Cu$_2$}-MOF-2**, **{Zn}-MOF** and {**Cd}-MOF**). The potential applications of these MOFs are explored by characterising their photophysical properties.

Chapter 5 describes the analytical methods experimental synthesis of the ligands and MOFs detailed in this thesis.

Chapter 6 summarises the research undertaken, provides concluding remarks and expands on potential future applications for the materials described in this thesis.

Table of contents

2 - A robust thin-film cobalt-based MOF derivative for water oxidation catalysis

3 - Direct synthesis and applications of mixed-metal MOFs

4 - Triazine-Functionalised Metal-Organic Frameworks

5 - Experimental

Abbreviations

1D	One dimensional
2D	Two dimensional
3D	Three dimensional
ar	Aromatic
BET	Brunauer-Emmett-Teller
bpy	2,2'-Bipyridine
CC	Carbon cloth
CN_3TAP	2,4,6-Tris(4-(4-ethynylbenzonitrile)phenyl)-1,3,5-triazine
CP	Carbon paste
CV	Cyclic voltametric
D	Donor
d	Doublet
dcbpy	2,2′-Bipyridine-4,4′-dicarboxylate
DCM	Dichloromethane
dd	Double doublet
DFT	Density functional theory
DMF	N,N-Dimethylformamide
DMSO	Dimethyl sulfoxide
EDX	Energy dispersive X-ray
FTO	Fluorine-doped tin oxide
HAADF	High-angle annular dark-field imaging
H_3BTB	1,3,5-Tris(4-carboxyphenyl)benzene
H_3BTC	1,3,5-Benzenetricarboxylic acid
H_3TATP	1,3,5-Triazine-2,4,6-tribenzoic acid
HER	Hydrogen evolution reaction
HKUST	Hong Kong University of Science and Technology
IR	Infrared
IRMOF	Isoreticular metal-organic framework
LMCT	Ligand-to-metal charge transfer
J	Coupling constant
KPi	Potassium phosphate
LSV	Linear sweep voltammetry
m	Multiplet

MALDI	Matrix Assisted Laser Desorption/Ionisation
MBA	2-(5′-Methyl-[2,2′-bipyridin]-5-yl)acetate
m-BCB	1,3-Benzenedicarboxylate
m-BTEB	3,3',3"-(Benzene-1,3,5-triyltris(ethyne-2,1-diyl)tribenzoate
MeOH	Methanol
MIL	Matériaux de l′Institut Lavoisier
MLCT	Metal-to-ligand charge transfer
MM-MOFs	Mixed metal metal-organic frameworks
MOF	Metal-organic framework
MOL	Metal-organic layers
MOP	Metal-organic polyhedral
NHE	Normal hydrogen electrode
NF	Nickel foam
NMP	1-Methytl-2-pyrrolidone
NMR	Nuclear magnetic resonance
OER	Oxidation evolution reaction
PDC	Pyridinedicarboxylate
PMS	Post-synthetic modification
PS	Photosensitiser
PPh_3	Triphenylphosphine
Ppm	Parts per million
pto	Platinum oxide topology
PXRD	Powder X-ray diffraction
r	Correlation coefficient
S	Sensitiser
SBU	Secondary building unit
SEM	Scanning electron microscopy
SK	Supramolecular keplerate
St	Stretch
SSV	Steady-state voltammetry
TEM	Transmission electron spectroscopy
TGA	Thermogravimetric analysis
THF	Tetrahydrofuran
TCNQ	Tetracyanoquinodimethane

typ	2,2';6'2"-Terpyridine
trz	2-Phenyl-4,6-di(pyridin-2-yl)-1,3,5-triazine
FT-IR	Fourier-transform infrared
s	Singlet
SBU	Secondary building unit
STEM	Scanning transmission electron microscopy
SCXRD	Single-crystal X-ray diffreaction
SXI	scanning X-ray imaging
t	Triplet
tbo	Twisted boracite topology
TEOA	Triethanolamine
TEA	Triethylamine
TCM	Technology Centre Mongstad
THF	Tetrahydrofuran
TON	Reduction turnover numbers
UiO	Universitetet I Oslo
UV	Ultraviolet
XPS	X-ray photoelectron spectroscopy
XRD	X-ray diffraction
w	Weak
ε	Extinction coefficient
τ	Excited state lifetime

Chapter 1

Introduction

1.0 Introduction

1.1 Introduction to metal-organic frameworks

Metal-organic frameworks (MOFs) are an extensive subclass of coordination polymers, compromised of both organic and inorganic moieties, containing potential voids.[1] Since the pioneering work of Hoskins and Robson[2,3] on 'scaffolding-like' materials in the early 1990's, there has been exponential growth into the study of MOF synthesis and applications, with the number of reported discrete structures now exceeding 90,000 and the reported annual figure doubling every decade.[4,5] This surge in interest can be accredited to the ability to modulate the structure and pore characteristics of MOFs using a number of different approaches. Examples include, tuning the synthetic conditions,[6] post-synthetic modification[7] and surface deposition.[8] The variety of combinations of organic and inorganic units, as well as individual compositions allows for tuneable MOF functionalities, which are able to be adapted towards specific applications.[9]

1.2 Porous inorganic hybrid materials

Inorganic hybrid material is considered an umbrella term which encompasses molecular entities, nanocomposites and macroscopic mixtures.[10] A more defined definition attributes hybrid materials to covalently bonded materials that contain both distinct inorganic moieties (metal centres, metal-oxo clusters *etc.*) and organic components (organic ligands). These materials have a multifaceted appeal in both form and structure, influenced not only by the metallic properties but also by the organic functional groups, which can modulate the chemical properties of the metal units within the material. This can be achieved through the design of the organic group, by means of the electron withdrawing power of the ligand, conjugation of the linker and metal binding and chelating sites.

1.3 Metal-organic polyhedra

Metal-organic polyhedra (MOPs) or coordination cages are a class of supramolecular coordination complexes, consisting of metal ions or clusters, linked through polytopic organic struts to form discrete molecular structures with defined cavities.[11,12] These polyhedra are emerging as a complimentary supramolecular class to MOFs, with exciting applications in drug delivery by encapsulation,[13] catalysis[14] and selective gas and chemical

adsorption.[15] The classification of a MOP was recorded by Yaghi *et al.* to describe a porous structure from 12 {$Cu_2(CO_2)_4$}-paddlewheel SBUs known as *a*-MOP-1.[16] Presented in Figure 1.3.1, the cuboctahedron is comprised of 24 1,3-benzenedicarboxylate (*m*-BCB) organic linkers that connect 12 dicopper paddlewheels to form a supramolecular cage.

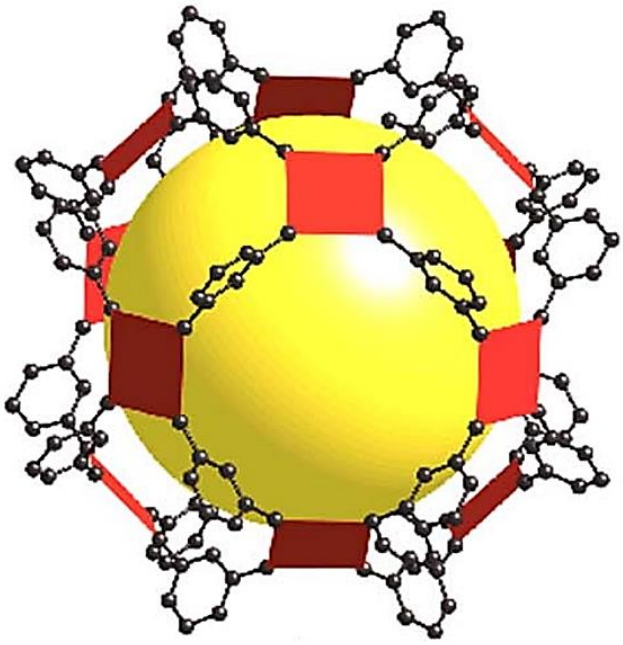

***Figure 1.3.1**: a-MOP-1. C, black; $Cu_2(CO_2)_4$, represented as red square SBU. The yellow sphere represents the largest Van der Waals sphere that can fit into the internal cavity. Hydrogen atoms were omitted for clarity.*[17]

As seen in Figure 1.3.1, inorganic SBUs (discussed in detail in Section 1.4) are also relevant in the reticular synthesis of MOPs.[12] The geometry of the organic linkers plays a major role in the self-assembly process. Of particular importance is the angle θ between the coordinating moieties in a ditopic linker and the angle η between the links of an inorganic SBU, which can define angles between coordinating functionalities in tritopic linkers. 3-functionalised phenolate groups provide favourable η angles for MOP formation.[12]

Just as isoreticular MOFs can be linearly extended to increase porosity (Section 1.4.2), MOPs with increasing central void diameters are being reported. 3,3',3''-(benzene-1,3,5-triyltris(ethyne-2,1-diyl)tribenzoate (*m*-BTEB) was synthesised by Schmitt *et al.* to produce coordination cage Supramolecular Keplerate-1 (SK-1) with exceptionally large internal diameters.[18] SK-1 contains 36 dicopper paddlewheels that are at the edge transitive vertices of 24 $BTEB^{3-}$ ligands yielding a closed (4,3)-coordination net (Figure 1.3.2). Void diameters for SK-1 lie in the range *ca.* 48-50 Å and the cross-sectional diameters of the MOP are one of the largest crystallographically characterised for porous supramolecular species.

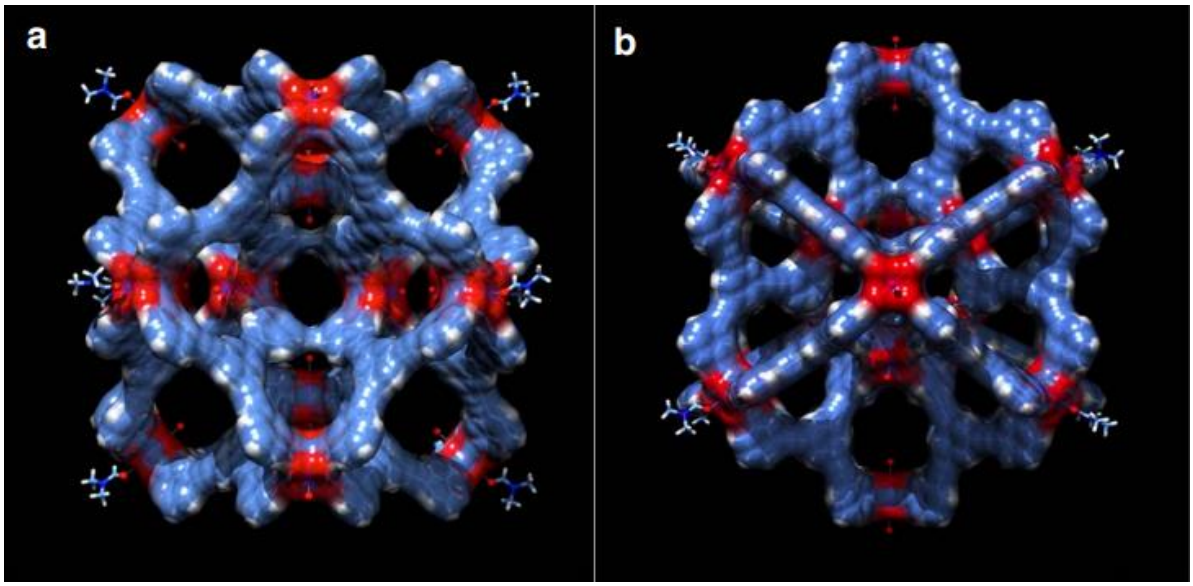

***Figure 1.3.2**: Space filling model of SK-1 down two different crystallographic axes. C, blue; O, red; dicopper paddlewheels, white. Coordinating water molecules were represented in ball and stick-representation. Adapted from Schmitt et al.*[18]

1.4 Design of MOFs

MOFs are coordination polymers that extend in two or three-dimensional space containing inorganic nodes, linked by multitopic organic struts to form an ordered network. Due to the efforts of Hoskins and Robson, along with Fujita[19] and Zaworotko,[20] it was identified that by combining organic struts and metal ions or clusters, the architecture of the resulting frameworks could be regulated. This process is now formally known as reticular synthesis, which is described as the 'stitching' of inorganic, polynuclear clusters into a predetermined, ordered network using organic struts, connected by relatively strong bonds.[21]

In reticular synthesis, secondary building units (SBUs) are defined as geometrically well-defined metal clusters, bound by their points of extension to organic struts, linking neighbouring SBUs in two or three dimensions.[21] {M-O-C} cluster SBUs are commonly employed as they provide rigidity to a framework as the metal ions are locked into their positions by the carboxylates of the organic struts, contrary to having one metal ion at a network vertex.[22] A range of common SBUs are presented in Figure 1.4.1. Multitopic organic struts also influence the geometry of the resulting framework, and thus can also be considered as SBUs.

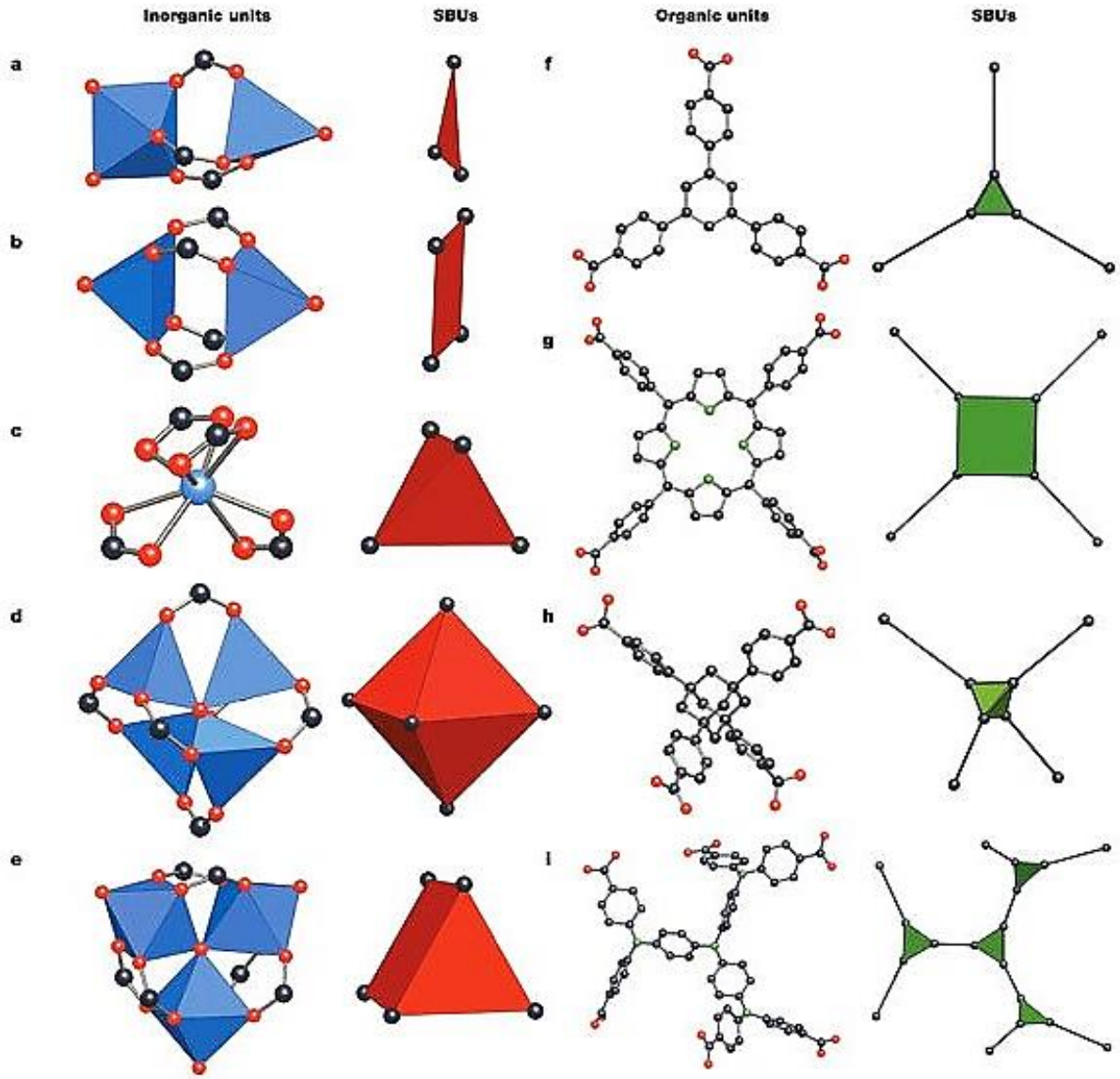

Figure 1.4.1*: Examples of preferred inorganic and carboxylate-organic units and representative SBUs. C, black; N, green; O, red. Inorganic metal-oxygen polyhedra are shown in blue, with SBU polyhedral defined by {M-O} in red. Organic polygons and polyhedra SBUs attached to carboxylates are shown in green. Adapted from Yaghi et al.*[23]

1.4.1 Topology

In general terms, topology simply describes the physical arrangement of a network of nodes with clearly defined connectivity. These nodes are often called ‘branch points’ and are analogous to inorganic SBUs as they correspond to a vertex of a framework.[24] Nets are formed when linking SBUs into an edge transitive network, here meaning that a connection between any two vertices will have a symmetry that maps it onto itself while preserving the overall connectivity. The topology of a net can be defined using the number of vertices of

the SBUs within the structure. The general notation (*n*,*p*) is used to describe nets, where *n* is the minimum number of connections needed to travel from a given node back to the original node without backtracking and *p* defines the number of primary connections a given node has to neighbouring nodes.[14]

Two nets with identical *n* and *p* can have different overall topologies. Two notable MOFs that contain the same nets is HKUST-1 (HKUST = Hong Kong University of Science and Technology)[26] and MOF-14.[27] Both contain dicopper paddlewheel nodes (Figure 1.4.2, b) linked to tritopic organic struts yielding (3,4)-coordinated nets, but have **tbo** and **pto** topologies respectively. Numerous factors dictate the overall topology of a MOF. In the case of (3,4)-coordinated nets, the dihedral angles of the outer phenyl rings in the tritopic ligand is theorised as the major influence for the formation of the framework.[28] HKUST-1 contains 1,3,5-benzenetricarboxylic acid (H_3BTC) struts, which do not contain peripheral phenyl rings, whereas MOF-14 contains 1,3,5-tris(4-carboxyphenyl)benzene (H_3BTB), with an average dihedral angle of 55 °. A more complex effect can be seen in the work of Yaghi *et al.*[28] In interpenetrated MOF-388 (**pto**) and non-interpenetrated MOF-399 (**tbo**), the central ring of the ligand is substituted for a triazine ring (MOF-388) and a phenyl ring (MOF-399). The triazine minimises the dihedral angle through intramolecular C-H···N bonding between the triazine and phenyl rings, allowing for a **pto** topology. This contradicts previous theories and highlights the effects of interpenetration on framework topologies, which are currently being investigated.[28]

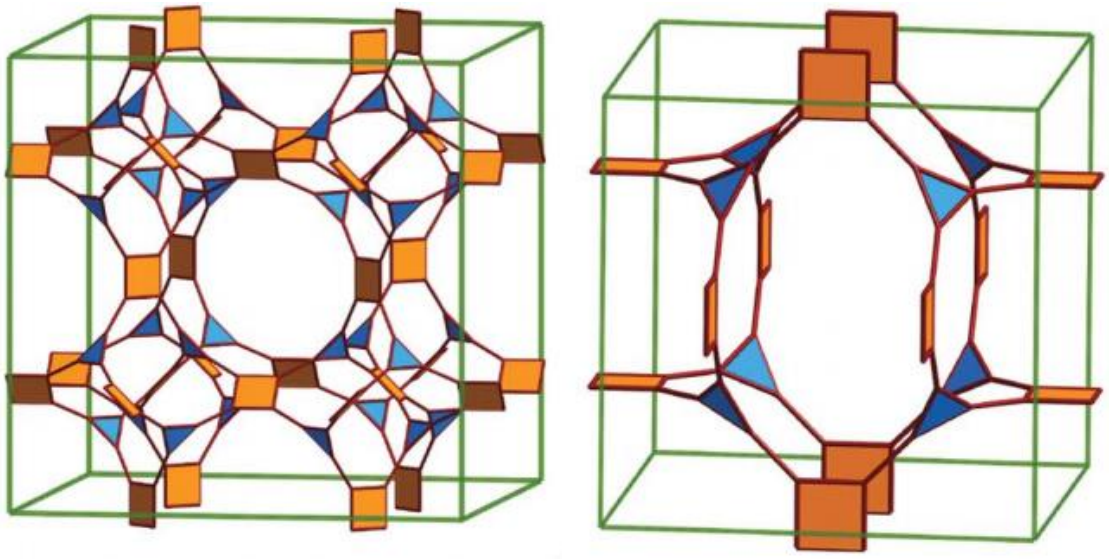

***Figure 1.4.2**: **tbo** (left) and **pto** (right) augmented nets describing two different (3,4)-nets. Adapted from Yaghi et al.*[29]

1.4.2 Reticular synthesis

The term reticular denotes net-like frameworks with similar topologies. A series of isoreticular MOFs (IRMOFs) may be synthesised by stepwise modification of the SBUs (*e.g.* length of the organic struts), while maintaining the same overall topology. This was first demonstrated by Yaghi *et al.* using supertetrahedral zinc acetate nodes ($\{Zn_4O(CO_2)_6\}$), held together by linear aromatic struts.[30] This series exhibits a **pcu** network containing a 6-coordinated, octahedral vertex extending in three dimensions with the general formula $\{Zn_4O(L)_3\}$ (with L denoting the organic strut). Linear extension of the struts increases the pore volume. The notion of using extended versions of a parent organic strut was also applied to extend the basic zinc acetate node with tritopic struts by Yaghi *et al.*[31] MOF-177, MOF-180 and MOF-200 are presented in Scheme 1.4.1. All exhibit a **qom** topology from (6,3)-coordinated nets, due to the inclusion of an extended series of struts with the same triangular geometry.

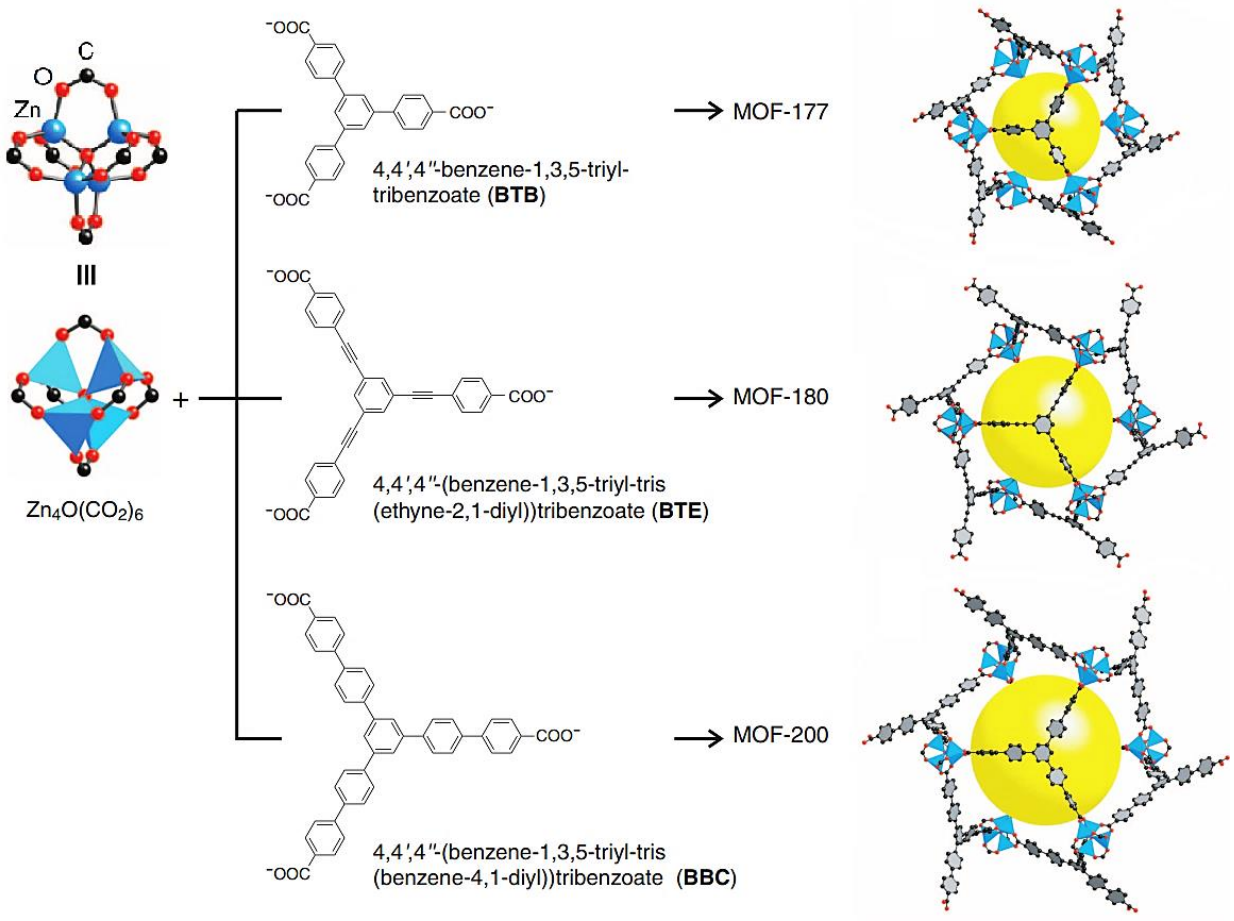

***Scheme 1.4.1**: $\{Zn_4O(CO_2)_6\}$ units (left) are formed from coordination of tritopic organic struts (middle) to form an isoreticular series of **qom** networks (right). C, black; O, red; Zn_4O, blue tetrahedra. The yellow spheres represent the largest Van der Waals sphere that*

can fit into the MOF cavities. Hydrogen atoms were omitted for clarity. Adapted from Yaghi et al.[31]

1.5 Synthesis

Evolving from the techniques employed in the synthesis of coordination polymers, a varied range of synthetic methods are used to synthesise MOFs. This includes solution-based systems, both at elevated temperatures,[6,32–34] and by using vapour diffusion,[35,36] electrochemical,[37–39] microwave-assisted,[40–42] sonochemical,[43–45] and mechanochemical approaches.[46,47] Currently, solvothermal synthesis remains the most commonly employed method of MOF crystal growth but other methods have become more prominent as MOF synthesis is tailored to suit particular applications. For example, electrochemical synthesis has been employed to develop thin-film MOFs for catalytic reactions, and microwave-assisted, sonochemical and mechanochemical approaches have become key in the kilogram-scale synthesis of MOFs for industrial use.[48,49]

1.5.1 Solvothermal synthesis

Many parameters can be altered to optimise growth of crystalline MOFs and MOPs, including, reaction time, solvent, pH, metal salt, metal to ligand ratio and concentration.[50] In particular, MOFs require that careful attention is given to temperature. MOFs are synthesised in a 'one-pot' reaction between metal salts and organic struts under solvothermal conditions.[51] Solvothermal synthesis is carried out at elevated pressure above the boiling point of the solvent, requiring high boiling point solvents, such as N,N-dimethylformamide (DMF), N.N-dimethylacetamide (DMA) and 1-methyl-2-pyrrolidone (NMP) to reach required temperatures.[6] Reaction temperatures are chosen to facilitate the enthalpy needed for the formation of structures with long-range order.[52] This process is frequently developed through trial and error, as control over reactants is limited.[53]

1.5.2 Choice of solvent

The judicious choice of solvent or solvent combinations are key to solvothermal synthesis as they influence the coordination behaviour of the metal ions and ligands.[54] As briefly mentioned, generally, high boiling point solvents are favoured due to their to ability reach high temperatures where soluble, partly soluble, or insoluble reactants can form metal-ligand bonds and grow networks.[55] In addition to their stability at elevated temperatures, dialkylamides such as DMF, DEF or DMA possess an innate ability to impart stabilisation effects on the reactants and intermediate structures during synthesis, through their polarity as well as controlling the rate of deprotonation of carboxylate ligands.[56] Many MOF

syntheses are carried out in mixed-solvent systems where the ratio of two or more solvents can alter the coordination modes of the metal ions or clusters. A prime example of this effect is seen in the work of Banerjee *et al.* where the self-assembly of $Mg(NO_3)_2 \cdot 6H_2O$ and 3,5-pyridinedicarboxylate (3,5-PDC) form three structurally distinct 3D networks, namely $Mg_3(3,5\text{-}PDC)_3(DMF)_3 \cdot DMF$, $Mg(3,5\text{-}PDC)(H_2O) \cdot (H_2O)$, and $Mg_4(3,5\text{-}PDC)_4(DMF)_2(H_2O)_2 \cdot 2DMF \cdot 4.5H_2O$, and one 1D coordination polymer, $[Mg(3,5\text{-}PDC)(H_2O)_2]$.[57] The materials were isolated individually after altering the solvent system using a combination of DMF, MeOH, EtOH and H_2O. As evident from the structural formulae, the topologies occur due to the variable coordination ability of the solvent molecules with the magnesium centres. H_2O molecules have a preferable coordination with the magnesium metal centres in comparison to the other polar solvents employed and were used as a template to synthesise the coordination networks.

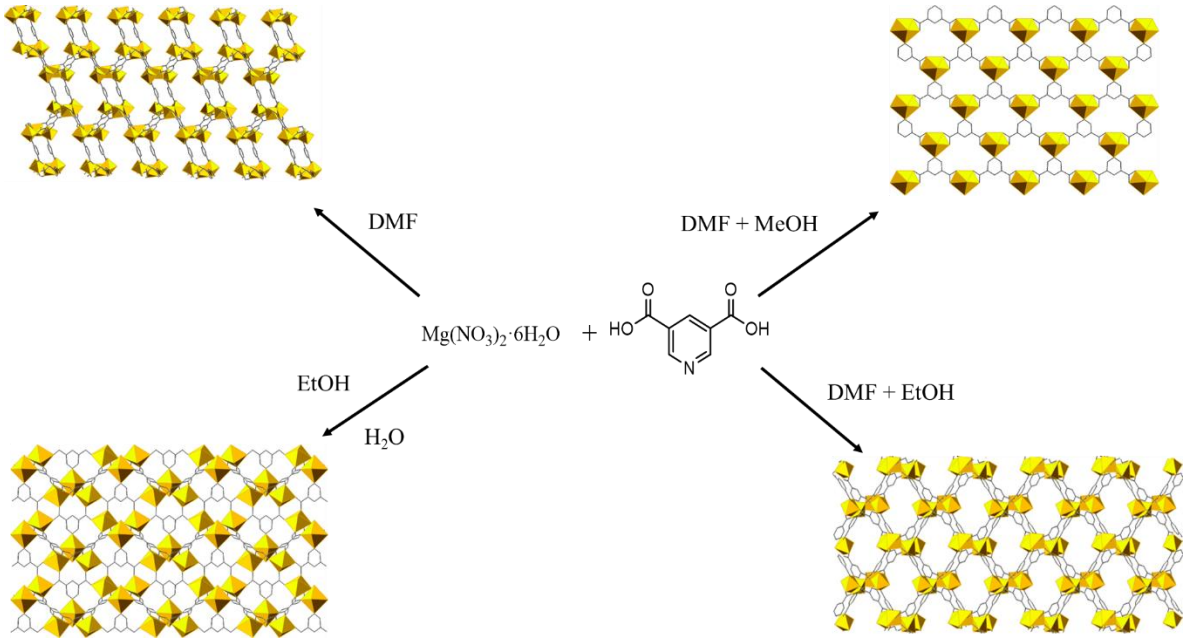

Figure 1.5.1*: Synthetic pathway to four different coordination structures using $Mg(NO_3)_2 \cdot 6H_2O$ and 3,5-PDC by varying the solvent mixture. Adapted from Banerjee et al.*[57]

1.5.3 Electrochemical deposition

MOFs can be readily synthesised by electrochemical means on conductive surfaces. The method is used to synthesise MOF thin layers in solution at ambient temperature and pressure.[58] In addition to this, deposition times are significantly shorter than those typical for solvothermal synthesis. This method can produce multiple MOF thin-films from the same ligand-metal solution and is fundamentally a cost-effective process.

There are two general deposition conditions, namely anodic and cathodic synthesis. Anodic electrodeposition involves the dissolution of the metal anode substrate in a linker containing electrolyte, with MOF formation occuring in the solution near the electrode surface. Initial nucleation occurs when a critical concentration of metal ions forms upon anodic dissolution of the metal substrate. Once MOF crystals nucleate on the substrate, no new nucleation is needed for the deposition to proceed. The four growth phases of anodic synthesis can be summarised as follows:

I. Initial nucleation, where the metal substrate begins to dissolve anodically in the solution containing the linker, and the first crystals nucleate on the electrode surface.
II. The growth of clusters, where nucleation events occur adjacent to pre-existing islands.
III. The intergrowth of crystals to form a layer. There are two steps to this phase. The self-closing behaviour of MOF thin-films are dictated by the different contributions of the applied potential (*E*) (Equation 1.5.3.1).[59]
IV. Crystal detachment from the surface as the layer becomes dense, leaving individual islands. This phase can be prevented by using shorter deposition times.

$$E = E_0 + \eta_{ohmic} + \eta_{conc} + \eta_{activation} \quad \text{(Eq. 1.5.3.1)}$$

where E_0 is the standard potential of the anodic reaction, $\eta_{activation}$ is the onset voltage of metal dissolution, η_{ohmic} is the ohmic drop due to the resistance and η_{conc} is the concentration overpotential.

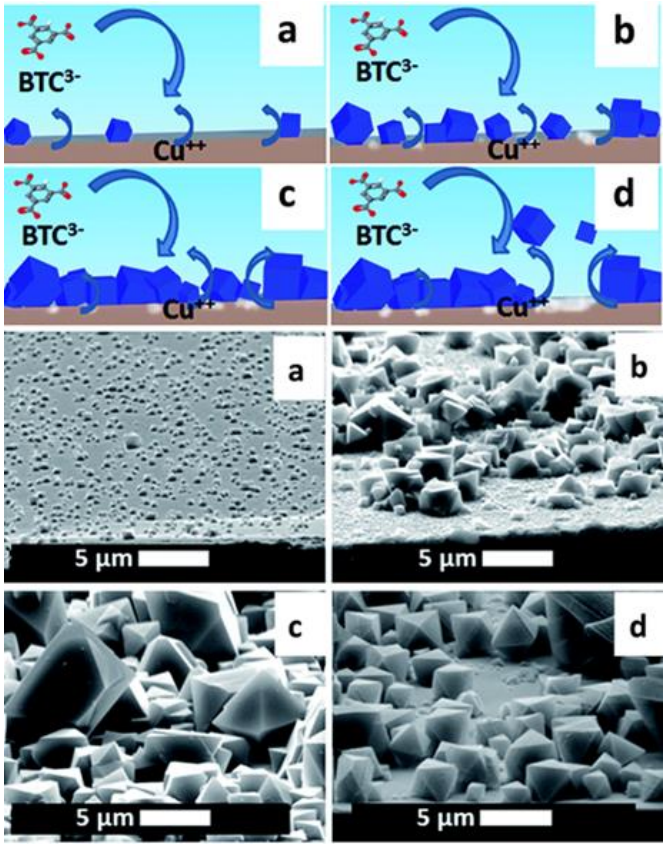

***Figure 1.5.2**: Mechanism of anodic electrodeposition onto a Cu-coated surface with the four growth phases: a) Initial nucleation; b) The growth of clusters; c) The intergrowth of crystals to form a layer; d) Crystal detachment from the surface. SEM images obtained on a Cu-coated wafer after 10 seconds, 10, 60 and 125 minutes. Figure adapted from Campagnol et al.*[60]

Under cathodic conditions, the metal ions and organic ligands are suspended in the electrolyte. The mechanism of cathodic electrodeposition is due to a change in the pH of the electrolyte adjacent to the electrode surface. This results in the formation of a pro-base at the cathode, usually oxoanions, such as nitrite ions that form from the *in-situ* reduction of nitrate ions in solution. The anions cause the local formation of OH^- which deprotonate the carboxylic acid ligands (Equation 1.5.3.3).

$$NO_3^- + H_2O + 2e^- \rightarrow NO_2^- + 2OH^- \quad \text{(Eq. 1.5.3.2)}$$

$$H_xL + OH^- \rightarrow NO_2^- + H_{x-1}L + H_2O \quad \text{(Eq. 1.5.3.3)}$$

This is achieved by the reduction of water in the solution, yielding oxide or hydroxide ions which may also be directly required as ligands for the generation of certain metal cluster SBUs. The positively charged metal ions in solution are attracted by the negative potential

at the electrode substrate surface and the local presence of deprotonated ligands. This initiates the self-assembly and deposition of MOF crystals which are confined to the conductive substrate surface. The subsequent growth of MOFs at the electrode surface allows for facile surface functionalisation. The synthetic approach is particularly useful for electrocatalytic studies using MOFs as surface-bound catalysts.

1.5.4 Microwave-assisted synthesis

Microwave-assisted synthesis is an energy efficient technique of heating with fast crystallisation due to high nucleation rates.[61] It has been proven as an effective method to produce nano-scale MOFs with high purity and uniform crystal morphology.[62] Microwave-assisted synthesis converts electromagnetic energy into thermal energy by creating a dipole moment in the reactants inside a Teflon reaction vessel that rotates to align with the electromagnetic field. From this, the sample is heated using kinetic energy generated from the constant alignment collisions between molecules in the vessel.[63]

1.5.5 Heat-treatment of MOFs

MOFs are ideal catalysts due to their high number of active sites, but often are not stable under harsh conditions. Heat-treatment of MOFs has become an increasingly popular post-modification in electrocatalyst, fuel cell and ion battery production.[64] Thermal treatment of MOFs can be conducted *via* annealing under inert gas (most commonly N_2 or Ar) or calcination in oxygen or air. Annealing is used to convert the carbon framework to a graphitic material which will be more robust to extreme conditions in comparison to the organic ligands.[65]

Materials obtained from the thermal activation of MOFs have key advantages when compared to their parent structures, most notably higher resistance to corrosion by acidic/alkaline electrolytes and improved electrolytic conductivity.[66] However, such materials still retain internal pores intrinsic to the MOF precursor material and the uniform distribution of catalytic centres affixed to the carbon support due to the location of metal ions or clusters in the MOF framework.

In the work of Pandiaraj *et al.*, MOF-5 was used as a template for the design of an oxygen reduction catalyst.[67] This was achieved *via in situ* graphitic carbon nitride polymerisation by grinding MOF-5 and melamine together before heat treatment, and doping the heat-treated MOFC with melamine in an ethanol solution prior to an additional heat treatment *via in situ* melamine polymerisation (Figure 1.5.3). The resulting MOFCN900

obtained excellent catalytic activity for the oxygen reduction reaction, with an onset potential of 0.035 V (vs. Hg/HgO) in alkaline medium. In addition to this, the system exhibited high durability and tolerance to methanol.

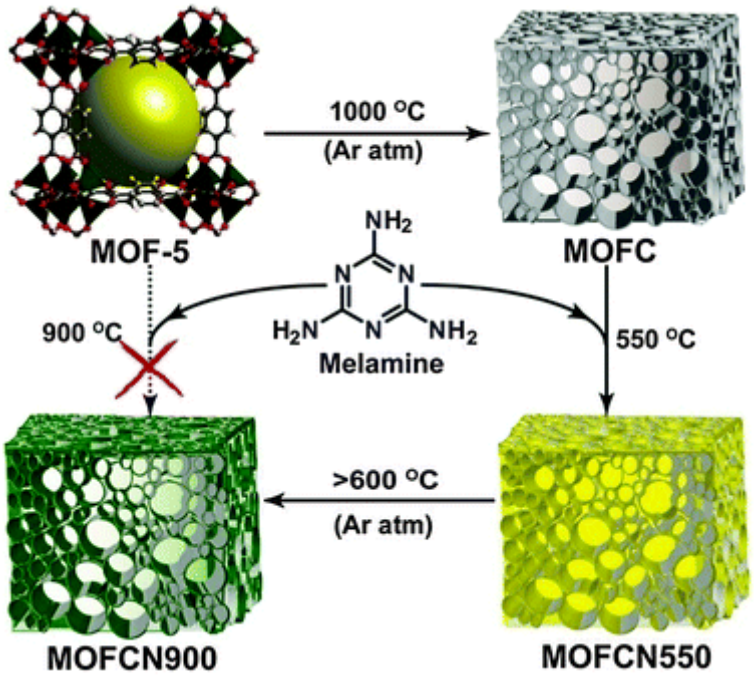

***Figure 1.5.3**: Construction of N-doped porous carbon after impregnation of melamine into the pores of annealed MOF-5 followed by carbonisation at temperatures above 600 °C. Adapted from Pandiaraj et al.*[67]

1.6 Properties and applications of MOFs

The primary interest of materials science is the discovery of new materials and the prediction and understanding of their properties. The high porosity and surface area of MOFs allows for interaction with guest molecules and makes them especially suitable for gas/chemical storage and separation,[68–70] catalysis,[71–73] drug delivery[74–76] and imaging.[77–79] In recent years the notion of MOFs as organised light-harvesters has been explored with the incorporation of photosensitising nodes into the framework.[80–82]

1.6.1 Porosity

A well-known advantage of MOFs is their low-density, arising from their porous nature.[83] This provides voids on the micro- and meso-scale which can expose their functionalities for applications in gas sorption and separation. Designing MOFs with high porosity and developing suitable activation methods for preserving and accessing their pore space have been a common theme in MOF research. The design of MOFs with permanent

ultrahigh (Brunauer–Emmett–Teller (BET) ≥ 6000 m^2 g^{-1}) surface areas is driven by the void space per weight and is achieved by incorporating rigid extended organic ligands.[84]

1.6.2 Interpenetration

MOFs can exhibit a number of entanglement structures. Interpenetration is an important subgroup that refers to the catenation of two or more individual nets, either identical or distinct, within a MOF structure.[85] The interpenetration of MOFs is a common phenomenon in systems with long, linearly extended ligands. In a single net structure, as ligand length increases, so does the accessible void volume within the formed network. This space can then enable the formation of additional networks, decreasing the void volume, but does not prevent the synthesis of MOFs with large surface areas.[86] Interpenetration can be encouraged by non-covalent bonds such as van der Waals forces and π-π interactions, which may bestow resulting MOF structure with enhanced stability and flexibility.[87] In interpenetrated MOFs, each individual net is found at a maximum displacement from one another. In the second subgroup, the distance between nets is at its minimum, formally known as interweaving. Due to the nature of both interpenetration and interweaving, a single network within an entangled structure cannot be extracted without the breaking of metal-ligand bonds.[88]

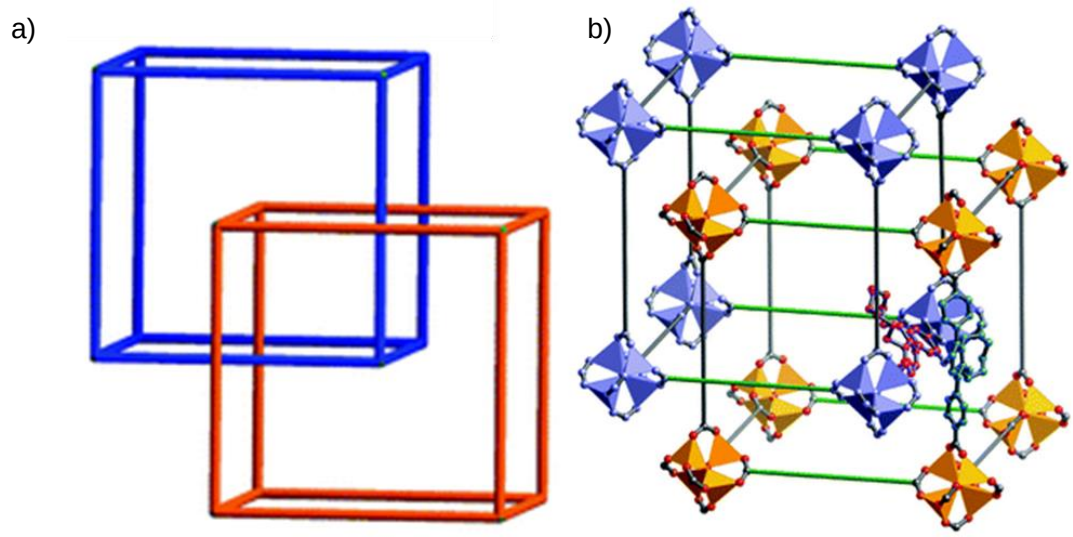

Figure 1.6.1*: a) Simplified representations of an interpenetrated MOF. b) Interpenetration of MOF–BC-4 showing π-π stacking between two central phenyl rings, highlighted in pink. Adapted from Liu et al.*[89]

Crystal engineering methods can be used to control the pore size of a MOF. Interpenetration is a synthetic approach that has been implemented to alter pore sizes and

synthesise MOFs that have a gas-adsorption selectivity for a particular gas molecule within a mixture.[90] The synthesis of pure-phase interpenetrated MOF-5 was confirmed using single-crystal X-ray diffraction in the work of Kim *et al.*[91] Modification of the pH during solvothermal synthesis, resulted in the catenated structure over traditional MOF-5. The pore size distribution was obtained from Ar sorption experiments at 87 K and showed one main peak at 6.7 Å which was consistent with the single crystal structure. Compared to traditional MOF-5, interpenetrated MOF-5 showed an enhanced thermal stability as well as a higher tolerance to moisture. Despite its overall smaller surface area, the interpenetrated MOF showed a significantly higher gravimetric and volumetric hydrogen uptake than MOF-5 at atmospheric pressure due to its higher enthalpy of adsorption. Overall, the MOF showed a higher volumetric hydrogen uptake than MOF-5 at room temperature, up to a maximum of 100 bar.

1.6.3 Gas storage

Gas storage and separation are valuable to many aspects of society, including environmental protection (CO_2 capture), energy storage (H_2 and CH_4) and industrial synthesises (NH_3 and CO). Currently, gas fuels are predominantly stored by compression in steel vessels with internal pressures up to 1000 bar.[92] The internal pressure of these containers can be decreased by incorporating porous solids such as zeolites, but these possess poor selectivity and require complicated activation processes.[93] The separation of gases has found a lot of academic attention in recent years due to environmental applications, such as the selective absorption of greenhouse and toxic gases. MOFs can embody large pore sizes, possess stability at high temperatures and low pressures, have relatively simple activation processes and can possess selective affinities between adsorbates. This has consequently put focus on these materials as candidates for selective gas storage.[31,94] Many established MOFs are already commercially available for gas sorption (Table 1.6.1).

Table 1.6.1*: Gas uptake for a variety of MOFs commercially available at Sigma Aldrich Ltd. and commonly utilised for gas separation.*

MOF	Ligand	Metal	Gas	BET Surface Area ($m^2\ g^{-1}$)	Capacity at 300 k (mmol g^{-1})	Pressure (bar)	Ref.
MOF-74	H_4DOBDC	Mg	CO_2	1425	5.28	$1x10^{-3}$	[95]

MOF-5	BDC	Zn	H_2	7100	1.13	100	[96]
HKUST-1	BTC	Cu	CH_4	1850	11.74	35	[97]
MOF-74	H_4DOBDC	Fe	CO	1360	6.04	1.2	[98]
UiO-66	NH_2BDC	Zr	NH_3	1067	10.5	1.0	[99]

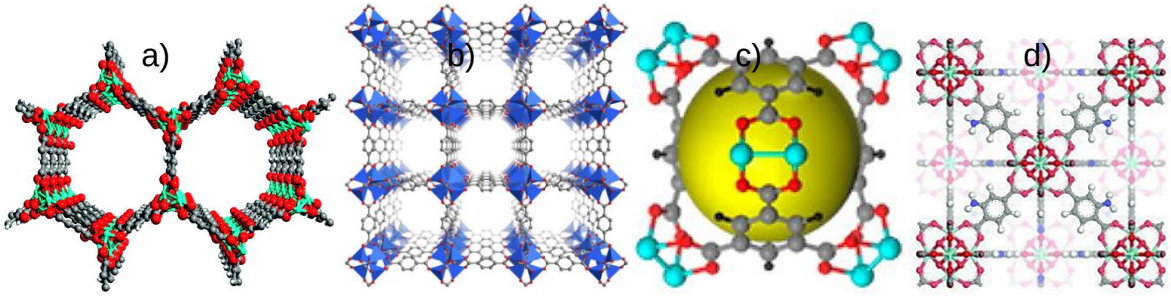

***Figure 1.6.2**: Commercial MOFs mention in Table 1.6.1, MOF-74[100] (a), MOF-5[23] (b), HKUST-1[97] (c) and UiO-66 (Universitetet i Oslo)[101] (d).*

1.6.4 Gas separation

With the use of fossil fuels rising to *approx.* 37 billion tonnes in 2018, the need for effective measures to separate greenhouse gases from gas mixtures has never been higher.[102] CO_2 capture in MOFs centres around optimisation of phys- and chem- adsorption interactions between the framework and CO_2 molecules.[103] At present there are three experimental approaches in MOF synthesis to enhance such interactions:

I. Functionalising organic linkers with polar groups (e.g. -OH, -CN, -NO_2, -SH). As CO_2 possesses a large quadrupole moment, polarising the molecules can enhance affinity.[104]
II. Generating vacant metal sites through MOF activation for CO_2 coordination.[105]
III. Functionalising pores with Lewis-base, nitrogen-containing, triazoles[106] and amines.[107]

A drawback of many MOFs is their instability in water. This becomes a problem when utilised commercially to extract CO_2 from pressurised air with a considerable water vapour content. HKUST-1 is an excellent CO_2 adsorption MOF, but uptake is halved at 8 % relative humidity (RH).[108] As a result a number of moisture-stable CO_2 capture MOFs have been developed. MIL-100(Fe) is a mesoporous material with {$Fe_3O(H_2O)_2$} clusters and BTC ligands.[109] The MOF shows excellent results, with CO_2 uptake reaching 26 mg g^{-1} at 3%

(RH) and low adsorption enthalpies on repeated cycles. At 40 % RH, the total CO_2 capture reached 105 mg g^{-1}, showing a five-fold increase compared to anhydrous conditions.[110] The result suggest the solubility of CO_2 is enhanced by water in the mesopores. The MOF InMOF-1 contains biphenyl-3,3',5,5'-tetracarboxylate (BPTC) and binuclear {$In_2(\mu_2$-OH)} building blocks.[111] Due to the -OH functional group, there was a significant increase of *approx.* 11 wt. % in CO_2 capture under 20 % RH, a two-fold increase compared to anhydrous conditions. This can be attributed to CO_2 confinement effects induced by water molecules as the -OH functional groups inside the pores act as a directing agent for water in the pores result in more efficient packing.[112]

1.6.5 Catalysis

1.6.5.1. Electrical conductivity of MOFs

The application of MOFs in electrocatalytic reactions is a relatively recent focus of interest in contrast to gas sorption and photocatalysis. High electrical conductivity is rare in MOFs, yet it allows for diverse applications in electrocatalysis,[113,114] charge storage[115] and chemiresistive sensing,[116,117] among others. Initially, MOFs were not considered for such electrocatalytic-based applications due to the evident low charge carrier ability of commonly employed linkers and instead were generally considered electrically insulating materials.[118] MOFs incorporating simple, non-conjugated, redox inactive linkers with chelating metal binding sites resulted in a low density of electrical charge carriers and no evident low-energy charge transport pathways within the ligand structure, and as a result the MOF.[119] As ligand design and crystal engineering became more commonplace, investigations began into the synthesises of conductive MOFs.

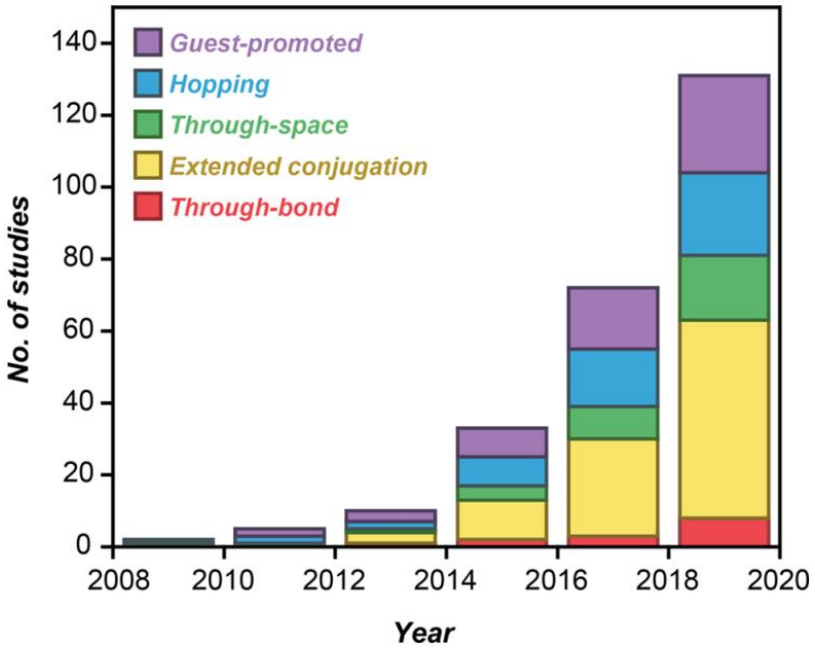

***Figure 1.6.3**: Histogram showing the number of papers focusing on aspects of electrical conductivity in MOFs from 2008 and further categorised by the design strategy employed. Adapted from Xie et al.*[119]

Favourable electrocatalytic conditions exhibit a catalyst which has a high charge carrier transport. The first report of a conductive MOF was reported by Takishi *et al*. in 2009 with $Cu[Cu(pdt)_2]$ (pdt = 2,3-pyrazinedithiol), a MOF constructed from copper-thiol bonds with a recorded conductivity of 6×10^{-4} S cm^{-1}.[120] The metal-sulphur bonds carry greater conductivity in contrast to metal-oxygen bonds and chelating binding sites.[121] In the years proceeding there has been great progress made in conductivity values. These advancements can be attributed to the development of organic ligands that give rise to facile electron transfer within the MOF. MOFs which incorporate organic linkers with fully π-conjugated ligand systems such as aromatic, double and triple bonded systems, have been proven to increase overall conductivity in both 2- and 3-dimensional MOFs in comparison to structurally similar framworks which contain non-conjugated linker moieties.[122] Guest molecules can also be introduced into the framework to create alternative, low-energy pathways.[123] This method is of great interest as it involves not the synthesis of new materials, but the modification of common, understood, pre-established MOFs, highlighted with the research undertaken on a conductive analogue of HKUST-1. The conductivity of the $\{Cu_2\}$-based MOF increased from 1×10^{-4} to 7×10^{4} μS cm^{-1} upon the inclusion of highly conjugated, bridging tetracyanoquinodimethane (TCNQ) molecules.[124] The inclusion of guest molecules is commonly employed with the deposition of MOFs on thin-film surfaces,

having an additive increase in the overall conductivity by decreasing the thickness of the MOF and thus minimising the electron transport distance to the electrode surface while allowing facile guest molecule adsorption.[125]

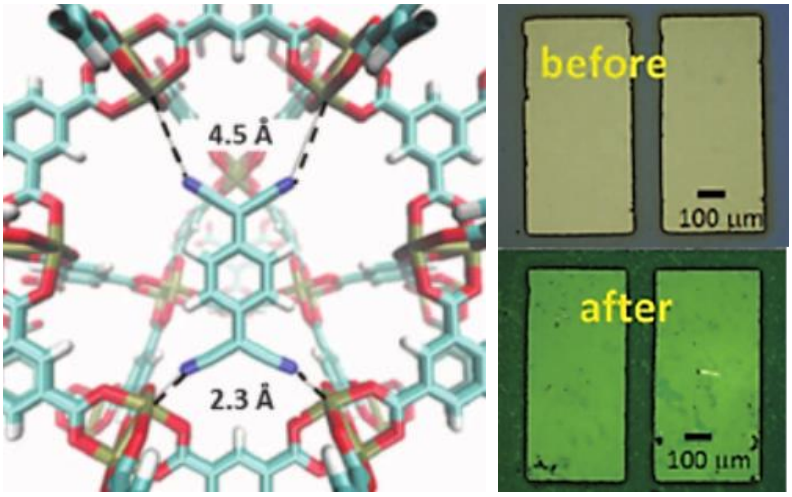

Figure 1.6.4*: a) The minimum-energy configuration for TCNQ@$Cu_3(BTC)_2$. b) Optical images of thin-film HKUST-1 before and after TCNQ infiltration. Adapted from Talin et al.*[124]

1.6.5.2. Water splitting

Fossil fuels are abundant, cheap, easy to store and have a high power density.[126] However, the consumption of these fuels results in the release of CO_2 into the atmosphere and in turn, climate change. Despite a decrease in output in 2020 due to the global pandemic, CO_2 emissions are set to rebound in 2021 to 33 billion tonnes, growing by 4.5 % in comparison to 2019, the second largest increase recorded.[127] One of the proposed alternatives is to use hydrogen as a clean, carbon free fuel. The sustainability of this alternative depends heavily on the method in which the electricity and energy sources are generated. Water splitting by electrolysis (or artificial photosynthesis) for the production of hydrogen gas is seen as a clean method of production. Unfortunately, commercial electrolysis of water currently only accounts for 3-4% of total hydrogen production globally.[128] The remainder is produced from fossil-fuel transformations, such as steam reforming from hydrocarbons.[129]

The overall process of water splitting requires four separate electron transfer events that are coupled to an anode which can facilitate the four electron and four proton coupled splitting of water, known as the oxidation half reaction (Equation 1.6.5.2). The protons and electrons are recombined forming H_2 at the cathode, i.e., the reduction half reaction

(Equation 1.6.5.1). The water oxidation step of the process is particularly challenging due to its high energy demand (ΔG = 4.92 eV). In comparison to hydrogen formation, it is the bottleneck in water electrolysis. Catalysing the oxygen evolution reaction is key to all water splitting technologies for energy conversion. Water splitting has been identified as an important technology to produce an alternative, sustainable, and renewable energy source.

$$4H^+ + 4e^- \rightarrow 2H_2 \qquad E^0 = 0.00 \text{ eV} \qquad \text{(Eq. 1.6.5.1)}$$

$$2H_2O \rightarrow O_2 + 4H^+ + 4e^- \qquad E^0 = -1.23 \text{ eV} \qquad \text{(Eq. 1.6.5.2)}$$

1.6.5.3. Hydrogen evolution reaction

Pristine MOFs and MOF-derived materials have been shown to make promising hydrogen evolution catalysts.[130,131] In particular, MOFs with intrinsic acid-stability are highly reported as HER active materials as acidic solutions allow for lower energy barriers and thus increased catalytic activity.[132] The work of Liu *et al.* reports the synthesis of Co-MOF nanorods on carbon fibre paper, subjected to phosphorisation using cobalt phosphide (CoP) to enhance electron transfer from CoP to the MOF structure (Figure 1.6.5).[133] CoP/Co-MOF/CF exhibited excellent stability in *aq.* 0.5 M H_2SO_4, 1M KOH and 1 M PBS buffer solution. It also outperformed both Co-MOF and CoP particles with an overpotential of 34 mV at a current density of 10 mA cm^{-2} in 0.5 M H_2SO_4. This is close to that of Pt/C (25 mV), and lower than Co-MOF and CoP, which showed overpotentials of 75 and 89 mV, respectively at an identical current density.

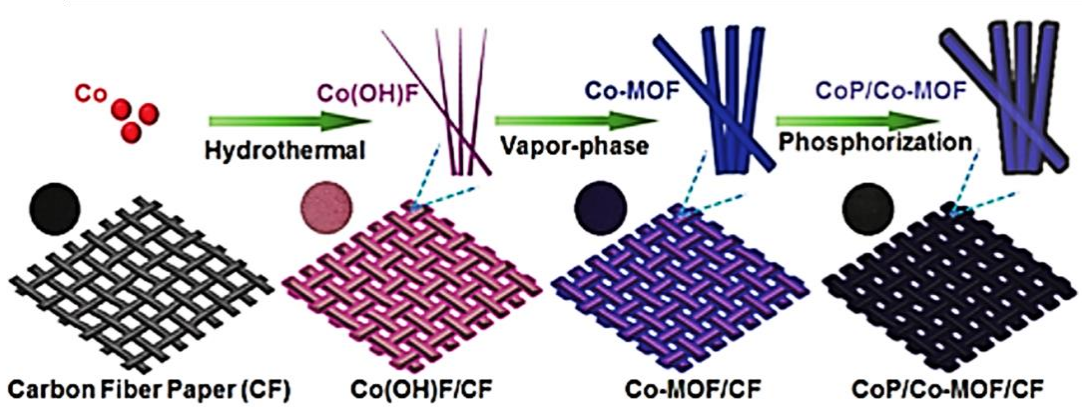

Figure 1.6.5*: The fabrication process of CoP/Co-MOF. Figure adapted from Liu at al.*[133]

1.6.5.4. Oxygen evolution reaction

The catalysis of the oxygen evolution reaction is critical to all methods of water splitting materials. The first step in the overall water splitting reaction is a rather complex process involving the transfer of four electrons and four protons, displaying high energy demanding steps and a high activation barrier for the O−O bond formation.[134] As this is the rate limiting step in the overall water-splitting reaction, the effectiveness of a potential catalyst relies on its efficiency to catalyse the endergonic anodic reaction. Over recent decades, heterogeneous and homogenous water oxidation catalysts such as noble metal oxides[135,136] and related molecule-based Ir(II)[137] and Ru(II)[138] complexes have shown excellent performances with satisfactory conversion rates. However, the need for expensive trace metals limits their usefulness in large-scale applications and inhibits the commercialisation of electrochemical water splitting technologies. Candidate catalysts encounter an additional difficulty due to the strong oxidising conditions and intermediates associated with water oxidation, and often leads to the decomposition of the catalyst during the reaction. The removal of four electrons and two water molecules to generate O_2 results in a reaction with slow kinetics and usually requires a high overpotential to achieve a sufficient reaction rate and current density for viable green energy applications.

The bimetallic MOF series CTGU-10a-d was reported by Zhou *et al.* based on trinuclear carboxylate clusters connected *via* (6,6)-connected **nia** nets to hexadentate carboxylate ligands.[139] Four isostructural transition-metal MOFs were synthesised with the general formula $[NH_2(CH_3)_2][M_3(\mu_3\text{-}OH)(H_2O)_3(BHB)]$ (where BHB = 2,6-diamino-8-(2-dimethyl-aminoethylsulfanylmethyl)-3H-quinazolin-4-one and M3 = Co_3, Co_2Ni, $CoNi_2$ and Ni_3). The {$CoNi_2$} metal combination CTGU-10c2 was identified as the best material for OER catalysis, with an overpotential of 240 mV at a current density of 10 mA cm^{-2} and a Tafel slope of 58 mV dec^{-1}. In addition to this the MOF exhibited a long-term stability in excess of 50 h in highly alkaline solution. The MOF's activity is superior to that of RuO_2 and confirms the potential for high-performing pure-phase MOF-OER electrocatalysts, alongside pristine MOF catalysts summarised in Table 1.6.2.

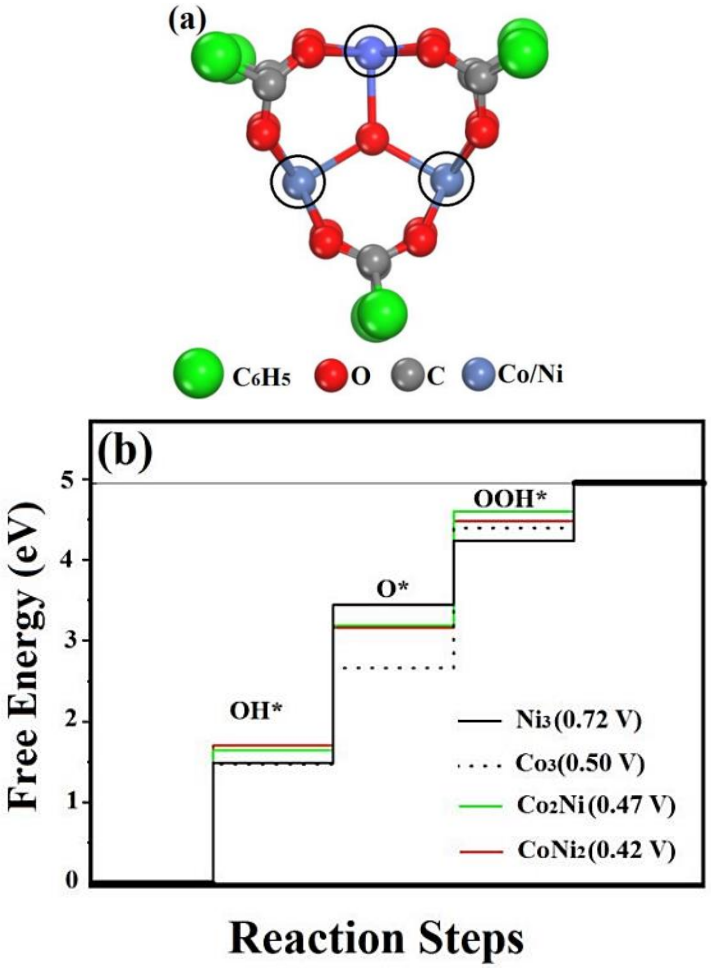

***Figure 1.6.6**: a) The DFT model of the different metal arrangements of the MOF series. b) The Gibbs free energy for the intermediate states involved in OER showing the overpotentials calculated using the maximum ΔG derived from the profile. Adapted from Zhou et al.*[139]

***Table 1.6.2**: Summary of OER performance of pristine MOF catalysts incorporating earth-abundant metals.*

Catalyst	Conditions	η @ j = 10 m A/cm^2 (mV)	Tafel slope (mV/dec)	Ref.
Fe/$Ni_{2.4}$/$Co_{0.4}$–MIL-53	1 M KOH	219	52	[140]
NiFe-MOF-74	1 M KOH	223	72	[141]
$Co_{0.6}Fe_{0.4}$–MOF-74	1 M KOH	280	56	[142]

CoCd–BNN	0.1 M KOH	353	110	[143]
NiVFe-MOF	1 M KOH	225	34	[144]
$CoNi_2$-MOF	1 M KOH	240	58	[139]
CoP/CoCu-MOF	1 M KOH	295	65	[145]

Practical OER catalysts must function for extended periods of time with high oxygen evolution rates under the operational conditions of the devices into which they are integrated. In addition to this, potential commercially successful OER catalysts should be made of reliably inexpensive earth-abundant materials. In this respect, current efforts focus on homo and heterometallic oxides,[146,147] phosphides,[148] carbides,[149,150] or heterogenised molecular compounds, consisting of earth-abundant metal ions, notably Co(II),[151] Fe(II),[152] Ni(II),[153] Mn(II)[154,155] and Cu(II),[156] as well as metal-substituted graphitic materials.[157] Although pure-MOF OER catalysts have been previously reported, the modification of MOFs into hybrid materials *via* deposition on a conductive substrate or controlled *via* pyrolysis or annealing has come to the fore in recent years.[66] The synergistic nature means that these hybrid materials overcome the potential limitations of MOFs such as conductivity and charge transfer while retaining porosity, high surface area and access to catalytic centres, not commonly seen in traditional nanomaterials. Overall, these systems have been noted as a more commercially viable solution to electrochemical water splitting (Table 1.6.3).

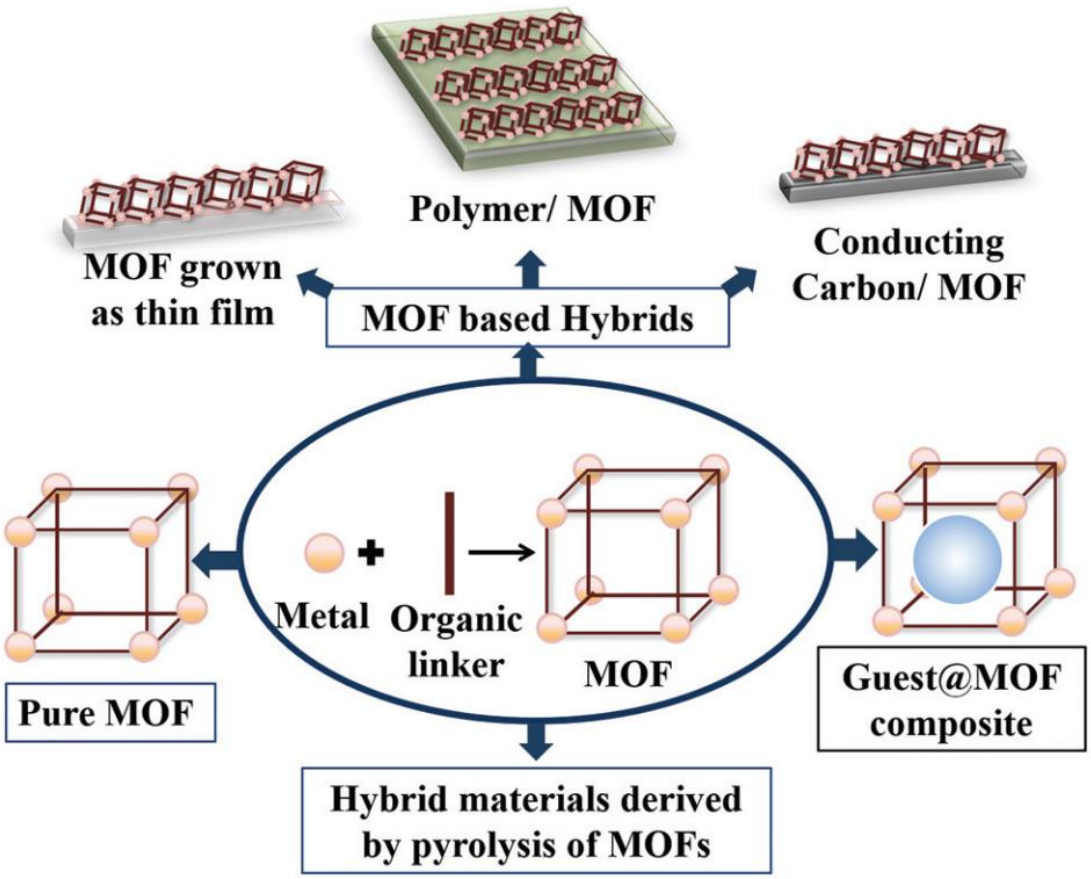

***Figure 1.6.7**: Design strategy of MOF-based catalysts using pristine MOFs, guest@MOFs, MOF-based hybrid materials and materials derived by pyrolysis of MOFs. Adapted from Mukhopadhyay et al.*[158]

One of the first successful MOF-hybrid catalysts was the Co_3O_4-carbon porous nanowire array system reported by Ma *et al.* in 2014 using a MOF precursor.[159] A Co(II) MOF with naphthalenedicarboxylate ligands was grown on Cu foil *via* solvothermal synthesis, resulting in individual pillar structures on the Cu foil surface. The material was then annealed at 450 °C under N_2, carbonising the MOF into a porous carbon nanowire assembly containing cobalt oxide particles imbedded within the structure (Figure 1.6.8). OER studies were conducted on the system in 1 M KOH solution and exhibited greater activity than IrO_2 at the same pH, as well as enhanced activity compared to bulk Co_3O_4, and the parent MOF. The precursor MOF and cobalt oxide showed Tafel slopes of 142 mV dec^{-1}, and 123 mV dec^{-1}, respectively. The Co_3O_4-carbon arrays revealed a significantly lower Tafel slope of 70 mVdec^{-1} in addition to reaching a prolonged current density of 140 mA cm^{-2} without degradation or becoming detached from the Cu foil despite its pillared structure.

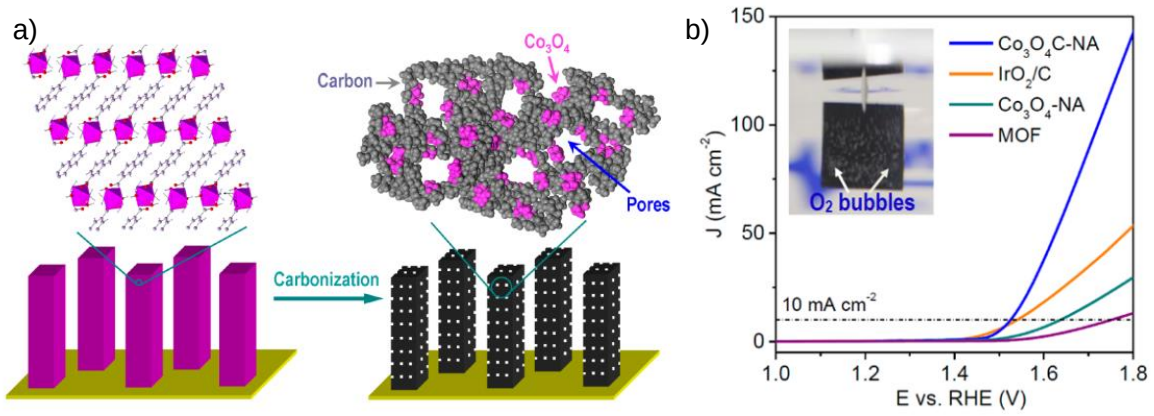

***Figure 1.6.8**: a) The synthesis of the hybrid Co_3O_4-C arrays. b) Linear sweep voltammogram experiments comparing the OER activity of Co_3O_4-C/Cu, IrO_2/C, Co_3O_4 and the precursor MOF. Adapted from Ma et al.*[159]

MIL-100(Fe) is composed of 1,3,5-benzenetricarboxylic acid (BTC) ligands and {FeO_6} octahedrons. The MOF possesses a flexible structure and improved stability due to the existence of high valence metal ions, in which the reversible redox reaction between Fe^{2+} and Fe^{3+} are the key aspects of this promising cathode catalyst.[160] The work of Li *et al.* involved the deposition of MIL-100(Fe) on 3D nickel foam (NF) *via* solvothermal synthesis to form a MIL-100(FeNi)/NF electrode to increase mass transport within the material.[161] These factors enabled the catalyst to produce an OER performance with a current density of 100 mA cm^{-1}, an onset overpotential of 245 mV and a Tafel slope value of 30.4 mV dec^{-1}.

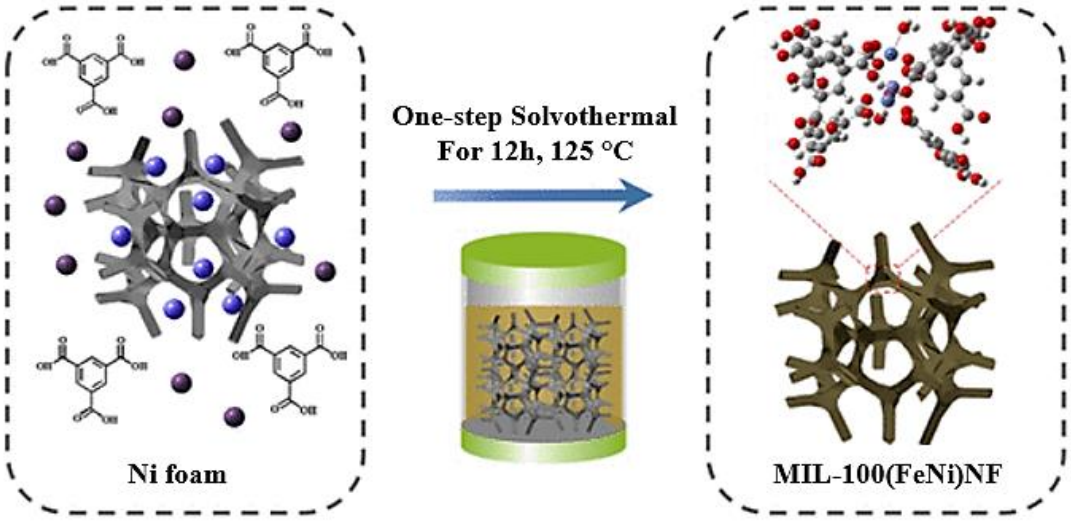

***Figure 1.6.9**: Synthesis of MIL-100(FeNi)/NF. C, grey; O, red; Fe(II), purple, hydrogen; white. Adapted from Li et al.*[161]

***Table 1.6.3**: Summary of OER performance of MOF-based catalysts in 1 M aq. KOH solution.*

Catalyst	Active sites	η @ j = 10 m A/cm^2 (mV)	Tafel slope (mV/dec)	Ref.
Co_6W_gC@NC	$CoO_x/Co(OH)_2$	159	45	[162]
MIL-100(FeNi)/NF	1 M KOH	243	30	[161]
Ru-NiFe-MOF/NF	$Ni(OH)_2$	205	50	[163]
FeNi@NCNT	FeNi alloy	300	48	[164]
2D Co_3O_4/CBDC	Co_3O4_4	208	50	[165]
CoMo–H	CoOO-MoO_2	312	69	[166]
NF@NC-$CoFe_2O_4$/C	$CoFe_2O_4$	240	45	[167]
Co_9S_8/NSCNFs-850	Co_9S_8	302	54	[168]
$CoSe_2$-450	$CoSe_2$	330	79	[169]
$CoTe_2$@NCNTFs	$CoTe_2$	340	83	[170]
CoP/rGO-400	CoP	330	66	[171]
NiCoP/C nanoboxes	NiCoP	330	96	[172]
H_3LCoCN-800	$Co_2P_2O_7$	320	64	[173]

1.6.6 Photocatalysis

Artificial photocatalysis is concerned with the design of materials that can absorb and convert solar energy into chemical energy. The field has had successes in the photocatalytic splitting of water into H_2[174,175] and O_2,[176,177] photodegradation of organic molecules,[178] and CO_2 photoreduction.[179,180] Metal SBUs often contain coordination sites not occupied by the multinodal organic struts (e.g. solvent molecules) which can be evacuated upon heating the MOF at elevated temperatures under vacuum.[181] This generates Lewis acid and coordinatively unsaturated sites around the metal ions that can act as catalytic sites. MOFs can be synthesised to incorporate such metal sites to act as solid Lewis acids and thus as heterogeneous catalysts for reactions catalysed by these specific vacant sites. With the introduction of photosensitising units within the MOF structure, solar energy can be funnelled to these catalytic centres. The processes of photosynthesis for both water splitting and CO_2 photoreduction can be simplified for potential artificial analogues. There are three crucial steps essential for sunlight to be converted to chemical energy:[182] First, visible and UV-light are absorbed by a photosensitiser to create a charge separation of states and a long-lived excited state. Next, redox equivalents are created and migrate to nearby catalytic centres. Finally, oxidation and reduction half reactions occur with the redox equivalents (electrons and holes) at the catalytic centres.

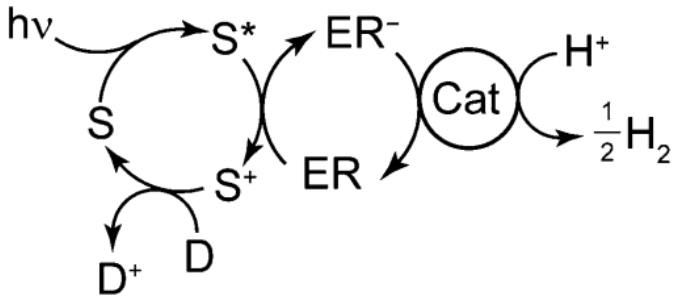

Figure 1.6.10*: General scheme for photocatalytic H_2 production. The sensitiser (S) absorbs photons, and its excited state* is *oxidatively quenched by the electron relay (ER), which then transfers an electron from its reduced state (ER^-) to the catalyst producing H_2. The oxidised sensitiser (S^+) is then reduced by the sacrificial electron donor (D). The reaction is generally thermodynamically favoured. Adapted from Teets et al.*[183]

Embedding a sensitiser within the struts of a catalytically active MOF structure allows for, in principle, a single, solid-state structure that contains a regular array of photosensitiser and catalytic centres, to combine the three crucial steps. The use of ligands with extended π-electron delocalisation can act as an electron relay to funnel electrical energy to the catalytic site.

1.6.6.1. Photophysical properties of Ru(II) complexes

Photolysis of water was first demonstrated by Fujishima and Honda using a TiO_2 electrode.[184] Since then large amounts of research has been focused on TiO_2-type photocatalyts.[185–187] A drawback of this is that TiO_2 possesses a relatively large band gap energy (3.2 eV) requiring UV-light for photocatalytic activity.[188] UV-light accounts for *approx.* 5 % of global solar irradiation, leading to low photocatalytic efficiency.[189] In recent years, with the need for sustainable renewable energy sources growing, the development of visible-light-responsive photocatalysts has come to the fore.[175]

Ruthenium polypyridines are a group of photoactive complexes, which absorb especially within the visible-light range, with strong photoredox abilities. $[Ru(bpy)_3]^{3+}$ (bpy = 2,2'-bipyridine) is one of the most frequently exploited photosensitisers as it is a highly-emissive complex.[190] Problems arise when substituting bipyridine rings for MOF applications, as the complex can exist as two isomers, with little control over geometry when substituting the pyridine rings.[191] $[Ru(tpy)_2]^{2+}$ (tpy = 2,2';6'2''-terpyridine) exhibits weak emissions ($\Phi < 5\times10^{-6}$) and a short lived excited state (τ) (120 ps). However, ruthenium-terpyridine complexes have been gathering interest as they have only one geometric isomer, a broad absorption range in the visible spectrum (λ_{max} = 472 nm vs 452 nm for $[Ru(bpy)]^{2+}$) and due to the ease of substitution at the 4-position of the central pyridine ring of the ligand, can construct linear supramolecular assemblies.[192,193] Substituting extended π-systems with coordination nodes, has the cooperative effect of extending the luminescent lifetime.[194] The substitution of the 4-position of both the central and peripheral pyridine rings in MOF assembly has not been reported to date.

Incorporating π-accepting ligands can manipulate the energy of metal d-orbitals to reduce the energy of the ^{1}MLCT and thus the ^{3}MLCT resulting in a red shift of λ_{max} with respect to $[Ru(tpy)_2]^{2+}$ and improved luminescence lifetimes.[195] Hanan *et al.* substituted the central pyridine ring for a triazine in $[Ru(tpy)(trz)]^{2+}$ (where trz = 2-phenyl-4,6-di(pyridin-2-yl)-1,3,5-triazine) in Figure 1.6.11, resulting in a λ_{max} (absorption) = 281 nm, ε = 50,600 $M^{-1}cm^{-1}$, λ_{max} (emission) = 700 nm and τ = 9 ns.[196] The significant increase in the excited state lifetime can be attributed to stabilisation of the ^{3}MLCT state due to the planar structure of the ligand from coplanarity arising from intramolecular hydrogen bonding between the nitrogen atoms on the triazine ring and hydrogens on the peripheral phenyl ring. The enhanced photophysical properties of trz-based ruthenium complexes have only been reported by Hanan *et al.*.[195,196] These promising complexes warrant future work into the

incorporation of photosensitising ligands into MOFs. This can be achieved through functionalisation of the 4-position on the three pyridine rings with carboxylic acid functionalities.

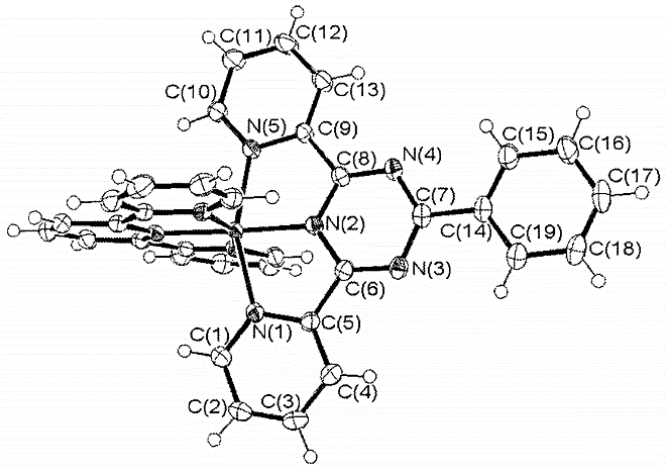

Figure 1.6.11*: Crystal structure of complex [Ru(tpy)(trz)]$^{2+}$. Adapted from Hanan et al.*[196]

1.6.6.2. Ru(II) Photosensitisers Incorporated-MOFs for Photocatalytic Applications

One of the first MOFs to incorporate a ruthenium poylpyridine was Ti-MOF-Ru(tpy)$_2$, synthesised by Tayao *et al*. using a bis(4'-(4-carboxyphenyl)-terpyridine)Ru(II) complex as a strut between Ti-oxo clusters.[197] Ti-MOF-Ru(tpy)$_2$ promotes photocatalytic H_2 production from water using triethanolamine (TEOA) as a sacrificial electron donor under visible-light irradiation between 420-620 nm. 2.1 μmol of H_2 was evolved per 6 h cycle using a Xe lamp, without the presence of a cocatalyst, and 10.9 μmol when employing H_2PtCl_6 as a cocatalyst. Single-crystal X-ray diffraction was not obtained for the structure but PXRD patterns shows peaks at *approx.* 6° (2θ), characteristic of the Ru(typ)$_2$-based linker.

Another ruthenium-based MOF showing photocataylitic properties is Ru-MOF-2 (Cd[Ru(dcbpy)$_2$(bpy)$_2$]·3(H_2O), where dcbpy = 2,2′-bipyridine-4,4′-dicarboxylate), synthesised by Zhang *et al*..[198] It is an interpenetrated, photocatalytically active MOF, capable of CO_2 photoreduction. It contains Cd(II) centres coordinated to five oxygen atoms from four Ru(4,4′-dcbpy)$_2$(bpy)$_2$ units, interpenetrating *via* π-π stacking interactions connecting dcbpy^{2-} ligands between neighbouring nets. The structure has broad absorption bands in the range 400-650 nm with a luminescence life time of 6.45 μs. It is a competitive CO_2 photoreduction catalyst, with formation rates ($R_{product}$) of 71.7 μmol (g of catalyst)$^{-1}$ h^{-1} obtained using visible light in the presence of TEOA as a sacrificial agent, improving on previously reported photoactive MOFs and light-responsive semiconductors.[199–201]

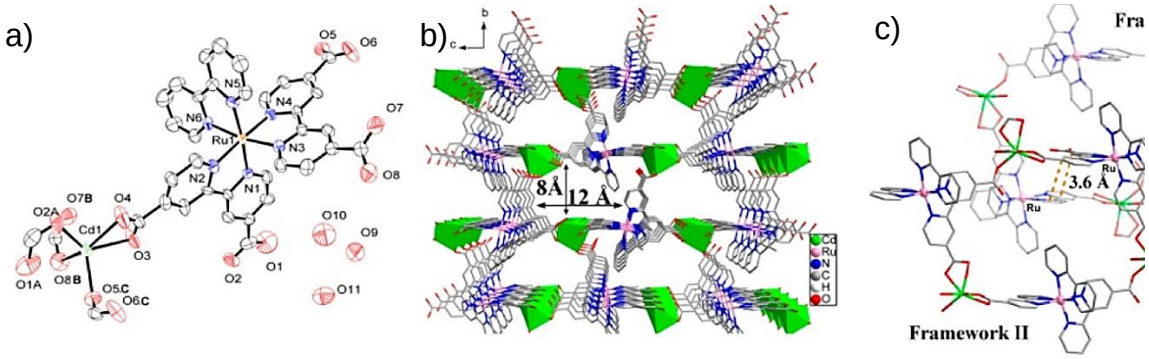

Figure 1.6.12*: a) The asymmetric unit of Ru-MOF-2 b) Two interpenetrated nets showing void channel dimensions. c) The π-stacking interaction between nets. Adapted from Zhang et al.*[198]

High thermal and photic durability and extended recyclability arise from interpenetration when comparing Ru-MOF-2 with its non-interpenetrated analogue Ru-MOF-1. Both structures exhibit comparable CO_2 photoreduction potential, producing 16.1 and 17.2 μmol of COO^- in 6 h with a quantum yield of 0.51 % and 0.54 % using irradiation at 475 nm, respectively but Ru-MOF-2 retained its structural integrity over time, with COO^- production only decreasing from 16.1 to 14.8 μmol after six, 6 h cycles.

Due to the excellent absorptivity of most photosensitisers, only the superficial layers of a MOF get the opportunity to absorb light. In addition, efficiency is limited by diffusion of radicals or intermediates through MOF channels. These challenges can be overcome by synthesising photosensitising 2D metal-organic layers (MOLs).[202] Hf_{12}-Ru-Re is a MOL synthesised by Lin *et al*. with incorporated Ru(II) nodes which are adjacent to six {Re(MBA)$(CO)_3$Cl} (MBA = 2-(5′-methyl-[2,2′-bipyridin]-5-yl)acetate) catalytic ligands, templated into stacked layers *via* Hf_{12} clusters, seen in Figure 1.6.13.[203] Electron transfer can be facilitated as the distance between ruthenium photosensitisers and rhenium catalytic centres is *ca.* 1.3 nm. The MOL exhibits high CO_2 to CO reduction turnover numbers (TONs) of 8613 under an artificial light source and a maximum of 670 in 6 h of sunlight, with an *approx.* 98 % selectivity for CO over COO^-.

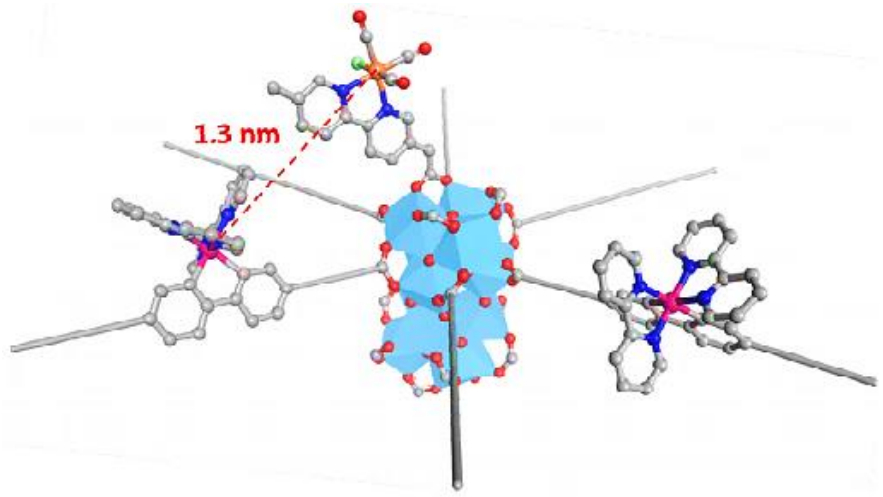

***Figure 1.6.13**: Arrangement of Re and Ru centres around Hf_{12} clusters. Re to Ru distances are 1.3 nm. Ligand backbone simplified as grey rods; O, red; Ru, pink; Re, orange; HfO, blue tetrahedra. Adapted from Lin et al.*[203]

1.7 Aims and objectives

The central aim of this research is to synthesise a series of novel MOFs that can be modified through inorganic SBU and organic linker variations. A series of organic linkers based on the triangular SBU with carboxylic acid donor sets are investigated, extending from both a benzene and a 1,3,5-triazine core. The carboxylic acid moieties are expected to react with oxophilic metal centres to afford robust, porous MOFs, having applications as water oxidation catalysts and large pore volumes for gas uptake. The electrocatalytic water oxidation of monometallic Co-based and mixed-metal MOFs are investigated. From a structural perspective, the use of flexible acetylene groups and coplaner peripheral phenyl-triazine rings are incorporated into the design of the organic ligands to investigate the effects of such groups on the resulting MOF structures. In addition to the investigation of pristine MOFs, modifications such as the growth MOF thin films on a conductive substrate, and the use of MOFs as self-sacrificing templates *via* thermal treatment is also explored. It is hoped that these methods can be used to improve the electrocatalytic water oxidation activity of these MOF-derived systems in comparison to the precursor MOF material.

For these purposes, the following ligands were employed:

H_3BTEB = 4,4',4''-(benzene-1,3,5-triyltris(ethyne-2,1-diyl))tribenzoic acid
H_3TAP = Trimethyl-4,4',4''-(((1,3,5-triazine-2,4,6-triyl)tris(benzene-4,1-diyl))tris(ethyne-2,1-diyl))tribenzoate
H_3TAM = Trimethyl-3,3',3''-(((1,3,5-triazine-2,4,6-triyl)tris(benzene-4,1-diyl))tris(ethyne-2,1-diyl))tribenzoate

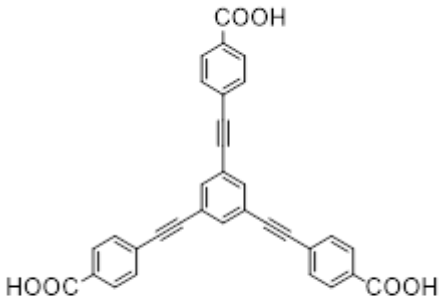

H_3BTEB

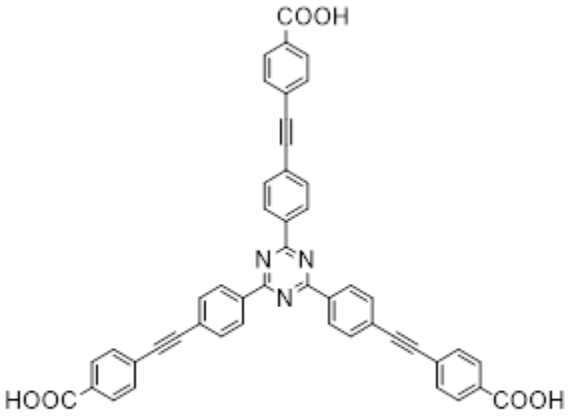

H_3TAP

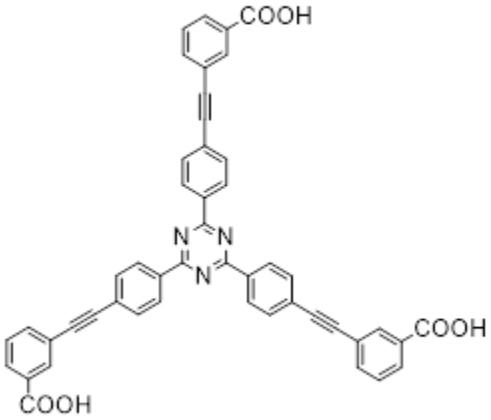

H_3TAM

The results include ligand and solvothermal MOF synthesis, the electrodeposition of MOFs on a series of conductive substrates and heat-treatment of the frameworks to afford core@carbon materials. The structural and physiochemical characterisation of the prepared structures are also documented, including water oxidation and gas absorption experiments.

Chapter 2 details the thermal treatment of a Co(II)-based MOF to afford a core@shell material, both as a bulk material and after electrodeposition on fluorine doped tin oxide (FTO) and carbon cloth (CC) electrodes following a general cathodic deposition procedure. The porosity of the carbonised material is investigated using N_2 gas sorption. The suitability and stability to the electrocatalytic water oxidation of the MOF-derived materials are compared, as are they to the precursor **{Co$_5$}-MOF**.

Chapter 3 advances the general synthetic pathway of crystal growth and annealing developed in Chapter 2 to include the incorporation of a second metal ion in the initial synthesis to produce a series of mixed-metal MOFs. An isoreticular Co(II)/Ni(II) analogue

of **{Co$_5$}-MOF** is reported as are three structurally identical MM-MOFs based on a {M_3} trinuclear SBU incorporating apical coordinated solvent molecules. These materials were applied in water oxidation catalysis studies.

Chapter 4 deals with the synthesis and characterisation of highly interpenetrated Cu(II)-, Zn(II)- and Cd(II)-MOFs from the implementation of a 1,3,5-triazine based ligand. Using the extended triazine ligand template, the physiochemical and luminescent properties of ligands and the resulting MOFs are studied for their potential applications.

1.8 Bibliography

1 S. R. Batten, N. R. Champness, X.-M. Chen, J. Garcia-Martinez, S. Kitagawa, L. Öhrström, M. O'Keeffe, M. P. Suh and J. Reedijk, *CrystEngComm*, 2012, **14**, 3001–3004.

2 B. F. Hoskins and R. Robson, *J. Am. Chem. Soc.*, 1989, **111**, 5962–5964.

3 B. F. Hoskins and R. Robson, *J. Am. Chem. Soc.*, 1990, **112**, 1546–1554.

4 S. M. Moosavi, A. Nandy, K. M. Jablonka, D. Ongari, J. P. Janet, P. G. Boyd, Y. Lee, B. Smit and H. J. Kulik, *Nat. Commun.*, 2020, **11**, 1–10.

5 H. Furukawa, K. E. Cordova, M. O'Keeffe and O. M. Yaghi, *Science*, 2013, **341**, 1230444–1230444.

6 N. Stock and S. Biswas, *Chem. Rev*, 2012, **112**, 933–969.

7 S. M. Cohen, *Chem. Rev.*, 2012, **112**, 970–1000.

8 J. Liu, B. Lukose, O. Shekhah, H. K. Arslan, P. Weidler, H. Gliemann, S. Bräse, S. Grosjean, A. Godt, X. Feng, K. Müllen, I.-B. Magdau, T. Heine and C. Wöll, *Sci. Rep.*, 2012, **2**, 921.

9 T. D. Bennett, A. H. Fuchs, A. K. Cheetham and F.-X. Coudert, *Dalt. Trans.*, 2016, **45**, 4058.

10 J. M. García-Martínez and E. P. Collar, *Polymers (Basel).*, 2021, **13**, 1–4.

11 T. R. Cook, Y.-R. Zheng and P. J. Stang, *Chem. Rev*, 2013, **113**, 734–777.

12 D. J. Tranchemontagne, Z. Ni, M. O'Keeffe and O. M. Yaghi, *Angew. Chem., Int. Ed.*, 2008, **47**, 5136–5147.

13 Y.-R. Zheng, K. Suntharalingam, T. C. Johnstone and S. J. Lippard, *Chem. Sci.*,

2015, **6**, 1189–1193.

14 M. Yoshizawa, N. Sato and M. Fujita, *Chem. Lett.*, 2005, **34**, 1392–1393.

15 S. Hong, M. Oh, M. Park, J. W. Yoon, J.-S. Chang and M. S. Lah, *Chem. Commun.*, 2009, **0**, 5397.

16 M. Eddaoudi, J. Kim, J. B. Wachter, H. K. Chae, M. O'Keeffe and O. M. Yaghi, *J. Am. Chem. Soc.*, 2001, **123**, 4368–4369.

17 N. L. Rosi, M. Eddaoudi, J. Kim, M. O'Keeffe and O. M. Yaghi, *CrystEngComm*, 2002, **4**, 401–404.

18 K. Byrne, M. Zubair, N. Zhu, X. P. Zhou, D. S. Fox, H. Zhang, B. Twamley, M. J. Lennox, T. Düren and W. Schmitt, *Nat. Commun.*, 2017, **8**, 15268.

19 M. Fujita, Y. J. Kwon, O. Sasaki, K. Yamaguchi and K. Ogura, *J. Am. Chem. Soc.*, 1995, **117**, 7287–7288.

20 S. Subramanian and M. J. Zaworotko, *Angew. Chem., Int. Ed.*, 1995, **34**, 2127–2129.

21 D. J. Tranchemontagne, J. L. Mendoza-Cortés, M. O'Keeffe and O. M. Yaghi, *Chem. Soc. Rev.*, 2009, **38**, 1257.

22 M. Eddaoudi, D. B. Moler, H. Li, B. Chen, T. M. Reineke, M. O'Keeffe and O. M. Yaghi, *Acc. Chem. Res.*, 2001, **34**, 319–330.

23 O. M. Yaghi, M. O'Keeffe, N. W. Ockwig, H. K. Chae, M. Eddaoudi and J. Kim, *Nature*, 2003, **423**, 705–714.

24 M. Li, D. Li, M. O'Keeffe and O. M. Yaghi, *Chem. Rev.*, 2014, **114**, 1343–1370.

25 L. Öhrström, Öhrström and Lars, *Crystals*, 2015, **5**, 154–162.

26 S. S.-Y. Chui, S. M.-F. Lo, J. P. H. Charmant, A. G. Orpen and I. D. Williams, *Science*, 1999, **283**, 1148–50.

27 W. R. Wikoff, L. Liljas, R. L. Duda, H. Tsuruta, R. W. Hendrix and J. E. Johnson, *Science*, 2000, **289**, 2129–2133.

28 H. Furukawa, Y. B. Go, N. Ko, Y. K. Park, F. J. Uribe-Romo, J. Kim, M. O'Keeffe and O. M. Yaghi, *Inorg. Chem.*, 2011, **50**, 9147–9152.

29 O. Delgado-Friedrichs, M. O'Keeffe and O. M. Yaghi, *Acta Crystallogr. Sect. A Found. Crystallogr.*, 2006, **62**, 350–355.

30 M. Eddaoudi, J. Kim, N. Rosi, D. Vodak, J. Wachter, M. O'Keeffe and O. M. Yaghi, *Science*, 2002, **295**, 469–472.

31 H. Furukawa, N. Ko, Y. B. Go, N. Aratani, S. B. Choi, E. Choi, A. O. Yazaydin, R. Q. Snurr, M. O'Keeffe, J. Kim and O. M. Yaghi, *Science*, 2010, **329**, 424–8.

32 S. Khoshhal, A. A. Ghoreyshi, M. Jahanshahi and M. Mohammadi, *RSC Adv.*, 2015, **5**, 24758–24768.

33 C. Pang, L. Gao, A. Chaturvedi, N. Bao, K. Yanagisawa, L. Shen and A. Gupta, *J. Mater. Chem. C*, 2015, **3**, 12077–12082.

34 K. Nakashima, Y. Toshima, Y. Kobayashi, Y. Ishikawa and M. Kakihana, *J. Asian Ceram. Soc.*, 2019, **7**, 544–550.

35 I. S. Kim, S. Ahn, N. A. Vermeulen, T. E. Webber, L. C. Gallington, K. W. Chapman, R. L. Penn, J. T. Hupp, O. K. Farha, J. M. Notestein and A. B. F. Martinson, *J. Am. Chem. Soc.*, 2020, **142**, 242–250.

36 Y. Chen, C. Yang, X. Wang, J. Yang, K. Ouyang and J. Li, *J. Mater. Chem. A*, 2016, **4**, 10345–10351.

37 N. Campagnol, E. Rezende Souza, D. E. De Vos, K. Binnemans and J. Fransaer, *Chem. Commun.*, 2014, **50**, 12680–12683.

38 I. Hod, W. Bury, D. M. Karlin, P. Deria, C. W. Kung, M. J. Katz, M. So, B. Klahr, D. Jin, Y. W. Chung, T. W. Odom, O. K. Farha and J. T. Hupp, *Adv. Mater.*, 2014, **26**, 6295–6300.

39 R. Ameloot, L. Stappers, J. Fransaer, L. Alaerts, B. F. Sels and D. E. De Vos, *Chem. Mater.*, 2009, **21**, 2580–2582.

40 J. H. Liao, P. L. Chen and C. C. Hsu, *J. Phys. Chem. Solids*, 2001, **62**, 1629–1642.

41 E. H. L. Falcão, Naraso, R. K. Feller, G. Wu, F. Wudl and A. K. Cheetham, *Inorg. Chem.*, 2008, **47**, 8336–8342.

42 C. Chen, X. Feng, Q. Zhu, R. Dong, R. Yang, Y. Cheng and C. He, *Inorg. Chem.*, 2019, **58**, 2717–2728.

43 W. J. Son, J. Kim, J. Kim and W. S. Ahn, *Chem. Commun.*, 2008, 6336–6338.

44 L. G. Qiu, Z. Q. Li, Y. Wu, W. Wang, T. Xu and X. Jiang, *Chem. Commun.*, 2008, 3642–3644.

45 Z. Q. Li, L. G. Qiu, W. Wang, T. Xu, Y. Wu and X. Jiang, *Inorg. Chem. Commun.*, 2008, **11**, 1375–1377.

46 Z. Wang, Z. Li, M. Ng and P. J. Milner, *Dalt. Trans.*, 2020, **49**, 16238–16244.

47 J. Beamish-Cook, K. Shankland, C. A. Murray and P. Vaqueiro, *Cryst. Growth Des.*, 2021, **21**, 3047–3055.

48 M. Taddei, P. V. Dau, S. M. Cohen, M. Ranocchiari, J. A. Van Bokhoven, F. Costantino, S. Sabatini and R. Vivani, *Dalt. Trans.*, 2015, **44**, 14019–14026.

49 M. Rubio-Martinez, C. Avci-Camur, A. W. Thornton, I. Imaz, D. Maspoch and M. R. Hill, *Chem. Soc. Rev.*, 2017, **46**, 3453–3480.

50 N. Stock and S. Biswas, *Chem. Rev.*, 2012, **112**, 933–969.

51 H. Zheng, Y. Zhang, L. Liu, W. Wan, P. Guo, A. M. Nyström and X. Zou, *J. Am. Chem. Soc.*, 2016, **138**, 962–968.

52 M. Bosch, S. Yuan, W. Rutledge and H.-C. Zhou, *Acc. Chem. Res.*, 2017, **50**, 857–865.

53 R. J. Kuppler, D. J. Timmons, Q.-R. Fang, J.-R. Li, T. A. Makal, M. D. Young, D. Yuan, D. Zhao, W. Zhuang and H.-C. Zhou, *Coord. Chem. Rev.*, 2009, **253**, 3042–3066.

54 R. Seetharaj, P. V. Vandana, P. Arya and S. Mathew, *Arab. J. Chem.*, 2019, **12**, 295–315.

55 P. Long, H. Wu, Q. Zhao, Y. Wang, J. Dong and J. Li, *Microporous Mesoporous Mater.*, 2011, **142**, 489–493.

56 J. F. Coetzee and T. H. Chang, *Pure Appl. Chem.*, 1986, **58**, 1541–1545.

57 D. Banerjee, J. Finkelstein, A. Smirnov, P. M. Forster, L. A. Borkowski, S. J. Teat and J. B. Parise, *Cryst. Growth Des.*, 2011, **11**, 2572–2579.

58 M. Li and M. Dincă, *J. Am. Chem. Soc.*, 2011, **133**, 12926–12929.

59 X. Zhang, K. Wan, P. Subramanian, M. Xu, J. Luo and J. Fransaer, *J. Mater. Chem. A*, 2020, **8**, 7569–7587.

60 N. Campagnol, T. R. C. Van Assche, M. Li, L. Stappers, M. Dinca, J. F. M. Denayer, K. Binnemans, D. E. De Vos and J. Fransaer, *J. Mater. Chem. A*, 2016, **4**, 3914–3925.

61 W. Liang and D. M. D'alessandro, *Chem. Commun.*, 2013, **49**, 3706–3708.

62 J. Klinowski, F. A. Almeida Paz, P. Silva and J. Rocha, *Dalt. Trans.*, 2011, 40, 321–330.

63 P. P. Bag, X. S. Wang and R. Cao, *Dalt. Trans.*, 2015, **44**, 11954–11962.

64 X. Hu, X. Lou, C. Li, Q. Chen, Q. Yang and B. Hu, *New J. Chem.*, 2017, **41**, 6415–6419.

65 L. Oar-Arteta, T. Wezendonk, X. Sun, F. Kapteijn and J. Gascon, *Mater. Chem. Front.*, 2017, **1**, 1709–1745.

66 L. Lux, K. Williams and S. Ma, *CrystEngComm*, 2015, **17**, 10–22.

67 S. Pandiaraj, H. B. Aiyappa, R. Banerjee and S. Kurungot, *Chem. Commun.*, 2014, **50**, 3363–3366.

68 Y. Li and R. T. Yang, *Langmuir*, 2007, **23**, 12937–12944.

69 J.-R. Li, R. J. Kuppler and H.-C. Zhou, *Chem. Soc. Rev.*, 2009, **38**, 1477.

70 K. Sumida, D. L. Rogow, J. A. Mason, T. M. McDonald, E. D. Bloch, Z. R. Herm, T.-H. Bae and J. R. Long, *Chem. Rev.*, 2012, **112**, 724–781.

71 L. Ma and W. Lin, *Top. Curr. Chem.*, 2010, **293**, 175–205.

72 L. Zhu, X.-Q. Liu, H.-L. Jiang and L.-B. Sun, *Chem. Rev.*, 2017, **117**, 8129–8176.

73 H. Zhang, X. Liu, Y. Wu, C. Guan, A. K. Cheetham and J. Wang, *Chem. Commun.*, 2018, **54**, 5268–5288.

74 M. Al Haydar, H. R. Abid, B. Sunderland and S. Wang, *Drug Des. Devel. Ther.*, 2017, **11**, 2685–2695.

75 X. Chen, R. Tong, Z. Shi, B. Yang, H. Liu, S. Ding, X. Wang, Q. Lei, J. Wu and W.

Fang, *ACS Appl. Mater. Interfaces*, 2018, **10**, 2328–2337.

76 M. X. Wu and Y. W. Yang, *Adv. Mater.*, 2017, **29**, 1606134.

77 J. Della Rocca, D. Liu and W. Lin, *Acc. Chem. Res.*, 2011, **44**, 957–968.

78 L. Chen, J.-W. Ye, H.-P. Wang, M. Pan, S.-Y. Yin, Z.-W. Wei, L.-Y. Zhang, K. Wu, Y.-N. Fan and C.-Y. Su, *Nat. Commun.*, 2017, **8**, 15985.

79 D. Liu, K. Lu, C. Poon and W. Lin, *Inorg. Chem.*, 2014, **53**, 1916–1924.

80 L. Zhang, P. Cui, H. Yang, J. Chen, F. Xiao, Y. Guo, Y. Liu, W. Zhang, F. Huo and B. Liu, *Adv. Sci.*, 2015, **3**, 1500243.

81 Z.-M. Zhang, T. Zhang, C. Wang, Z. Lin, L.-S. Long and W. Lin, *J. Am. Chem. Soc.*, 2015, **137**, 3197–3200.

82 D. Kim, D. R. Whang and S. Y. Park, *J. Am. Chem. Soc.*, 2016, **138**, 8698–8701.

83 H. Wang, Q. L. Zhu, R. Zou and Q. Xu, *Chem*, 2017, **2**, 52–80.

84 T. C. Wang, W. Bury, D. A. Gómez-Gualdrón, N. A. Vermeulen, J. E. Mondloch, P. Deria, K. Zhang, P. Z. Moghadam, A. A. Sarjeant, R. Q. Snurr, J. F. Stoddart, J. T. Hupp and O. K. Farha, *J. Am. Chem. Soc.*, 2015, **137**, 3585–3591.

85 Y. N. Gong, D. C. Zhong and T. B. Lu, *CrystEngComm*, 2016, 18, 2596–2606.

86 L. Carlucci, G. Ciani, D. M. Proserpio and S. Rizzato, *CrystEngComm*, 2002, **4**, 121–129.

87 M. Dincă and J. R. Long, *Angew. Chemie - Int. Ed.*, 2008, **47**, 6766–6779.

88 H. Erer, O. Z. Yeşilel and M. Arici, *Cryst. Growth Des.*, 2015, **15**, 3201–3211.

89 L. Liu, X. Wang, Q. Zhang, Q. Li and Y. Zhao, *CrystEngComm*, 2013, **15**, 841–844.

90 S. Ma, X. Sen Wang, D. Yuan and H. C. Zhou, *Angew. Chemie - Int. Ed.*, 2008, **47**, 4130–4133.

91 H. Kim, S. Das, M. G. Kim, D. N. Dybtsev, Y. Kim and K. Kim, *Inorg. Chem.*, 2011, **50**, 3691–3696.

92 D. W. Hill, in *Physics Applied to Anaesthesia*, Butterworths, 1972, vol. 37, pp. 110–161.

93 F. Schüth, K. S. W. Sing and J. (Jens) Weitkamp, *Handbook of porous solids*, Wiley-VCH, Weinheim Germany, 2002.

94 H. Li, K. Wang, Y. Sun, C. T. Lollar, J. Li and H.-C. Zhou, *Mater. Today*, 2018, **21**, 108–121.

95 J. A. Mason, K. Sumida, Z. R. Herm, R. Krishna and J. R. Long, *Energy Environ. Sci.*, 2011, **4**, 3030–3040.

96 S. S. Kaye, A. Dailly, O. M. Yaghi and J. R. Long, *J. Am. Chem. Soc.*, 2007, **129**, 14176–14177.

97 Y. Peng, V. Krungleviciute, I. Eryazici, J. T. Hupp, O. K. Farha and T. Yildirim, *J. Am. Chem. Soc.*, 2013, **135**, 11887–11894.

98 E. D. Bloch, M. R. Hudson, J. A. Mason, S. Chavan, V. Crocellà, J. D. Howe, K. Lee, A. L. Dzubak, W. L. Queen, J. M. Zadrozny, S. J. Geier, L.-C. Lin, L. Gagliardi, B. Smit, J. B. Neaton, S. Bordiga, C. M. Brown and J. R. Long, *J. Am. Chem. Soc.*, 2014, **136**, 10752–10761.

99 J. F. Van Humbeck, T. M. McDonald, X. Jing, B. M. Wiers, G. Zhu and J. R. Long, *J. Am. Chem. Soc.*, 2014, **136**, 2432–2440.

100 L. Valenzano, B. Civalleri, S. Chavan, G. T. Palomino, C. O. Areán and S. Bordiga,

J. Phys. Chem. C, 2010, **114**, 11185–11191.

101 M. Kandiah, M. H. Nilsen, S. Usseglio, S. Jakobsen, U. Olsbye, M. Tilset, C. Larabi, E. A. Quadrelli, F. Bonino and K. P. Lillerud, *Chem. Mater.*, 2010, **22**, 6632–6640.

102 R. B. Jackson, C. Le Quéré, R. M. Andrew, J. G. Canadell, J. I. Korsbakken, Z. Liu, G. P. Peters and B. Zheng, *Environ. Res. Lett.*, 2018, **13**, 120401.

103 E. González-Zamora and I. A. Ibarra, *Mater. Chem. Front.*, 2017, **1**, 1471–1484.

104 Z. Zhang, Z. Z. Yao, S. Xiang and B. Chen, *Energy Environ. Sci.*, 2014, **7**, 2868–2899.

105 M. P. Suh, H. J. Park, T. K. Prasad and D.-W. Lim, *Chem. Rev.*, 2012, **112**, 782–835.

106 A. Demessence, D. M. D'Alessandro, M. L. Foo and J. R. Long, *J. Am. Chem. Soc.*, 2009, **131**, 8784–8786.

107 R. Vaidhyanathan, S. S. Iremonger, G. K. H. Shimizu, P. G. Boyd, S. Alavi and T. K. Woo, *Science*, 2010, **330**, 650–653.

108 J. J. Low, A. I. Benin, P. Jakubczak, J. F. Abrahamian, S. A. Faheem and R. R. Willis, *J. Am. Chem. Soc.*, 2009, **131**, 15834–15842.

109 P. Horcajada, S. Surblé, C. Serre, D. Y. Hong, Y. K. Seo, J. S. Chang, J. M. Grenèche, I. Margiolaki and G. Férey, *Chem. Commun.*, 2007, **0**, 2820–2822.

110 E. Soubeyrand-Lenoir, C. Vagner, J. W. Yoon, P. Bazin, F. Ragon, Y. K. Hwang, C. Serre, J.-S. Chang and P. L. Llewellyn, *J. Am. Chem. Soc.*, 2012, **134**, 10174–10181.

111 J. Qian, F. Jiang, D. Yuan, M. Wu, S. Zhang, L. Zhang and M. Hong, *Chem.*

Commun., 2012, **48**, 9696–9698.

112 L. N. Ho, Y. Schuurman, D. Farrusseng and B. Coasne, *J. Phys. Chem. C*, 2015, **119**, 21547–21554.

113 A. J. Clough, J. W. Yoo, M. H. Mecklenburg and S. C. Marinescu, *J. Am. Chem. Soc.*, 2015, **137**, 118–121.

114 C. A. Downes, A. J. Clough, K. Chen, J. W. Yoo and S. C. Marinescu, *ACS Appl. Mater. Interfaces*, 2018, **10**, 1719–1727.

115 S. S. Shinde, C. H. Lee, J. Y. Jung, N. K. Wagh, S. H. Kim, D. H. Kim, C. Lin, S. U. Lee and J. H. Lee, *Energy Environ. Sci.*, 2019, **12**, 727–738.

116 M. L. Aubrey, M. T. Kapelewski, J. F. Melville, J. Oktawiec, D. Presti, L. Gagliardi and J. R. Long, *J. Am. Chem. Soc.*, 2019, **141**, 5005–5013.

117 Z. Meng, A. Aykanat and K. A. Mirica, *J. Am. Chem. Soc.*, 2019, **141**, 2046–2053.

118 C. Li, L. Zhang, J. Chen, X. Li, J. Sun, J. Zhu, X. Wang and Y. Fu, *Nanoscale*, 2021, 13, 485–509.

119 L. S. Xie, G. Skorupskii and M. Dincă, *Chem. Rev.*, 2020, **120**, 8536–8580.

120 S. Takaishi, M. Hosoda, T. Kajiwara, H. Miyasaka, M. Yamashita, Y. Nakanishi, Y. Kitagawa, K. Yamaguchi, A. Kobayashi and H. Kitagawa, *Inorg. Chem.*, 2009, **48**, 9048–9050.

121 S. K. Bhardwaj, N. Bhardwaj, R. Kaur, J. Mehta, A. L. Sharma, K. H. Kim and A. Deep, *J. Mater. Chem. A*, 2018, **6**, 14992–15009.

122 R. W. Day, D. K. Bediako, M. Rezaee, L. R. Parent, G. Skorupskii, M. Q. Arguilla, C. H. Hendon, I. Stassen, N. C. Gianneschi, P. Kim and M. Dincă, *ACS Cent. Sci.*, 2019, **5**, 1959–1964.

123 E. M. Johnson, S. Ilic and A. J. Morris, *ACS Cent. Sci.*, 2021, **7**, 445–453.

124 A. A. Talin, A. Centrone, A. C. Ford, M. E. Foster, V. Stavila, P. Haney, R. A. Kinney, V. Szalai, F. El Gabaly, H. P. Yoon, F. Léonard and M. D. Allendorf, *Science (80-.).*, 2014, **343**, 66–69.

125 I. F. Chen, C. F. Lu and W. F. Su, *Langmuir*, 2018, **34**, 15754–15762.

126 A. Kalair, N. Abas, M. S. Saleem, A. R. Kalair and N. Khan, *Energy Storage*, 2021, **3**, e135.

127 IEA, *Global Energy Review 2021 – Analysis - IEA*, 2021.

128 E. Connelly, A. Elgowainy, M. Ruth Peer Reviewed By, J. Vickers, K. Randolph, P. Levi, T.-Y. Kim, K. Zhang, A. Burgunder, A. By, N. Rustagi, F. Joseck, E. Miller and S. Satyapal, *DOE Hydrogen and Fuel Cells Program Record 19002: Current Hydrogen Market Size: Domestic and Global*, 2019.

129 M. Eyvaz, *Advances In Hydrogen Generation Technologies*, InTech, 2018.

130 Y. H. Budnikova, *Dalt. Trans.*, 2020, **49,** 12483–12502.

131 X. Wen and J. Guan, *Appl. Mater. Today*, 2019, **16**, 146–168.

132 R. Nivetha, K. Gothandapani, V. Raghavan, G. Jacob, R. Sellappan, P. Bhardwaj, S. Pitchaimuthu, A. N. M. Kannan, S. K. Jeong and A. N. Grace, *ACS Omega*, 2020, **5**, 18941–18949.

133 T. Liu, P. Li, N. Yao, G. Cheng, S. Chen, W. Luo and Y. Yin, *Angew. Chemie*, 2019, **131**, 4727–4732.

134 M. M. Najafpour, S. Heidari, S. E. Balaghi, M. Hołyńska, M. H. Sadr, B. Soltani, M. Khatamian, A. W. Larkum and S. I. Allakhverdiev, *Biochim. Biophys. Acta - Bioenerg.*, 2017, **1858**, 156–174.

135 G. R. Harriman A, Thomas J. M, Milward, *New J. Chem.*, 1987, **11**, 757–762.

136 A. Harriman, M. C. Richoux, P. A. Christensen, S. Mosseri and P. Neta, *J. Chem. Soc. Faraday Trans. 1 Phys. Chem. Condens. Phases*, 1987, **83**, 3001–3014.

137 X. Chen, G. Chen and P. L. Yue, *J. Phys. Chem. B*, 2001, **105**, 4623–4628.

138 J. Kamdar and D. Grotjahn, *Molecules*, 2019, **24**, 494.

139 W. Zhou, D. D. Huang, Y. P. Wu, J. Zhao, T. Wu, J. Zhang, D. S. Li, C. Sun, P. Feng and X. Bu, *Angew. Chemie - Int. Ed.*, 2019, **58**, 4227–4231.

140 F.-L. Li, Q. Shao, X. Huang and J.-P. Lang, *Angew. Chemie*, 2018, **130**, 1906–1910.

141 J. Xing, K. Guo, Z. Zou, M. Cai, J. Du and C. Xu, *Chem. Commun.*, 2018, **54**, 7046–7049.

142 X. Zhao, B. Pattengale, D. Fan, Z. Zou, Y. Zhao, J. Du, J. Huang and C. Xu, *ACS Energy Lett.*, 2018, **3**, 2520–2526.

143 K. Maity, K. Bhunia, D. Pradhan and K. Biradha, *ACS Appl. Mater. Interfaces*, 2017, **9**, 37548–37553.

144 L. Han, J. Xu, X. Zhu, F. Yang and X. Jia, *Mater. Today Energy*, 2020, **16**, 100419.

145 Z. Zou, J. Wang, H. Pan, J. Li, K. Guo, Y. Zhao and C. Xu, *J. Mater. Chem. A*, 2020, **8**, 14099–14105.

146 P. Zhang, L. Li, D. Nordlund, H. Chen, L. Fan, B. Zhang, X. Sheng, Q. Daniel and L. Sun, *Nat. Commun.*, 2018, **9**, 1–10.

147 F. Song, M. M. Busch, B. Lassalle-Kaiser, C. S. Hsu, E. Petkucheva, M. Bensimon, H. M. Chen, C. Corminboeuf and X. Hu, *ACS Cent. Sci.*, 2019, **5**, 558–568.

148 X. Zhang, L. Zhang, G. G. Zhu, Y. X. Zhu and S. Y. Lu, *ACS Appl. Mater.*

Interfaces, 2020, **12**, 7153–7161.

149 W. F. Chen, C. H. Wang, K. Sasaki, N. Marinkovic, W. Xu, J. T. Muckerman, Y. Zhu and R. R. Adzic, *Energy Environ. Sci.*, 2013, **6**, 943–951.

150 H. Vrubel and X. Hu, *Angew. Chemie - Int. Ed.*, 2012, **51**, 12703–12706.

151 P. Mei, Y. Yamauchi, M. Pramanik, A. Fatehmulla, A. M. Adhafiri, W. A. Farooq, Y. Bando, M. J. A. Shiddiky, Y. V. Kaneti, J. Lin and Y. Kim, *Electrochem. commun.*, 2019, **104**, 106476.

152 Z. Abdi, R. Bagheri, Z. Song and M. M. Najafpour, *Sci. Rep.*, 2019, **9**, 11499.

153 H. Feizi, R. Bagheri, Z. Jagličić, J. P. Singh, K. H. Chae, Z. Song and M. M. Najafpour, *Dalt. Trans.*, 2019, **48**, 547–557.

154 J. Soriano-López, R. Elliott, A. C. Kathalikkattil, A. M. Ako, M. Mulahmetović, M. Venkatesan and W. Schmitt, *ACS Sustain. Chem. Eng.*, 2020, **8**, 13648–13659.

155 G. Maayan, N. Gluz and G. Christou, *Nat. Catal.*, 2018, **1**, 48–54.

156 X. Liu, S. Cui, M. Qian, Z. Sun and P. Du, *Chem. Commun.*, 2016, **52**, 5546–5549.

157 C. Mo, J. Jian, J. Li, Z. Fang, Z. Zhao, Z. Yuan, M. Yang, Y. Zhang, L. Dai and D. Yu, *Energy Environ. Sci.*, 2018, **11**, 3334–3341.

158 S. Mukhopadhyay, O. Basu, R. Nasani and S. K. Das, *Chem. Commun.*, 2020, **56**, 11735–11748.

159 T. Y. Ma, S. Dai, M. Jaroniec and S. Z. Qiao, *J. Am. Chem. Soc.*, 2014, **136**, 13925–13931.

160 F. Sun, G. Wang, Y. Ding, C. Wang, B. Yuan and Y. Lin, *Adv. Energy Mater.*, 2018, **8**, 1800584.

161 C. Li, Y. Liu, G. Wang, L. Guan and Y. Lin, *ACS Sustain. Chem. Eng.*, 2019, **7**, 7496–7501.

162 J. Chen, B. Ren, H. Cui and C. Wang, *Small*, 2020, **16**, 1907556.

163 Y. Lin, L. Zhao, L. Wang and Y. Gong, *Dalt. Trans.*, 2021, **50**, 4280–4287.

164 Z. Tao, T. Wang, X. Wang, J. Zheng and X. Li, *ACS Appl. Mater. Interfaces*, 2016, **8**, 35390–35397.

165 J. Zhou, Y. Dou, A. Zhou, L. Shu, Y. Chen and J. R. Li, *ACS Energy Lett.*, 2018, **3**, 1655–1661.

166 F. Lyu, Y. Bai, Z. Li, W. Xu, Q. Wang, J. Mao, L. Wang, X. Zhang and Y. Yin, *Adv. Funct. Mater.*, 2017, **27**, 1702324.

167 X.-F. Lu, L.-F. Gu, J.-W. Wang, J.-X. Wu, P.-Q. Liao and G.-R. Li, *Adv. Mater.*, 2017, **29**, 1604437.

168 L. L. Wu, Q. S. Wang, J. Li, Y. Long, Y. Liu, S. Y. Song and H. J. Zhang, *Small*, 2018, **14**, 1704035.

169 X. Liu, Y. Liu and L. Z. Fan, *J. Mater. Chem. A*, 2017, **5**, 15310–15314.

170 X. Wang, X. Huang, W. Gao, Y. Tang, P. Jiang, K. Lan, R. Yang, B. Wang and R. Li, *J. Mater. Chem. A*, 2018, **6**, 3684–3691.

171 L. Jiao, Y. X. Zhou and H. L. Jiang, *Chem. Sci.*, 2016, **7**, 1690–1695.

172 P. He, X. Y. Yu and X. W. D. Lou, *Angew. Chemie - Int. Ed.*, 2017, **56**, 3897–3900.

173 T. Zhou, Y. Du, D. Wang, S. Yin, W. Tu, Z. Chen, A. Borgna and R. Xu, *ACS Catal.*, 2017, **7**, 6000–6007.

174 S. Ouyang, H. Tong, N. Umezawa, J. Cao, P. Li, Y. Bi, Y. Zhang and J. Ye, *J. Am.*

Chem. Soc., 2012, **134**, 1974–1977.

175 A. Kudo and Y. Miseki, *Chem. Soc. Rev.*, 2009, **38**, 253–278.

176 S. Lin, Y. Pineda-Galvan, W. A. Maza, C. C. Epley, J. Zhu, M. C. Kessinger, Y. Pushkar and A. J. Morris, *ChemSusChem*, 2017, **10**, 514–522.

177 C. Wang, Z. Xie, K. E. deKrafft and W. Lin, *J. Am. Chem. Soc.*, 2011, **133**, 13445–13454.

178 E.-H. Zhou, B.-H. Li, W.-X. Chen, Z. Luo, J. Liu, A. Singh, A. Kumar and J.-C. Jin, *J. Mol. Struct.*, 2017, **1149**, 352–356.

179 S. Guo, H. Zhang, Y. Chen, Z. Liu, B. Yu, Y. Zhao, Z. Yang, B. Han and Z. Liu, *ACS Catal.*, 2018, **8**, 4576–4581.

180 H.-Q. Xu, J. Hu, D. Wang, Z. Li, Q. Zhang, Y. Luo, S.-H. Yu and H.-L. Jiang, *J. Am. Chem. Soc.*, 2015, **137**, 13440–13443.

181 J. E. Mondloch, O. Karagiaridi, O. K. Farha and J. T. Hupp, *CrystEngComm*, 2013, **15**, 9258.

182 T. Zhang and W. Lin, *Chem. Soc. Rev.*, 2014, **43**, 5982–5993.

183 T. S. Teets and D. G. Nocera, *Chem. Commun. Chem. Commun*, 2011, **47**, 9268–9274.

184 A. Fujishima and K. Honda, *Nature*, 1972, **238**, 37–38.

185 X. Chen and A. Selloni, *Chem. Rev.*, 2014, **114**, 9281–9282.

186 M. Kapilashrami, Y. Zhang, Y.-S. Liu, A. Hagfeldt and J. Guo, *Chem. Rev.*, 2014, **114**, 9662–9707.

187 G. Liu, H. G. Yang, J. Pan, Y. Q. Yang, G. Q. (Max) Lu and H.-M. Cheng, *Chem.*

Rev., 2014, **114**, 9559–9612.

188 K. Hashimoto, H. Irie and A. Fujishima, *Jpn. J. Appl. Phys.*, 2005, **44**, 8269–8285.

189 H. Xu, S. Ouyang, L. Liu, P. Reunchan, N. Umezawa and J. Ye, *J. Mater. Chem. A*, 2014, **2**, 12642.

190 E. M. Kober and T. J. Meyer, *Inorg. Chem.*, 1982, **21**, 3967–3977.

191 E. Baranoff, J.-P. Collin, L. Flamigni and J.-P. Sauvage, *Chem. Soc. Rev.*, 2004, **33**, 147.

192 M. Abrahamsson, M. Jäger, R. J. Kumar, T. Österman, P. Persson, H.-C. Becker, O. Johansson and L. Hammarström, *J. Am. Chem. Soc.*, 2008, **130**, 15533–15542.

193 E. A. Medlycott and G. S. Hanan, *Coord. Chem. Rev.*, 2006, **250**, 1763–1782.

194 Y. Sun, M. El Ojaimi, R. Hammitt, R. P. Thummel and C. Turro, *J. Phys. Chem. B*, 2010, **114**, 14664–14670.

195 E. A. Medlycott and G. S. Hanan, *Chem. Soc. Rev.*, 2005, **34**, 133–142.

196 M. I. J. Polson, N. J. Taylor and G. S. Hanan, *Chem. Commun.*, 2002, **2**, 1356–1357.

197 T. Toyao, M. Saito, S. Dohshi, K. Mochizuki, M. Iwata, H. Higashimura, Y. Horiuchi and M. Matsuoka, *Chem. Commun.*, 2014, **50**, 6779–6781.

198 S. Zhang, L. Li, S. Zhao, Z. Sun and J. Luo, *Inorg. Chem.*, 2015, **54**, 8375–8379.

199 D. Sun, Y. Fu, W. Liu, L. Ye, D. Wang, L. Yang, X. Fu and Z. Li, *Chem. - A Eur. J.*, 2013, **19**, 14279–14285.

200 Y. Fu, D. Sun, Y. Chen, R. Huang, Z. Ding, X. Fu and Z. Li, *Angew. Chem., Int. Ed.*, 2012, **51**, 3364–3367.

201 R. Ren, Z. Wen, S. Cui, Y. Hou, X. Guo and J. Chen, *Sci. Rep.*, 2015, **5**, 10714.

202 Y. Chen, D. Wang, X. Deng and Z. Li, *Catal. Sci. Technol.*, 2017, **7**, 4893–4904.

203 G. Lan, Z. Li, S. S. Veroneau, Y. Y. Zhu, Z. Xu, C. Wang and W. Lin, *J. Am. Chem. Soc.*, 2018, **140**, 12369–12

Chapter 2

A robust thin-film cobalt-based MOF derivative for water oxidation catalysis

2.0 Introduction

Metal-organic frameworks (MOFs) are hybrid coordination materials characterised by their high surface area and internal porosity, formed from organic linkers and inorganic nodes. MOFs have the ability to act as self-sacrificing templates after thermal treatment, retaining their porosity.[1] These methods can be used to improve the electrocatalytic water oxidation activity of a MOF. In this chapter a porous and highly stable cobalt containing core@shell material is presented and its use as water oxidation catalyst is explored. Cobalt is an earth-abundant metal and cobalt(II)-containing polyoxometalates[2] as well as cobalt oxides[3] have been shown to provide relatively cheap catalysts for water oxidation with good activity. Similar annealed materials have been reported to catalyse the oxygen evolution reaction with improved activity due to their electronic conductivity and a higher resistance to corrosion by the electrolyte, allowing for long-term stability in basic aqueous solutions.[4]

The ligand 4,4',4''-(benzene-1,3,5-triyltris(ethyne-2,1-diyl)tribenzoic acid (H_3BTEB), was initially chosen as it has previously been used within the research group to synthesise a range of MOFs containing Zn(II),[5] Cu(II),[6] and lanthanide ions.[7] It incorporates the capacity to form both highly porous and stable MOFs, desirable properties for MOF-based catalysts.

The pentanuclear MOF $Me_2NH_2[Co_5(BTEB)_3(\mu_3\text{-}OH)_2(H_2O)_2(DMF)_2]$ (**{Co_5}-MOF**) is annealed under N_2 at 500 °C to yield **Co@C-500**. Slow heating of the MOF to 500 °C over a four hour period allows for the resulting structure to retain a degree of porosity of **{Co_5}-MOF**. This is advantageous as it ensures access to the catalytic centres as opposed to amorphous cobalt oxide in a carbon-based binder.

This chapter details the synthesis of **Co@C-500** from the previously reported **{Co_5}-MOF** *via* carbonisation. Characterisation of the material is detailed including PXRD, FT-IR and Raman spectroscopy, SEM, TEM and STEM imaging and EDX and XPS analysis. Applications of **Co@C-500** for N_2 gas sorption are explored. In addition to this, **{Co_5}-MOF** can be electrochemically synthesised on a conductive surface, such as a fluorine-doped tin oxide coated film. This thin-film can also be annealed under inert conditions to yield a strongly electrode-bound OER catalysts, namely **Co@C-500**/FTO and **Co@C-500**/CC, explored extensively as catalysts for the water oxidation reaction at pH 7.2 and 13.5. Post-catalytic characterisation confirms the stability of the material to long term bulk catalysis.

2.1 Synthesis of 4,4',4''-(-(benzene-1,3,5-triyltris(ethyne-2,1-diyl))tribenzoic acid, (H_3BTEB)

Polycarboxylates are the first and at present, still the most readily employed organic struts in MOF synthesis, with the effects of position and extension having well-studied influences on the topology of the resulting MOFs.[8] The tritopic, polycarboxylates ligand 4,4',4''-(benzene-1,3,5-triyltris(ethyne-2,1-diyl))tribenzoic acid (**H_3BTEB**) was synthesised using a modified literature procedure (Scheme 1.2.1). The synthesis follows a well-utilised four-step synthesis from a tri-halogenated aromatic core *via* two Sonogashera cross-coupling reactions and subsequent base-catalysed deprotections to afford an extended ridged ligand suitable for the synthesis of numerous porous MOFs.[5,9]

1,3,5-tris((trimethylsilyl)ethynyl)benzene was synthesised using a Sonogashira coupling reaction.[10] 1,3,5-tribromobenzene was dissolved with ethynyltrimethylsilane in diisopropylamine. A [Pd(II)(PPh_3)$_2$$Cl_2$] catalyst and Cu(I)I co-catalyst were added to the solution and the mixture was heated to 60 °C for 24 hours under N_2. The reaction was subsequently cooled to room temperature before the solvent was removed under vacuum. The crude product was dissolved in DCM and washed with an aqueous NH_3 solution. The product was run through a silica plug with hexane to yield pure 1,3,5-tris((trimethylsilyl)ethynyl)benzene.

The second step of the reaction synthesis involves the removal of the silyl groups. 1,3,5-tris((trimethylsilyl)ethynyl)benzene was dissolved with K_2CO_3 in a 1:1 DCM/MeOH solution, and stirred at 35 °C for 4 hours. The solvent was removed under vacuum and K_2CO_3 was removed by separation in H_2O/DCM. The crude product was purified using a silica column with a DCM mobile phase yielding pure 1,3,5-triethynylbenzene.

An additional Sonogashira cross-coupling reaction was carried out to add the carboxylate functionalities to the tritopic core. 1,3,5-triethynylbenzene and methyl-4-iodobenzoate were refluxed in a THF/TEA reaction mixture at 80 °C for 24 hours under N_2. This was purified by washing the crude compound as in the first step and then running the product though a silica column with hexane:THF (1:2) and recrystalised from C_2H_5OH to yield pure trimethyl 4,4',4''-(benzene-1,3,5-triyltris(ethyne-2,1-diyl))tribenzoate.

The final step involves a base-catalysed de-esterification to remove the methyl groups to form the carboxylic acids. This was achieved by stirring trimethyl 4,4',4''-(benzene-1,3,5-

triyltris(ethyne-2,1-diyl))tribenzoate with excess LiOH in a solvent mixture of THF:H_2O (1:1) for 3 hours at room temperature. THF was removed under vacuum leaving a solution in H_2O. The reaction mixture was acidified slowly to pH 2 using a 1 M HCl solution, precipitating crude product. This was washed with deionised H_2O, dried under vacuum and then purified using column chromatography using a THF mobile phase yielding pure 4,4',4''-(benzene-1,3,5-triyltris(ethyne-2,1-diyl)tribenzoic acid, **H_3BTEB**.

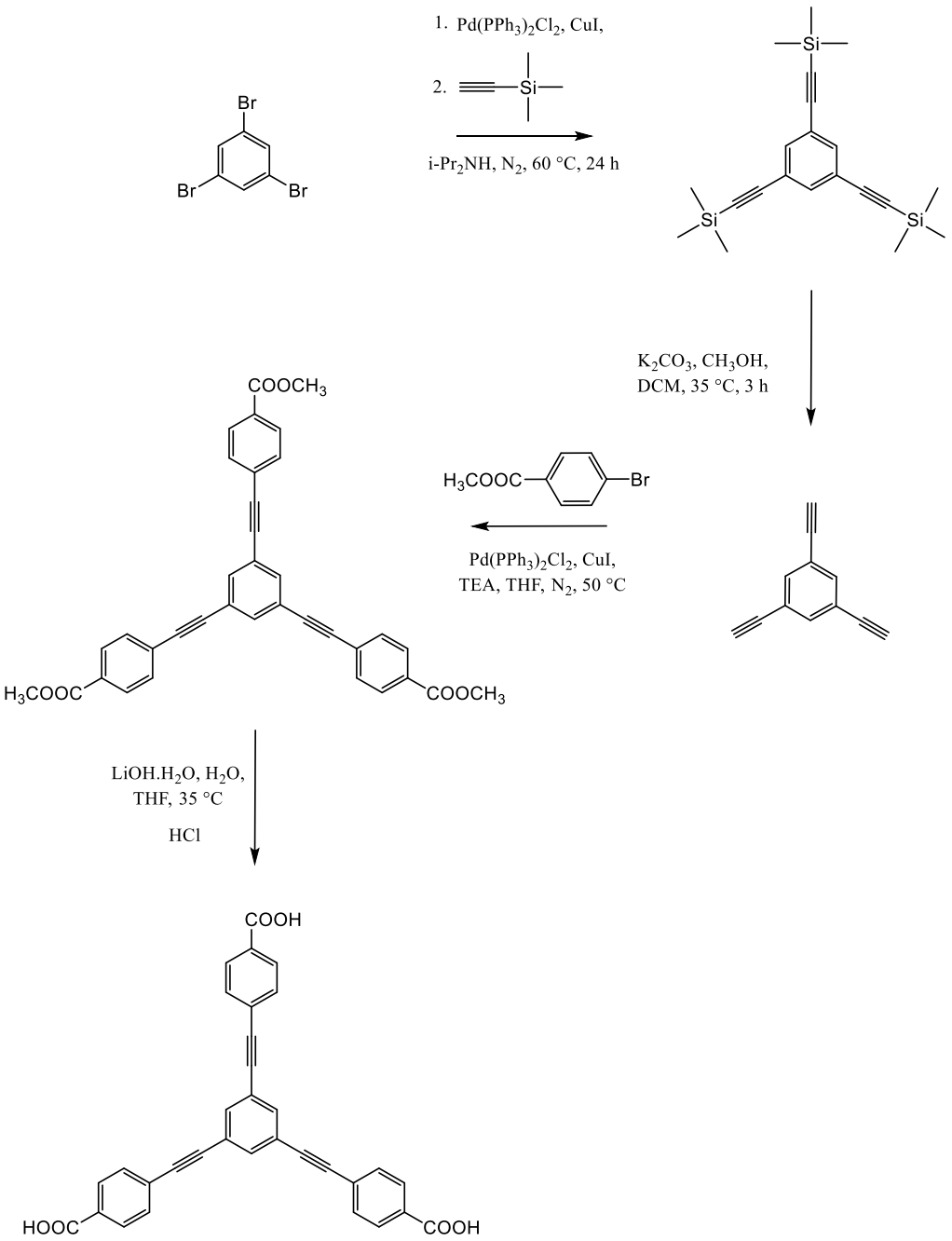

Scheme 2.1.1: *Synthetic procedure for the synthesis of of 4,4',4''-(-(benzene-1,3,5-triyltris(ethyne-2,1-diyl))tribenzoic acid, (**H_3BTEB**) from 1,3,5-tribromobenzene.*

The ^{1}H-NMR spectrum confirmed the formation of **H_3BTEB**. A singlet signal at 7.90 ppm with an integration of three protons corresponding to H-atoms located on the central phenyl ring of the organic ligand. Two doublet signals found at 8.01 and 7.73 ppm, both of which integrate to six protons can be attributed to the twelve H-atoms on the remaining phenyl rings. The hydroxylate protons can be found at 13.21 ppm, also with an integration of 3. Residual solvent peaks for both H_2O and DMSO are found below 4 ppm. (Figure 2.2.1). The ^{1}H-NMR spectrum is in agreement with the literature reported synthesis of the ligand.[11–13]

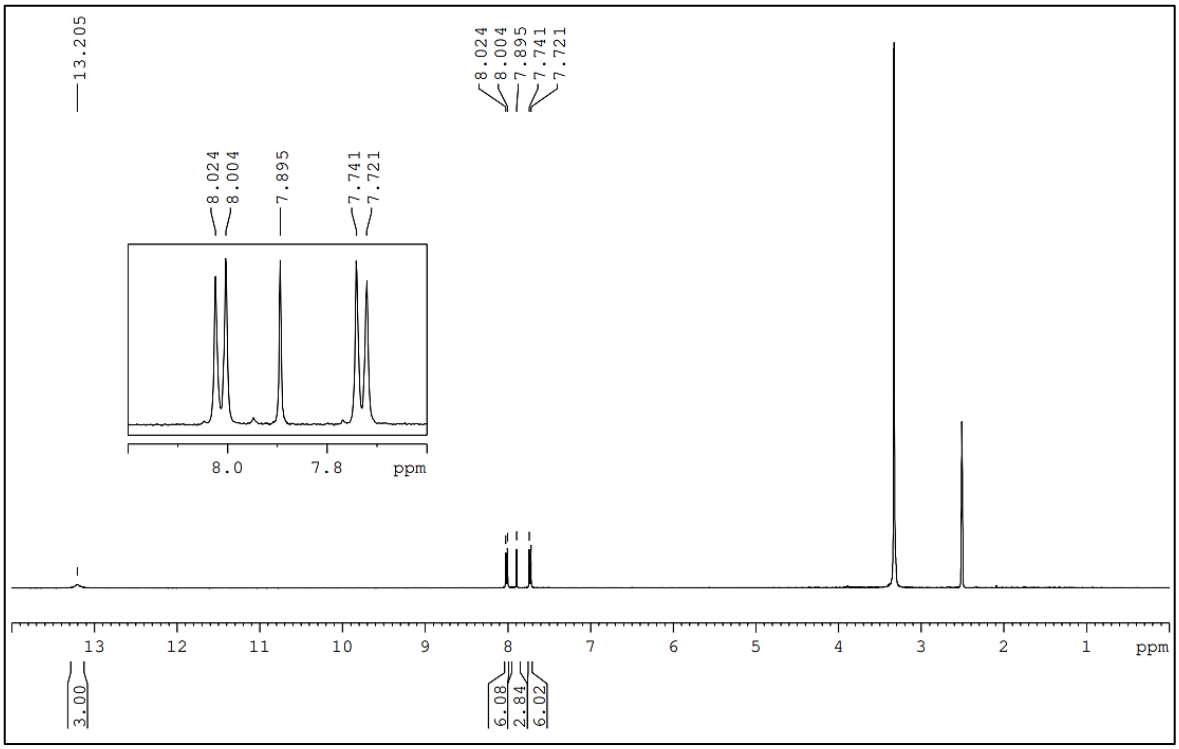

Figure 2.1.1: *Synthetic procedure for the synthesis of of 4,4',4''-(benzene-1,3,5-triyltris(ethyne-2,1-diyl))tribenzoic acid, (**H_3BTEB**) from 1,3,5-tribromobenzene.*

2.2 $Me_2NH_2[Co_5(BTEB)_3(\mu_3\text{-}OH)_2(H_2O)_2(DMF)_2]$, ({$Co_5$}-MOF)

2.2.1 Synthesis and structure of {Co_5}-MOF

The self-assembly of **{Co_5}-MOF** was previously reported and described by Dr. Kevin Byrne. **H_3BTEB** was heated in DMF with $Co(NO_3)_2{\cdot}6H_2O$ in a 1:2 mole ratio at 90°C for 48 hours. Phase-pure purple single crystals of **{Co_5}-MOF** were formed in the reaction mixture and were suitable for single crystal X-ray analysis. A yield of *ca.* 43% was obtained.

{Co$_5$}-MOF crystallises in the monoclinic space group *C*2/*c* with the molecular formula $Me_2NH_2[Co_5(\mathbf{BTEB})_3(\mu_3\text{-}OH)_2(H_2O)_2(DMF)_2]$.

{Co$_5$}-MOF contains a pentanuclear {Co$_5$} inorganic SBU, stabilised by nine carboxylate moieties derived from the fully deprotonated **H$_3$BTEB** ligand via bidentate bridging modes. Two ligands also contain weakly bound carboxylate moieties. The remaining coordination sites of the {Co$_5$} cluster is occupied by two μ_3-OH^- molecules and two monodentate coordinating DMF molecules, the anticipated catalytically active sites for the OER reaction. All Co ions adopt a +2 oxidation state.

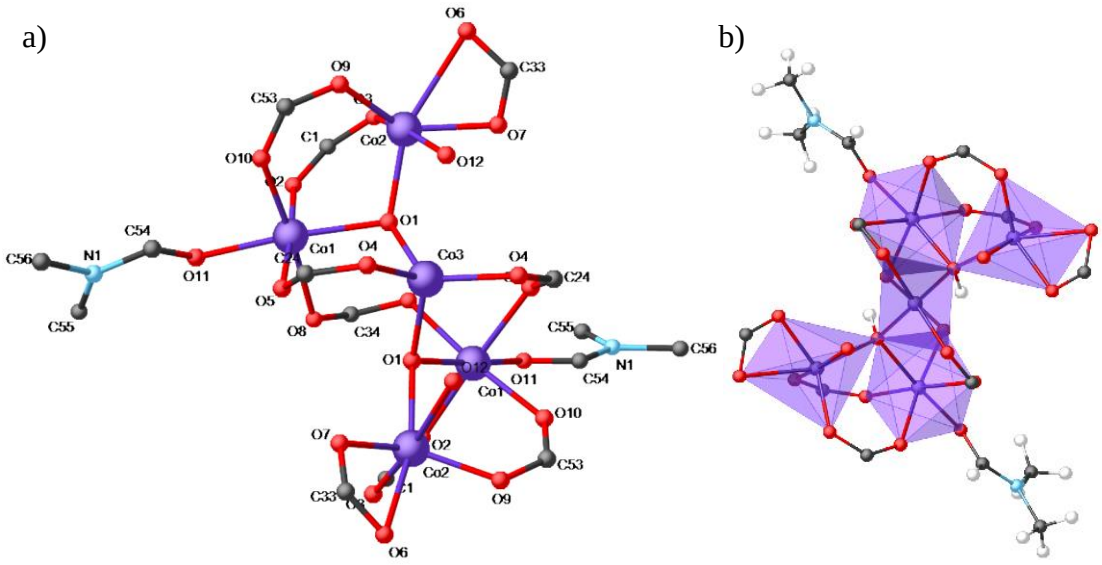

Figure 2.2.1: *a)* ***{Co$_5$}-MOF*** *SBU with two μ_3-bridging OH^- groups, nine coordinated BTEB carboxylate ligand, two DMF molecules and two H_2O molecules. Hydrogen atoms were omitted for clarity. b) View down the crystallographic b-axis using a polyhedral representation to highlight the coordination environment of the four octahedral coordinated Co(II) atoms and one tetrahedral surrounded Co(II) atom. Colour scheme: Co: purple, O: red, C: grey, N: pale blue, H: white.*

The main feature of the structure of **{Co$_5$}-MOF** the pentanuclear cobalt-cluster SBU representing a 9-connecting node. The stabilising **BTEB^{3-}** can be grouped into 3×3 arrays whose struts point in three distinct directions. This binding geometry is dictated by the shape and nature of the organic ligand and results in a 3D MOF structure with a dual-

interpenetrated 'honeycomb' topology as portrayed when viewing down the crystallographic *c*-axis (Figure 1.3.3.).

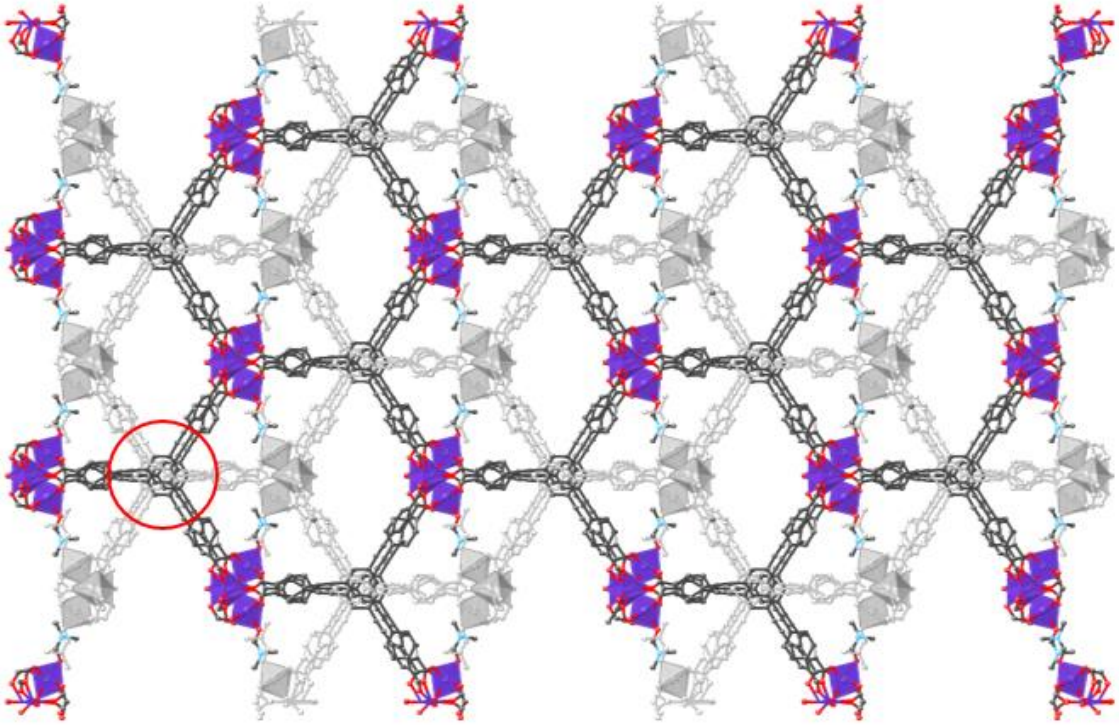

***Figure 2.2.2**: Honeycomb topology of **{Co$_5$}-MOF** with one net highlighted, viewed down the crystallographic c-axis. Areas which contain parallel displacement π-π interactions between different nets are highlighted by a red circle. Colour key: Co purple, O red, N pale blue, C grey. Hydrogen atoms were omitted for clarity.*

***Table 2.2.1**: Crystallographic details for data collected on **{Co$_5$}-MOF**.*

Identification code	**{Co$_5$}-MOF**
Empirical formula	$C_{105}H_{63}Co_5N_2O_{24}$
Formula weight	2031.22
Temperature/K	120
Crystal system	Monoclinic
Space group	*C*2/*c*
a	25.154(5) Å
b	36.948(7) Å
c	19.512(4) Å
α	90.00°
β	123.47°
γ	90.00°
Volume	15126(5) Å^3
Z	4
Density (calculated)	0.892 g/cm^3

Absorption coefficient (μ)	0.585 mm^{-1}
F(000)	4136.0
Crystal size	0.5 × 0.4 × 0.3 mm^3
Radiation	MoKα (λ = 0.71073)
Theta range for data collection	1.10 to 26.02°
Index ranges	-30 ≤ h ≤ 31, -44 ≤ k ≤ 22, -25 ≤ l ≤ 24
Reflections collected	37414
Independent reflections	15154 [R_{int} = 0.0516]
Completeness to theta = 25.68°	100%
Refinement method	Full-matrix least-squares on F^2
Data/restraints/parameters	15154/11/625
Goodness-of-fit on F^2	0.942
Final R indexes [I>=2σ(I)]	R_1 = 0.0543, wR_2 = 0.1433
Final R indexes [all data]	R_1 = 0.0851, wR_2 = 0.1514
Largest diff. peak/hole	0.665/-0.659 e $Å^{-3}$

Synthesised crystals of **{Co_5}-MOF** were ground into powder form and a PXRD pattern was recorded on an APEX II DUO X-ray diffractometer to characterise the phase-purity of the synthesised bulk material. The PXRD pattern was measured in a quartz capillary at 220 K to obtain low-angle (2θ < 10 °) reflections and to avoid any loss of crystallinity of the MOF associated with solvent evaporation. The experimental pattern between 2θ = 4 and 40 °, and a simulated PXRD pattern obtained from the single crystal X-ray diffraction data are directly comparable, confirming the phase-purity of the synthesised material.

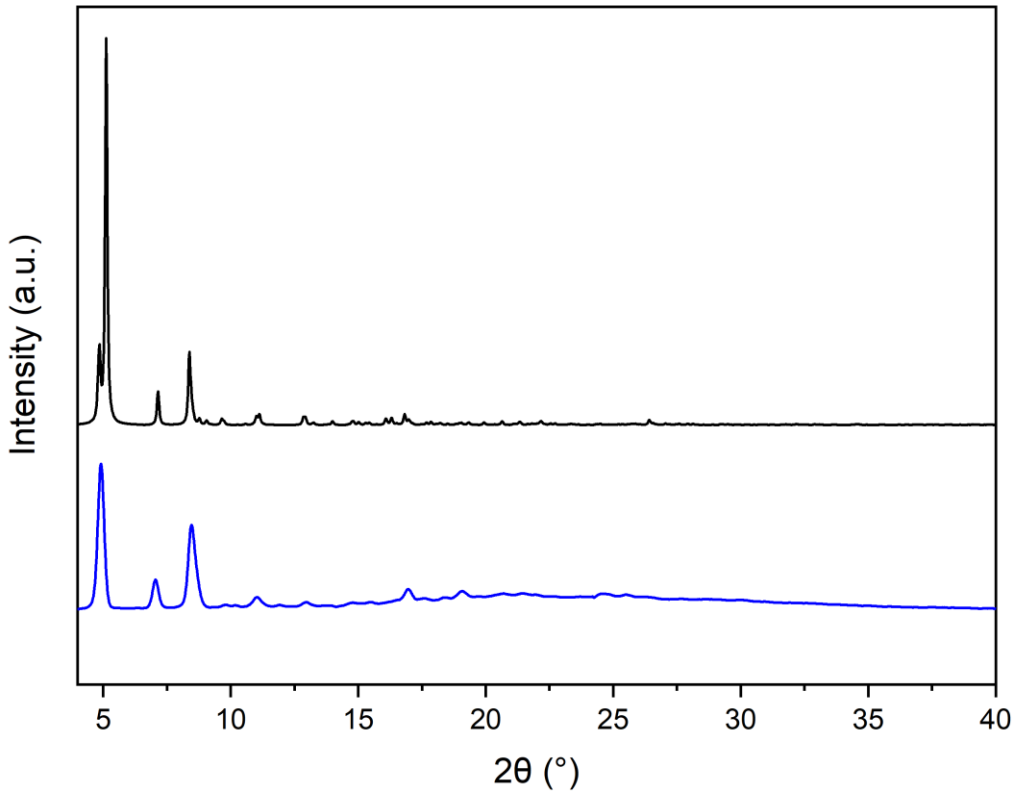

***Figure 2.2.3**: PXRD patterns of **{Co$_5$}-MOF**, calculated from the single crystal data (black) and measured crystals (blue).*

2.3 Carbonisation of {Co$_5$}-MOF

Heat treatment of MOFs has been recently explored to overcome certain challenges faced when using MOF catalysts in water splitting experiments. Namely, a number of highly active MOFs suffer from low stability in aqueous solutions outside of the neutral pH range.[14] Through controlled heating of the bulk material above the decomposition temperature of the organic ligand component, the desirable properties of the material are retained such as the porosity and thus the accessibility to active sites, while the conductivity of the framework is improved with the conversion of the linkers to a carbon-based matrix. Calcination of MOFs generally result in the formation of a solid-state material whereas carbonisation under inert atmosphere facilities no loss of organic components as CO_2 upon heating. **Co@C-500** was synthesised from the carbonisation of **{Co$_5$}-MOF** in an effort to improve the MOF catalytic activity under alkaline pH conditions.

2.3.1 Synthesis of Co@C-500

The as-prepared, 5.0 mg of crystalline **{Co_5}-MOF** was transferred to a quartz crucible and annealed at 500 °C for 4 h in a Pyris 1 PerkinElmer thermogravimetric analyser with a heating temperature rate of 3 °C min^{-1} under an N_2 atmosphere. The MOF was annealed in an inert atmosphere and above the melting point of **H_3BTEB** to produce **Co@C-500**, cobalt oxide nanoparticles dispersed within a porous graphite matrix (Co@C); this matrix act as protective shell for the dissolutions of Co ions in the electrolyte during catalysis experiments while also retaining a level of the porosity of **{Co_5}-MOF**.

2.3.2 Physicochemical characterisation of Co@C-500

For X-ray powder diffraction (PXRD) characterisation, **Co@C-500** was ground into a fine powder and a PXRD pattern was recorded on a Bruker D2 Phaser powder X-ray diffractometer to confirm the formation of cobalt oxide from **{Co_5}-MOF** after thermal treatment. The PXRD pattern was measured in a zero-background sample holder plate with a powder well. The experimental pattern obtained and previously reported data for Co_3O_4 containing heat treated material were compared and shown to have identical patterns, confirming the formation of spinel cobalt oxide in the sample. The PXRD of Co_3O_4 nanoparticles annealed at 500 °C is shown in Figure 2.3.1, which indicates the cobalt oxide has cubic phase structure. The peak positions (2θ = 19.0 º, 31.3 º, 36.9 º, 38.6 º, 44.9 º, 59.41 º and 65.3 º) and relative intensities obtained for the Co_3O_4 match nanomaterials heat treated at 500 ºC.[15] Nine major signals are visible in the measured pattern between 2θ = 10 and 70 º. The observed diffraction peaks were indexed as (111), (220), (311), (222), (400), (422), (511) and (440) planes of Co_3O_4. A peak at 27.1 º corresponds to the (002) of graphite. The (101) and (004) planes for graphite are of much lower intensity to the (002) and are lost under the (400) and (422) of Co_3O_4. No additional peaks other than peaks due to spinel cobalt oxide were observed, indicating phase purity of the cobalt core and the complete conversion of the MOF to **Co@C-500**.

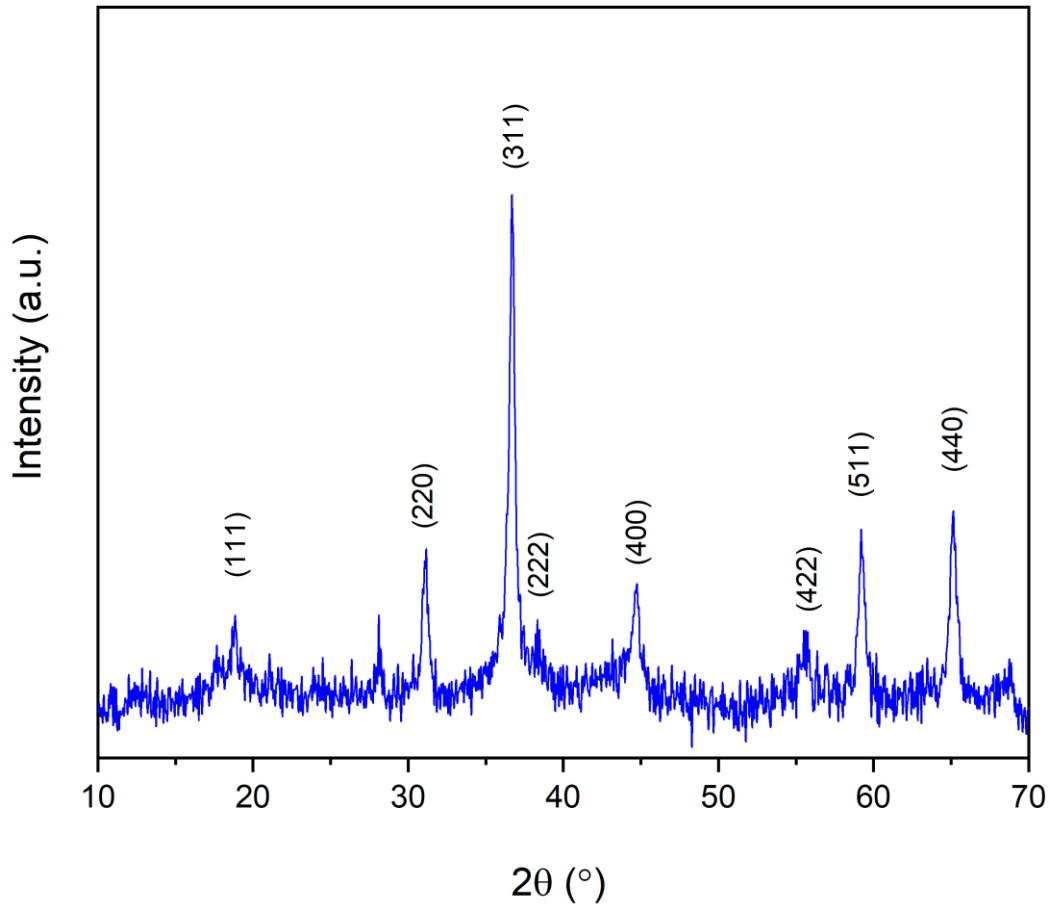

***Figure 2.3.1**: PXRD patterns of **Co@C-500**.*

2.3.3 Raman spectroscopy

The Raman spectra of **Co@C-500** was obtained using a sample ground into a fine power on a glass slide. The measurement was obtained using a Renishaw-1000 micro-Raman spectrometer equipped with a magnification objective (50×) and a cooled CCD camera system, which was calibrated prior to measurements using an internal Si standard wafer. The sample was excited using a 785 nm laser with a spectral resolution of 1 cm^{-1}. Each spectrum was averaged over 100 measurements with an accumulation time of 10 seconds. As shown in Figure 2.3.2, **Co@C-500** exhibits bands at 482, 520, 621, 690 cm^{-1}. The prominent Raman peaks correspond to the *Eg* (482 cm^{-1}), *F2g* (519 and 621 cm^{-1}), *A1g* (690 cm^{-1}) modes of the Co_3O_4 crystalline phase. This result confirms that the crystalline structure of the **Co@C-500** can be identified by Raman spectroscopy. Below 1000 cm^{-1} a large band typical of graphic materials is reported.

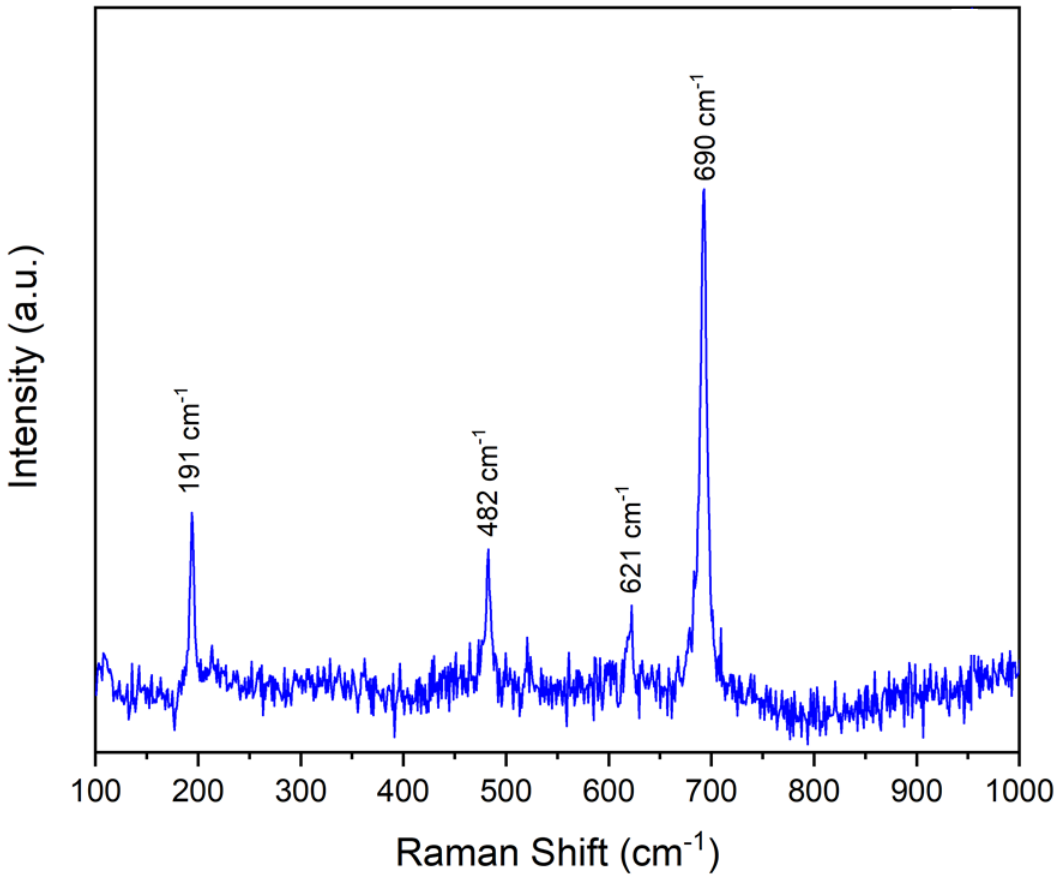

***Figure 2.3.2**: Raman spectrum of **Co@C-500**.*

2.3.4 Transmission electron microscopy

High-resolution transmission electron microscopy (HR-TEM) is the most commonly used technique for imaging non-periodic local structures of crystalline materials, which are not suitable for single crystal diffraction.[16] TEM was used to collect structural information on both the cobalt oxide core and carbon shell of **Co@C-500**. The bulk sample was sonicated in isopropanol to isolate individual particles before drop casting onto a lacey carbon support film on a copper TEM grid. The grid was loaded into a FEI Titan 80 – 300kV FEG S/TEM for analysis. Images were obtained under an operating acceleration voltage of 300 kV with an informational resolution limit of 0.1 nm. Images were processed using the Image J software package. Bright field imaging reveals the formation of spherical nanoparticles within a porous graphitic mesh. An overview was obtained to highlight the density of the core particles which appear to aggerate into clusters (Figure 2.3.3). From the imaging data reported, no observable 'free' oxides were found outside the bounds of the graphitic material.. The porosity of the shell can be seen from the overview, but the pore sizes were smaller than the recommended resolution so were subsequently deduced using gas sorption experiments.

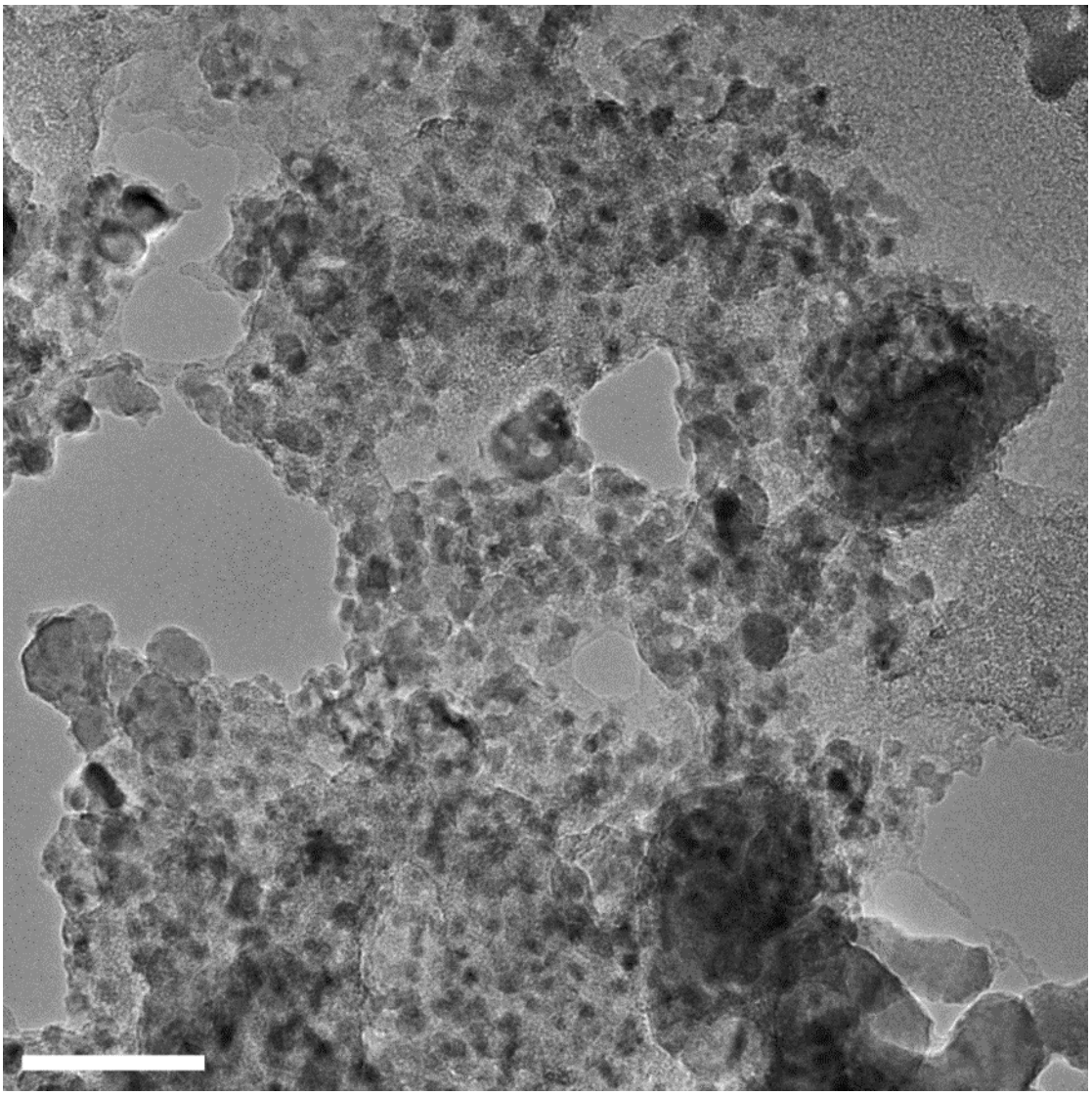

***Figure 2.3.3**: Overview TEM image of **Co@C-500** showing clusters and single particles of Co_3O_4. Scale bar: 50 nm.*

The Lattice spacing is in line with typical nanoplatelet Co_3O_4 with the spacing indicative of the (111) planes visible (Figure 2.3.4). Co_3O_4 nanoparticles are relatively homogeneously distrusted throughout the porous matrix, with the dispersed particle diameter of approx. 3 – 9 nm. Larger particles appear to be due to clusters of oxides.

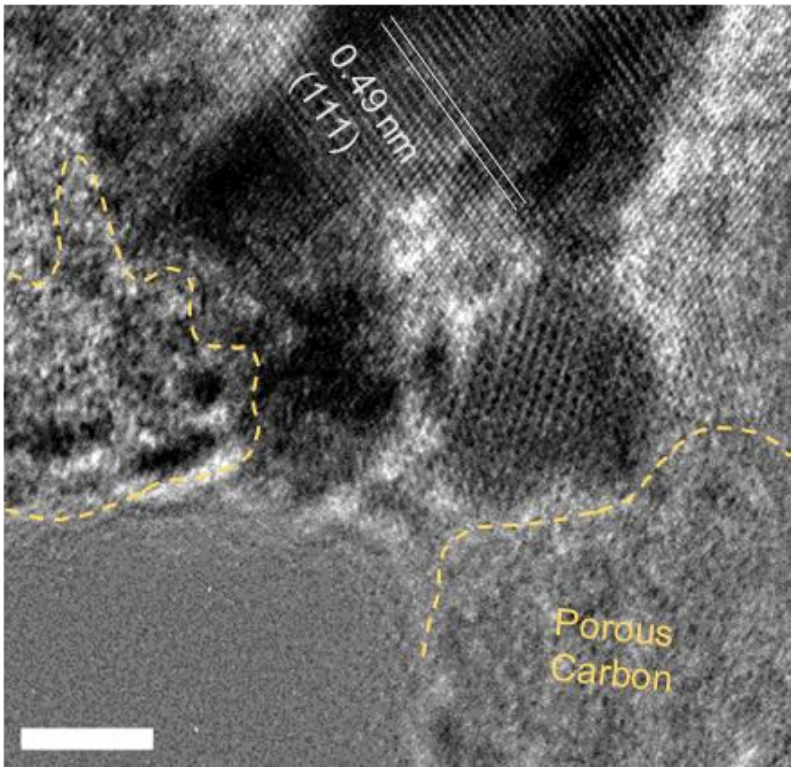

Figure 2.3.4*: TEM imaging of* ***Co@C-500*** *displaying the crystalline lattice core of* Co_3O_4 *within a graphitic shell. Scale bar: 5nm.*

2.3.5 Gas sorption studies

The slow temperature gradient employed in the carbonisation of **{Co_5}-MOF** to **Co@C-500** should allow for a degree of porosity to be obtained. Gas sorption experiments were conducted to deduce the pore sizes of the resulting structure. After heat-treatment, volumetric N_2 gas sorption was recorded on an activated bulk sample of **Co@C-500** in a 0 – 1 bar pressure window using a Quantachrome Autosorb-iQ gas analyser. 17 mg of the as-prepared sample was transferred to a quartz measurement sample cell and subjected to vacuum and activated at 200 °C for 10 hours. The accurate weight of the activated sample was recorded prior to analysis.

2.3.5.1. N_2 adsorption studies

The N_2 gas sorption shows a reversible type-I isotherm at 77 K with a steep uptake at low partial pressures as the micropores are occupied (Figure 2.3.5). A maximum uptake of 191 cm^3/g at 1 P/P_0 was obtained. This step is consistent with the presence of small pores of *ca.* 2 nm in diameter and confirming **Co@C-500** as a microporous material.

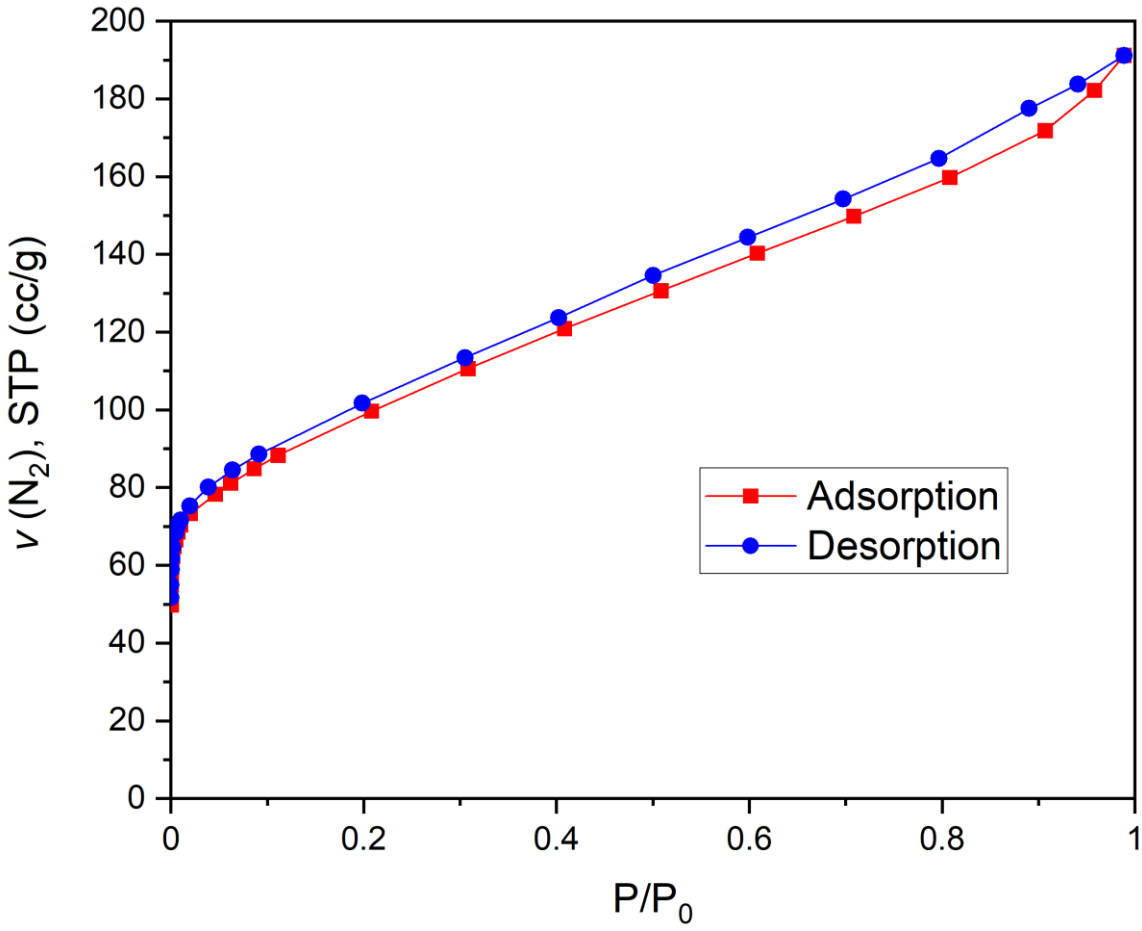

***Figure 2.3.5**: N_2 sorption isotherm of **Co@C-500** measured at 77K.*

2.3.5.2. BET surface area determination

The BET (Brunauer-Emmett-Teller) surface area of **Co@C-500** was determined from the linear region of the N_2 adsorption isotherm at 77 K before the micropore filling step. The BET equation (Equation 2.3.1) for a surface area measurement was used for the analysis of the data.

$$\frac{1}{W[(P_0/P)-1]} = \frac{1}{W_m C} + \frac{C-1}{W_m C}\left(\frac{P}{P_0}\right) \qquad \text{(Eq. 2.3.1)}$$

Where P and P_0 are the equilibrium and the saturation pressure of adsorbates at the temperature of adsorption. W is the weight of the gas adsorbed at the relative pressure P/P_0. C is referred to as the BET constant, proportional to the energy of the adsorption of the first adsorbed monolayer and is a used as a measure of the degree of adsorbent/adsorbate interaction. W_m is the weight of the adsorbate of a monolayer of surface coverage.

The BET equation can be present as the linear plot of $1/[W((P_0/P)-1)]$ against P/P_0 with **Co@C-500** as the adsorbent and N_2 as the adsorbate. The slope of the line, $s = (C - 1)(W_mC)$ and the intercept $i = 1/(W_mC)$ are used to compute the BET C-constant. The BET surface area, or the specific surface area (S_{BET}) was calculated from the total surface area (S_{total}) (Equation 2.3.2 and Equation 2.3.3).

$$S_{BET} = \frac{S_{total}}{w} \qquad \text{(Eq. 2.3.2)}$$

$$S_{total} = \frac{W_m N A_{cs}}{M} \qquad \text{(Eq. 2.3.3)}$$

Where w is the weight of the adsorbent, N is Avogadro's number and M is the molar mass of the adsorbate. A_{cs} is the cross-sectional area for a close placed nitrogen monolayer, which is known to be 16.2 $Å^2$ at 77 K. A BET surface area of *ca.* 348 $m^2\ g^{-1}$ was found for **Co@C-500** (Figure 2.3.6). This is comparable to activated carbon and other porous carbon-based materials.

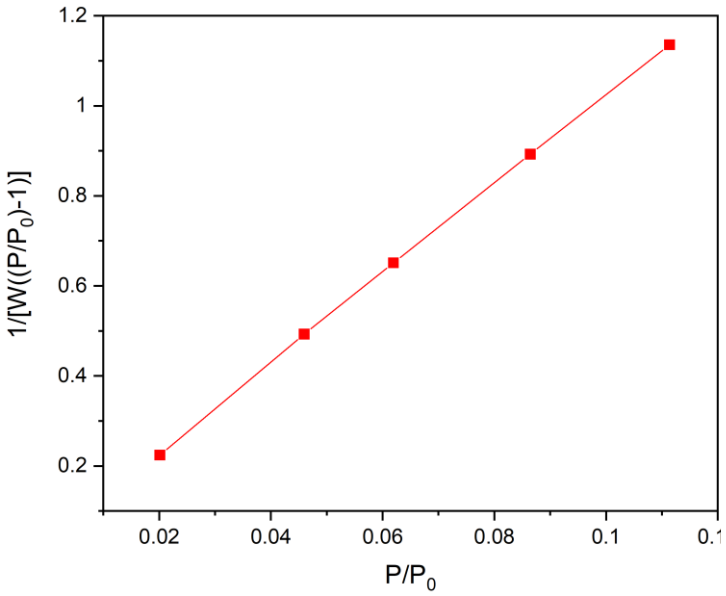

Slope	9.968
Intercept	2.97 x 10^{-2}
C constant	337.228
r (correlation coefficient)	0.999901
BET surface area	348.341 m^2/g

***Figure 2.3.6**: a) Plot of the linear region used to obtain the BET surface area of **Co@C-500**, b) Table of the values obtained from the BET Plot.*

2.3.5.3. DFT calculations to determine pore-size distribution

The gas sorption isotherm can provide insight into the microstructure of the analysed material. The theoretical pore sizes of MOFs can be estimated from the single crystal data of the material but this is not possible with carbonised materials. The pore-size distribution is of significant importance when analysing non-defined materials such as **Co@C-500** when

specifically using the N_2 adsorption at 77 K. The capillary condensation occurring in a selected pore can be directly related to the size of the pore and as a result the condensation pressure can be used as an indication of the pore size distribution. In the case of **Co@C-500**, a broad distribution of pore sized < *approx.* 20 nm is expected. Density Functional Theory (DFT) can be used as a practical method of determining this distribution of pore sizes, assuming for simple cylindrical pores such as expected in graphitic materials. This method is specifically useful in relation to the experimental capillary condensation pressures as it relates to a singular geometry resulting in converging simulation results. DFT calculations were conducted using the Quantachrome ASiQwin package in combination with the N_2 adsorption isotherm obtained at 77 K. The model for the calculation is the NLDFT equilibrium model (N_2 at 77 K on carbon slit pore developed for cylindrical pore in similar carbon-based materials to compare the isotherm with theoretical absorbents). The results show that **Co@C-500** is predominately a classical microporous material with a decreasing distribution above 2 mn (Figure 2.3.7).

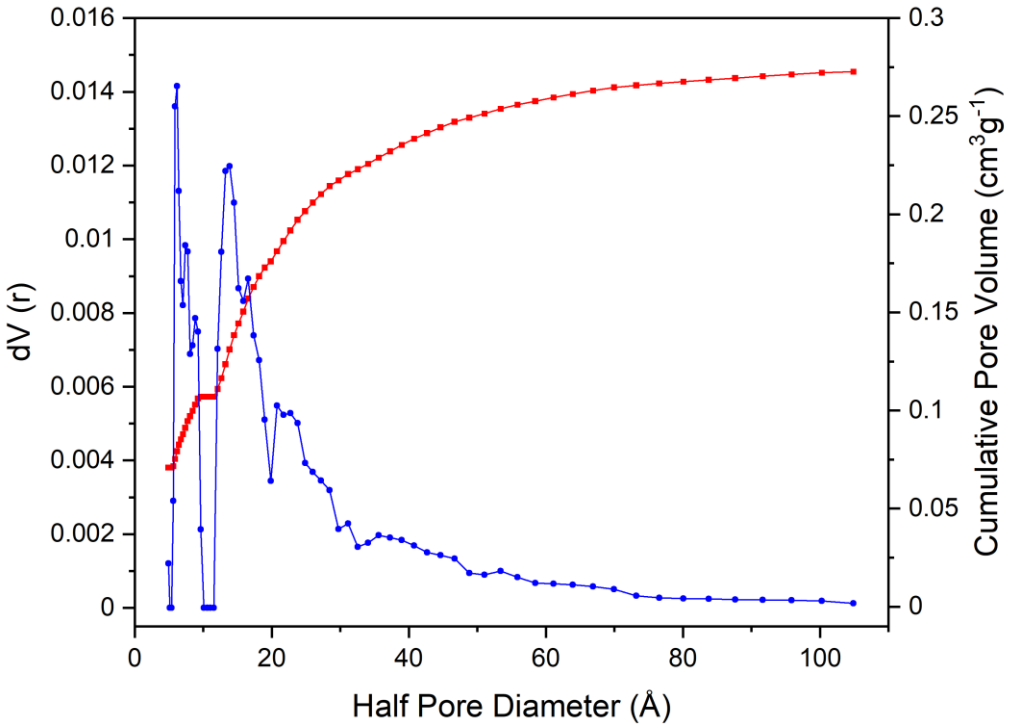

***Figure 2.3.7**: Pore size distribution of **Co@C-500** (blue) and cumulative pore volume (red) calculated from DFT.*

2.4 Electrodeposition of {Co_5}-MOF

Recent applications of MOFs and MOF based materials focus on use in catalysis for water splitting and organic transformations.[17] A key advantage for potential catalysts is their ability to form adherent, microporous layers on top of conductive substrates, improving the conductivity between the catalyst and the electrode surface when compared to other deposition techniques such as drop casting or spin coating.[18] The formation of **Co@C-500** is possible via a thin-film MOF intermediate. **{Co_5}-MOF** was successfully deposited on both fluorine-doped tin oxide (FTO) and carbon cloth (CC) electrodes following a general cathodic procedure.

2.4.1 General Synthesis of {Co_5}-MOF/electrode

The synthesis **Co@C-500**/electrode was conducted via the electrochemical formation of **{Co_5}-MOF** by deposition on an electrode surface to secure strong physicochemical contacts between catalysts and conductive supports. It was found that thin-film coatings of **{Co_5}-MOF** form on FTO glass and CC electrodes. **{Co_5}-MOF** was deposited on 1 x 2 cm FTO-coated glass slides, masked to 1 cm^2 areas. The solution was compromised of $Co(NO_3)_2 \cdot 6H_2O$ (69 mg, 0.236 mmol), $NaNO_3$ (20 mg) and **H_3BTEB** (73 mg, 0.143 mmol) in a deaerated 0.1 M solution of $(NBu_4)PF_6$ in DMF:H_2O (100:1, 15 mL). The deposition substrate working electrode, Pt-wire counter electrode and an $Ag/Ag(cryptand)^+$ reference electrode were immersed in the solution under a N_2 stream and a potential of -1.5 V vs. $Ag/Ag(cryptand)^+$ was applied for 5 mins to achieve light purple film coatings. (Figure 2.4.1). The film-coated FTO electrodes were removed from the reaction solution and washed with DMF and $CHCl_3$ to remove unreacted cobalt ligand and salts from the film surface before drying in air.

The optimisation of MOF synthesis is closely associated with ligand deprotonation.[19] The addition of water and nitrates during electrodeposition has been previously reported.[20,21] Both have been shown to be critical to facilitate the deprotonation of carboxylic acids of **H_3BTEB** and to avoid the formation of H_2 bubbles on the electrodes during the deposition.[20] NO_3^- ions have been previously shown to improve the surface smoothness and uniformity of the electrodeposited films. It was found that the smoothness of the films and the attachment of the coatings to the FTO surface was enhanced by the addition of NO_3^- ions *via* $NaNO_3$ into the solution.

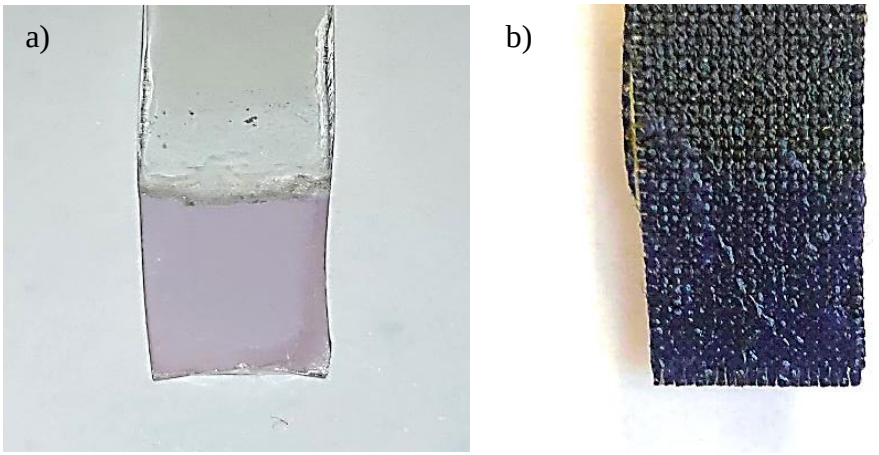

***Figure 2.4.1**: Film of **{Co$_5$}-MOF** deposited on a FTO (a) and a carbon cloth (b) at -1.5 V vs. Ag/Ag(cryptand)$^+$ using an H_2O/DMF a reaction solution containing $NaNO_3$.*

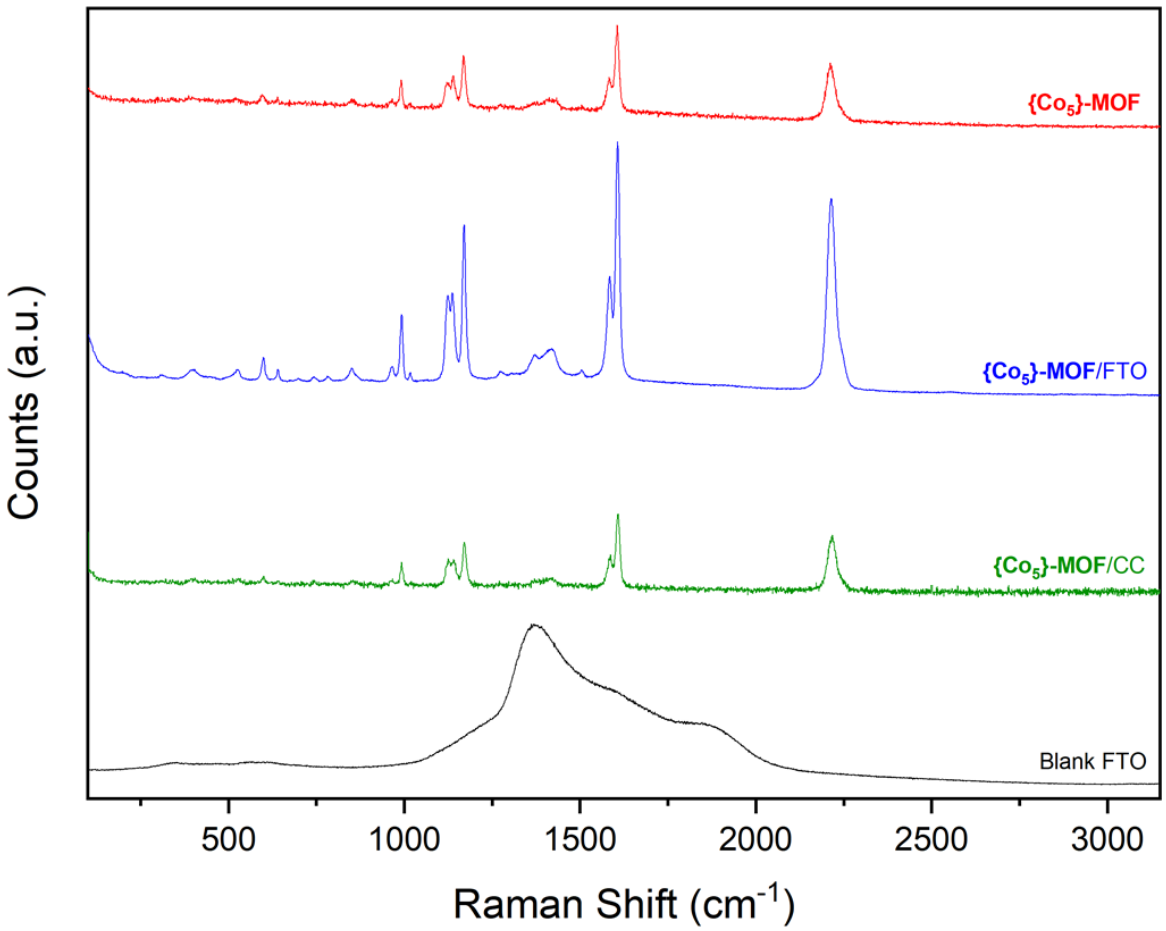

***Figure 2.4.2**: Raman spectra of crystalline **{Co$_5$}-MOF** and the FTO surface after electrochemical deposition.*

2.5 Synthesis of Co@C-500/FTO and Co@C-500/CC

{Co5}-MOF/electrode was subsequently annealed in a tube furnace under N_2 gas at 500 °C. The temperature was set at the max temperature at which the FTO electrode retains a constant resistivity.[22] The furnace was heated to 500 °C for 4 hours before being maintained at 500 °C for 3 hours and then cooled to room temperature under N_2. At temperatures above 500 °C, typical CoO_x structures are expected to be obtained as well as the decomposition of the organic ligand which has a melting point of approx. 390 °C. At 500 °C, spinel Co_3O_4 is formed, encased in the carbon matrix, provided by the organic ligands of **{Co$_5$}-MOF**. After heat-treatment, the coated film on the electrode was removed from the furnace and washed with DMF to remove any free particles. The electrodes was rinsed with MilliQ water and dried in air. On the basis of structure and composition characterisation, the formula of the product is identical to **Co@C-500**. The complete pathway to **Co@C-500**/FTO can be seen below. (Scheme 2.5.1).

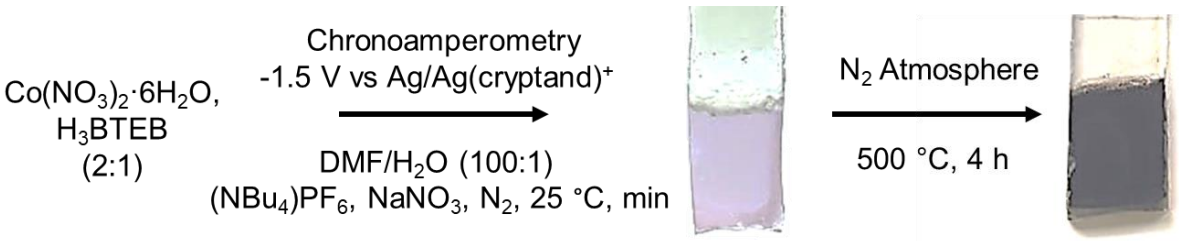

***Scheme 2.5.1**: **Co@C-500**/FTO synthesised from the electrodeposition coating of **{Co$_5$}-MOF** on an FTO electrode.*

The pathway to **Co@C-500**/CC takes an identical approach with a pre-treated carbon cloth as the working electrode. The carbon cloth electrode underwent pre-treatment *via* sonication in *conc*. HNO_3 for 2 hours. The cloths were subsequently washed with MilliQ water before drying in air.

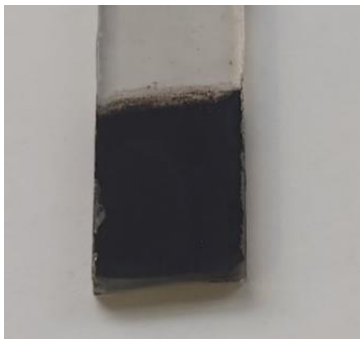

***Figure 2.5.1**: Film of **Co@C-500**/FTO after heat treatment at 500 °C.*

2.6 Physicochemical characterisation of thin-film Co@C-500

A difference of the electrodeposition of MOFs compared to their solvothermal synthesised counterparts is that the framework assembles under a relatively short duration. This results in more amorphous structures on the electrode surface and the single crystal data cannot be extracted. Due to this additional analysis methods were required to confirm the formation of the core@shell structure after heat treatment. **Co@C-500**/FTO was characterised using both bulk and surface sensitive techniques. From the FT-IR and Raman results it is assumed that **Co@C-500**/CC forms the same material when prepared in an identical manner.

2.6.1 Powder X-ray diffraction

The PXRD pattern of **Co@C-500**/FTO was recorded on a Bruker D2 Phaser diffractometer. The PXRD pattern was measured in a zero-background sample holder plate with a well into which the FTO was positioned. Again, the formation of spinel cobalt oxide is presented (Figure 2.6.1). The peak positions (2θ = 19.0 º, 31.2 º, 36.9 º, 38.6 º, 44.9 º, 59.41 º and 65.3 º). The pattern obtained matched that of **Co@C-500** after carbonisation of crystalline **{Co$_5$}-MOF** confirming that both routes of synthesise yield the same final product. Eight signals for cobalt oxide are visible in the measured pattern between 2θ = 10 and 70 º. The observed diffraction peaks were indexed as (111), (220), (311), (222), (400), (422), (511) and (440) planes. A small peak at 27.1 º corresponds to the (002) of graphite. A blank FTO was measured and used for background correction.

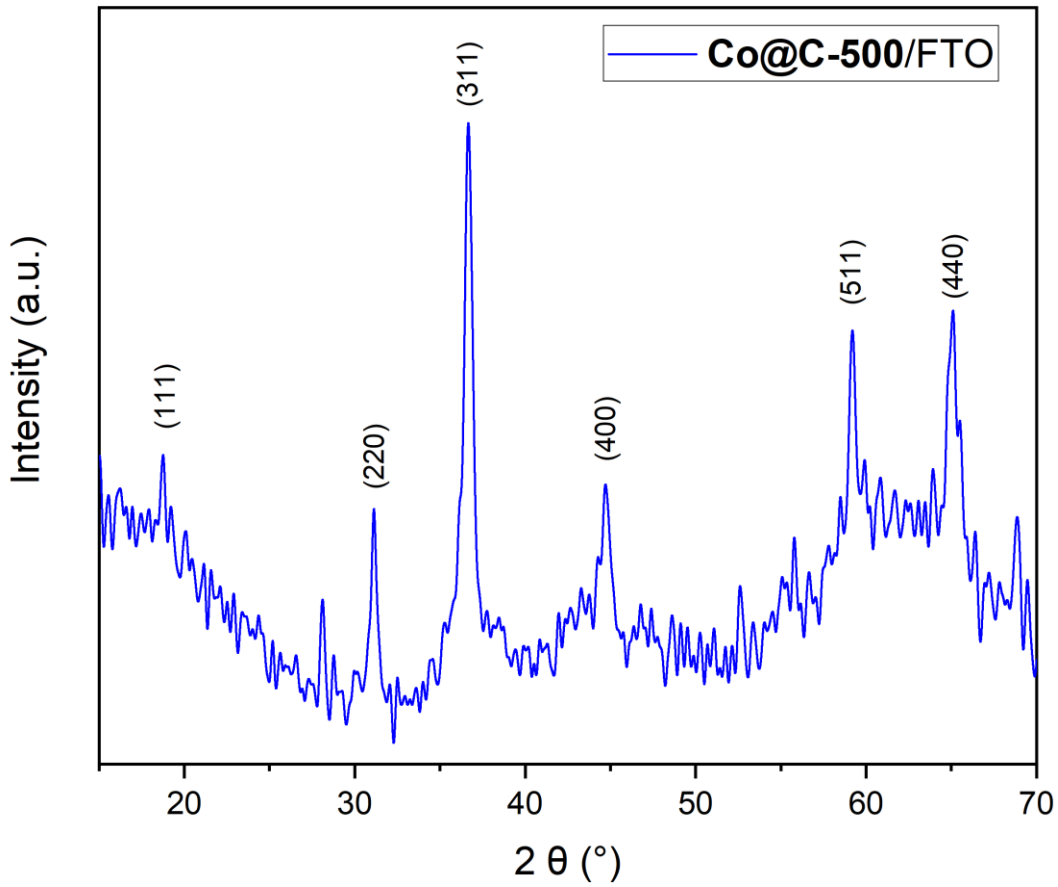

***Figure 2.6.1**: PXRD pattern of **Co@C-500**/FTO.*

2.6.2 Raman and FT-IR

The Raman spectra of **Co@C-500**/FTO was obtained from the electrode surface. The measurement was obtained using a Renishaw-1000 micro-Raman spectrometer equipped with a magnification objective (50×) and a cooled CCD camera system, which was calibrated prior to measurements using the 520 cm^{-1} peak of an internal Si standard wafer. The sample was excited using a 785 nm laser with a spectral resolution of 1 cm^{-1}. Both spectra were averaged over 100 measurements with an accumulation time of 10 seconds. Both samples exhibit the same bands as the bulk powder **Co@C-500** sample at 482, 520, 621, 690 cm^{-1} (Figure 2.6.2). These peaks correspond to the *Eg* (482 cm^{-1}), *F2g* (519 and 621 cm^{-1}), *A1g* (690 cm^{-1}) modes of the spinel cobalt oxide crystalline phase. Below 1000 cm^{-1} a large band typical of amorphous graphite is reported. The spectra confirm that **Co@C-500** can be synthesised on both FTO and CC electrode surfaces.

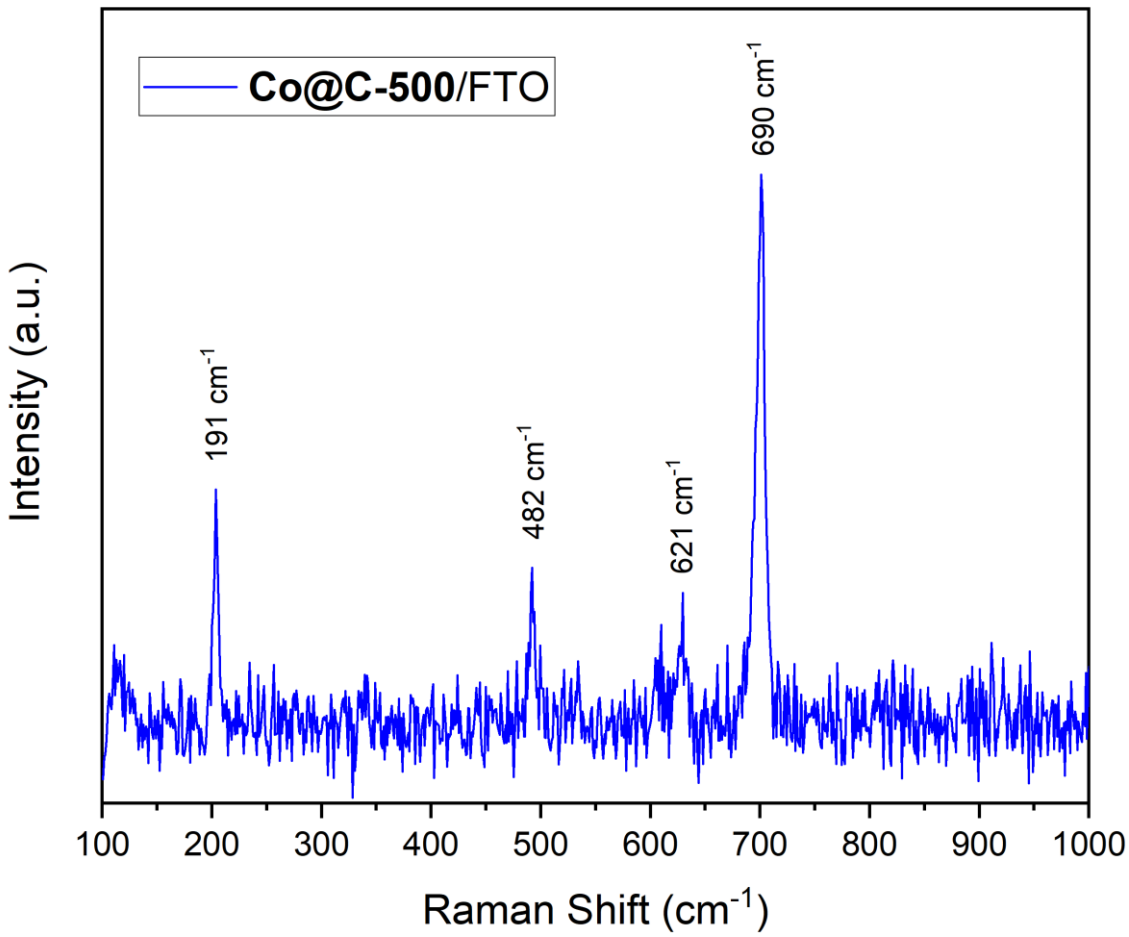

***Figure 2.6.2**: Raman spectrum of **Co@C-500**/FTO.*

Fourier transform infrared (FT-IR) spectroscopy of the thin film surfaces was recorded on a PerkinElmer Spectrum One FT-IR spectrometer using a universal ATR sampling accessory. The experimental data was collected and processed using Spectrum v5.0.1 (2002 PerkinElmer Instrument LLC) software. A scan rate of 16 scans per minute with a resolution of 6 scans in the range 4000-500 cm^{-1} was recorded for both species. The strong bands at 2800–3000 cm^{-1} indicate the presence of an aliphatic –CH stretching. The two vibrations at 1415 and 1384 cm^{-1} are due to CH_2 bending vibration and CH_3 bending vibrations. The resonance at 115 cm^{-1} indicates a C–O stretching region. The bands at 1250 and 1152 cm^{-1} are due to C–C skeletal vibration. The strongest signal recorded at 955 cm^{-1} is attributed to the distributed C=C bending mode. The FT-IR spectra for **Co@C-500** synthesised on FTO and carbon cloth show a high degree of similarities in the fingerprint region. Both are in agreement with spectra obtained from porous oxygenated graphite samples activated *via* carbonisation at 480 °C.[23] The presence of oxygen within the framework is in agreement with the XPS data recorded for **Co@C-500**/FTO.

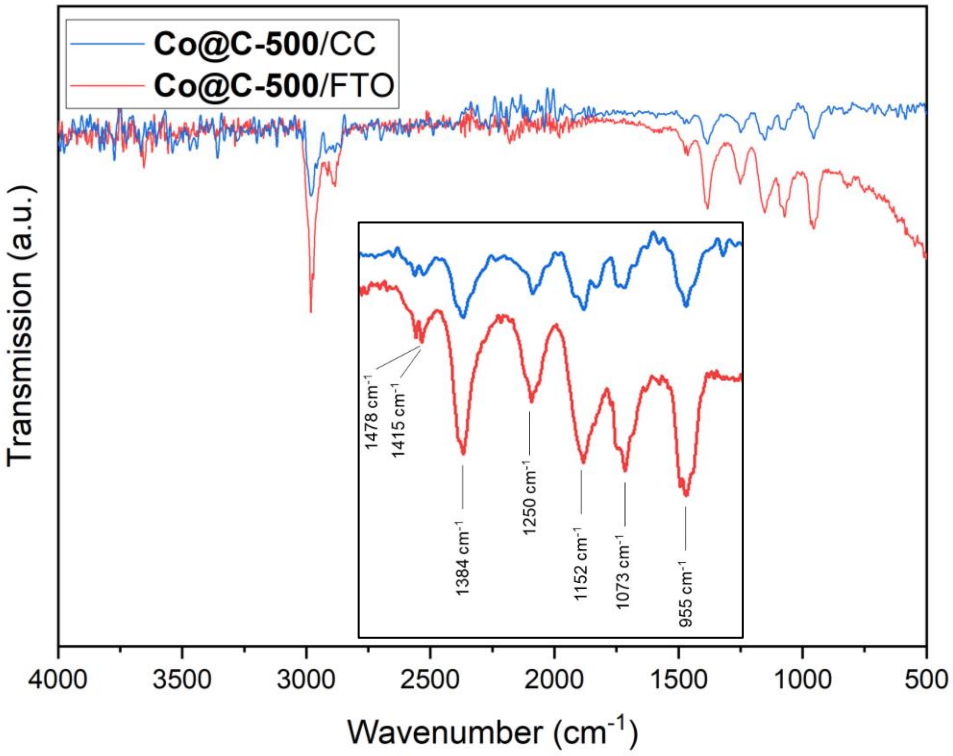

***Figure 2.6.3**: FT-IR spectra of **Co@C-500**/CC (blue) and **Co@C-500**/FTO (red). Fingerprint region enlarged in insert.*

2.6.3 Scanning electron microscopy

Scanning electron microscopy (SEM) was used to image the surface of **Co@C-500** on an FTO glass slide. After synthesis, the films were adhered to adhesive carbon tabs atop aluminium SEM stubs and loaded into a Zeiss ULTRA Plus scanning microscope with an acceleration voltage in the range 2 – 30 kV under a $1x10^{-5}$ mbarr vacuum. The InLens imaging detector was selected to highlight the contrast between changes in the film height.

A cross section could be obtained of **Co@C-500** by tilting the sample holder to a 90° angle and imaging the edge of the film (Figure 3.6.4). A film thickness with an average thickness of *approx.* 7 µm was imaged. This value is equivalent to an electrodeposition time of 5 minutes at -1.5 V but could be altered by adjusting the deposition time of the cobalt MOF. A thickness in this range was seen to optimal as films synthesised with longer deposition times (with a thickness in excess of 10 µm) were prone to detaching from the FTO surfacing during OER experiments at high potential due to excessive gas bubble formation that could not be removed through vigorous agitation of the aqueous solution.

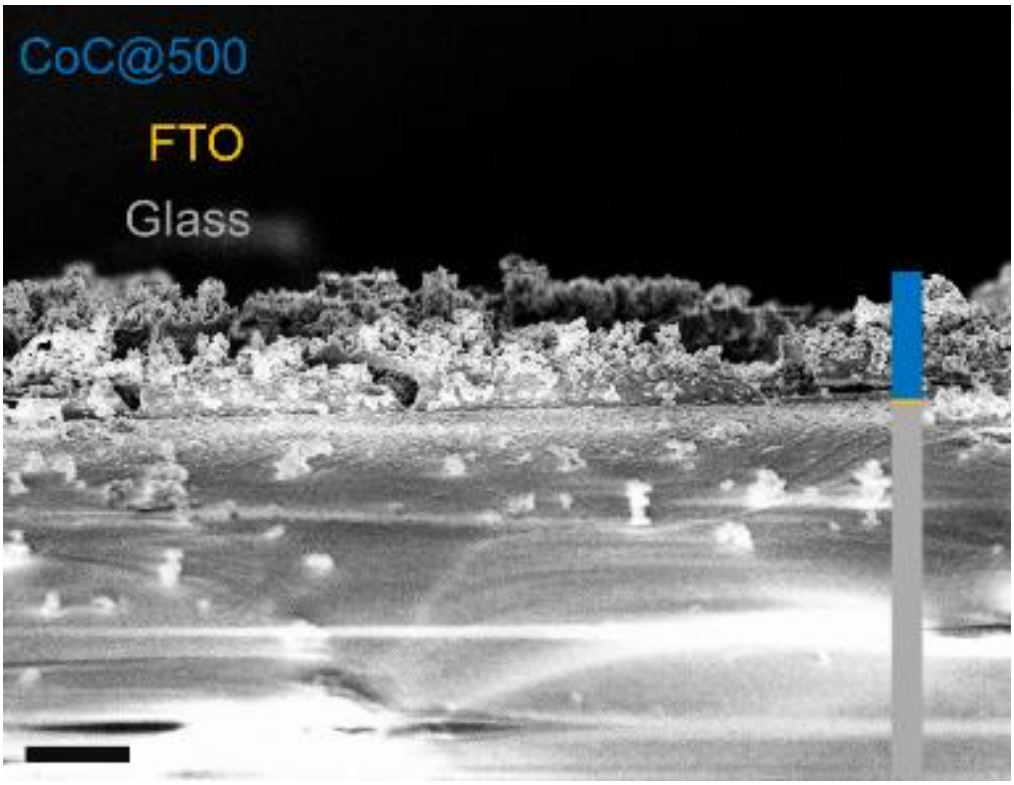

Figure 2.6.4*: SEM image of* ***Co@C-500****/FTO showing a cross section of the FTO film. Scale bar: 10 μm.*

A uniform surface coverage of **Co@C-500** can be observed (Figure 2.6.5, a). In the case of the MOF thin-film, individual particles attach to the electrode surface and appear to grow in aggregates outward, connected to other individual particles forming aggregates. The heat-treated material on FTO appears to retain the same even surface coverage and particle morphology, likely due to the controlled heating rate during the annealing stage and the strong adhesion to the film surface from electrodeposition of the parent MOF. This is in contrast to the TEM images obtained for the bulk material (Section 1.3.4) affirming that having **{Co$_5$}-MOF** bound to an electrode support results in non-aggregating cobalt oxide particles. This is optimal to increase the surface area of the catalytic centres for water oxidation experiments.

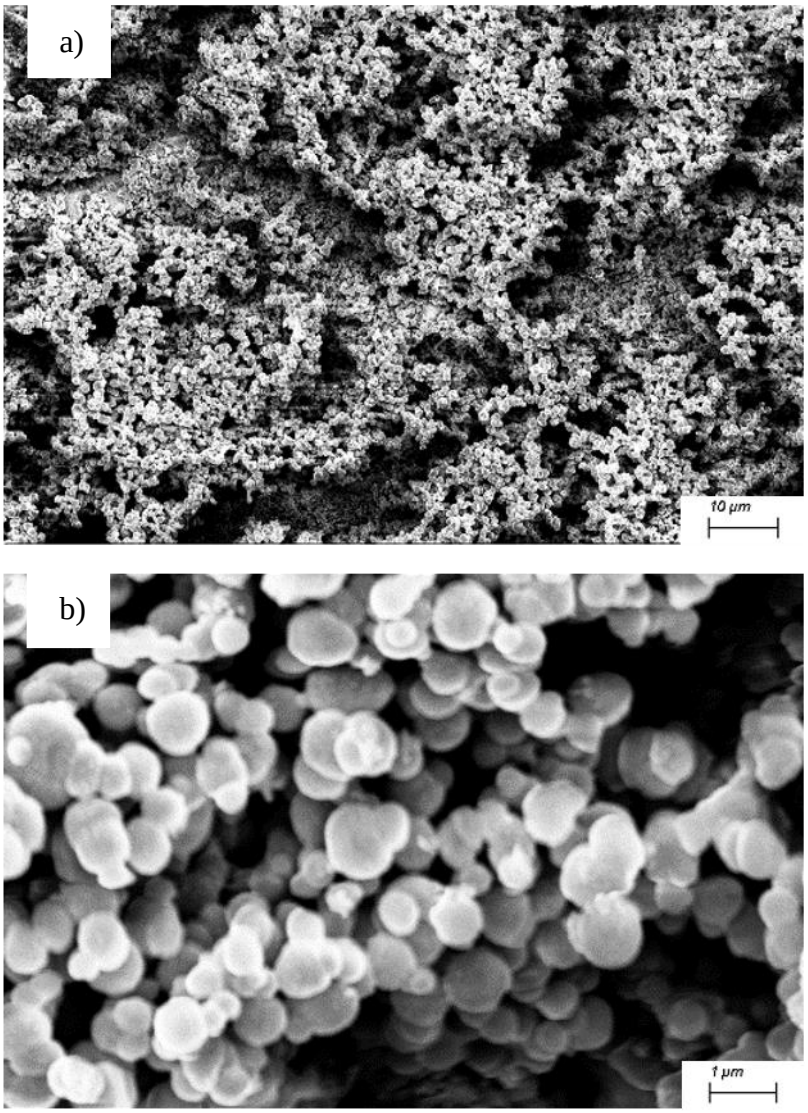

Figure 2.6.5*: The even distribution of* ***Co@C-500*** *on the FTO surface (a) and the morphology and size of the surface particles (b).*

2.6.4 X-ray photoelectron microscopy

The mixed metal oxidation state of cobalt spinel-based materials is beneficial in the enhancing of electrochemical reactions.[24,25] However, complications can arise in identifying these compound in relation to other cobalt compounds. X-ray photoelectron spectroscopy (XPS) is useful in the determination of the mixed oxidation Co ion states to study observable electron shells for both cobalt and oxygen, along with the valence states of the elements. An additional advantage is the extensive characterisation recorded for Co_3O_4 in the literature as well as the National Institute of Standards and Technology (NIST) XPS database, to which results can be compared.

XPS was used for the analysis of the surface of the **Co@C-500**/FTO film surface before and after bulk catalysis at pH 13.5. XPS was performed on a Phi Versa Probe III analyser equipped with a 1487 eV Rowland circle monochromatic Al Kα X-ray source. Samples were adhered to background-corrected adhesive tabs and imaged before analysis using scanning X-ray imaging (SXI) to identify good measurement positions. The survey scan was conducted using a 200 µm spot size with a 224 eV pass energy in 0.4 eV increments. Individual orbitals were analysed on the same sample area at 26 eV for the O 1s and the C 1s and 55 eV for the Co 2p. All orbitals' scans used 0.05 eV increment steps.

An overview spectrum **Co@C-500**/FTO showed the abundance of carbon on the film surface (Figure 2.6.6). This is in agreement with the TEM and STEM imaging of the film, in which the cobalt oxide particles are embedded within the carbon structure. Minute amounts of tin (Sn 3d at *approx*. 490 eV) and potassium (K 2s at *approx*. 295 eV) are visible in the spectrum from contamination from the FTO film surface and from the catalytic experiments in KPi and KOH buffer.

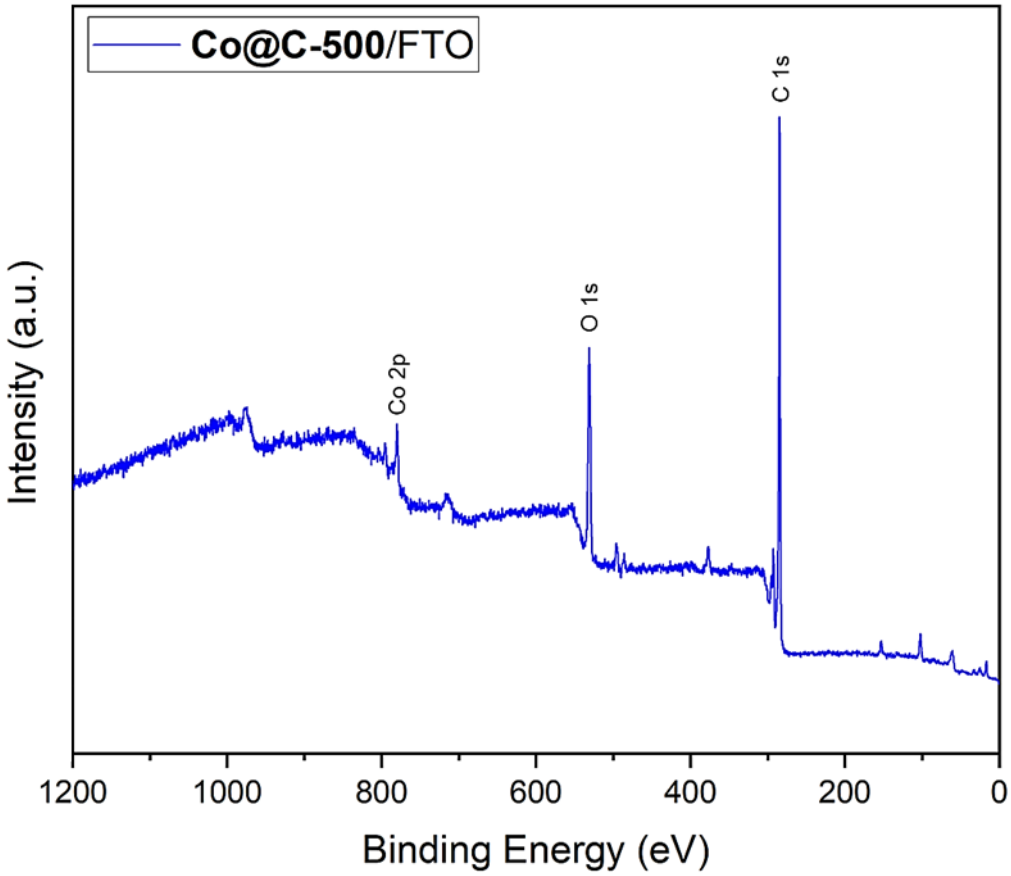

***Figure 2.6.6**: XPS overview spectrum of **Co@C-500**/FTO with intensity measured in counts per second.*

It is possible to distinguish between Co oxidation states using the satellite peak features of the Co 2p orbitals and thus between mixed-oxidation state Co_3O_4 and $Co^{II}O_x$ species. Co(II) has observable satellite bands at *approx*. 785 eV and 802 eV.[26] These satellites were visible in the XPS spectrum of **{Co$_5$}-MOF** in which all Co ions have a 2+ oxidation state. It has been reported that only Co(II) in octahedral sites shows a significant satellite structures.[27] The low-spin, diamagnetic nature of octahedral Co(III) ions and the weaker crystal field effect of tetrahedral coordination for the Co(II) ion result in similar X-ray photoemission binding energies, yielding sharper 2p peak and loss of prominent satellites for the spinel, despite the existence of the Co(II)/Co(III) oxidation states in this material (Figure 2.6.7).[28] These diminished satellite structures, with not entirely $2p_{3/2}/2p_{1/2}$ binding energies, are better able to distinguish between rocksalt CoO and cobalt spinel structures with octahedrally coordinated Co(III). For **Co@C-500**/FTO, the Co $2p_{3/2}$ and Co $2p_{1/2}$ were found at a binding energy of 779.8 and 795.2 eV respectively with any satellite artefacts being indistinguishable from the baseline.

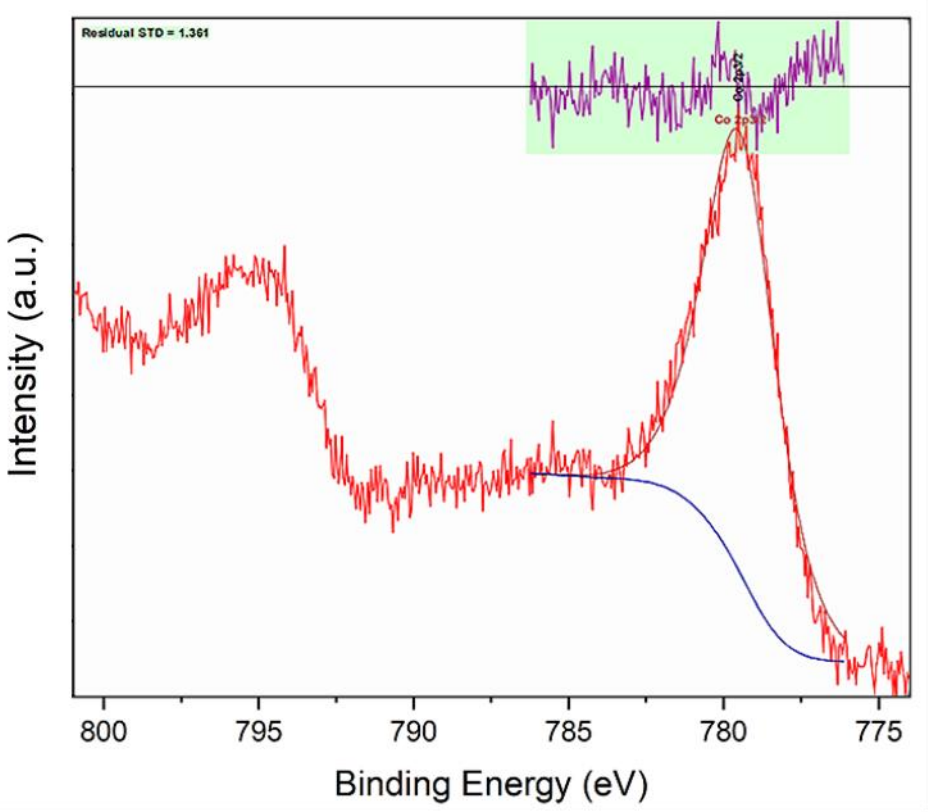

***Figure 2.6.7**: Co 2p sample area scan overview spectrum of **Co@C-500**/FTO with intensity measured in counts per second.*

The C 1s region is indicative of graphitic C=C sp^2 with a peak at 284.7 eV which is in agreement with the carbonisation of MOF-5[29] and Prussian blue polymers.[30] The heat-treatment of MOF-5 retained sp^3 carbon environments from the carboxylate linkers up until calcination at 450 °C also with secondary carbon environment at a higher binding energy. **Co@C-500**/FTO was prepared via heating to 500 °C so it can be assumed that the framework is fully decomposed. There is an obvious additional peak with a higher binding energy at 285.8 eV for **Co@C-500**/FTO, which corresponds to the C–C and C–O–C as a result of pyrolysis at high temperature.[31] The presence of C–O–C can be confirmed in the O 1s spectrum.

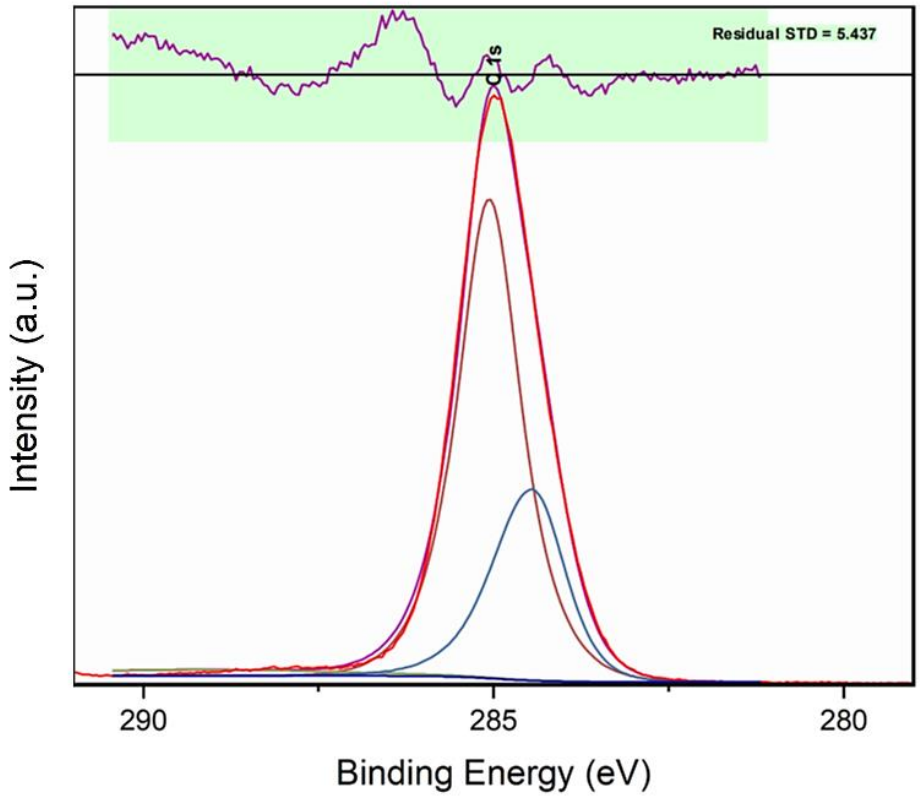

Figure 2.6.8: *C 1s sample area scan overview spectrum of* ***Co@C-500****/FTO with intensity measured in counts per second.*

The O 1s region displays a main oxygen peak at 529.7 eV, which has previously been reported for O^{2-} ions in the Co_3O_4 lattice (Figure 2.6.9). A second peak of similar intensity to 529.7 eV can be seen at a higher binding energy of *approx.* 532.0 eV which can be defined as a combination of surface hydroxyls from the film deposition synthesis,[32,33] under coordinated O^- atoms,[32,34,35] chemisorbed oxygen into the graphite matrix,[36] as well as potential errors in peak fitting as the two O species appear to be of equal intensity. However,

previously reported thin-film Co_3O_4 also display two significant distinctive oxygen environments without a matrix.[37]

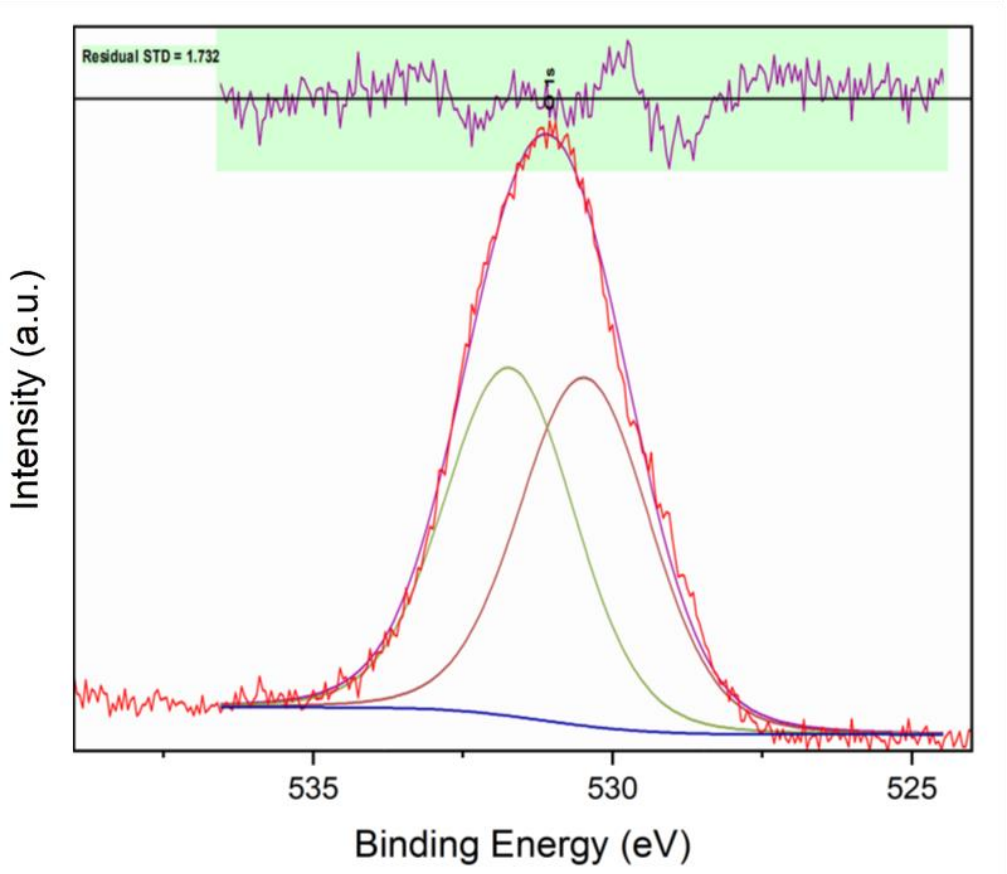

***Figure 2.6.9**: O 1s sample area scan overview spectrum of **Co@C-500**/FTO with intensity measured in counts per second.*

The relative surface concentration ratio of O and Co (C_O/C_{Co}) can be estimated using the integrated XPS intensity values (I_i) and the previously standardised sensitivity factor (S_i) of S_{Co}/S_O = 5.43[38] (Equation 2.6.1). For **Co@C-500**/FTO, C_O/C_{Co} was found to be 1.42 ± 0.15, which is in agreement with the stoichiometric ratio within error.[39]

$$\frac{C_O}{C_{Co}} = \frac{I_O/S_O}{I_{Co}/S_{Co}} \qquad \text{(Eq. 2.6.1)}$$

2.7 Water oxidation studies

Due to their porosity and highly crystalline nature, MOFs contain a high number of assessable active sites. A drawback of many MOFs is their instability in water or at high or

low pH values, at which the splitting of water is most facile.[40] This develops into a problem when utilised commercially to perform water-oxidation catalysis in aqueous solution. MOFs have been extensively studied for certain green-energy applications, namely catalysis and gas storage/separations. What is currently less explored, is the use of MOFs as templates or precursors for energy conversion and storage devices. Thermally activated MOFs display distinct advantages compared to their parent materials, including electrolytic conductivity and a higher resistance to corrosion by the electrolyte, allowing for long-term stability in basic aqueous solution. **{Co$_5$}-MOF** has been previously explored as a water oxidation catalyst. As with many MOF-based catalysts, a drawback was the need for a neutral pH buffer during the experiments. Experiments carried out in alkaline pH resulted in the decomposition of the {**Co$_5$}-MOF**. To better compare {**Co$_5$}-MOF** and **Co@C-500** water oxidation catalysis experiments were conducted for both species on FTO electrodes at pH 7.2.

2.7.1 Water oxidation studies at neutral pH

Washed films of **Co@C-500**/FTO and {**Co$_5$}-MOF**/FTO were used as the working electrode in combination with a Pt-mesh counter-electrode and an Ag/AgCl (3 M) reference electrode to complete the three-electrode configuration. Linear sweep voltammetry (LSV) was performed in aqueous solutions of KNO_3 (1M) and KPi buffer (50 mM, pH 7.2) was used at 20°C. A scan rate of 1 mV sec^{-1} was used in a 0.5 – 1.2 V range vs Ag/AgCl and converted to potential versus the normal hydrogen electrode (NHE) (Figure 2.7.1).

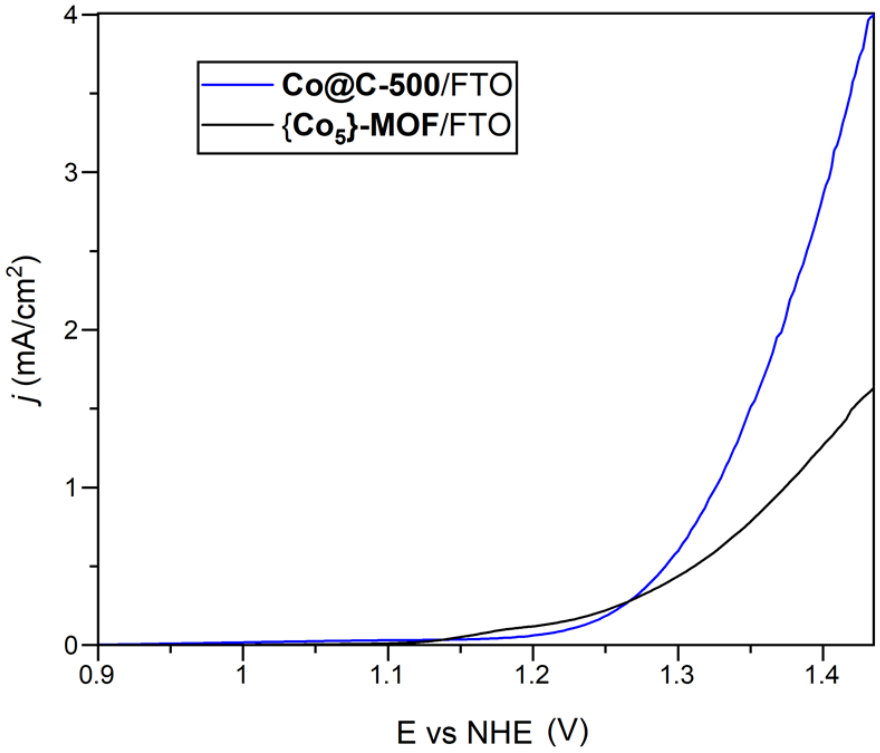

***Figure 2.7.1**: LSV showing the comparative electrochemical behaviour of **Co@C-500**/FTO and **{Co$_5$}-MOF**/FTO.*

The onset overpotential is the potential difference above the equilibrium water oxidation onset potential, determined by the point at which the current for the reaction is first observed.[41] Onset potentials for **Co@C-500**/FTO and **{Co5}-MOF**/FTO (Figure 2.7.2 and Table 2.7.1) were estimated and reported from the intersection points between the tangent lines of the Faradaic (current density > 0.2 mA/cm^2) and non-Faradaic (current density < 0.01 mA/cm^2) currents.

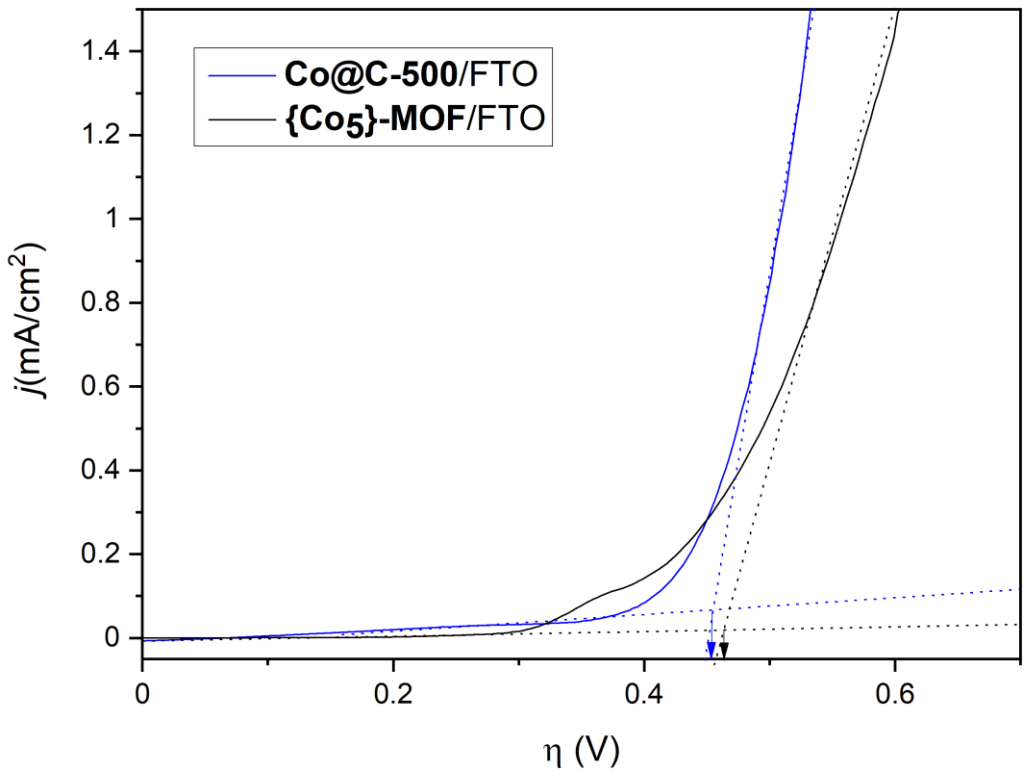

***Figure 2.7.2**: Estimation of the onset overpotential of **Co@C-500**/FTO and **{Co$_5$}-MOF**/FTO from the LSV data between the Faradaic and non-Faradaic currents.*

Tafel plots for **Co@C-500**/FTO and **{Co$_5$}-MOF**/FTO were derived from the LSV experiments. The plots were examined using overpotential values in the range which H_2O oxidation is observed. Tafel slopes were obtained for both in a similar range as both catalysts possess similar onset overpotentials. The Tafel slope is determined from the rate-determining step of the electrochemical process. For **Co@C-500**/FTO and **{Co$_5$}-MOF**/FTO, Tafel slopes of 98 and 175 mV dec^{-1} were obtained, respectively (Table 2.7.1).

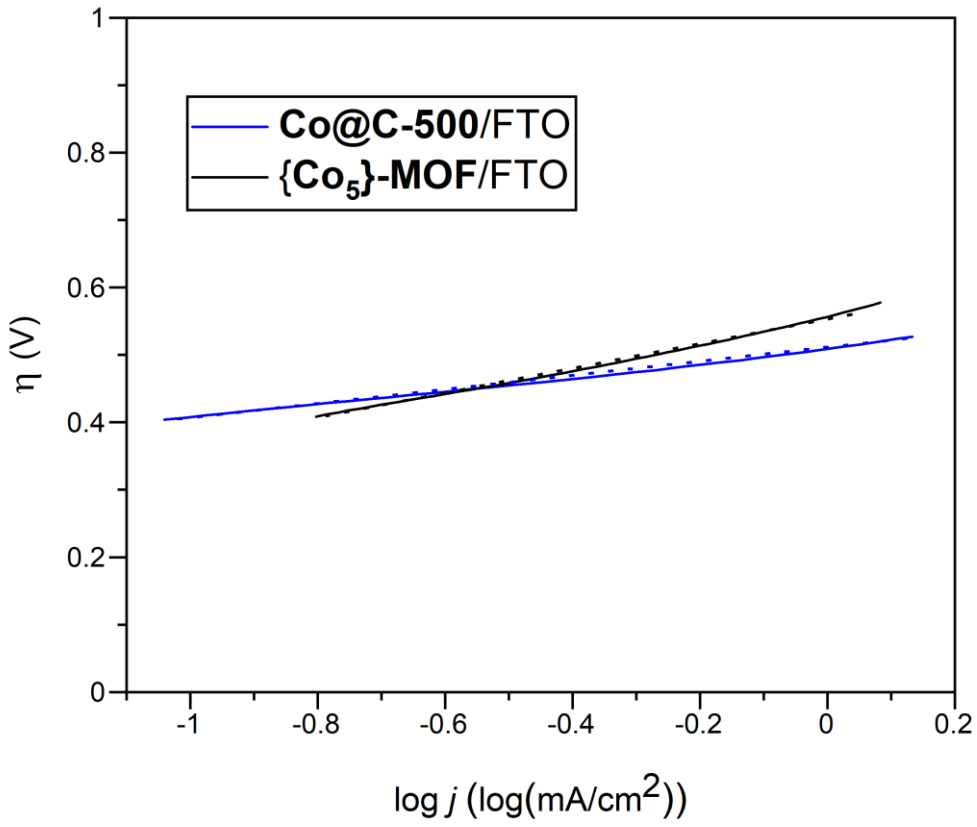

***Figure 2.7.3**: Tafel regions of **Co@C-500**/FTO and **{Co$_5$}-MOF**/FTO.*

The increase in activity of **Co@C-500**/FTO, achieving current densities in excess of 4 mA cm^{-2} relative to the parent MOF, is attributed to synergism between metal centres, as electron charge no longer needs to travel along long, organic ligands.[42] {**Co$_5$}-MOF**/FTO displays good catalytic activity at pH 7 and stability as a pristine MOF catalyst, with a Tafel slope of 175 mV dec^{-1}. **Co@C-500**/FTO sees similar activity as {**Co$_5$}-MOF**/FTO in respect to catalytic onset, both having similar onset overpotentials (455 and 465 mV, respectively). However, **Co@C-500**/FTO shows a drastic improvement in Tafel slope (98 mV dec^{-1} and 175 mV dec^{-1}, respectively) meaning that the material undergoes a different, and more efficient catalytic pathway.

***Table 2.7.1**: Summary of results from water oxidation experiments of **Co@C-500**/FTO and **{Co5}-MOF**/FTO in 50 mM KPi aq. solution (pH 7.2).*

Compound	η_{Onset} (mV)	Tafel Slope (mV/dec)	η @ j = 1mA/cm^2 (mV)
Co@C-500/FTO	454	98	507
{Co5}-MOF/FTO	464	175	559

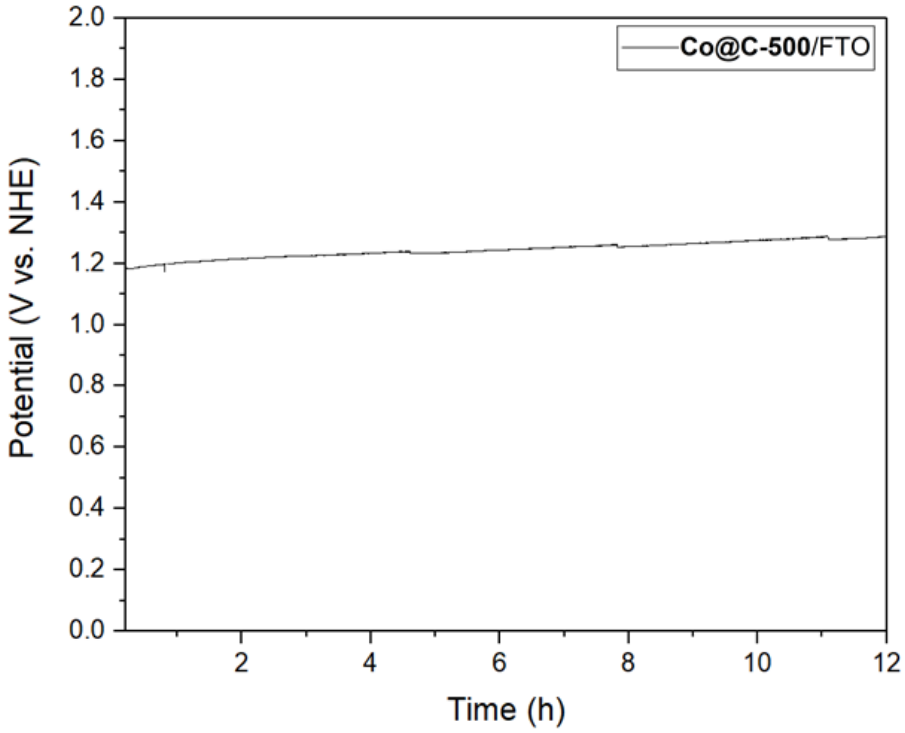

***Figure 2.7.4**: Chronopotentiometry of **Co@C-500**/FTO. Current density set at 1 mA/cm^2 in 50 mM KPi aq. solution (pH 7.2).*

2.7.2 Water oxidation studies at alkaline pH

Thin-film **Co@C-500** was also examined under alkaline (aq. 0.1 M KOH, pH 13.5) conditions, a pH at which **{Co5}-MOF** degrades over time. In addition to LSV experiments, steady-state experiments, namely steady-state voltammetry (SSV) experiments were used in conjunction with the basic solution. An initial potential of +0.2 V was applied, increasing in increments of +0.05 V. As O_2 bubbles form on the FTO surface during the polarising curve at higher potential values, the resulting current could stabilise before each incremental potential increase. This allowed for a more accurate current being recorded. This approach allowed LSV and steady-state experiments to be directly compared. The results obtained in alkaline solution were presented versus the reversable hydrogen eletrode (RHE) to take into account the pH. Potentials were converted from E vs. Ag/AgCl to E vs. RHE using Equation 2.7.1.

$$E\,(RHE) = E\,(Ag/AgCl) + (0.059 \cdot pH) + E_0\,(Ag/AgCl) \qquad \text{(Eq. 2.7.1)}$$

Where E (Ag/AgCl) is the experimental potential obtained and E_0 (Ag/AgCl) is the known standard Ag/AgCl electrode potential. Both the LSV and SSV were plotted against the RHE, thus the results could be compared directly.

As previously mentioned, issues arise when measuring the true onset overpotential and Tafel slope of **Co@C-500**/FTO under normal LSV conditions where the polarising curve is conducted in a cell with a stirring bar to remove bubbles from the electrode surface with an experimental scan rate of 1 mV sec^{-1}. Gas formation on the surface was unavoidable and could not be diffused into the solution *via* stirring as O_2 was produced more rapidly than it could be removed. This resulted in varying current densities as not all of the electrode surface was in contact with the solution. This can be seen in the LSV plot and more importantly, the noise is evident in the Tafel plot extracted from the LSV data (Figure 2.7.5). SSV was employed to overcome this problem and the values reported from this experiment likely corresponds to the true Tafel slope for the material.

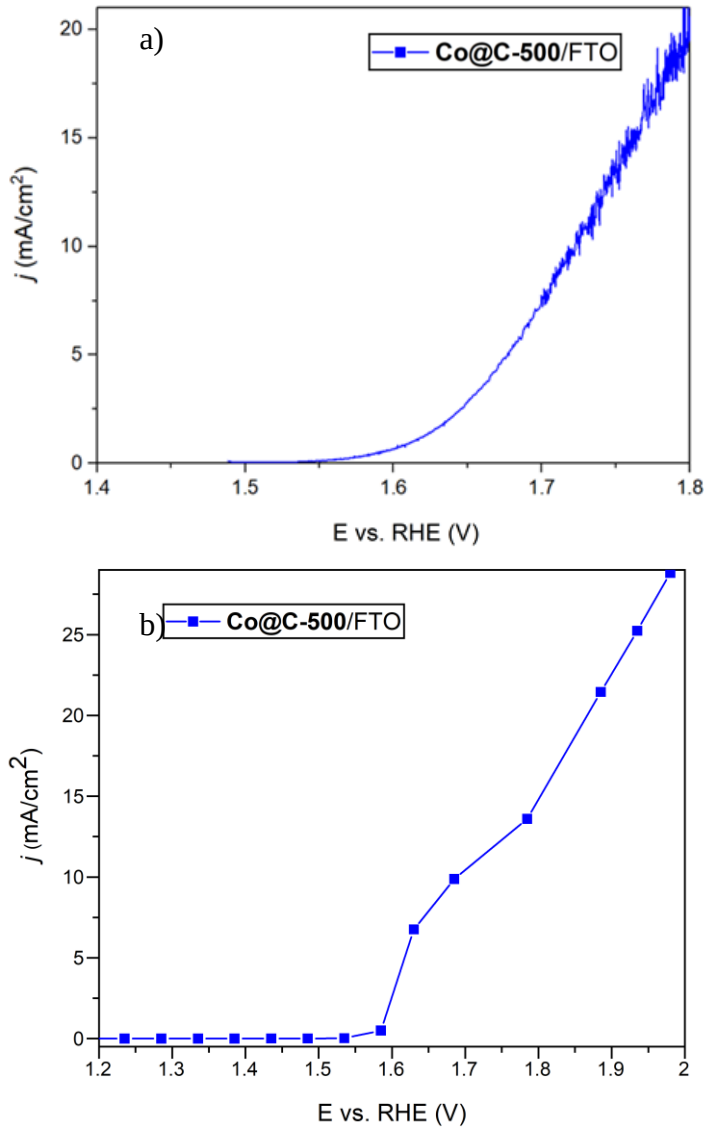

***Figure 2.7.5**: LSV (a) and SSV (b) showing the electrochemical behaviour of **Co@C-500**/FTO.*

Once again, the Tafel plots for **Co@C-500**/FTO were derived from the LSV and SSV experiments. The plots were examined using overpotential values in the range which catalytic activity begins. A line of best fit was found for the Tafel plot for **Co@C-500**/FTO under LSV condition as noise (shown in grey, Figure 2.7.6) was present in this region. Differences seen in the Tafel slopes obtained under the two methods of data collection may be explained by this issue.

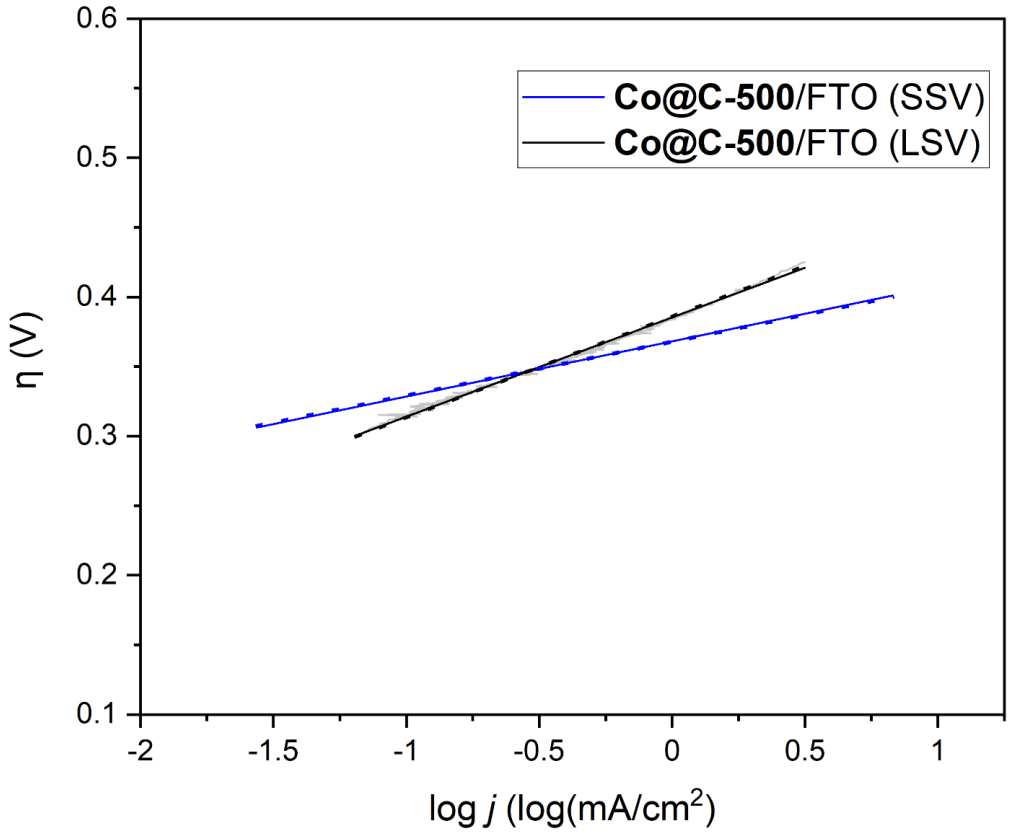

***Figure 2.7.6**: Tafel regions of **Co@C-500**/FTO extracted from both the LSV and SSV experimental results. Untreated data for the SSV curve is displayed in grey.*

***Table 2.7.2**: Summary of results from water oxidation experiments of **Co@C-500**/FTO in aq. KOH (1M) solution (pH 13.5).*

Compound	Tafel Slope (mV dec^{-1})
Co@C-500/FTO **(**LSV)	74
Co@C-500/FTO **(**SSV)	40

Bulk water electrolysis was performed to test the hydrolytic and oxidative stability of the electrodeposited catalyst under electrocatalytic conditions Chronoamperometry was used to evaluate the stability of the films. This demonstrates the long-term stability of **Co@C-500**/FTO electrodes. Chronopotentiometry experiments were performed at a constant 1 mA cm^{-2} employing a 1 cm^2 **Co@C-500**/FTO electrode. The experiments were conducted in a H-cell using a pH 7.2, 50 mM KPi buffer, with KNO_3 (1M) as the electrolyte and using a pH 13.5 KOH solution (Figure 2.7.7).

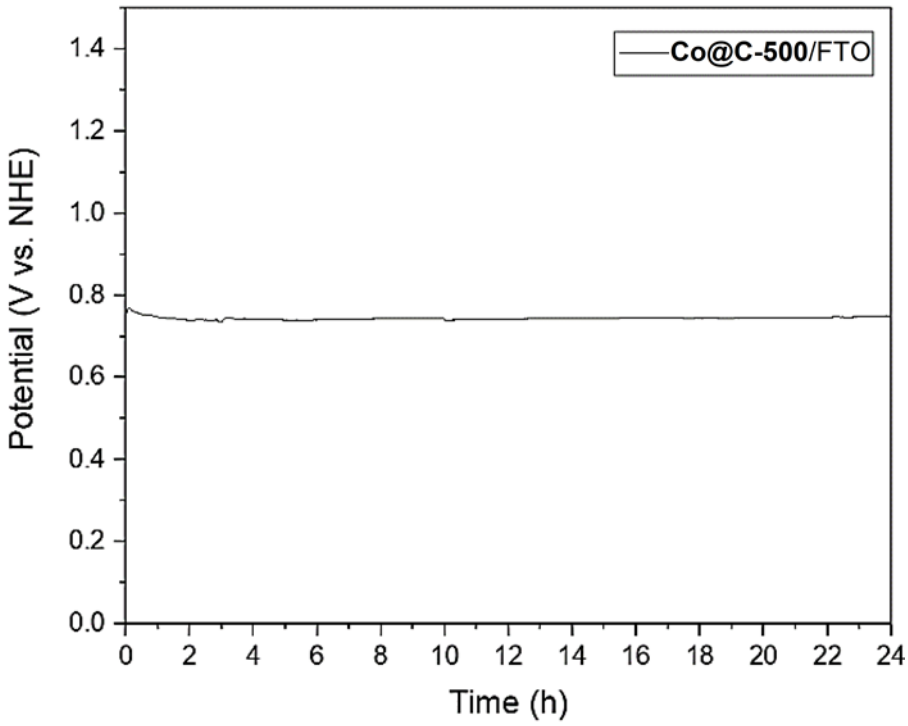

Figure 2.7.7: Chronopotentiometry of **Co@C-500**/FTO at pH 13.5, with current set at +1 mA.

The experiments concluded that **Co@C-500**/FTO displays an onset overpotential of 320 mV, reaching 400 mV at 1 mA cm^{-2}. It was possible to obtain this from the chronopotentiometry experiment as opposed to the polarising curves to avoid discrepancies. The Tafel slope of 40 mV dec^{-1} shows similar activity to solution based CoO_x materials,[43] and minor improvements compared to electrodeposited crystalline Co_3O_4, with a Tafel slope of 49 mV dec^{-1}.[44] The overpotential at which the current density reaches 10 mA/cm^2 is used as one of the benchmarks to compare robust heterogeneous water catalysis, something that could not be achieved by **{Co5}-MOF**. An overpotential of 455 mV at pH 13.5 places the **Co@C-500**/FTO in the midrange of catalysts that can operate at this current density.[45] The Tafel slope observed for **Co@C-500**/FTO in alkaline solution is consistent with the oxidation of CoOOH to CoO_2 being the rate-determining step.[44]

The long-term stability of **{Co5}-MOF**/FTO is only seen under neutral pH conditions. Under basic conditions the catalytic activity of the MOF is lost, seen under bulk catalysis experiments. Where **{Co5}-MOF**/FTO falls short, **Co@C-500**/FTO catalyses the OER in 0.1 M aq. KOH with an onset overpotential of 320 mV and a Tafel slope of 40 mV

dec^{-1}. In addition, it can reach current densities > 10 mA/cm^2, at which the overpotential reached is commonly used as a standard to compare OER catalysts.

2.7.3 Water oxidation studies of Co@C-500 using a carbon cloth electrode

Co@C-500/CC was also examined under alkaline (aq. 0.1 M KOH, pH 13.5) conditions with the standard three-electrode setup with **Co@C-500**/CC used as the working electrode. Due to the woven nature of the electrode, **Co@C-500** adhered to strands of the cloth (seen in SEM imaging) as opposed to forming a uniform thin film, O_2 evolution did not become an issue and LSV experiments could be used in good faith. Again, the results obtained were presented versus the reversible hydrogen eletrode (RHE) to take into account the pH. Potentials were converted from E vs. Ag/AgCl to E vs. RHE using Equation 2.7.1 (Section 2.7.2).

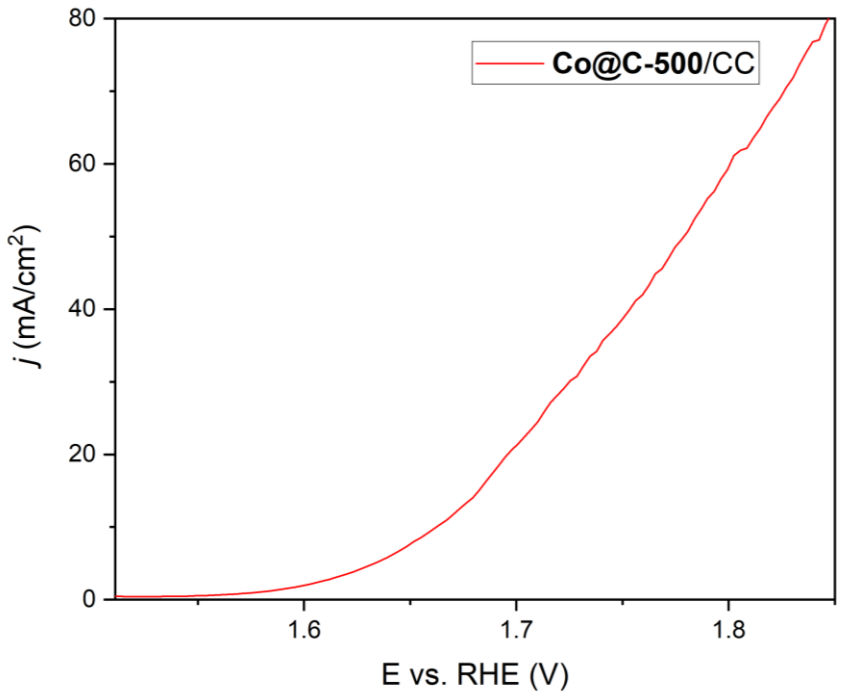

***Figure 2.7.8**: LSV showing the electrochemical behaviour of **Co@C-500**/CC.*

The most interesting feature of **Co@C-500**/CC is the current densities the material can achieve, *approx.* 60 mA/cm^2 versus 20 mA cm^{-2} for CC and FTO at 1.8 V vs RHE, respectively. The film possesses a surface area of 1 cm^2, but unlike the FTO glass surface, deposition of the MOF onto the surface favours aggregation of particles to individual strands of the cloth as opposed to initial particles attaching to the electrode surface and appear to grow in aggregates across the FTO surface to join with other individual particles to form

aggregates. The ability of the MOF to impregnate the cloth in combination with deposition possible on both sides of the electrode allow for a higher surface area of the electrode to be in close proximity with the catalyst. The onset overpotential calculated was seen to be identical to that of **Co@C-500**/FTO with a calculated onset overpotential of 320 mV further confirming that the same catalytic species can be synthesised on two different electrode surfaces.

2.8 Post-catalytic characterisation

After bulk electrolysis experiments under alkaline conditions, **Co@C-500**/FTO was washed with MilliQ water and characterised to confirm structural stability and identify the true catalytic species. Co-containing MOFs in aqueous solution can lead to $[Co(aq.)]^{2+}$ leaching into solution that form electrode bound CoO, another OER catalyst. The carbon-matrix bound cobalt centres in **Co@C-500**/FTO inhibit Co ions leaching into the solution. The porous structure and presence Co_3O_4 are believed to be responsible for the excellent OER reaction of the material. The formation of CoO would thus reduce the catalytic activity. No traces of CoO were found post-catalysis.

2.8.1 Scanning transmission electron microscopy

Scanning transmission electron microscopy (STEM) was used observe any changes in the morphology during catalysis. The top layers of the thin film were removed from the FTO electrode using a scalpel before the material was sonicated in isopropanol. Dispersed particles were extracted *via* drop casting onto a lacey carbon support film on a copper TEM grid. The grid was loaded into a FEI Titan 80 – 300kV FEG S/TEM for analysis. Images were obtained under an operating acceleration voltage of 300 kV with an informational resolution limit of 0.1 nm and processed using the Image J software package.

On first glance, it can be observed that cobalt oxide particles are still retained within the graphitic shell structure, but the morphology of the carbon shell has been somewhat altered and become more ‘shell-like’ as akin to other heat-treated MOFs (Figure 2.8.1).[46] Before catalysis graphitic material formed spherical-like particles encapsulating the cobalt centers. Bulk chronopotentiometry appears to only effect the surface of the aggregates, likely due to a combination of gas evolution and prolonged periods in basic solution which can break graphite down into simpler aliphatic structures.

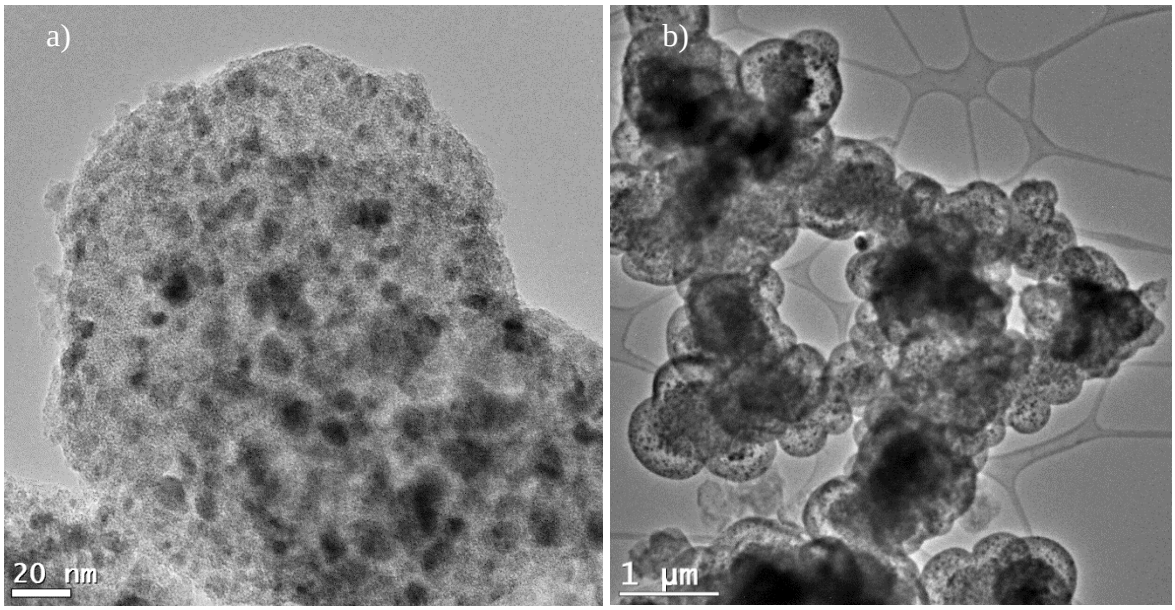

Figure 2.8.1: TEM image of a carbon aggregate **Co@C-500**/FTO before (a) and overview STEM image after (b) bulk catalysis at pH 13.5, with current set at +1 mA.

The investigation into the dispersion of cobalt oxide particles was further verified by performing scanning transmission electron microscopy (STEM) and high angle angular dark field imaging (HAADF-STEM) measurements. HAADF is a STEM technique which produces an annular dark field image formed by very high angle, incoherently scattered electrons (Rutherford scattered from the nucleus of the atoms) as opposed to Bragg scattered electrons. This technique is highly sensitive to variations in the atomic number of atoms in the sample and allows for Z-contrast images. This technique makes the location of cobalt specifics within the structure more facile. In combination with STEM imaging, this technique gives insight into the 3-dimensional structures of by giving contrast between changes in height within the sample. What is observed is the microstructure of solid-state cobalt oxide suspended within the graphitic matrix. Individual Co_3O_4 nanoparticles have an average particle size in the range of 3 – 7 nm, whereas the encompassing carbon shells have a diameter in the range 0.6 – 1.2 µm. The graphitic shells aggregate in a way which is indicative of **{Co$_5$}-MOF** on FTO. Only morphology of the carbon matrix is altered, likely due to formation of bubbles on the electrode surface during bulk chronopotentiometry experiments. Despite this, it demonstrates that the cobalt nanomaterials are encapsulated within the structure.

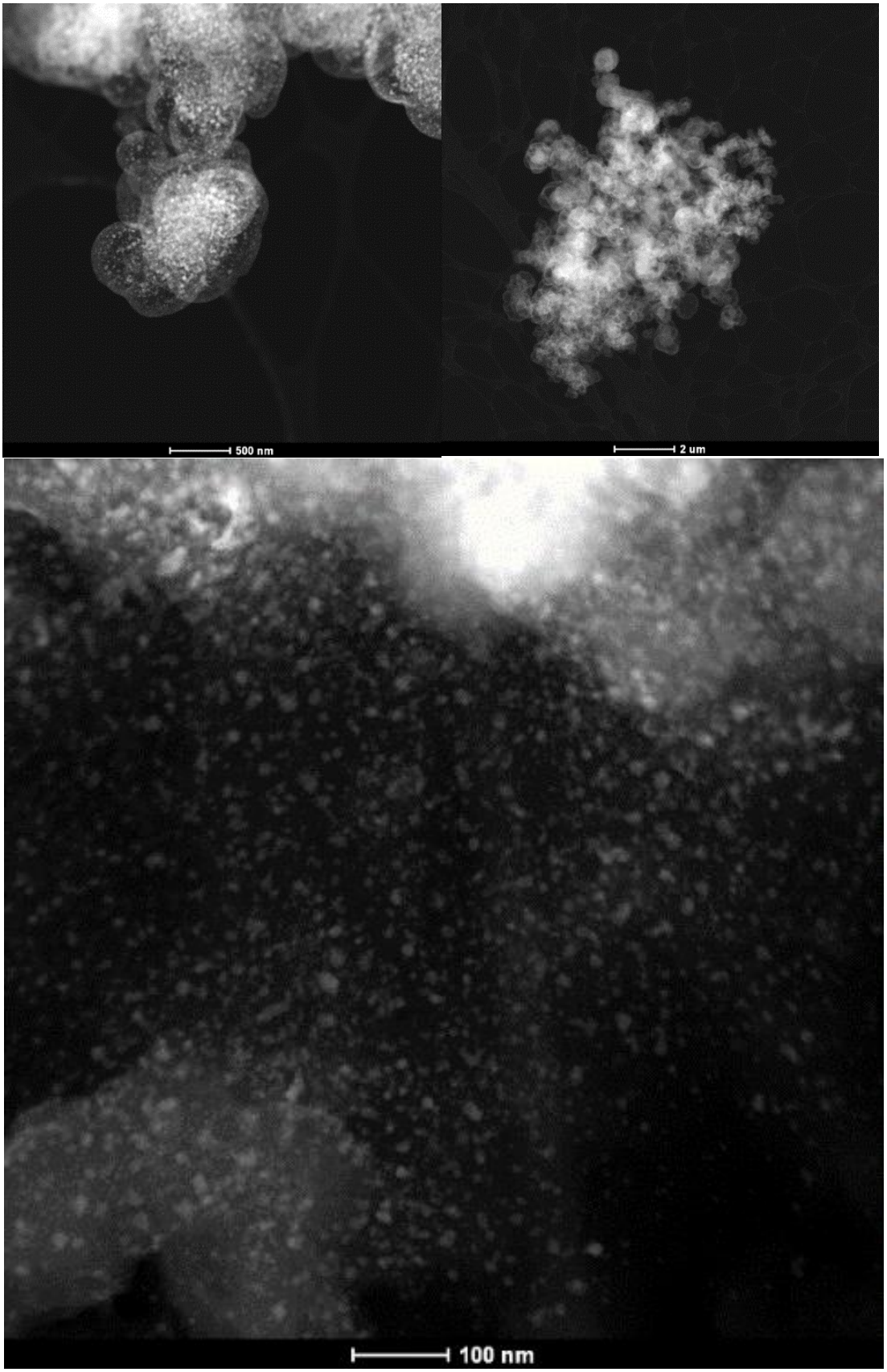

Figure 2.8.2: HAADF-STEM imaging of **Co@C-500**/FTO aggregates after catalysis.

2.8.2 Energy dispersive X-ray spectroscopy

Energy dispersive X-ray spectroscopy (EDX) was used to analyse the atomic ratio of cobalt to oxygen in comparison to the freshly synthesised material. This technique can provide a rough Co:O estimate as it has a lower accuracy for elements with a lower Z-number. After bulk catalysis, the sample was soaked in MilliQ water for 24 hours, changing the solution four times to ensure the removal of any salts disused within the pores. The FTO was adhered to adhesive carbon tabs atop aluminium SEM stubs and loaded into a Zeiss ULTRA Plus scanning microscope with the 20mm² Oxford Inca EDX detector. An acceleration voltage of high current 20 kV was used for EDX data collection. The raw data was processed using the Inca 7.2 software package. The SEM overview area highlights the surface constitution **Co@C-500**/FTO in agreement with STEM and HAADF-STEM imaging where Co_3O_4 centres can be seen charging. EDX analyses confirm the structural stability of **Co@C-500**/FTO after the experiments (Figure 2.8.3), where the Co:O ratio is preserved within error.

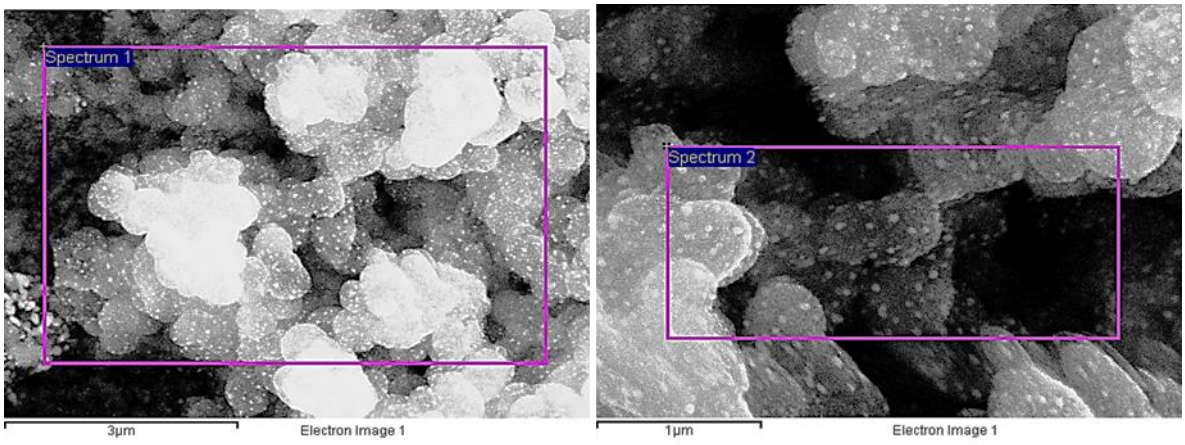

Figure 2.8.3*: Areas chosen for EDX analysis of spectrum 1 and 2 presented in Table 2.8.1.*

Table 2.8.1*: Results of EDX analysis on* ***Co@C-500****/FTO.*

Element	Spectrum 1	Spectrum 2	Adverage (Ratio)
O K	55.06	55.12	1.23 (2.5)
Co K	44.94	44.88	1 (2)

2.8.3 Powder X-ray diffraction

Bulk characterisation of **Co@C-500** post-catalysis was carried out *via* PXRD. The film was removed from the FTO surface using a scalpel and placed into a polyamide

capillary using a resin binder to seal the open ends of the capillary to securely pack the sample. A PXRD pattern was recorded on an APEX II DUO X-ray diffractometer to compare to the spectrum recorded on a newly synthesised **Co@C-500**/FTO. Characterisation of the FTO electrode after bulk catalysis shows characteristic of spinel cobalt oxide peaks in the PXRD spectra (Figure 2.8.4). Although it is noted that the graphite associated peaks, namely the (101) and (004) at approx. 46 ◦ and 55 ◦, respectively, have become noticeably broader and which would correspond to the physical changes seen in the shell structure from STEM imaging.

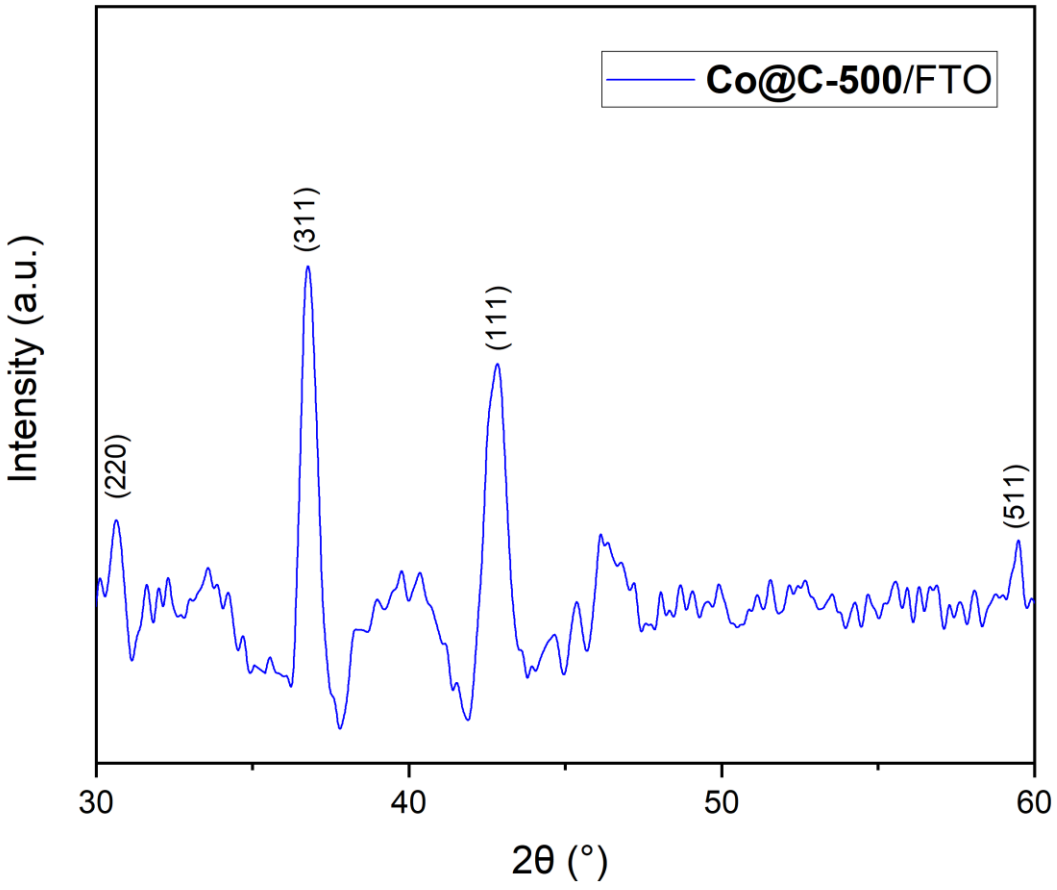

***Figure 2.8.4**: PXRD of **Co@C-500**/FTO after bulk catalysis at pH 13.5.*

2.8.4 Raman spectroscopy

The surface of **Co@C-500**/FTO is in constant contact with the alkaline solution and the formation of O_2 molecules during chronopotentiometry experiments. Raman was utilised as a surface sensitive characterisation technique to detect the identification of addition species forming on the electrode surface during bulk electrocatalysis. **Co@C-500** was measured on the FTO surface using a Renishaw-1000 micro-Raman spectrometer equipped with a magnification objective (50×) and a cooled CCD camera system. The sample was

excited using a 785 nm laser at 1 % laser power to isolate the surface of the material. 100 acquisitions were acquired with an accumulation time of 10 seconds per acquisition. The pre- and post-bulk catalytic Raman spectra possess identical peaks at 428, 520, 621 690 cm^{-1} and a large band > 1000 cm^{-1}. It was not possible to deduce any change in the carbon species from the spectrum but confirms there is no appearance of other CoO_x species on the surface.

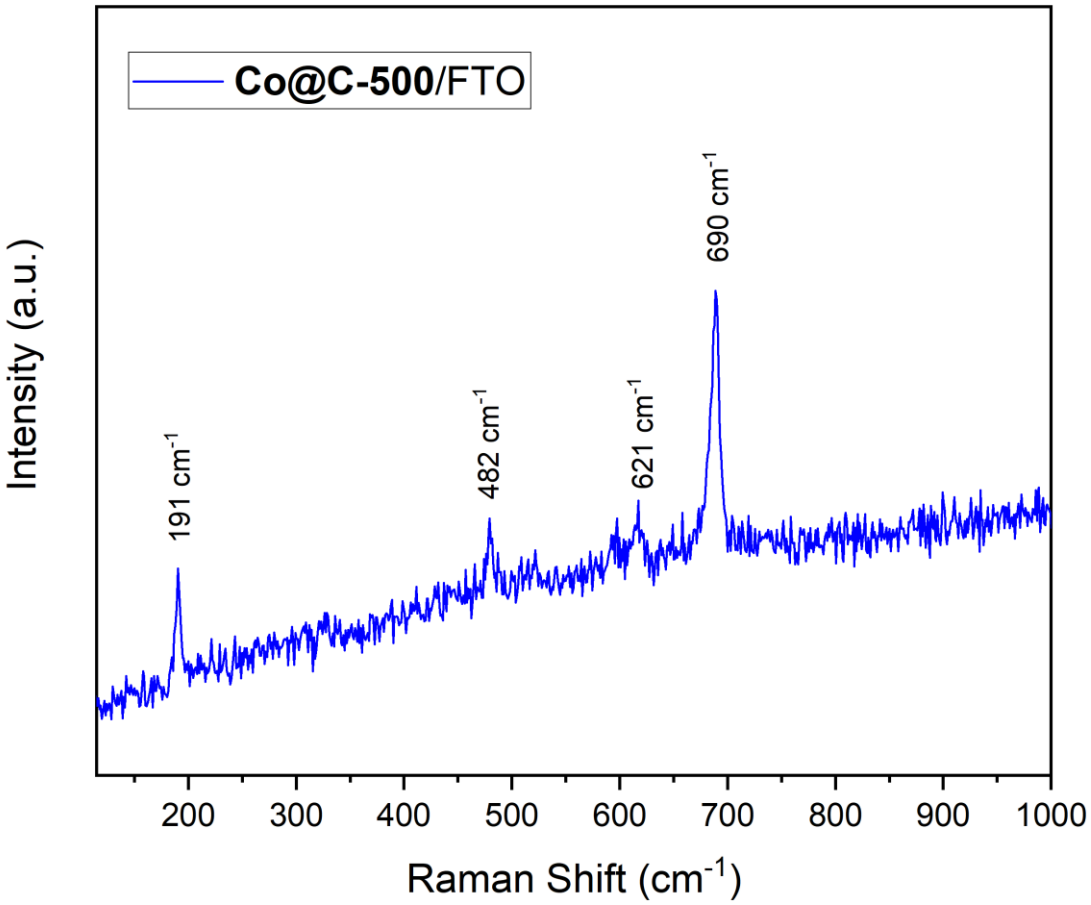

***Figure 2.8.6**: Raman spectrum of **Co@C-500**/FTO after bulk catalysis.*

2.8.5 X-ray photoelectron spectroscopy

XPS was employed as another surface sensitive characterisation technique, this time able to determine any change in carbon associated environments. **Co@C-500** was removed from the FTO surface and adhered to a background-corrected adhesive tabs and imaged before analysis using scanning X-ray imaging (SXI) to identify good measurement position. XPS was performed on a Phi Versa Probe III analyser equipped with a 1487 eV Rowland circle monochromatic Al Kα X-ray source. Elemental orbitals were analysed on the same sample area at 26 eV for the O 1s and the C 1s and 55 eV for the Co 2p. All orbitals scans used 0.05 eV increment steps.

As mentioned in Section 1.6.4, it is possible to distinguish between Co oxidation states using the satellite peak features of the Co 2p orbitals and thus between mixed-oxidation state Co_3O_4 and $Co^{II}O_x$ species due the Co(II)/Co(III) atoms in spinel cobalt oxide exhibiting diminished satellite structures with a mixture of $2p_{3/2}/2p_{1/2}$ binding energies. For the post-catalytic sample, the Co $2p_{3/2}$ and Co $2p_{1/2}$ were found at a binding energy of 779.8 and 795.2 eV respectively with any satellite artefacts being indistinguishable from the baseline, in agreement with the spectrum reported for newly synthesised film.

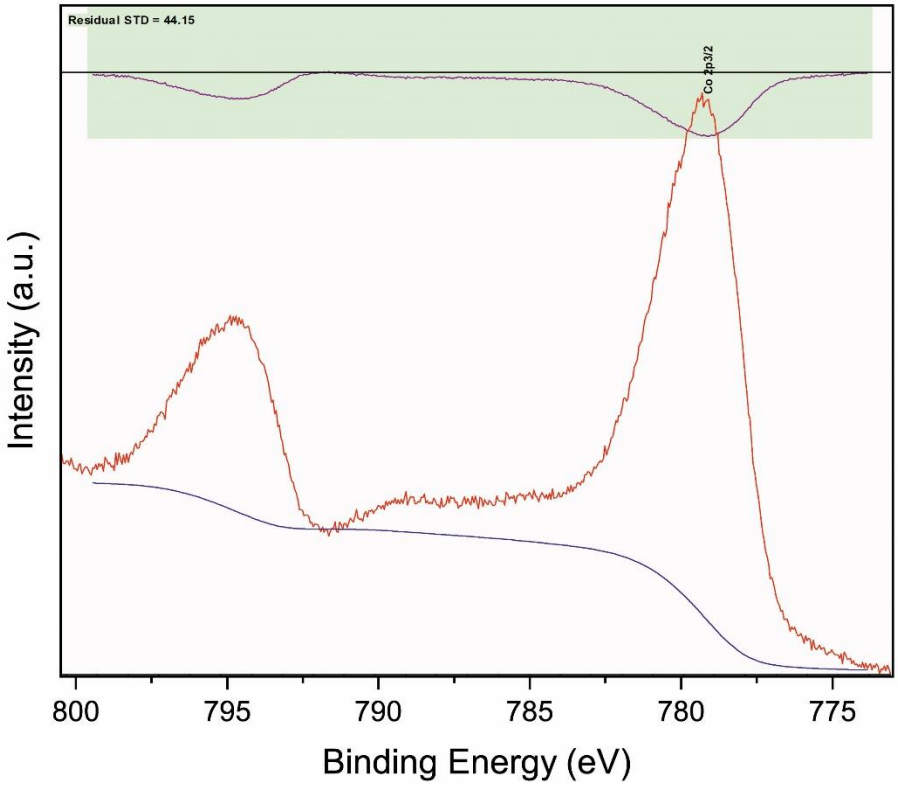

***Figure 2.8.7**: Co 2p sample area scan overview spectrum of post-catalysis **Co@C-500**/FTO with intensity measured in counts per second.*

The O 1s region is relatively unchanged, now displaying a main oxygen peak at 529.8 eV, which has previously been reported for O^{2-} ions in the Co_3O_4 lattice (Figure 2.8.9). The second peak, seen at a higher binding energy of *approx.* 233.1 eV, has surprisingly diminished in intensity. As mentioned, this peak can be attributed to a number of oxygen species within the carbon shell structure as well under coordinated O^- atoms within the cobalt oxide particles, commonly seen when materials are carbonised under inert conditions. Bulk catalysis appears to have changed the composition of the graphitic matrix and loss of surface hydroxyls or C –O –C defects within the matrix are removed.

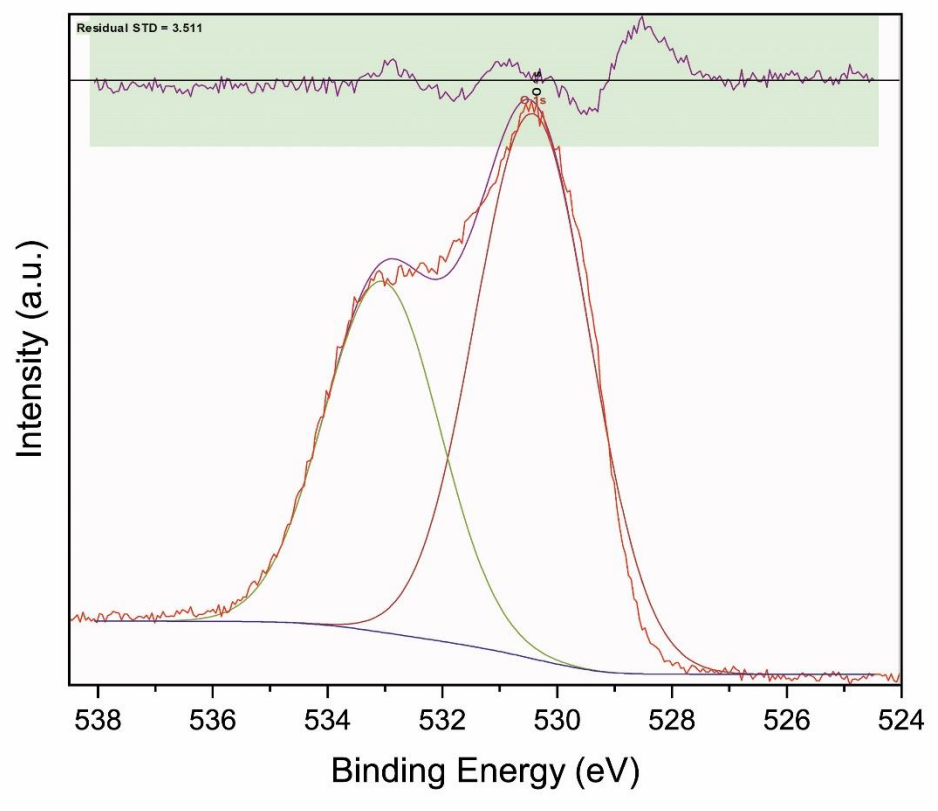

Figure 2.8.9*: O 1s sample area scan overview spectrum of post-catalysis* ***Co@C-500****/FTO with intensity measured in counts per second.*

In confirmation with the TEM, there is both a structural and chemical change in the structure of the C 1s region. The peak indicative of graphitic non-oxygenated C=C sp^2 can be found at 284.5 eV. Additional peaks at higher binding energies are liked to C–C sp^3 at 285.3, C–O at 286.4 eV and C=O at 289.4 eV, indicative of graphite oxide.[47] It possible that some contamination was obtained during transport of the sample for XPS analysis, however it has been reported that such oxygenated carbon species can transform during long term exposure to electrocatalytic conditions.[48]

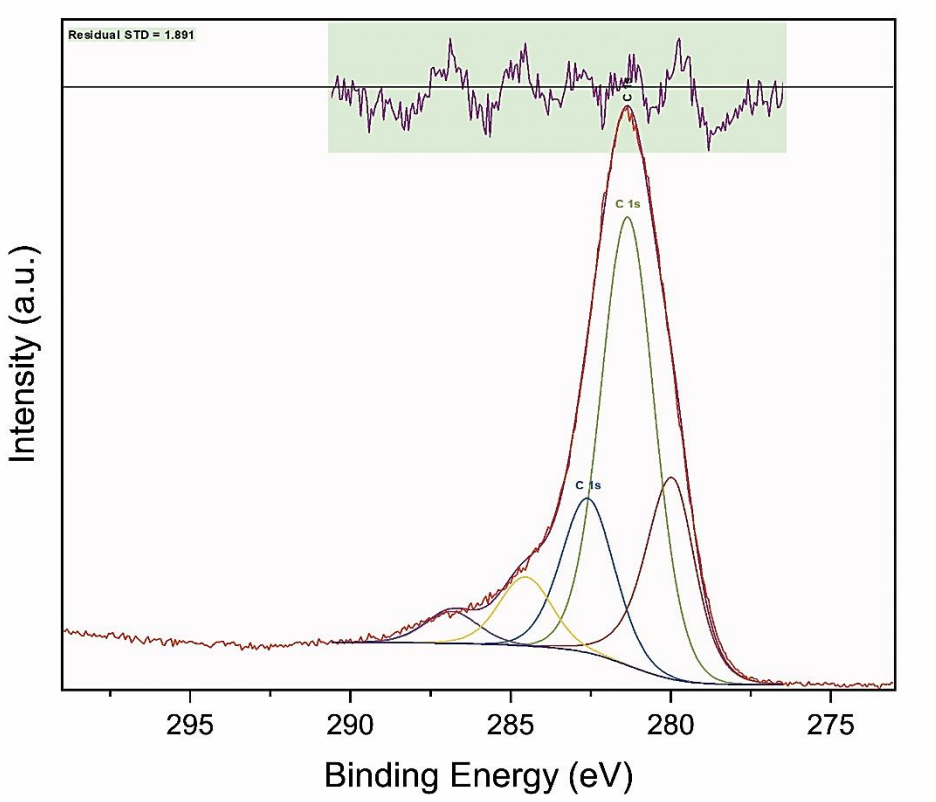

***Figure 2.8.10**: C 1p sample area scan overview spectrum of post-catalysis **Co@C-500**/FTO with intensity measured in counts per second.*

2.9 Conclusions

A synthetic strategy to afford a stable water oxidation catalyst was presented using an electrochemically synthesised metal-organic framework as a template. **Co@C-500** was produced *via* the heat-treatment of **{Co5}-MOF** under an inert atmosphere and characterised to conform the structural change via PXRD, Raman and FT-IR spectroscopy, TEM, STEM and SEM. The activated material was subjected to gas sorption analysis to confirm that a degree of porosity was retained during the carbonization step. The N_2 gas uptake yielded a reversable type-I isotherm with a BET surface area of 348 m^2/g.

The method of electrodeposition and post synthetic heat-treatment afforded homogenous, monodispersed catalytic sites within a porous graphitic framework on both FTO coated glass and carbon cloth electrodes. Various characterisation and imaging methods suggest a close structural and constitutional relationship between **Co@C-500** from solvothermally synthesised MOF crystals and the electrochemically synthesised materials. The electrochemical performance of **Co@C-500**/FTO was investigated under neutral pH conditions and compared to the activity of **{Co5}-MOF**/FTO. A noticeable decrease of the Tafel slope was observed.

Co@C-500/FTO and **Co@C-500**/CC were also tested for their catalytic ability under alkaline conditions. Both electrodes could reach current densities well in excess of 10 mA/cm^2 with an additional decrease in the onset overpotential and Tafel slopes compared to **{Co5}-MOF** and **Co@C-500** at pH 7.2.

Post-catalytic characterisation of thin-film **Co@C-500** after bulk catalysis at pH 13.5 for 24 h highlight the structural stability of the material under basic conditions. The thin film remains intact on the FTO surface despite excessive O_2 bubble evolution during OER experiments. Other CoO_x species could not be identified. Electron imaging shows that the core-shell structure is retained.

Overall, **Co@C-500** fulfills the criteria of immobilising a catalytically active molecular oxide unit inside a porous graphitic framework The main advantage of the new material was its ability to be readily synthesised electrochemically in contrast to other cobalt oxide based electrocatalysis, and its ability to sustain long-term catalysis under alkaline pH conditions, something not possible in the MOF-based parent structure.

2.10 References

1 X. Liu, L. Zhang and J. Wang, *J. Mater.*, 2021, **7**, 440–459.

2 J. Soriano-López, S. Goberna-Ferrón, L. Vigara, J. J. Carbó, J. M. Poblet and J. R. Galán-Mascarós, *Inorg. Chem.*, 2013, **52**, 4753–4755.

3 X. Deng and H. Tüysüz, *ACS Catal.*, 2014, **4**, 3701–3714.

4 L. Lux, K. Williams and S. Ma, *CrystEngComm*, 2015, **17**, 10–22.

5 N. Zhu, G. Tobin and W. Schmitt, *Chem. Commun.*, 2012, **48**, 3638–3640.

6 N. Zhu, D. Sensharma, P. Wix, M. J. Lennox, T. Düren, W. Y. Wong and W. Schmitt, *Eur. J. Inorg. Chem.*, 2016, **2016**, 1939–1943.

7 G. Tobin, S. Comby, N. Zhu, R. Clérac, T. Gunnlaugsson and W. Schmitt, *Chem. Commun.*, 2015, **51**, 13313–13316.

8 O. M. Yaghi, M. O'Keeffe, N. W. Ockwig, H. K. Chae, M. Eddaoudi and J. Kim, *Nature*, 2003, **423**, 705–714.

9 D. Sensharma, N. Zhu, S. Tandon, S. Vaesen, G. W. Watson and W. Schmitt, *Inorg. Chem.*, 2019, **58**, 9766–9772.

10 K. Sonogashira, Y. Tohda and N. Hagihara, *Tetrahedron Lett.*, 1975, **16**, 4467–4470.

11 Q. Yao, A. Bermejo Gómez, J. Su, V. Pascanu, Y. Yun, H. Zheng, H. Chen, L. Liu, H. N. Abdelhamid, B. Martín-Matute and X. Zou, *Chem. Mater.*, 2015, **27**, 5332–5339.

12 H. Furukawa, N. Ko, Y. B. Go, N. Aratani, S. B. Choi, E. Choi, A. O. Yazaydin, R. Q. Snurr, M. O'Keeffe, J. Kim and O. M. Yaghi, *Science*, 2010, **329**, 424–8.

13 N. Kobayashi and M. Kijima, *J. Mater. Chem.*, 2008, **18**, 1037–1045.

14 X. Liu, X. Wang and F. Kapteijn, *Chem. Rev.*, 2020, **120**, 8303–8377.

15 T. Y. Ma, S. Dai, M. Jaroniec and S. Z. Qiao, *J. Am. Chem. Soc.*, 2014, **136**, 13925–13931.

16 L. Liu, D. Zhang, Y. Zhu and Y. Han, *Commun. Chem.*, 2020, **3**, 1–14.

17 Y. H. Budnikova, *Dalt. Trans.*, 2020, **49**, 12483–12502.

18 N. Campagnol, T. R. C. Van Assche, M. Li, L. Stappers, M. Dinca, J. F. M. Denayer, K. Binnemans, D. E. De Vos and J. Fransaer, *J. Mater. Chem. A*, 2016, **4**, 3914–3925.

19 M. Li and M. Dincă, *J. Am. Chem. Soc.*, 2011, **133**, 12926–12929.

20 N. Campagnol, T. R. C. Van Assche, M. Li, L. Stappers, M. Dinca, J. F. M. Denayer, K. Binnemans, D. E. De Vos and J. Fransaer, J. Mater. Chem. A, 2016, **4**, 3914–3925.

21 M. Li and M. Dincă, *Chem. Mater.*, 2015, **27**, 3203–3206.

22 D. Fikri, A. H. Yuwono, N. Sofyan, T. Arini and L. H. Lalasari, in *AIP Conference Proceedings*, 2017, vol. 1826, p. 20003.

23 H. Shang, Y. Lu, F. Zhao, C. Chao, B. Zhang and H. Zhang, *RSC Adv.*, 2015, **5**, 75728–75734.

24 F. Lyu, Q. Wang, S. M. Choi and Y. Yin, *Small*, 2019, 15, 1804201.

25 I. Roger, M. A. Shipman and M. D. Symes, *Nat. Rev. Chem.*, 2017, 1, 1–13.

26 T. J. Chuang, C. R. Brundle and D. W. Rice, *Surf. Sci.*, 1976, **59**, 413–429.

27 Z. X. Shen, J. W. Allen, P. A. P. Lindberg, D. S. Dessau, B. O. Wells, A. Borg, W. Ellis, J. S. Kang, S. J. Oh, I. Lindau and W. E. Spicer, *Phys. Rev. B*, 1990, **42**, 1817–1828.

28 S. C. Petitto and M. A. Langell, *J. Vac. Sci. Technol. A Vacuum, Surfaces, Film.*, 2004, **22**, 1690–1696.

29 S. Gadipelli and Z. Guo, *Chem. Mater.*, 2014, **26**, 6333–6338.

30 Y. Zeng, G. F. Chen, Z. Jiang, L. X. Ding, S. Wang and H. Wang, *J. Mater. Chem. A*, 2018, **6**, 15942–15946.

31 J. Lu, W. Zhou, L. Wang, J. Jia, Y. Ke, L. Yang, K. Zhou, X. Liu, Z. Tang, L. Li and S. Chen, *ACS Catal.*, 2016, **6**, 1045–1053.

32 B. A. Sexton, A. E. Hughes and T. W. Turney, *J. Catal.*, 1986, **97**, 390–406.

33 S. C. Petitto and M. A. Langell, *J. Vac. Sci. Technol. A Vacuum, Surfaces, Film.*, 2004, **22**, 1690–1696.

34 H. C. Zeng and Y. Y. Lim, *J. Mater. Res.*, 2000, **15**, 1250–1253.

35 J. Haber, J. Stoch and L. Ungier, *J. Electron Spectros. Relat. Phenomena*, 1976, **9**, 459–467.

36 J. Vaari, J. Lahtinen and P. Hautojärvi, *Catal. Letters*, 1997, **44**, 43–49.

37 G. A. Carson, M. H. Nassir and M. A. Langell, *J. Vac. Sci. Technol. A Vacuum, Surfaces, Film.*, 1996, **14**, 1637–1642.

38 M. A. Langell, J. G. Kim, D. L. Pugmire and W. McCarroll, *J. Vac. Sci. Technol. A Vacuum, Surfaces, Film.*, 2001, **19**, 1977–1982.

39 A. Taylor, *J. Chem. Technol. Biotechnol.*, 2007, **53**, 215–215.

40 T. Takashima, K. Hashimoto and R. Nakamura, *J. Am. Chem. Soc.*, 2012, **134**, 1519–1527.

41 R. Wang, K. Wang, Z. Wang, H. Song, H. Wang and S. Ji, *J. Power Sources*, 2015, **297**, 295–301.

42 Y. Xu, F. Zhang, T. Sheng, T. Ye, D. Yi, Y. Yang, S. Liu, X. Wang and J. Yao, *J. Mater. Chem. A*, 2019, **7**, 23191–23198.

43 L. Trotochaud, J. K. Ranney, K. N. Williams and S. W. Boettcher, *J. Am. Chem. Soc.*, 2012, **134**, 17253–17261.

44 J. A. Koza, Z. He, A. S. Miller and J. A. Switzer, *Chem. Mater.*, 2012, **24**, 3567–3573.

45 I. Roger, M. A. Shipman and M. D. Symes, *Nat. Rev. Chem.*, 2017, **1**, 0003.

46 Y. Feng, H. S. Han, K. M. Kim, S. Dutta and T. Song, *J. Catal.*, 2019, **369**, 168–174.

47 Y. Yamada, H. Yasuda, K. Murota, M. Nakamura, T. Sodesawa and S. Sato, *J. Mater. Sci.*, 2013, **48**, 8171–8198.

48 M. Blasco-Ahicart, J. Soriano-Lopez, J. J. Carbo, J. M. Poblet and J. R. Galan-Mascaros, *Nat. Chem.*, 2018, **10**, 24–30.

Chapter 3

Direct synthesis and applications of mixed-metal MOFs

3.0 Introduction

Mixed-metal MOFs (MM-MOFs) are defined as MOFs that contain two or more metal ions within the structure and aim to introduce multiple functionalities within a single framework.[1] This is advantageous for numerous applications, particularly in improving the stability and catalytic activity of a MOF compared to the monometallic MOF analogue.[1] MM-MOFs can generally be synthesised via three discreet synthetic routes: The direct solvothermal synthesis from two or more discreet metal salts and organic ligand moieties allows for control over the ratio of metallic contribution; post-synthetic treatment of a homometallic MOF allows for formation of MM-MOFs that can only be synthesised from the monometallic analogue. These methods focus on modifying the inorganic SBU components. Lastly, an auxiliary metal can be introduced by using a metalloligand which introduces a metallic component to both the organic and inorganic SBU units of a MOF.[2]

The ligand 4,4',4''-(benzene-1,3,5-triyltris(ethyne-2,1-diyl)tribenzoic acid (**H_3BTEB**), was again selected as the organic component as it has previously been used within the research group to synthesise a range of MOFs, in particular tri- and penta-nuclear Zn(II) MOFs which are used as a template in the synthesis of **{Co_5}-MOF** and now, to incorporate additional metallic moeities.[3] From the work detailed in Chapter 2, it is proven to have the capacity to form both highly porous and stable MOFs, in addition to its ability to be deposited electrochemically.

This chapter details the synthesis and characterisation of a series of MM-MOFs using a 'one pot' strategy for applications in gas sorption and water oxidation by incorporating an additional metal component into the known MOF templates of the (M_3) **TCM-1** and {M_5} **{Co_5}-MOF** with the hopes to decrease the overpotential for the electrochemical water oxidation reaction with respect to the monometallic MOF template.[3]

As discussed in chapter 2, MOFs can also be synthesised on thin films with advantageous properties for catalysis. The direct electrodeposition of MM-MOF has not been currently reported. Herein, the electrodeposition of **{$(CoNi)_5$}-MOF** on both FTO and CC electrodes is outlined. The thin-film MOF was subsequentially heat-treated at 500 °C under N_2 to yield a typical core@shell material **CoNi@C-500** exhibiting Co/Ni oxide cores embedded within a carbon shell, explored as a catalyst for the OER reaction at neutral and alkaline pH.

3.1 Synthesis of 4,4',4''-(benzene-1,3,5-triyltris(ethyne-2,1-diyl))tribenzoic acid (H_3BTEB)

The tritopic ligand 4,4',4"-(benzene-1,3,5-triyltris(ethyne-2,1-diyl))tribenzoic acid (**H_3BTEB**) is a well-known carboxylic acid linker employed for synthesis of various MOFs,[4,5] as well as **{Co_5}-MOF**. This ligand was reproduced via a modified four-step procedure from 1,3,5-tribromobenzene, described in detail in Section 2.1.

3.2 Direct synthesis methodologies

MM-MOFs are readily synthesised by employing multiple metal salts as the metal precursor in various synthetic techniques such as the slow diffusion, solvothermal, slow evaporation sonication and mechanochemical methods.

The addition of a second metallic moiety was first explored using the trinuclear Zn(II) archetype with the **H_3BTEB** ligand. Previous successes were reported with the incorporation of additional Co (II) moieties into the trinuclear core, discussed in Section 2.4. Building on this research, an isostructural Mn/Zn MM-MOF is reported in Section 2.3. This provides initial confirmation that the trinuclear and pentanuclear MOFs synthesised using the **H_3BTEB** ligand can be altered to include additional metal moieties under direct synthesis, where the conditions for synthesis are retained, with inclusion of a second metal (II) salt in the reaction solution.

Subsequently, the well-established synthesis of **{Co_5}-MOF** is altered to introduce Ni(II) moieties into the pentanuclear cluster, following the consistent synthetic guidelines. As summarised in Chapter 1, in addition to the successful synthesis of bulk **{Co_5}-MOF** crystals, the MOF can be deposited electrochemically onto a range of thin-film electrodes. These electrodes and bulk crystalline MOF samples serve as a precursor for the formation of core@shell metal oxide materials within a carbon matrix. Modifying the robust synthetic method to include a secondary metal component results in an isostructural bimetallic MOF, namely **{$(CoNi)_5$}-MOF**. A main advantage of the direct synthetic scheme allows for **{$(CoNi)_5$}-MOF** to be synthesisable on both FTO and CC electrodes with control over the metal proportions, something that has proved difficult in mixed-metal MOF synthesis, as metal-exchange or metal insertion are the most commonly methods of introducing a second

metallic component. Consequentially, this MM-MOF provides a new templated for synthesis of Co/Ni oxide materials after undergoing heat-treatment.

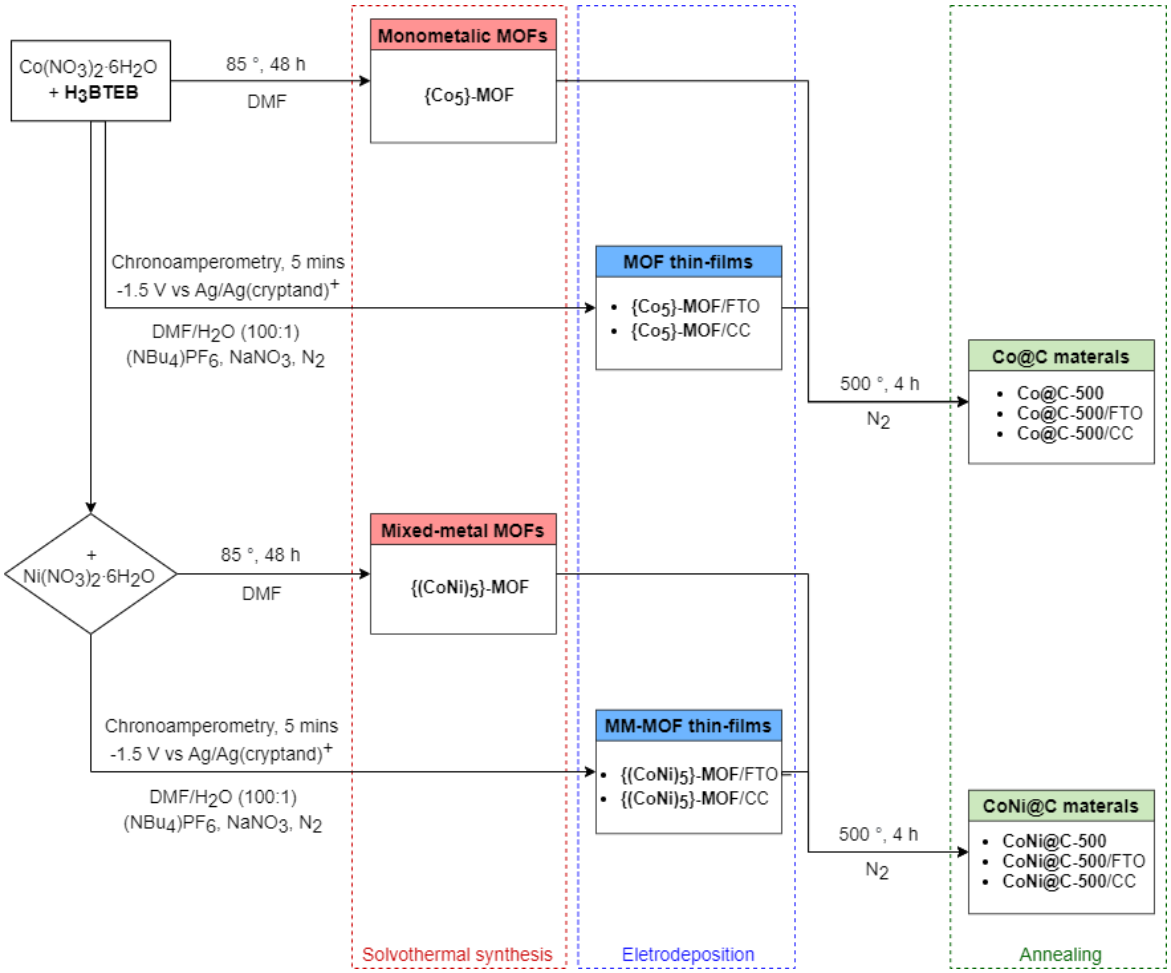

***Scheme 3.2.1**: The general synthetic pathway for the formation of crystalline **{Co5}-MOF**, thin-film **{Co5}-MOF** and heat-treated materials using **{Co5}-MOF** as a template. The addition of nickel (II) nitrate to the initial reactions allows for the formation of a new MM-MOF analogue of pentanuclear MOF, **{(CoNi)5}-MOF**.*

3.3 $[(MnZn)_3(BTEB)_2](H_2O)_2$ ($\{(MnZn)_3\}$-MOF)

{(MnZn)3}-MOF was synthesised via a reaction between **H3BTEB**, $MnCl_2 \cdot H_2O$ and $Zn(NO_3)_2.6H_2O$ in DMF at 90 °C, yielding colourless crystals suitable for analysis by single-crystal X-ray diffraction. Refinement of the crystal data revealed that **{(MnZn)3}-MOF** crystallises in the tetragonal crystal system in the space group $P4_322$. The individual respective atom positions of the Mn and Zn atoms could not be resolved from the single crystal data so are represented by M(II) and M(II)' respectively.

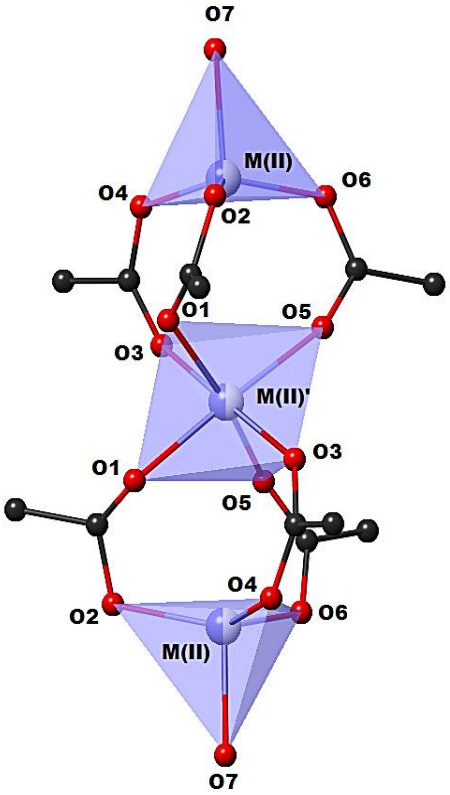

***Figure 3.3.1**: Detailed representation of the coordination environment of the metal centres, M(II) = Mn(II)/Zn(II), in the trinuclear unit of **{(MnZn)$_3$}-MOF**. Solvent molecules and hydrogen atoms of the C-atoms have been omitted for clarity. Colour Scheme: C black, O red, Mn/Zn slate blue.*

The asymmetric unit of **{(MnZn)$_3$}-MOF** contains two distinct metal ions in their +2 oxidation state, one fully deprotonated BTEB^{3-} ligand, and one coordinated H_2O molecule. The metal centre, M(II), is linked via three bidentate bridging carboxylate moieties from three distinct fully deprotonated **BTEB**$^{3-}$ ligands. A third M(II) centre in the SBU is generated through symmetry operations and is linked *via* three bidentate bridging carboxylates from **BTEB**$^{3-}$. This results in a six-connected tri-nuclear hourglass-shaped SBU (Figure 3.3.1). The coordination environment of M(II) is tetrahedral and is completed by a capping H_2O molecule located at the apical position. The central M(II)' atom has an octahedral coordination environment. The three M^{2+} centres are *approx*. collinear with an M(II)-M(II) angle of *approx*. 178 °. The metal composition of the cluster could not be determined by SCXD. The interatomic distances and bond angles around the two metal centres have been reported (Table 3.3.1).

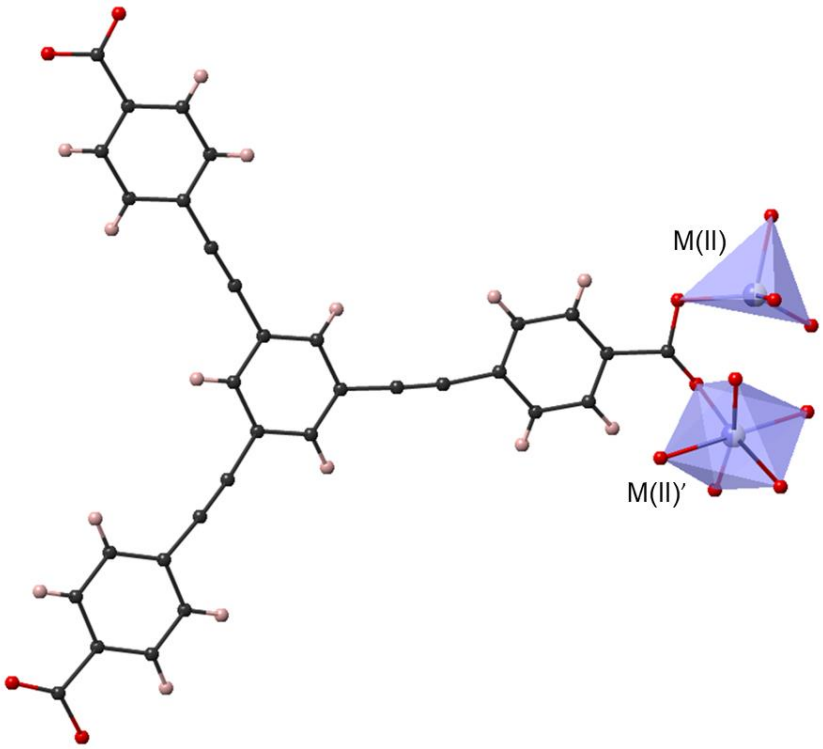

***Figure 3.3.2**: The asymmetric unit of **{(MnZn)$_3$}-MOF** comprised of one organic ligand and the labelled tetrahedral M(II) and octahedral M(II)'. Colour key: M(II)/M(II)' slate blue, O red, C black, H light pink.*

Each trinuclear SBU is connected to six deprotonated **BTEB^{3-}** ligands, and each **BTEB^{3-}** ligand is connected to three SBUs (Figure 3.3.2). The overall structure is doubly interpenetrated, with pairs of aromatic interactions between the symmetry-related nets. Each individual net is chiral, as two **BTEB^{3-}** ligands link SBUs along a 4_3 screw axis along the crystallographic *c*-axis (Figure 3.3.3). A centroid-centroid distance of *ca*. 4.3 Å between the phenyl groups in different nets confirms the 'T-shaped' π – π stacking interactions as the distance between phenyl rings lies in the typical range for such interactions.[6] The MOF has a density of 498 kg/m^3 (constitutional solvent molecules in the channels deleted). The packing structure of **{(MnZn)$_3$}-MOF** is shown in Figure 3.3.3 and the average distance between the two layers is ca. 20.42 Å. The compound is isostructural to the monometallic **TCM-1** Zn-analogue which has been previously reported within the research group.[5]

a)

b)

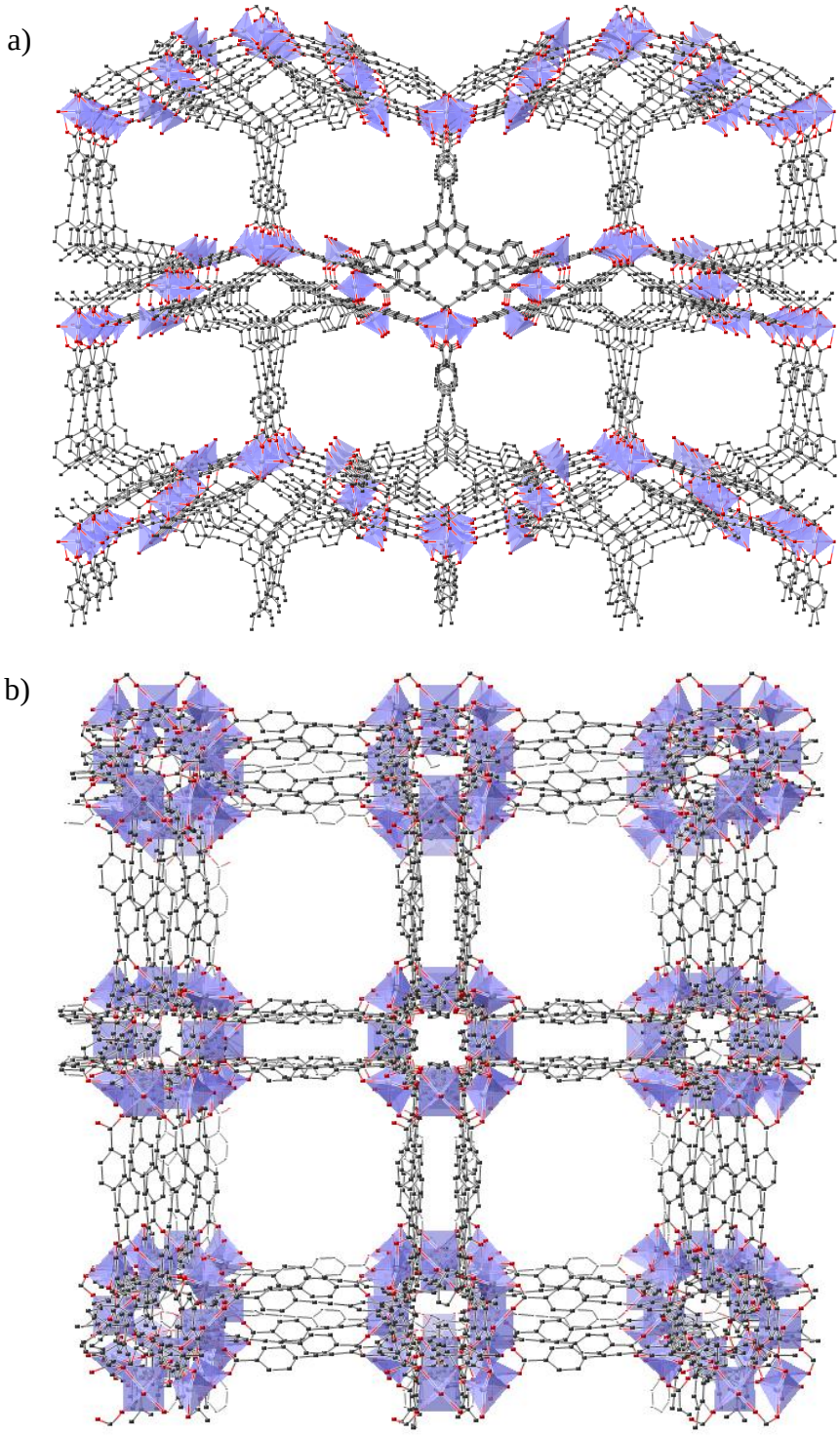

***Figure 3.3.3**: a) Crystal structure of **{(MnZn)$_3$}-MOF** when viewed down the crystallographic a-axis. b) Crystal structure of **{(MnZn)$_3$}-MOF** when viewed down the crystallographic c-axis. Colour Scheme: C black, O red, Mn/Zn slate blue.*

Table 3.3.1*: Selected bond distances and angles of coordination environments found in* ***{(MnZn)$_3$}-MOF****.*

Atoms	Distance [Å]	Atoms	Angle [°]
M(II)'-O(1)	**2.100 (11)**	O(5)-M(II)'-O(5)#	**91.0 (6)**
M(II)'-O(3)	**2.149 (7)**	O(5)-M(II)'-O(1)	**94.8 (5)**
M(II)'-O(5)	**2.081 (10)**	O(5)-M(II)'-O(1)#	**169.2 (4)**
		O(1)-M(II)'-O(1)#	**80.9 (8)**
M(II)-O(2)	**2.003 (9)**	O(5)-M(II)'-O(3)	**95.1 (3)**
M(II)-O(4)	**1.962 (8)**	O(5)-M(II)'-O(3)#	**83.5 (3)**
M(II)-O(6)	**1.980 (9)**		
M(II)-O(7)	**2.080 (8)**		
		O(1)-M(II)'-O(3)	**87.0 (3)**
		O(1)#-M(II)'-O(3)	**94.6 (3)**
		O(3)-M(II)'-O(3)#	**178.0 (4)**
		O(6)-M(II)-O(2)	**118.5 (4)**
		O(4)-M(II)-O(7)	**97.7 (4)**
		O(6)-M(II)-O(7)	**100.5 (5)**
		O(2)-M(II)-O(7)	**102.3 (4)**

Table 3.3.2: *Crystal data and structure refinement for* ***{(MnZn)$_3$}-MOF****.*

Identification code	**{(MnZn)$_3$}-MOF**
Empirical formula	$C_{66}H_{34}Mn_{0.5}O_{14}Zn_{2.5}$
Formula weight	1241.82
Temperature	215(2) K
Wavelength	1.54184 Å
Crystal system	Tetragonal
Space group	$P4_322$
Unit cell dimensions	a = 20.4221(17) Å, b = 20.4221(17) Å, c = 39.721(4) Å α = 90°; β = 90°; γ = 90°
Volume	16566(3) Å^3
Z	4

Density (calculated)	0.498 mg/m^3
Absorption coefficient	0.923 mm^{-1}
F(000)	2518
Crystal size	0.22 x 0.05 x 0.05 mm^3
Theta range for data collection	2.163 to 40.089°
Index ranges	-13<=h<=15, -17<=k<=13, -33<=l<=33
Reflections collected	35017
Independent reflections	5061 [R_{int} = 0.0614]
Completeness to theta = 40.089°	99.9 %
Absorption correction	Semi-empirical from equivalents
Max. and min. transmission	0.7479 and 0.5917
Refinement method	Full-matrix least-squares on F2
Data / restraints / parameters	5061 / 219 / 327
Goodness-of-fit on F^2	1.002
Final R indices [I>2σ (I)]	R1 = 0.0437, wR2 = 0.1156
R indices (all data)	R1 = 0.0778, wR2 = 0.1323
Absolute structure parameter	-0.68(6)
Largest diff. peak and hole	0.105 and -0.099 e.Å^{-3}

3.4 Physicochemical characterisation of {(MnZn)$_3$}-MOF

As previously discussed, the atom positions of both Mn(II) and Zn(II) within the trinuclear unit could not be determined using the data collected from single crystal diffraction data of the MOF. Bulk characterisation of the material was required to investigate the composition of the MOF and to evaluate the crystal order. The purity and nature of the bulk material was further confirmed using PXRD, FT-IR and Raman spectroscopy and TGA analysis. The elemental composition was investigated using EDX and XPS spectroscopy.

3.4.1 X-ray powder diffraction

Crystals of **{(MnZn)$_3$}-MOF** were ground into a powder for X-ray powder diffraction analysis. A PXRD pattern was recorded to characterise the phase purity of the synthesised bulk material. The PXRD pattern was measured in a capillary in DMF at 220 K to obtain low angle peaks and to avoid loss of crystallinity associated with solvent evaporation from the sample (Figure 3.4.1). The experimental pattern and the simulated

PXRD pattern, based on the single crystal X-ray diffraction data, match closely, confirming the phase-purity of the synthesised material. Two major signals are visible in the measured pattern below 2θ = 5°. The most intense of these signals is found at a 2θ angle of 4.31° and is resolved in the calculated pattern at 4.35°. The latter signal is found at an angle of 4.89 ° and is resolved in the calculated pattern at 4.86 °. The relative intensities of these signals decrease in the measured pattern most likely because of preferred crystal orientation effects. Additional signals at 2θ > 5 ° can be seen in both patterns. The signals at 6.12° and 6.53° match closely with the reflections in the simulated pattern. A broad background signal in the range 5 ° < 2θ > 25 ° can be attributed to measurements being collected within the capillary.

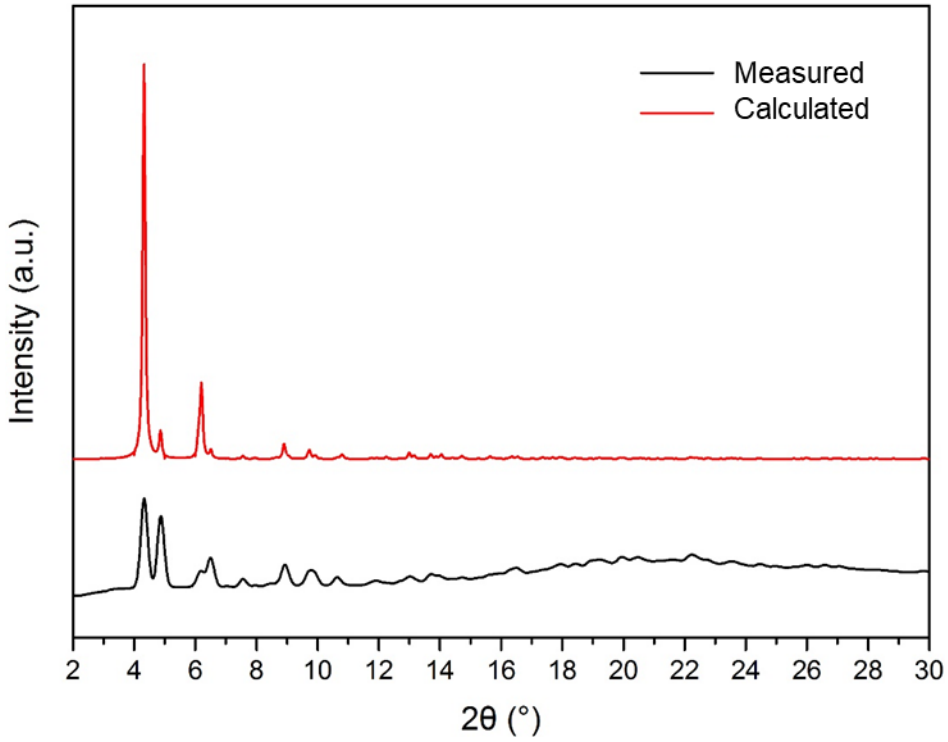

***Figure 3.4.1**: PXRD patterns of experimentally measured crystals of **{(MnZn)$_3$}-MOF** in capillary (black) and the simulated diffraction pattern from the single crystal data (red).*

3.4.2 Raman spectroscopy

Raman spectroscopic methods were used to characterize crystals of **{(MnZn)$_3$}-MOF**. The Raman spectra of **H$_3$BTEB** and **{(MnZn)$_3$}-MOF** confirm the presence of the ligand inside the MM-MOF (Figure 3.4.2). The signals at 993 cm^{-1} in the spectrum of **{(MnZn)$_3$}-MOF** and of **H$_3$BTEB** derive from CH rocking vibrations.[7] Bands in the spectrum of **{(MnZn)$_3$}-MOF** at 1121, 1142 and 1173 cm^{-1} derive from C-C single bond vibrations. Two corresponding bands can be identified in the spectrum of **H$_3$BTEB** at 1122 and 1167 cm^{-1}. In the spectrum of **{(MnZn)$_3$}-MOF**, the most intense signals derive from

the aromatic C=C bond vibrations and appear at 1584 and 1605 cm^{-1}. In the spectrum of **H_3BTEB**, related bands can be identified at 1582 and 1608 cm^{-1}, respectively. Another prominent signal is found at 2217 cm^{-1} and derives from the alkyne C≡C vibration in the spectrum of **{(MnZn)$_3$}-MOF**. The corresponding signal appears at 2217 cm^{-1} in the spectrum of **H_3BTEB**.[8]

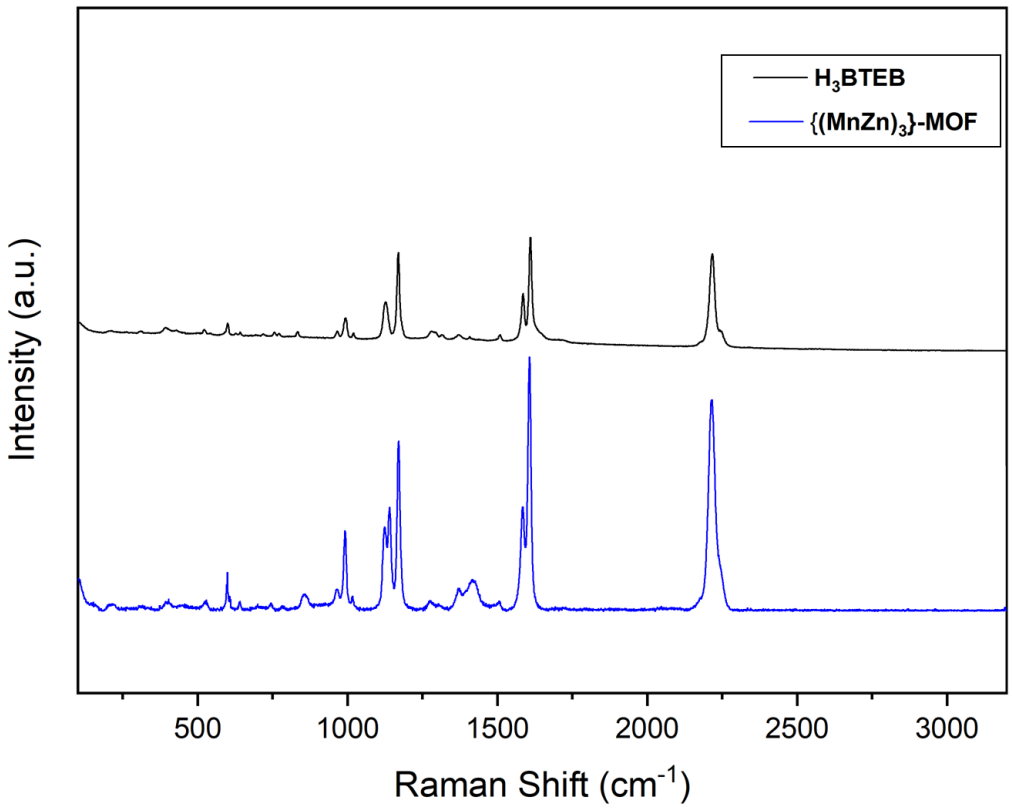

***Figure 3.4.2**: Raman spectra of **H_3BTEB** (black) and **{(MnZn)$_3$}-MOF** (blue).*

3.4.3 Scanning electron microscopy and energy dispersive X-ray spectroscopy

Scanning electron microscopy (SEM) was used to image crystals of **{(MnZn)$_3$}-MOF** deposited on an FTO glass slide. After synthesis, the bulk sample was washed with DMF, dried in air and adhered to adhesive carbon tabs atop an aluminium SEM stub. The sample was loaded into a Zeiss ULTRA Plus scanning microscope with an acceleration voltage in the range 2 – 30 kV under a $1x10^{-5}$ mbarr vacuum using the InLens imaging detector.

Monodispersed, single crystals of **{(MnZn)$_3$}-MOF** can be seen to have rod-like shape (Figure 3.4.3). The elemental analysis was recorded using energy-dispersive X-ray spectroscopy (EDX). The relative metal percentages of Zn and Mn were evaluated as shown in Table 3.4.1. The results point to a Mn:Zn atomic ratio in **{(MnZn)$_3$}-MOF** of close to 1:4

(1:3.68). This deviates from the ratio of Mn/Zn used in the synthesis. It suggests that trimers of monometallic $\{Zn_3\}$ may form in tandem with $\{Mn_1Zn_2\}$ mixed-metal trimers in a 1:1 ratio.

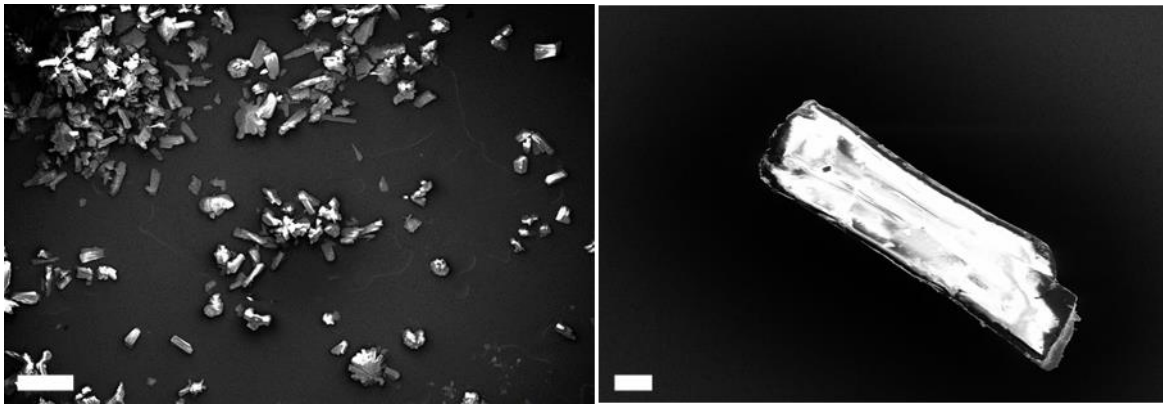

***Figure 3.4.3**: SEM images **{(MnZn)$_3$}-MOF**. Scale bar: 200 µm (left) 10 µm (right).*

***Table 3.4.1**: EDX spectroscopy showing the Mn:Zn relative metal percentages in **{(MnZn)$_3$}-MOF** over the bulk sample.*

Elements	Mn	Zn
Spectrum 1 (atomic %)	0.48	1.52
Spectrum 2 (atomic %)	0.35	1.64
Spectrum 3 (atomic %)	0.52	1.84
Mean ratio	1	3.68

3.4.4 X-ray photoelectron spectroscopy

XPS was used for the analysis of metal environments of **{(MnZn)$_3$}-MOF**. XPS was performed on a Phi Versa Probe III analyser equipped with a 1487 eV Rowland circle monochromatic Al Kα X-ray source. Crystals were adhered to background-corrected adhesive tape and imaged before analysis using scanning X-ray imaging (SXI) to identify good measurement positions (Figure 3.4.4, insert). The survey scan was conducted using a 200 µm spot size with a 224 eV pass energy in 0.4 eV increments. Individual orbitals were analysed on the same sample area at 26 eV for the O 1s and the C 1s and 55 eV for the Mn and Zn 2p. All orbitals scans applied 0.05 eV increment steps. Firstly, an overview spectrum of **{(MnZn)$_3$}-MOF** was obtained, identifying C, O and both Zn and Mn within the small spot size (Figure 3.4.4).

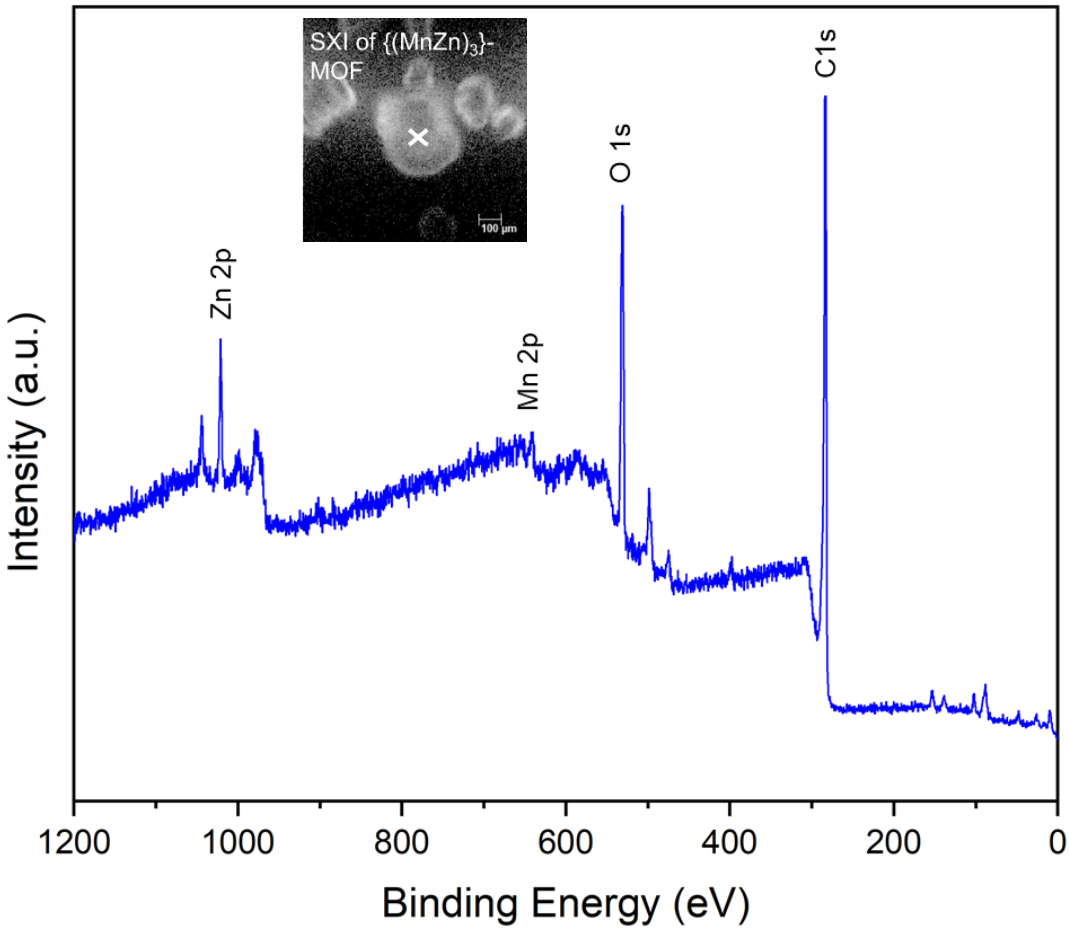

***Figure 3.4.4**: The XPS survey spectra overview of freshly synthesised crystals of **{(MnZn)$_3$}-MOF**. Intensity measured in counts per second. Insert, SXI image of **{(MnZn)$_3$}-MOF** to conform measurement position*

The O 1s spectra can provide some further insight into the metal ion distribution within the inorganic trimer. Assuming solvent molecules are removed due to the ultra-high vacuum environment of the XPS chamber, all O peaks will be related to the six bridging oxygens of the **BTEB^{3-}** ligands. The spectrum identifies two distinct O 1s environments at binding energies of 531.87 and 533.67 eV. These peaks were similar enough in binding energy to assume they are from the same O species, shifted by the electron environment alone. The fitted peaks could be integrated to *approx.* 1:1 (51%:49%). From the XPS analysis, it was also found that the MOF has a Zn/Mn ratio of *approx.* 2:1 (Table 3.4.2). The binding energy of an element is dependent upon the local chemical environment of that element. The electrophilic nature of the coordinated metal will displace the electron density to the O atom and the binding energy decreases as a result, leading to a red shift in binding energy. The degree to which a metal will affect such a shift is dependent on the electronegativity value. Considering the electronegativity values of the Mn and Zn being

1.55 and 1.65, respectively, and the Zn/Mn ratio in the MOF, the exact positions of the metals within the structure can be approximated.

There are two tetrahedral metal positions within the trinuclear unit, each coordinated by three oxygen atoms, and the central octahedral metal position on the SBU is coordinated by six oxygen atoms when ignoring those of the labile solvent molecule. This leads to the conclusion that the Mn^{2+} ions are likely located in the central octahedral positions and the two Zn^{2+} ions are assigned to the tetrahedral positions. In this configuration, six O atoms coordinate to Mn(II) ions and six to Zn(II) ions (three to each Zn ion), resulting in an equal number of Mn–O and Zn–O bonds. This is in agreement with the 1:1 integration of the fitted peaks. If the Mn^{2+} ion was located in one of the two tetrahedral sites, the integration of the individual fitting would be 1:3.

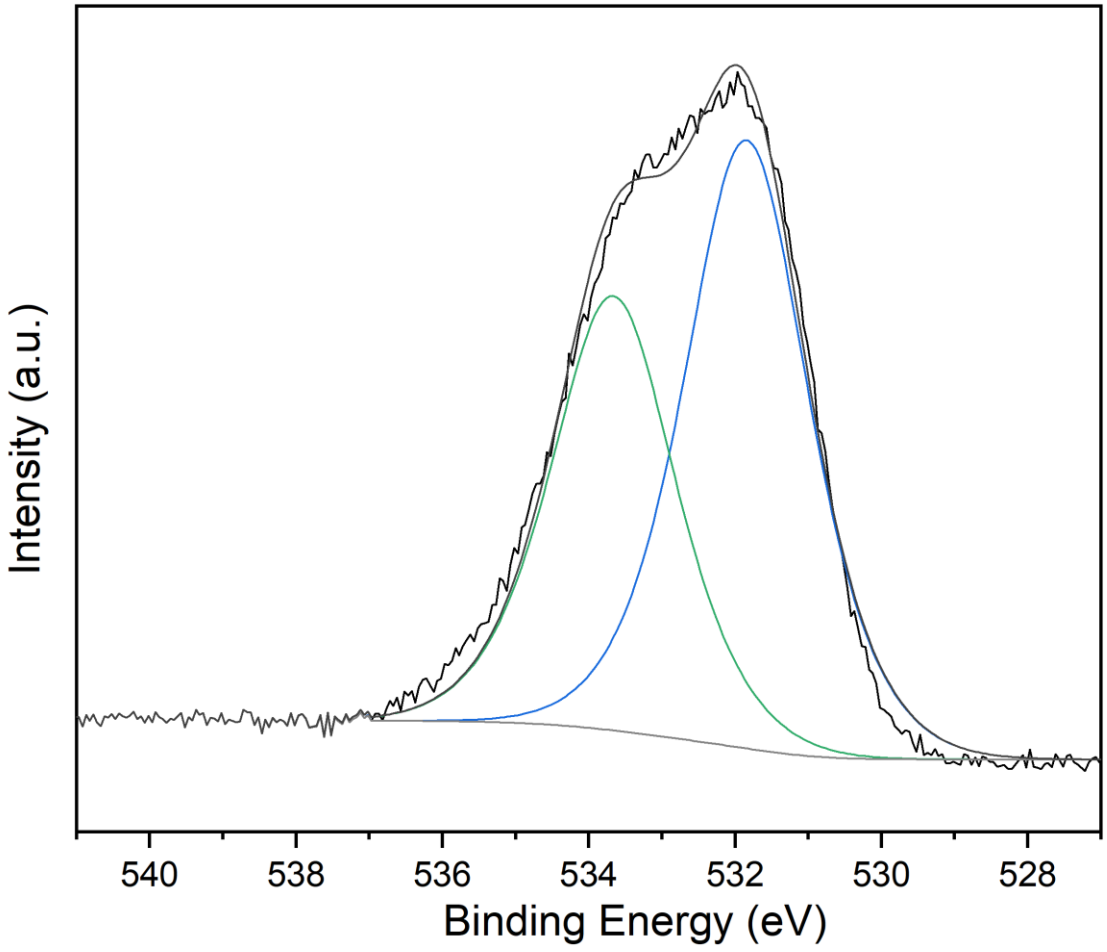

***Figure 3.4.5**: The O 1s XPS spectrum of **{(MnZn)$_3$}-MOF** with intensity measured in counts per second.*

***Table 3.4.2**: Elemental ratio determined from XPS analysis.*

Element	*% (Ratio)*
Zn	0.6 (1.8)
Mn	0.4 (1.2)

3.4.5 Computational modelling of the {M_3} SBU

Computational modelling was performed using a simplified model of the trinuclear unit chosen to explore possible {M_3} SBU configurations and to assess the stabilities of different metal ion configurations. The XPS and EDX spectra were recorded for the MOF, both in agreement that zinc is the predominant metal in the MOF structure, with the XPS dataset yielding *approx.* 2:1 Zn/Mn ratio. Assuming that there is a degree of positional order in the inorganic SBU in **{(MnZn)$_3$}-MOF**, modelling was performed on the different configurations possible for a {Mn_1Zn_2} SBU. The SBUs were modelled using DFT employing a non-periodic environment. The calculations were carried out using the gaussian09[9] program, with the PBE0[10,11] function in conjunction with the SDDALL[12] basis libraries, with an effective core potential value for both zinc and manganese, and 6-31g(d)[13] basis set for C and O, and 6-31g(p)[14] basis set for H. The standard convergence criteria contains 225 radial shells, with each shell containing 974 angular points. Only the high-spin configuration for Mn(II) was modelled as the low-spin d^5 configuration can be excluded. To capture the proper electronic picture, the SBU was simplified by replacing the **BTEB^{3-}** ligands with simple benzoate ligands and modelling the unit as an isolated complex. The stability of the {M_3} SBU was found to be superior when the central octahedral coordinated position contained a Mn^{2+} ion rather than a Zn^{2+} ion (Table 3.4.3).

***Table 3.4.3:** Stabilisation energy calculations for the two possible metal ion configurations of the {Mn_1Zn_2} SBU in **{(MnZn)$_3$}-MOF**.*

	Multiplicity (no. of unpaired electrons + 1)	Energy (Hartrees)
Mn^{2+} ion in the central octahedral position and both Zn^{2+} ions in the peripheral positions of the SBU	6 (high spin)	-3573.90628086

Mn^{2+} ion in the peripheral tetrahedral position and both Zn^{2+} ions occupying the remaining positions of the SBU	6 (high spin)	-3573.89132888

The central position is identified as the more stable position for Mn^{2+} in this system, with a stabilisation energy of *approx.* 39 kJ/mol. The structure is predicted to be linear with a Zn-Mn-Zn angle of *ca.* 178 ° when Mn^{2+} occupies the middle position within the trinuclear SBU. When Mn occupies one of the side sites, bound to the labile solvent molecule, the calculated structure deviates from linearity, with a Zn-Zn-Mn angle of *ca.* 157°. The deviation from linearity is accompanied with changes in ligand arrangement and metal-ligand distances.

From the results of the computational modelling, XPS fitting and the Mn/Zn ratio obtained from the XPS and EDX data, it appears that the MM-MOF may contain order within the M_3 metal clusters. The proposed structure for **{(MnZn)$_3$}-MOF** is $[Mn_1Zn_2(BTEB)_2](H_2O)_2$, with a Mn^{2+} ion occupying the central octahedral position and two Zn^{2+} ions located in the tetrahedral sites. This is further supported by the electrochemical experiments conducted in section 2.5, where it is demonstrated that the location of Zn(II) ions in the tetrahedral position alters the catalytic activity in comparison to isostructural MM-MOFs.

3.4.6 Thermogravimetric analysis

Thermogravimetric analysis (TGA) of **{(MnZn)$_3$}-MOF** was performed in a N_2 atmosphere at a heating rate of 5 °C per minute (Figure 3.4.6). Crystals were transferred to the quartz measurement crucible and the MM-MOF was left to stand at 30 °C for 30 minutes before beginning the heating ramp to ensure all isopropanol had evaporated. The TGA experiment reveals an initial weight loss of 20.3% between 50 and 200 °C which can be attributed to the loss of loosely bound H_2O and DMF solvent molecules in the pores. Another thermogravimetric step of *ca*. 14.8% is observed between 85 to 380 °C which derives most likely from the removal of more strongly bound solvent molecules including coordination solvent molecules. This further indicates the ligand is stable to *approx.* 380 °C. There is a further weight loss in the range 380 - 690 °C that results from the decomposition of the organic ligand and subsequently the MM-MOF.

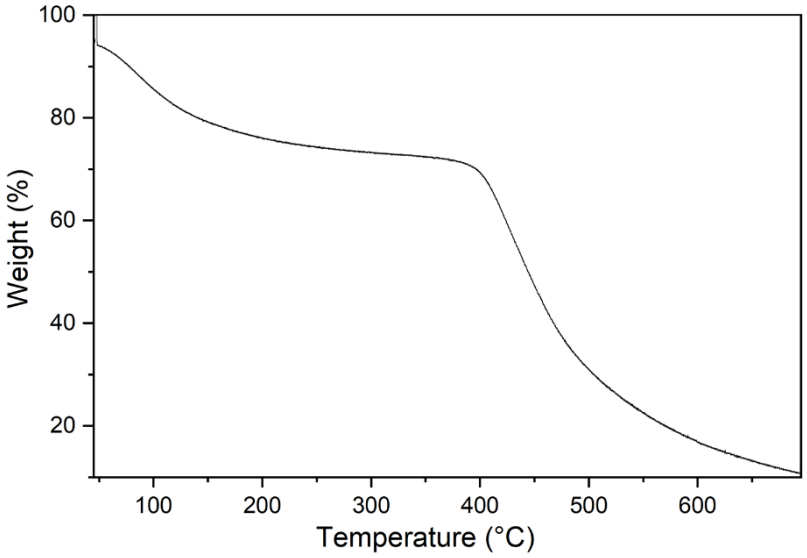

***Figure 3.4.6**: TGA of **{(MnZn)$_3$}-MOF** carried out in the N_2 atmosphere at a heating rate of 5 °C per minute.*

3.5 $[Co_1Zn_2(BTEB)_2](DMF)_2$ and $[Mn_1Co_2(BTEB)_2](H_2O)_2$

The MOFs **{(MnCo)$_3$}-MOF** and **{(CoZn)$_3$}-MOF**, isostructural Co/Zn and Co/Mn analogues of **{(MnZn)$_3$}-MOF** respectively, were previously synthesised by Dr. Kevin Byrne. The MOFs were synthesised when **H$_3$BTEB** and the corresponding metal nitrate salts (3:2:1 ratio) were heated in DMF at 90 °C for 72 hours. The optimisation of the synthesis of this compound was performed to achieve a yield in excess of 50 % and 85 % for **{(MnCo)$_3$}-MOF** and **{(CoZn)$_3$}-MOF**, respectively. The location of the individual metals within the structures were previously resolved using Co^{2+} as a reference ion. It is shown that Mn^{2+} has a preference for the central octahedral site in the $\{M_3\}$ unit and Zn^{2+} prefers to occupying the tetrahedral sites in the SBU.

In the case of **{(MnCo)$_3$}-MOF**, peripheral Co(II) centres make the MOF a potential candidate for water splitting. Due to the presence of Co(II) ions located at the peripheral tetrahedral sites in the $\{Mn_1Co_2\}$ SBU with labile solvent molecule sites, **{(MnCo)$_3$}-MOF** was expected to show water oxidation activity.[15] Previously, photo-induced water oxidation catalysis tests on this compound have shown promising O_2 evolution quantities and thus further verify the results. Electrochemical experiments for the OER were carried out for these MM-MOFs alongside the **{(MnZn)$_3$}-MOF**.

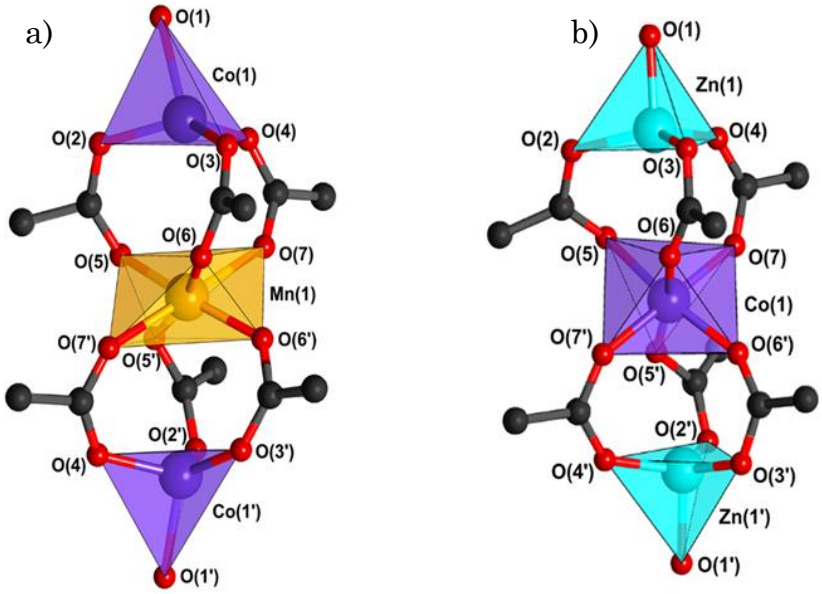

***Figure 3.5.1**: View of **{(MnCo)$_3$}-MOF** (a) and **{(CoZn)$_3$}-MOF** (b) showing the {M_3} SBU with coordinated bridging carboxylate groups from six ligands and two coordinated solvent molecules. key: Mn: yellow polyhedra, Zn: cyan polyhedra, Co purple polyhedra, O red, N pale blue, C grey.*

3.6 Electrocatalytic water oxidation

The polynuclear nature of the SBU of each of the {M_3} MM-MOFs with two weakly-bound solvent molecules on the axial positions of the trimetallic unit, allows for oxidation/electron-equivalents to be distributed over two sites per inorganic SBU. This prompted interest into the use of these structure for catalysis experiments for the oxygen evolution reaction (OER). **{(MnCo)$_3$}-MOF**, **{(CoZn)$_3$}-MOF** and **{(MnZn)$_3$}-MOF** were compared using a carbon paste (CP) electrode. Bulk crystals of the three samples were dried in air and ground with commercial carbon paste (CP) binder, made from conducting graphite powder and a pasting paraffin liquid. A catalyst loading of 20 wt-% was prepared for all MOFs by mixing 20 mg of CP and 5 mg of bulk catalyst in an agate mortar to obtain a catalyst loading of 20 wt-%. This blend was then packed inside the CP electrode pocket and polished to ensure a smooth electrode surface to minimise the threat of evolving oxygen dislodging the surface of the blend during catalytic experiments.

Cyclic voltammetry experiments were conducted using the catalysts in the potential range of 0.2 V to 1.4 V vs NHE in a 7.2 KPi pH buffer. Catalytic waves were observed at higher potentials for **{(MnCo)$_3$}-MOF**, **{(CoZn)$_3$}-MOF** which can be attributed to the

catalytic oxygen evolution half-reaction of water oxidation, whereas **{(MnZn)$_3$}-MOF** was inactive towards application of high potentials.

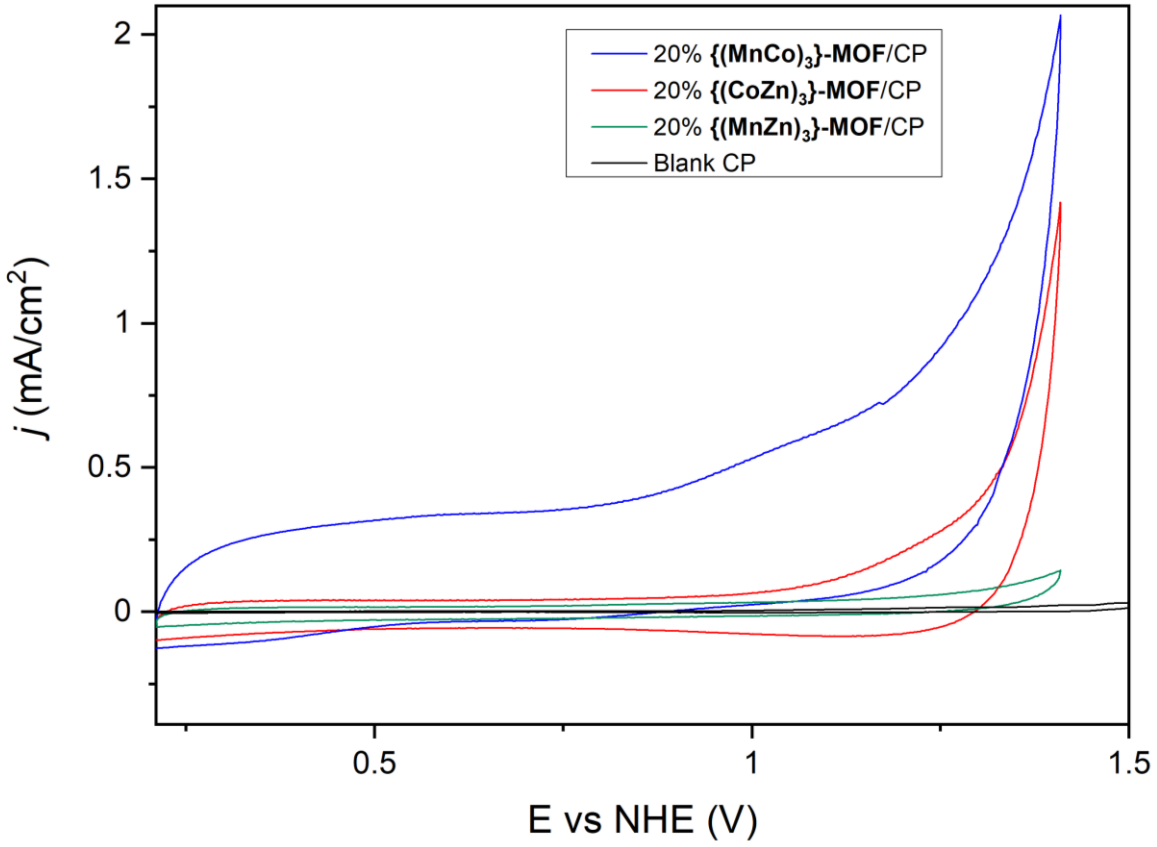

***Figure 3.6.1**: CV of 20 wt-% loading for **{(MnCo)$_3$}-MOF** (blue), **{(CoZn)$_3$}-MOF** (red) and **{(MnZn)$_3$}-MOF** (green) in air at a scan rate of 100 mV/s.*

To further understand the kinetics of the water oxidation, LSV experiments were performed revealing that the onset overpotential for the OER are 1.49, 1.31 and 1.26 V vs NHE for **{(MnZn)$_3$}-MOF**, **{(CoZn)$_3$}-MOF**, and **{(MnCo)$_3$}-MOF,** respectively (Figure 3.6.2). The polarising curves show there is a decrease in the rate of activity at higher potentials. This may be due to convective mass transport limitations due to accumulation of oxygen bubbles at the surface of the electrode and may be resolved by stirring the solution more vigorously or by employing a rotating disk electrode.

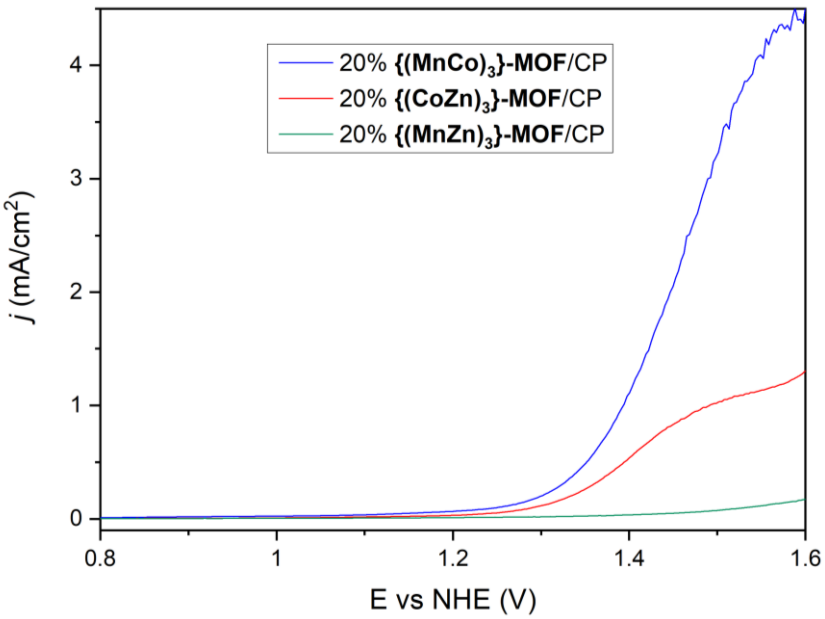

***Figure 3.6.2**: LSV for 20 wt-% catalyst loading of **{(MnCo)$_3$}-MOF** (blue), **{(CoZn)$_3$}-MOF** (red) and **{(MnZn)$_3$}-MOF** (green) at a rotation rate of 1000 rpm and a scan rate of 1 mV/sec.*

The onset potentials were estimated from the intersection points of the tangent lines of the Faradaic (current density > 0.2 mA/cm^2) and non-Faradaic (current density < 0.01 mA/cm^2) currents, which correspond to overpotentials of 463, 506 and 691 mV for **{(MnCo)$_3$}-MOF**, **{(CoZn)$_3$}-MOF**, and **{(MnZn)$_3$}-MOF**, respectively (Figure 3.6.3).

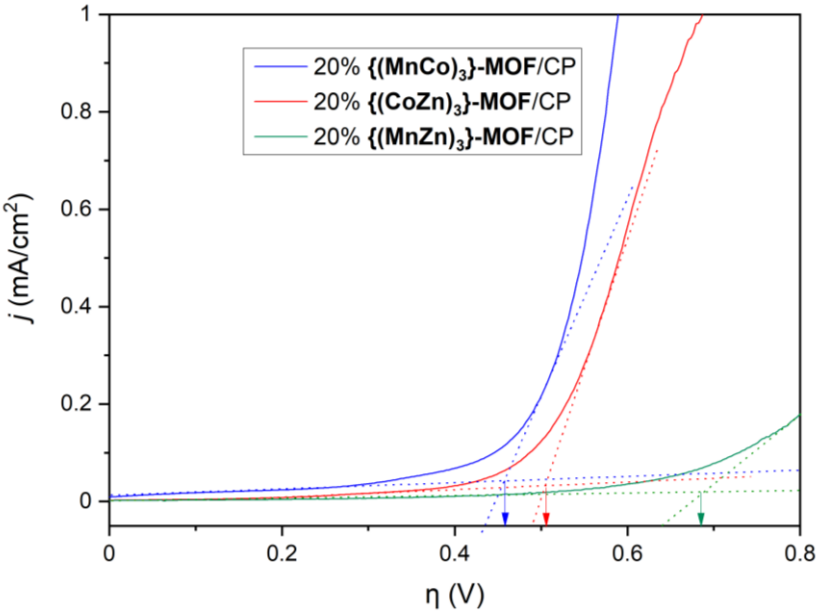

***Figure 3.6.3**: Onset potential of loading of **{(MnCo)$_3$}-MOF** (blue), **{(CoZn)$_3$}-MOF** (red) and **{(MnZn)$_3$}-MOF** (green) from LSV at 1000 rpm and scan rate 1 mV/sec.*

The Tafel slopes between the corresponding overpotential ranges of **{(MnCo)$_3$}-MOF**, **{(CoZn)$_3$}-MOF** and **{(MnZn)$_3$}-MOF** were found to be 134, 158 and 265 mV dec^{-1} respectively (Figure 3.6.4), indicating fast kinetics for the **{(MnCo)$_3$}-MOF** and **{(CoZn)$_3$}-MOF**.[16]

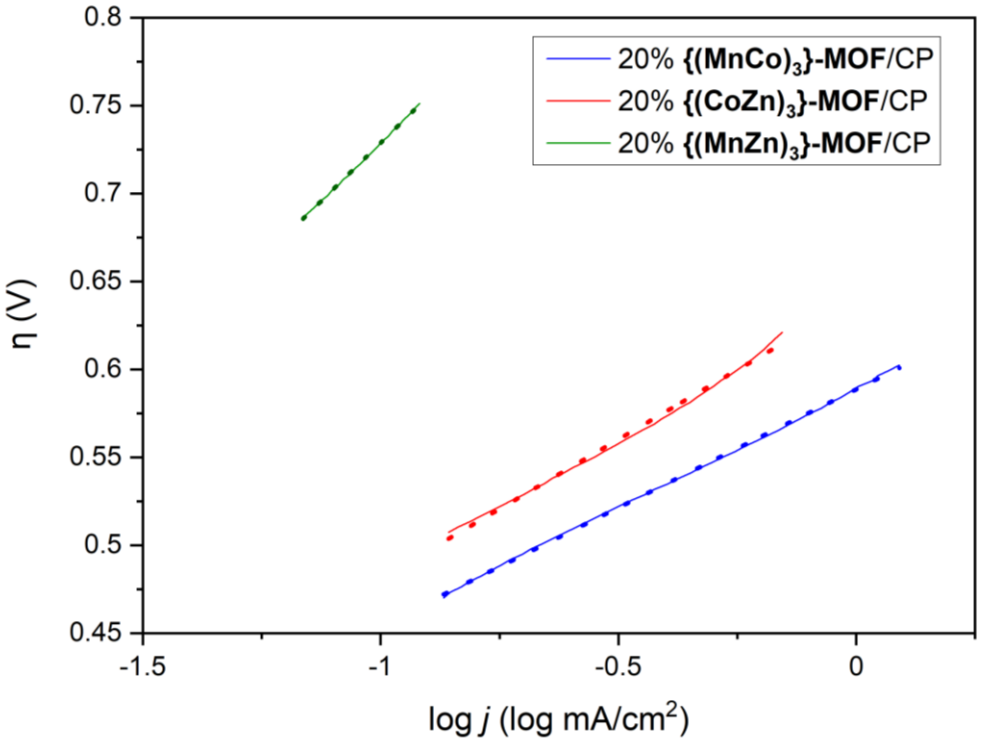

***Figure 3.6.4**: Tafel slopes for **{(MnCo)$_3$}-MOF** (blue), **{(CoZn)$_3$}-MOF** (red) and **{(MnZn)$_3$}-MOF** (green) in carbon paste electrodes at 20 wt-% catalyst loading.*

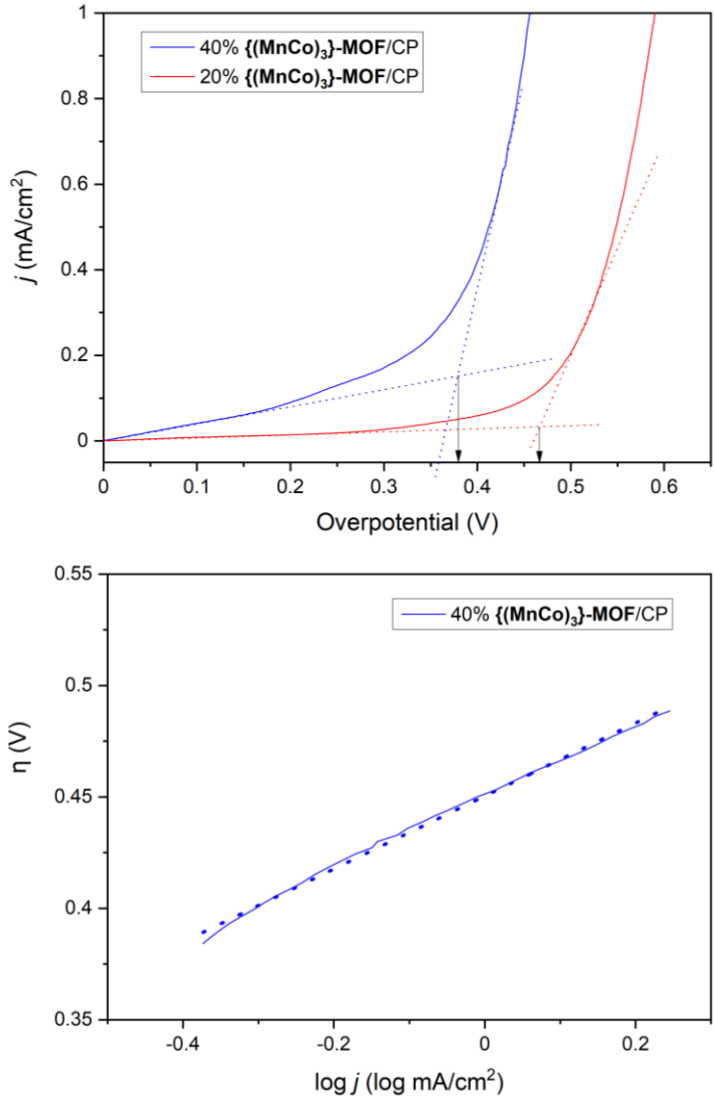

***Figure 3.6.5**: Onset potentials of **{(MnCo)3}-MOF** at catalyst loadings of 20 (red) and 40 wt-% (blue) in carbon paste, 1000 rpm and scan rate 1 mV/sec, inset: Tafel slope for 40 wt-% loading of **{(MnCo)3}-MOF**.*

The results obtained for the above discussed catalysts through CV and LSV experiments confirm that **{(MnZn)3}-MOF** is essentially inactive whilst **{(CoZn)3}-MOF** shows good activity and **{(MnCo)3}-MOF** is shown to be the best candidate of the series for electrocatalytic water oxidation. Therefore, a higher catalyst wt-% loading was tested using LSV to see the change in overpotential for **{(MnCo)3}-MOF**. Figure 3.5.4 shows considerable decrease in the overpotential of **{(MnCo)3}-MOF** at 40 wt-% to *ca.* 380 mV compared to 459 mV for 20 wt-% under the same experimental conditions. Further increase of catalyst loading in the carbon paste, made the electrode surface brittle and was inclined to break when subjected to high potentials. Table 3.6.1 shows the onset overpotentials, Tafel slopes and the overpotentials to reach 1 mA/cm^2 current density for these three catalysts.

***Table 3.6.1**: Summary of onset overpotentials, Tafel slopes and the current density at 1 mA/cm^2 obtained for each catalyst.*

Catalyst	η Onset (mV)	Tafel Slope (mV/dec)	η @ j = 1 mA/cm^2 (mV)
{(MnCo)$_3$}-MOF (40 wt-%)	380	164	457
{(MnCo)$_3$}-MOF (20 wt-%)	459	134	589
{(CoZn)$_3$}-MOF (20 wt-%)	506	158	688
{(MnZn)$_3$}-MOF (20 wt-%)	691	265	-

It should be noted that consecutive CV cycles of each of the three M_3 MM-MOF presented above demonstrated the loss of catalytic activity with subsequent CV cycles. These control experiments highlight the limited stability of these MM-MOFs due to oxidative and/or hydrolytic degradation.

However, the experiments serve as a proof of concept that addition of a second metal ion to pre-established MOF structures through direct synthesis is a reliable way to modify the catalytic activity of a MOF for the OER providing comparable results. Stability was favoured over activity, so focus was shifted to the well-stabilised $\{M_5\}$ MOF-based archetype **{Co$_5$}-MOF** structure, discussed in Chapter 2. The nature of the 9-connetected SBU of the MOF and its doubly interpenetrated nature lends to its stability in water and under bulk electrolysis conditions.

3.7 Pentanuclear MM-MOF {(CoNi)$_5$}-MOF

An isostructural Co/Ni MM-MOF analogue of **{Co$_5$}-MOF** was synthesised using a direct synthetic approach. The self-assembly of **{(CoNi)$_5$}-MOF** was observed from a solution of **H$_3$BTEB**, $Co(NO_3)_2{\cdot}6H_2O$ and $Ni(NO_3)_2{\cdot}6H_2O$ (1:3:2) mole ratio) in DMF at 85 °C within a time period of 48 hours. Phase-pure purple crystals of **{(CoNi)$_5$}-MOF** suitable for single crystal X-ray analysis formed in the reaction mixture. A yield of 25 % was obtained. **{(CoNi)$_5$}-MOF** crystallises in the monoclinic space group *C*2/*c*. The MOF has the overall formula $MeNH_2(CoNi)_5(\mu_3\text{-}OH)_2(BTEB)_3(H_2O)_2(DMF)_2$.

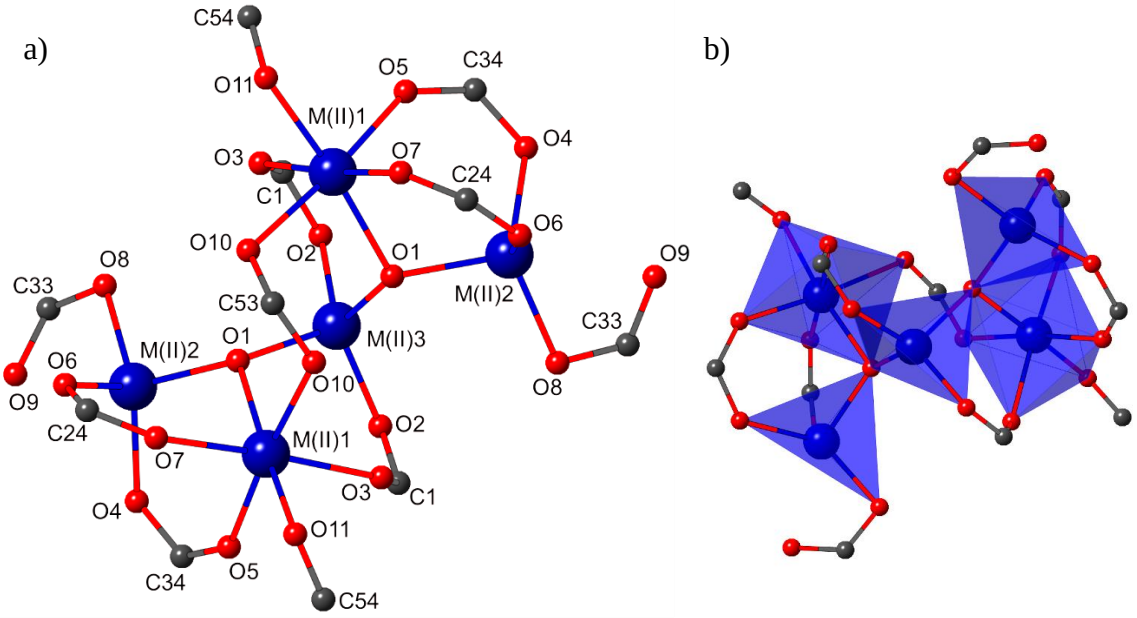

***Fig 3.7.1**: a) Detailed representation of the coordination environment of the metal centres, M = Co(II)/Ni(II), in the pentanuclear unit of **{(CoNi)$_5$}-MOF**. b) Polyhedra representation of M(II) ions within the pentanuclear SBU with {M(II)-O} bonds defined as the points of extension. Hydrogen atoms have been omitted for clarity. Colour Scheme: C grey, O red, M(II) blue.*

The asymmetric unit of **{(CoNi)$_5$}-MOF** is represented by a single {μ_3-OH}-centered triangular M(II) arrangement. It contains three crystallographically independent metal ions, a μ_3-OH- ligand, one coordinating DMF and two solvent molecules, along with one complete organic ligand and one half coordinating **BTEB^{3-}** ligand completed through a symmetry operation. **{(CoNi)$_5$}-MOF** contains a non-planar, pentanuclear SBU (Figure 3.7.2) and can be visualised as composed of two, symmetry-related, vertex-sharing, {μ_3-OH}-centered triangular M(II) arrangements.

The coordination environment of M(1) and M(2) is distorted octahedral, completed by DMF and H_2O solvent molecules respectively whereas M(3) adopts a distorted tetrahedral geometry with the bond angles varying between 102.5(5) and 115.5(6)° deviating from an ideal angle of 109.5 °. The M-OH bond distances in **{(CoNi)$_5$}-MOF** are found in the range 1.985(8)-2.071(6) Å. The M(1)–O(3) and M(1)-O(10) bonds are longer than for most reported Co(II) carboxylate bonds can be regarded within the scope of weak Co(II)-O interactions.[17]

***Table 3.7.1**: Selected bond distances and angles of coordination environments found in **{(CoNi)$_5$}-MOF**.*

Atoms	Distance [Å]	Atoms	Angle [°]
M(1)-O(7)	2.054 (8)	O(7)-M(1)-O (5)	95.5 (3)
M(1)-O(5)	2.055 (8)	O(7)-M(1)-O (11)	87.7 (3)
M(1)-O(11)	2.068 (8)	O(5)-M(1)-O (11)	90.9 (3)
M(1)-O(3)	2.138 (8)	O(7)-M(1)-O (1)	89.7 (3)
M(1)-O(1)	2.071 (6)	O(5)-M(1)-O (1)	96.9 (3)
		O(11)-M(1)-O (1)	171.9 (3)
M(1)-O(10)	2.144 (7)	O(7)-M(1)-O (3)	176.3 (3)
		O(11)-Co(1)-O (3)	88.7 (4)
		O(5)-M(1)-O (3)	83.8 (3)
M(2)-O(4)	1.967 (8)		
M(2)-O(8)	1.977 (15)		
M(2)-O(1)	1.985 (8)	O(4)-M(2)-O (8)	135.6 (8)
M(2)-O(6)	1.986 (8)	O(4)-M(2)-O (1)	106.5 (3)
M(3)-O(2)	1.904 (9)	O(8)-M(2)-O (3)	102.2 (6)
M(3)-O(1)	2.011 (7)	O(4)-M(2)-O (6)	102.5 (4)
		O(8)-M(2)-O (6)	106.0 (7)
		O(1)-M(2)-O (6)	98.6 (3)
		O(2)-M(3)-O (1)	102.6 (3)
		O(2)#-Co(3)-O (2)	123.4 (6)
		O(2)-Co(3)-O (1)	102.6 (3)
		O(1)-Co(3)-O (1)#	93.6 (4)

The 3D structure of **{(CoNi)$_5$}-MOF** is further characterised by two symmetry-equivalent interpenetrated nets (Figure 3.7.2). This twofold interpenetration is facilitated by parallel displacement π–π interactions between pairs of the central aromatic **BTEB^{3-}** phenyl ring moieties ranging 3.1-3.5 Å which is a typical distance for these types of interactions.[6] The interatomic distances and bond angles around the two metal centres have been reported in Table 3.7.2.

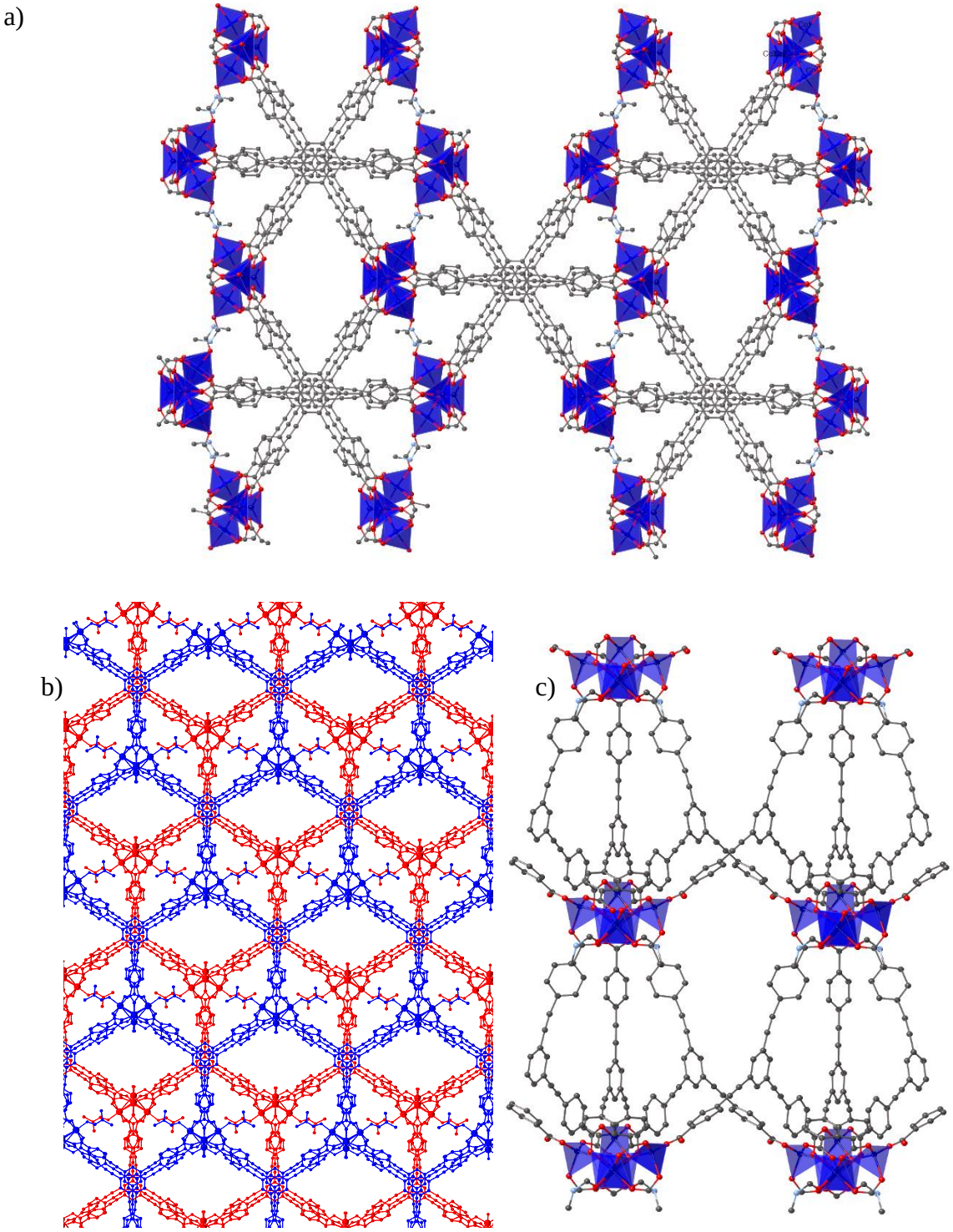

***Figure 3.7.2**: Doubly-interpenetrated (3,3)-coordinated nets in **{(CoNi)$_5$}-MOF** down the crystallographic c- axis (a) highlighting individual nets as red and blue (b) down the crystallographic c- axis. **c)** View down the crystallographic a-axis showing benzene rings edge to face interactions.*

***Table 3.7.2**: Crystallographic table for **{(CoNi)$_5$}-MOF**.*

Identification code	**{(CoNi)$_5$}-MOF**
Empirical formula	$C_{105}H_{62}Co_{3.33}N_2Ni_{1.67}O_{24}$
Formula weight	2029.85
Temperature	214(2) K
Wavelength	1.54184 Å
Crystal system	Monoclinic
Space group	*C* 2/c
Unit cell dimensions	a = 25.304(4) Å, b = 36.559(6) Å, c = 20.235(3) Å α = 90°; β = 124.52(3)°; γ = 90
Volume	15423(6) Å^3
Z	4
Density (calculated)	0.874 mg/m^3
Absorption coefficient	3.364 mm^{-1}
F(000)	4139
Crystal size	0.110 x 0.080 x 0.070 mm^3
Theta range for data collection	2.417 to 52.524°
Index ranges	-26<=h<=25, -37<=k<=37, -20<=l<=20
Reflections collected	8738
Independent reflections	8738 [R_{int} = 0.1110]
Completeness to theta = 52.524°	99.1 %
Absorption correction	Semi-empirical from equivalents
Max. and min. transmission	0.7504 and 0.5921
Refinement method	Full-matrix least-squares on F2
Data / restraints / parameters	8738 / 0 / 614
Goodness-of-fit on F^2	1.621
Final R indices [I>2σ (I)]	R1 = 0.1337, wR2 = 0.3924
R indices (all data)	R1 = 0.1706, wR2 = 0.4179
Largest diff. peak and hole	1.116 and -0.554 e.Å^{-3}

3.7.1 Powder X-ray diffraction analysis

For PXRD characterisation, crystals of **{(CoNi)$_5$}-MOF** were synthesised in bulk and ground into a powder to characterise the phase-purity of the synthesised bulk material. The PXRD pattern was measured in a quartz capillary in DMF at 220 K to obtain low angle peaks and to avoid loss of crystallinity associated with solvent evaporation from the sample (Figure 3.7.3). The experimental pattern and a simulated PXRD pattern obtained from the single crystal X-ray diffraction data match closely confirming the phase-purity of the synthesised material. Three major signals are visible in the measured pattern between 2θ = 4 and 10 °. The most intense of these signals is found at an angle of 4.89 ° and is resolved in the calculated pattern as two close sharp peaks at 5.11 ° and 4.86 °. The latter signal is found at an angle of 7.06 ° and is resolved in the calculated pattern at 7.16 °. Additional signals can be found in the simulated pattern. The measured data was background corrected to remove bands typical to the quartz capillary.

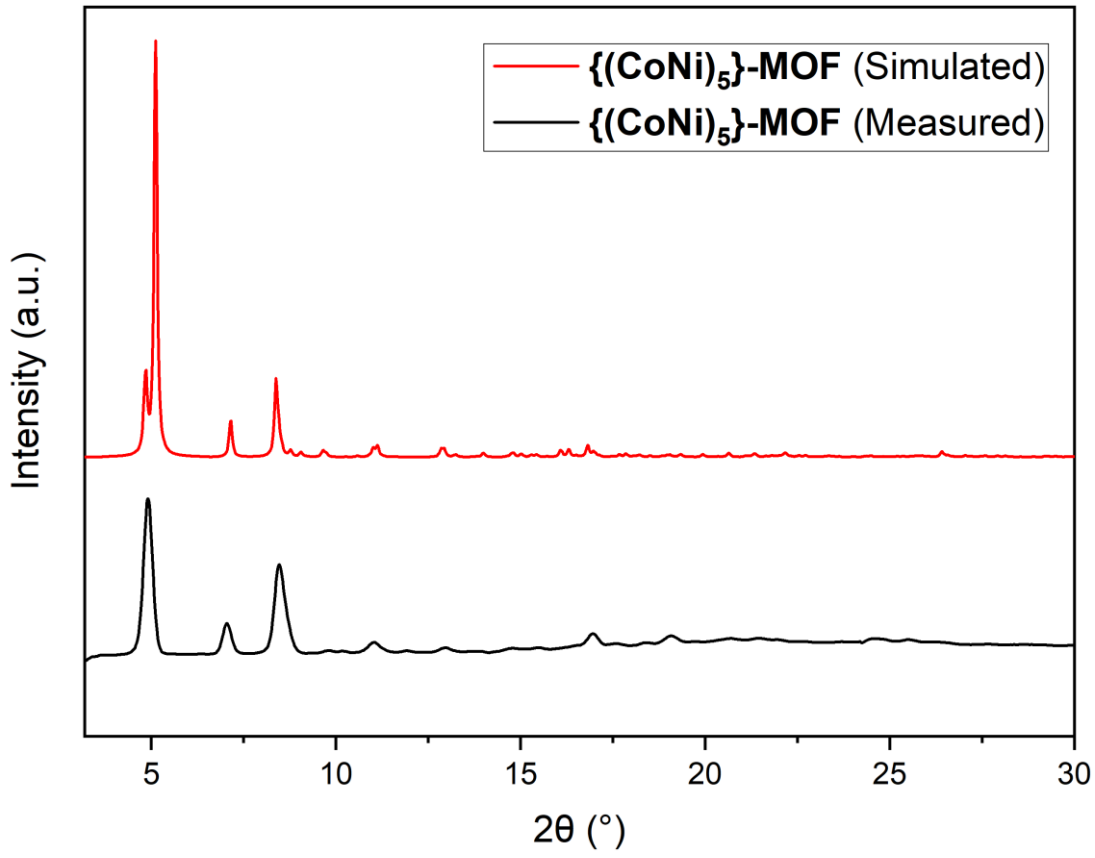

Figure 3.7.3: *PXRD patterns of* ***{(CoNi)$_5$}-MOF*** *measured crystals in capillary (black) and calculated from the single crystal data (red).*

3.7.2 Scanning electron microscopy and energy dispersive X-ray spectroscopy

Energy dispersive X-ray spectroscopy (EDX) was used to analyse the atomic ratio of cobalt to nickel within the MM-MOF. Crystals were soaked in DMF and water for 24 hours, changing the solution four times to ensure the removal of any salts disused within the pores before being dried under vacuum in a Schlenk line. Crystals of **{(CoNi)$_5$}-MOF** were placed onto a carbon tab, dried in air and analysed using EDX spectroscopy. The bulk sample was adhered to adhesive carbon tabs atop aluminium SEM stubs and loaded into a Zeiss ULTRA Plus scanning microscope with the 20mm² Oxford Inca EDX detector. An acceleration voltage of 20 kV under high current was applied to the sample. The raw data was processed using the Inca 7.2 software package. EDX analyses confirm the presence of both cobalt and nickel atoms within the sample. The relative metal percentages of Co and Ni were evaluated. The results point to a Co/Ni atomic ratio in **{(CoNi)$_5$}-MOF** of close to 2.5:1 (2.45:1) (Table 3.7.3).

***Table 3.7.3**: Quantitative results of EDX experiments for Co and Ni in **{(CoNi)$_5$}-MOF**.*

Element	Spectrum 1	Spectrum 2	Adverage (Ratio)
Co K*α*	69.85	67.84	68.85 (2.5)
Ni K*α*	30.15	32.16	31.16 (2)

3.7.3 Raman and FT-IR spectroscopy

Raman and FT-IR spectroscopic methods were used to characterise crystals of {**(CoNi)$_5$}-MOF**. The Raman spectra (Figure 3.7.4) of the ligand **H$_3$BETB** and {**(CoNi)$_5$}-MOF** closely match, confirming the presence of ligands within the MM-MOF. The signals at 993 cm^{-1} in the spectrum of {**(CoNi)$_5$}-MOF** and of **H$_3$BTEB** derive from CH rocking vibrations. Bands in the spectrum of {**(CoNi)$_5$}-MOF** at 1126, 1137 and 1171 cm^{-1} derive from C-C single bond vibrations. Two corresponding bands can be identified in the spectrum of **H$_3$BTEB** at 1122 and 1167 cm^{-1}. In the spectrum of {**(CoNi)$_5$}-MOF**, the most intense signals derive from the aromatic C=C bond vibrations and appear at 1586 and 1605 cm^{-1}. In the spectrum of **H$_3$BTEB**, related bands can be identified at 1582 and 1608 cm^{-1}, respectively. Another prominent signal is found at 2216 cm^{-1} and derives from the alkyne C≡C vibration in the spectrum of {**(CoNi)$_5$}-MOF**. The corresponding signal appears slightly shifted to 2217 cm^{-1} in the spectrum of **H$_3$BTEB**.[8]

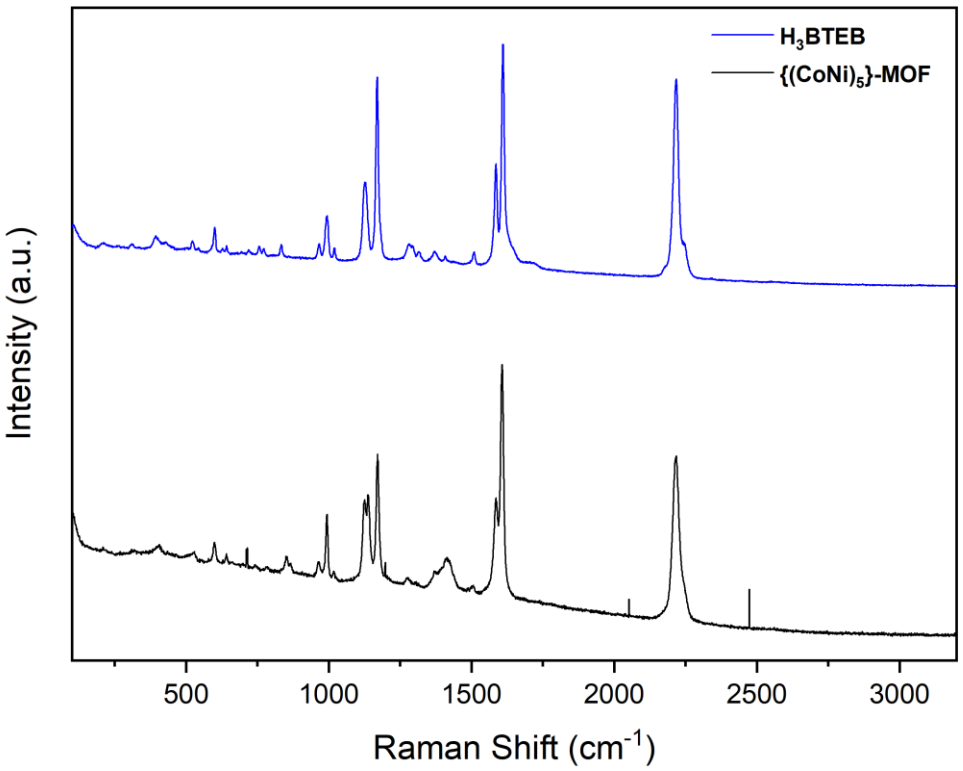

Figure 3.7.4**: Raman spectra of crystals* {**(CoNi)$_5$}-MOF** *(black) and* ***H$_3$BTEB *(blue).*

The FT-IR spectrum of {**(CoNi)$_5$}-MOF** reveals a strong band around 2342 cm^{-1} which is a typical signal for the atmospheric CO_2.[18] Bands at 1650 and 1582 cm^{-1} reveal C=C bond vibrations of aromatic moieties derived from the ligand, which are in agreement with the Raman spectrum.[19] Further, The stretches appearing at 1538 and 1380 cm^{-1} derive from the ν_{as}(COO) and ν_s(COO) stretches, respectively.[20] The Deacon-Phillips Δ value for {**(CoNi)$_5$}-MOF** is therefore 158 cm^{-1}, which is consistent with the bidentate bridging carboxylate binding mode observed in similar compounds.[21] The spectrum is in agreement with the FT-IR spectra obtained for {**(CoNi)$_5$}-MOF**/FTO and {**(CoNi)$_5$}-MOF**/CC (Section 3.10.7).

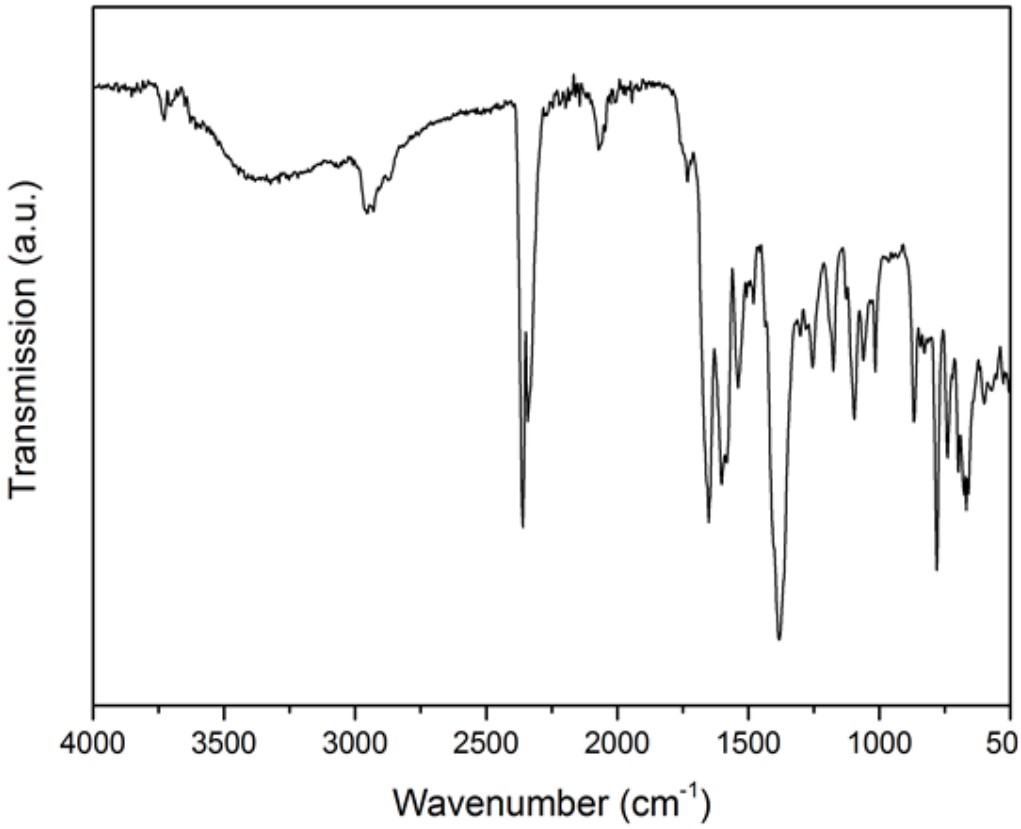

***Figure 3.7.5**: FT-IR spectra of crystals **{(CoNi)$_5$}-MOF**.*

3.7.4 Thermogravimetric analysis

TGA of **{(CoNi)$_5$}-MOF** was performed in an N_2 atmosphere at a heating rate of 4 °C per minute (Figure 3.7.6). It reveals an initial weight loss of *ca*. 10.7% between 25 and 90 °C which can be attributed to the loss of constitutional and loosely bound H_2O and DMF solvent molecules in the pores. Another thermogravimetric step of *ca*. 25.34% is observed between 90 to 380 °C which derives most likely from the removal of more strongly bound solvent molecules including coordination solvent molecules. There is a further weight loss of *ca*. 49.95% between 380 and 620 °C that results from the decomposition of the organic ligand and subsequently the MM-MOF.

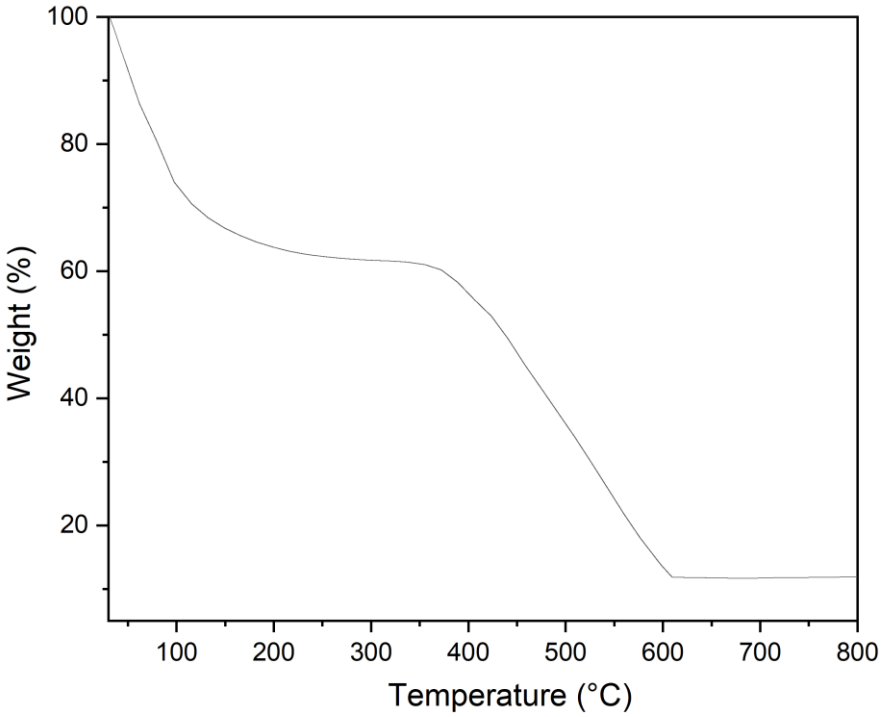

***Figure 3.7.6**: TGA of **{(CoNi)$_5$}-MOF** carried out in the N2 atmosphere at a heating rate of 5 °C per minute.*

3.7.5 Gas sorption experiments

It is expected that **{(CoNi)$_5$}-MOF** would give rise to a large surface area based on the gas uptake of **{Co$_5$}-MOF**. Crystals of **{(CoNi)$_5$}-MOF** were soaked in DMF for two days, replacing the solvent with new DMF daily to remove unreacted materials that could potentially be within the pores of **{(CoNi)$_5$}-MOF**. The sample was then pre-treated for activation by exchanging the DMF with n-hexane as lower surface tension solvents are favoured to avoid the loss of porosity of the structure during the activation step, with DMF and n-hexane having γ-vales of 36.8 and 19.0 mN/m, respectively. As DMF and n-hexane are immiscible, the activation of the MOF was achieved by replacing the DMF with ethanol and then DCM before finally exchanging DCM with n-hexane. Between each step, the crystals were left to soak in the solvent solution for two days, refreshing the solution with fresh solvent once per day. The crystals were transferred into a quartz measurement cell and the sample was activated by heating under vacuum at 150 °C for 24 hours.

3.7.5.1. N_2 adsorption studies

Volumetric N_2 gas sorption was recorded on an activated bulk sample of **{(CoNi)$_5$}-MOF** in a 0 – 1 bar pressure window using a Quantachrome Autosorb-iQ gas analyser. 23 mg of the as-prepared sample was transferred to a quartz measurement sample cell and

subjected to vacuum and activated at 200 °C for 10 hours. The accurate weight of the activated sample was recorded prior and after the analysis. The N_2 gas sorption data show a reversible type-I isotherm at 77 K with a steep uptake at low partial pressures as the micropores are occupied (Figure 3.7.7). A maximum uptake of 369 cm^3/g at 1 P/P_0 was recorded.

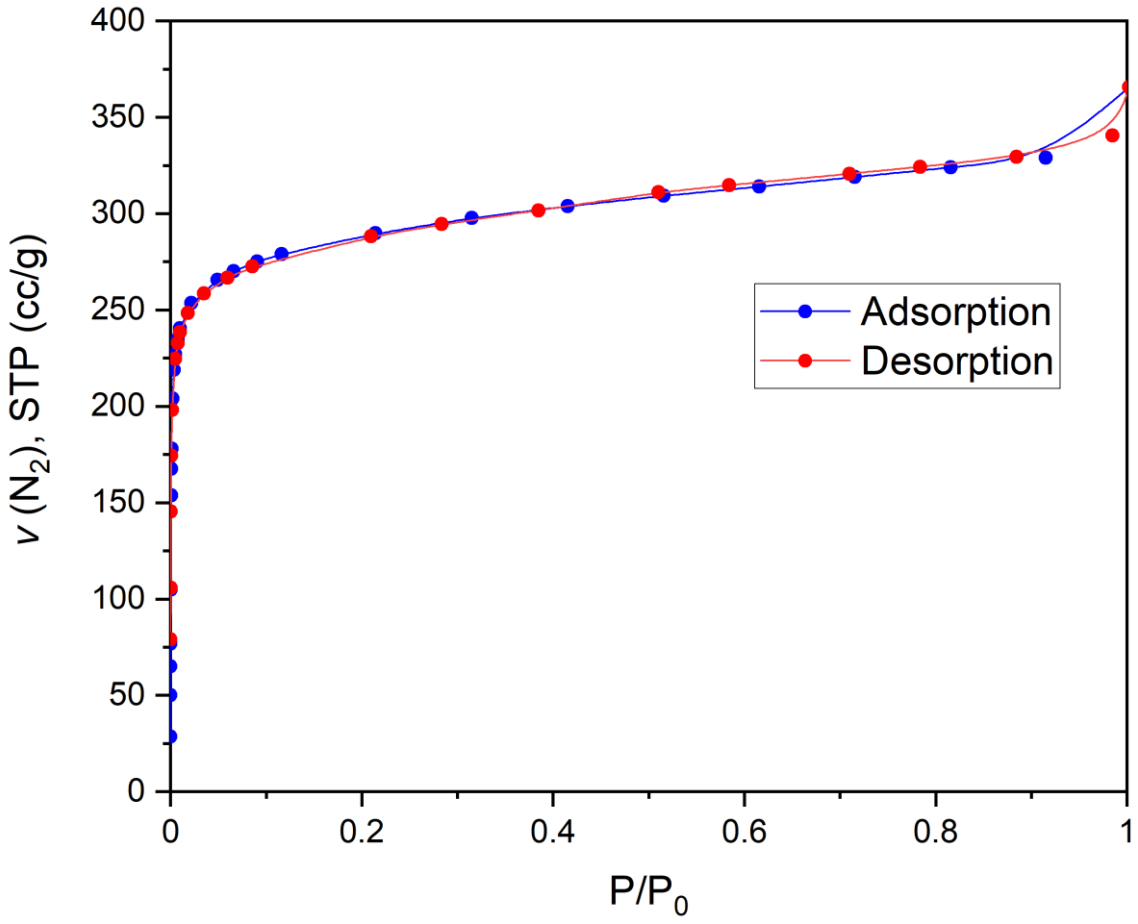

***Figure 3.7.7**: N_2 sorption isotherm of **{(CoNi)$_5$}-MOF** measured at 77K.*

3.7.5.2. BET surface area determination

The BET (Brunauer-Emmett-Teller) surface area of **{(CoNi)$_5$}-MOF** was determined from the linear region of the N_2 adsorption isotherm at 77 K before the micropore filling step. As mentioned in Chapter 2, The BET equation can be presented as the linear plot of $1/[W((P_0/P)-1)]$ against P/P_0 with **{(CoNi)$_5$}-MOF** as the adsorbent and N_2 as the adsorbate. The slope of the line, $s = (C - 1)(W_mC)$ and the intercept $i = 1/(W_mC)$ are used to compute the BET C-constant. The BET surface area, or the specific surface area (S_{BET}) was calculated from the total surface area at 77 K. A BET surface area of *ca.* 1115.0 m^2/g was found for **{(CoNi)$_5$}-MOF** (Figure 3.7.8). The points chosen for the BET plot were selected in accordance with Rouquerol *et al.*.[22]

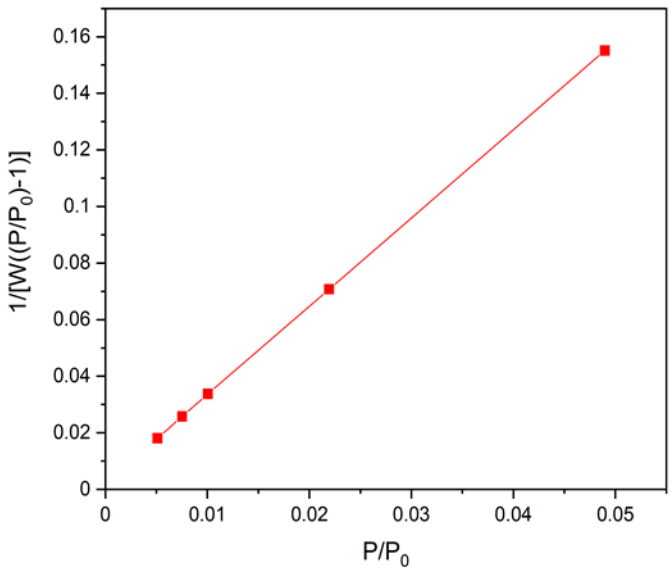

Slope	3.121
Intercept	2.28×10^{-3}
C constant	1367.274
r (correlation coefficient)	0.999999
BET surface area	1115.0 m^2/g

***Figure 3.7.8**: a) Plot of the linear region used to obtain the BET surface area of **{(CoNi)$_5$}-MOF**, b) Table of the values obtained from the BET plot.*

3.8 Electrochemical water oxidation studies of {(CoNi)$_5$}-MOF

The electrocatalytic activity of the heterometallic Co/Ni MM-MOF was first tested using the bulk synthesised crystals packed into a carbon paste electrode. The catalytic activity of **{Co$_5$}-MOF** has been previously reported using this method at pH 7.2. Identical conditions were chosen for **{(CoNi)$_5$}-MOF** so that the results could be directly compared to the monometallic counterpart. Crystals of the **{(CoNi)$_5$}-MOF** were dried in air and ground with commercial carbon paste (CP). A catalyst loading of 20 wt-% was prepared by mixing 20 mg of CP and 5 mg of catalyst in an agate mortar to obtain a catalyst loading of 20 wt-%. This blend was then packed inside the CP electrode pocket. A typical three-electrode setup was employed using the CP electrode as the working electrode, a Pt-mesh counter-electrode and an Ag/AgCl (3 M) reference electrode. LSV experiment were performed in aqueous solutions of KNO_3 (1M) and potassium phosphate (KPi) buffer (50mM, pH 7.2).

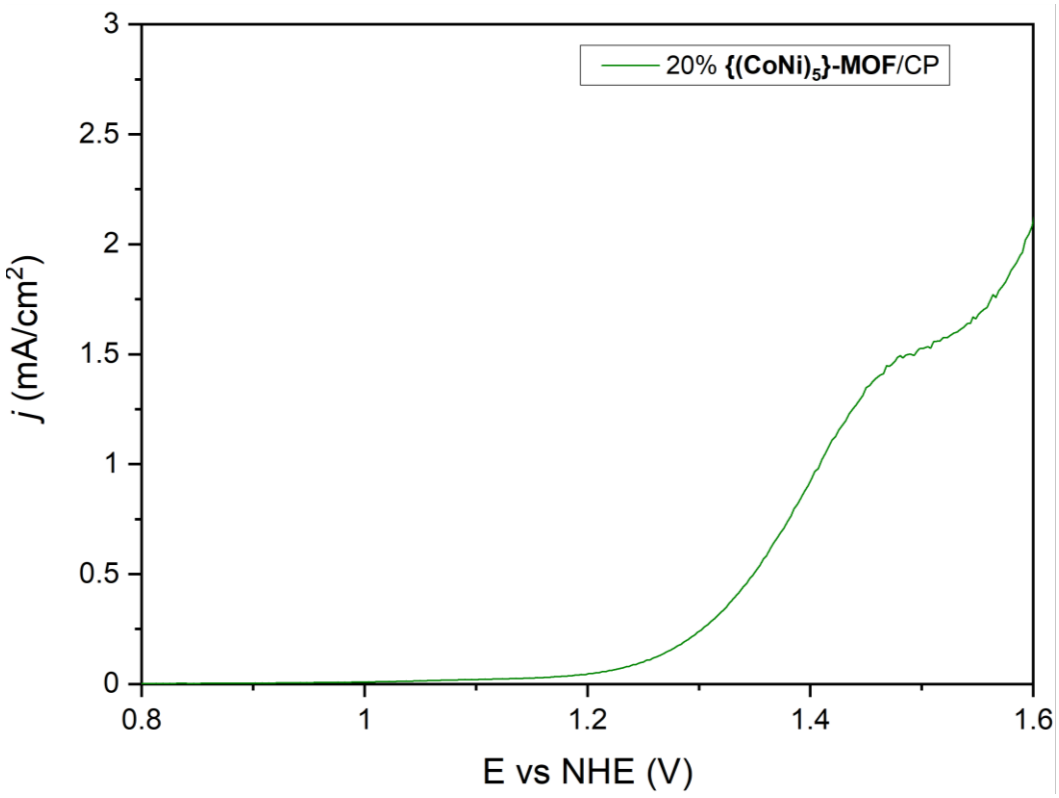

***Figure 3.8.1**: LSV for 20 wt-% catalyst loading of **{(CoNi)$_5$}-MOF**/CP at a rotation rate of 1000 rpm and a scan rate of 1 mV/sec.*

The LSV data reveals that the onset potential for OER is 1.26 and 1.20 V vs NHE for **{(CoNi)$_5$}-MOF** (Figure 3.8.1). This shows the effect of introducing a heteroatom to **{Co$_5$}-MOF** decreasing the activity when compared to its monometallic counterpart. The data gives an indication of the location of the Ni^{2+} ion on the cluster. As it affects the catalytic activity, it is likely that nickel centers occupy the positions coordinated by one of the solvent molecules. The onset potential was again estimated from the intersection point of the tangent lines of the Faradaic (current density > 0.2 mA/cm^2) and non-Faradaic (current density < 0.01 mA/cm^2) currents, giving overpotential values of 462 and 396 mV for **{(CoNi)$_5$}-MOF** (Figure 3.8.2).

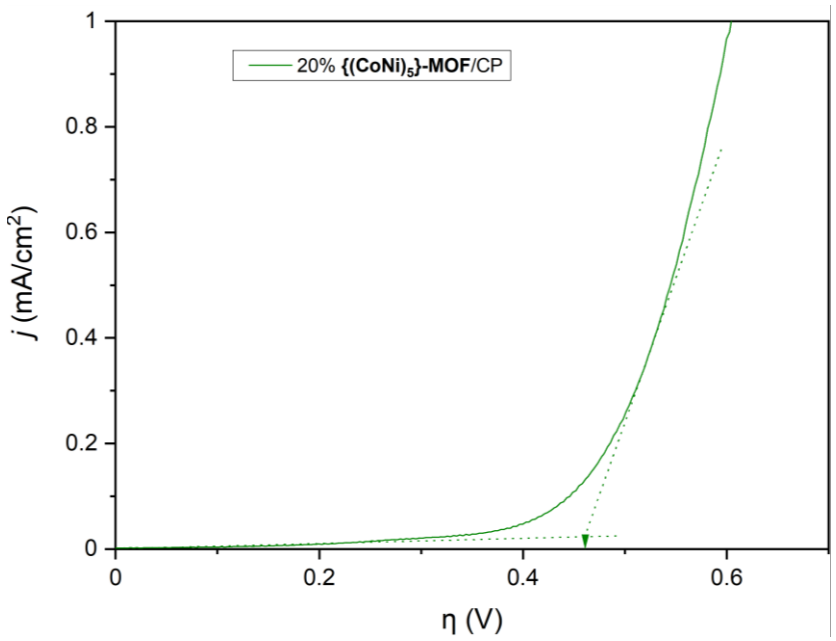

***Figure 3.8.2**: Estimation of the onset overpotential of 20 wt-% **{(CoNi)$_5$}-MOF**/CP from the LSV data between the Faradaic and non-Faradaic currents.*

The Tafel slope between the corresponding overpotential ranges of two catalyst blends was found to be 164 mV/dec for **{(CoNi)$_5$}-MOF**. This value is in range of similar experimental conditions reported in the literature for MOFs,[16] but lower than seen for **{Co$_5$}-MOF**/CP. The properties of the two {M$_5$} catalysts are compared in Table 3.8.1.

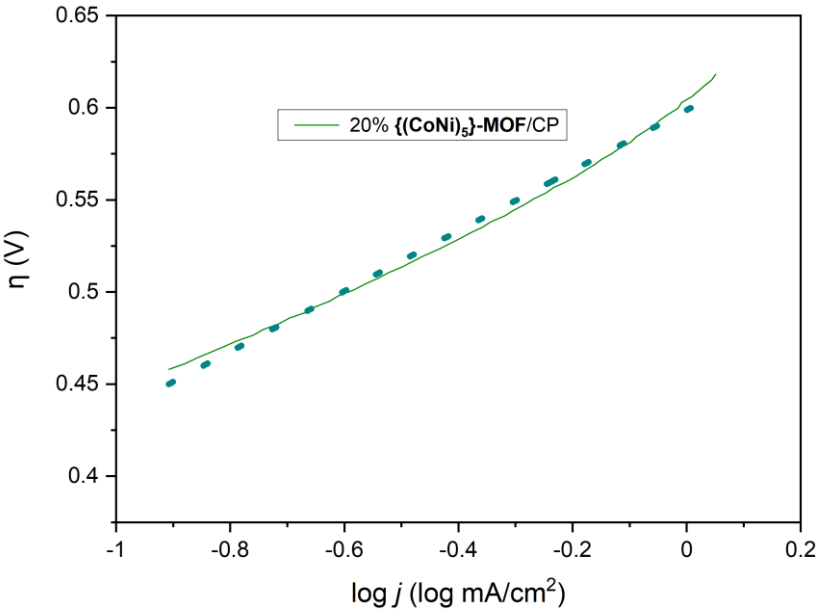

***Figure 3.8.3**: Tafel slope for **{(CoNi)$_5$}-MOF**/CP 20 wt-% catalyst loading.*

***Table 3.8.1**: Summary of overpotentials and Tafel slopes obtained for **{(CoNi)$_5$}-MOF** in comparison to **{Co$_5$}-MOF**.*

Compound	η_{Onset} (mV)	Tafel Slope (mV/dec)	η @ j = 1mA/cm^2 (mV)
{(CoNi)$_5$}-MOF	462	164	604
{Co$_5$}-MOF	396	113	492

3.9 Electrodeposition as synthetic approach

Thin-film MM-MOF materials are of interest in many fields, but not yet extensively studied for the OER.[23] Coating conductive materials with MOFs allows for the incorporation of the beneficial properties of MOFs into the electrocatalytic system. As detailed in Chapter 2, two different film-type electrode substrates were used, namely fluorine-doped tin oxide (FTO) and carbon cloth (CC) electrodes.

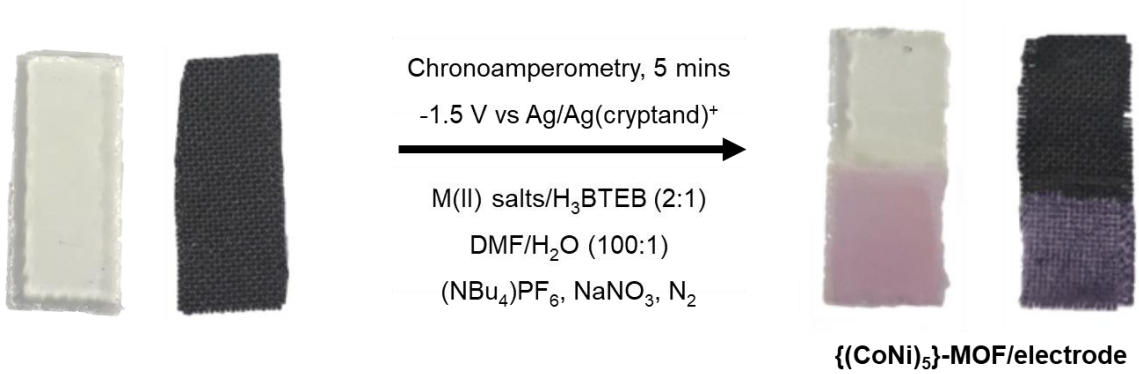

***Scheme 3.9.1**: Synthetic pathway for the deposition of Co (II) nitrate, Ni (II) nitrate and **H$_3$BTEB** onto the electrode surface to yield **{(CoNi)$_5$}-MOF**/electrode.*

The depositions of **{(CoNi)$_5$}-MOF**/FTO and **{(CoNi)$_5$}-MOF**/CC films were carried out using the same procedures as described in Section 2.5. On completion of chronoamperometry, light purple films were observed on the respective substrates. They were subsequently washed with DMF and MilliQ water and dried in air.

3.10 Physiochemical characterisation of thin-film {(CoNi)$_5$}-MOF

Before annealing, the synthesised thin-films were characterised to compare with **{Co$_5$}-MOF**/electrode films in terms of structural formation to confirm that the general electrodeposition synthesis resulted in the desired and expected framework structures. In addition to this, the MM-MOF is subjected to elemental analysis to confirm the uptake of nickel into the established thin-film MOF structure using direct synthesis approaches.

3.10.1 Scanning electron microscopy

The formation of **{(CoNi)$_5$}-MOF** on the FTO surface yielded evenly dispersed particles on the electrode surface identical to that of **{Co$_5$}-MOF**/FTO and **Co@C-500**/FTO discussed in detail in Chapter 2. In the case of the **{(CoNi)$_5$}-MOF**/CC film, as for the FTO substrate, a film was visible. However in contrast to the FTO electrodes, the coating on carbon cloth did not form a uniform layer, of which the thickness could be established by cross-sectional SEM imaging. An overview image shows the boundary between the MOF coating and the bare carbon cloth (Figure 3.10.1). From this it appears that the particles penetrate into the surface of the CC electrode as opposed to forming a layer as seen for the coating of FTO electrodes.

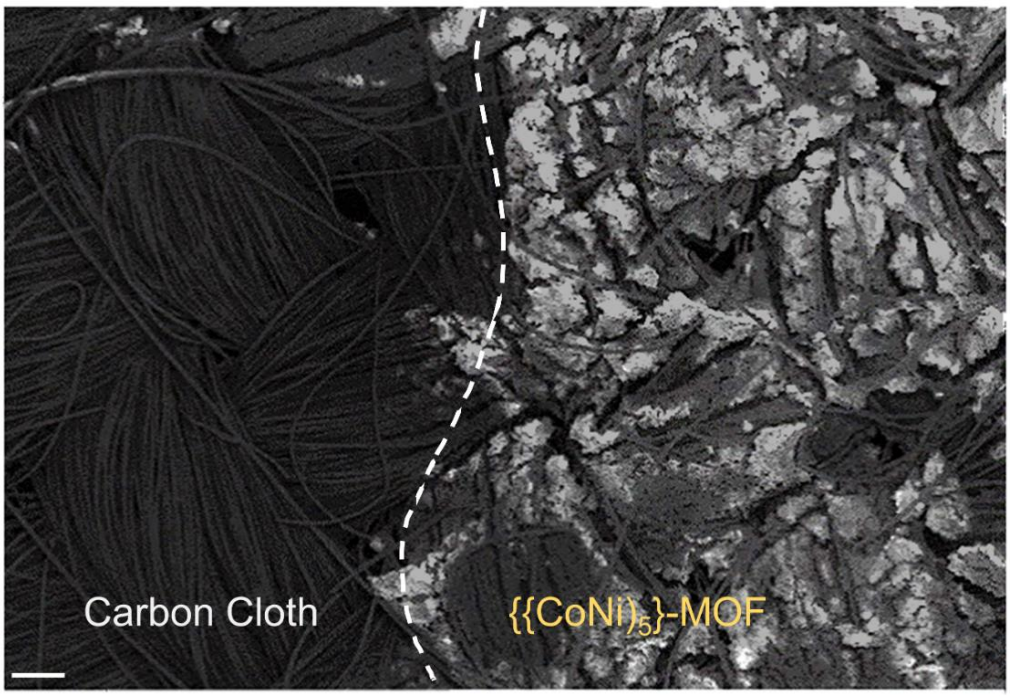

***Figure 3.10.1**: Overview SEM image of **{(CoNi)$_5$}-MOF**/CC at the film boundary after electrodeposition was carried out at -1.5 V vs. Ag/Ag(cryptand)$^+$ for a duration 5 minutes. Scale bar: 100 µm.*

To further investigate the method and structure of the formation of **{(CoNi)$_5$}-MOF** on carbon cloth, the surface of the cloth was sputter coated using a non-conductive material to reduce sample charging and improve edge resolution. The sample was placed into a Gatan Precision Etching and Coating System (PECS) with an Au/Pd sputter coater target disc. The chamber was flushed with Ar gas three times, evacuating the system before each addition of Ar gas. The sample was sputtered for 15 seconds with an ion energy of 2 KeV in order to coat the sample with a uniform layer of Au/Pd. This allowed for high-resolution SEM imaging with depth definition of **{(CoNi)$_5$}-MOF** on the cloth surface.

With traditional electrodeposition on carbon cloth substrates, the surface coverage can be controlled by the applied potential and deposition time.[24] With deposition for extended times on the FTO substrate, the thick films formed at deposition times in excess of 10 mins were prone to detaching from the FTO electrode during OER experiments when high potential was applied. However, this occurrence was not observed while using carbon cloth as a substrate. The overview image highlights that the carbon cloth has potential to be fully coated in **{(CoNi)$_5$}-MOF** by increasing the deposition time (Figure 3.10.2, a)). Imaging of individual strands highlights that individual particles coat the strands of the cloth but also act as nucleation sites for aggregate formation (Figure 3.10.2, b)).

A difficulty of SEM imaging is that it excels with respect to the analysis of the surface composition but becomes exceedingly more difficult with film thickness. This problem is somewhat alleviated due to the intrinsic void spaces between the individual carbon fibres. Images can be obtained of carbon strands below the surface of the cloth, and particles of **{(CoNi)$_5$}-MOF** can be identified adhered to these sub-surface strands (Figure 3.10.2, c)). From this, it is evident that the MOF can diffuse into the pores within the cloth substrate, resulting in a pseudo-2D electrode with high surface area for catalytic applications. The individual particles are in the range of 15 – 25 nm (Figure 3.10.2, d)).

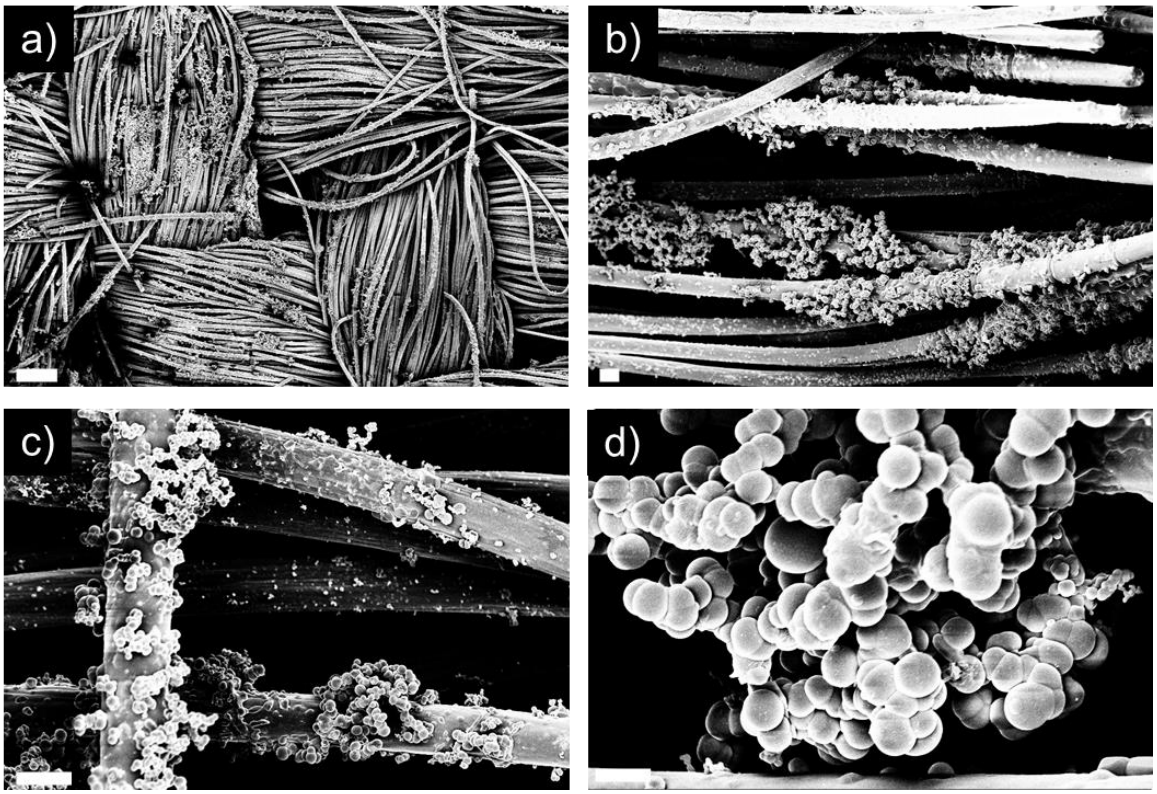

***Figure 3.10.2**: SEM images of electrodeposited **{(CoNi)$_5$}-MOF** on a carbon cloth substrate after sputtering coating the surface with Au/Pd. Scale bars: **a)** 100 μm, **b)** 10 μm, **c)** 10 μm, and **d)** 3 μm.*

The woven nature of the carbon cloth provides a porous framework that facilitates a high number of nucleation sites. The experimental approach in combination with the porous nature of the substrate allows for the production of a microporous compound deposited within a macroporous substrate. The individual strands of the cloth act as anchors to which the MM-MOF adheres (Figure 3.10.3). This deposition and formation method, results in an electrode with extremely high intrinsic surface area. The method provides a facile synthetic approach for electrocatalytic applications allowing the preparation of porous electrodes with a high number of active sites per volume. In addition to coating individual strands (Figure 3.10.3, b)), the particles form clusters extending into the spaces between individual carbon strands (Figure 3.10.3, c)). By increasing the deposition time of **{(CoNi)$_5$}-MOF** onto the carbon cloth electrode, it is surmised that the strands of the cloth could be uniformly coated.

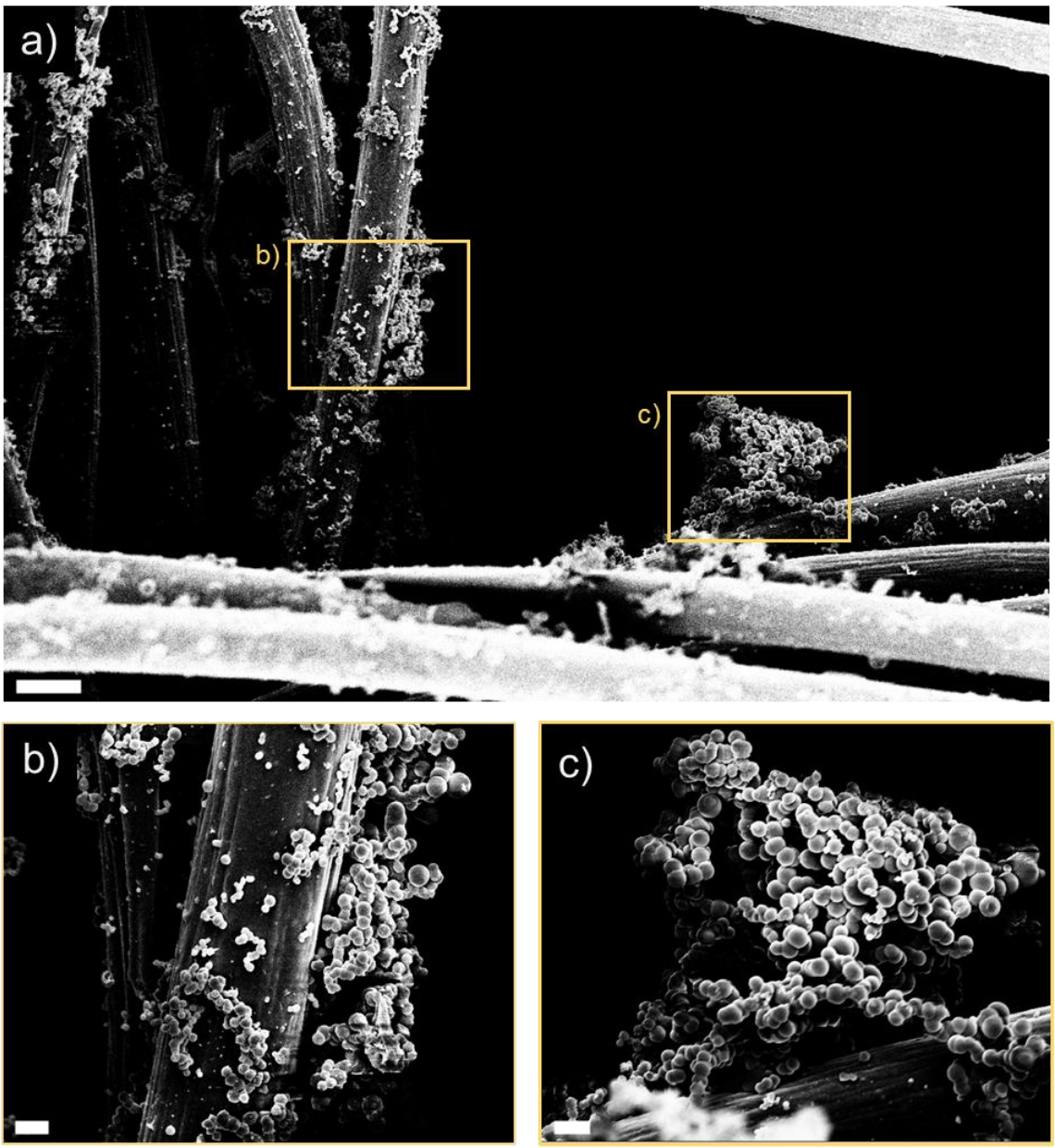

***Figure 3.10.3**: a) Overview SEM image of electrodeposited **{(CoNi)$_5$}-MOF** on a carbon cloth substrate after sputtering coating the surface with Au/Pd. **b)** SEM image focusing on an individual carbon strand, demonstrating how the MOF adheres to individual fibres of the carbon cloth. **c)** The formation of aggregates extending into the void space between carbon strands. Scale bars: a) 10 µm, b) 2 µm, c) 2 µm.*

3.10.2 Energy dispersive X-ray spectroscopy

EDX was used to analyse the ratio of Co/Ni on the surface of the thin films. This was crucial to confirm the incorporation of Ni(II) into the MOF. EDX mapping was also carried out on **{(CoNi)$_5$}-MOF**/FTO to confirm that cobalt and nickel atoms are equally distributed over the surface as opposed to the co-formation of two monometallic MOF structures.

Before EDX analysis, **{(CoNi)$_5$}-MOF**/FTO and **{(CoNi)$_5$}-MOF**/CC were soaked in MilliQ water for 24 hours, changing the solution twice to ensure the removal of any salts disused within the pores from the electrodeposition step. For detailed quantitative EDX analysis, the sample electrodes were adhered to adhesive carbon tabs atop aluminium SEM stubs and loaded into a Zeiss ULTRA Plus scanning microscope equipped with a 20 mm² Oxford Inca EDX detector. An acceleration voltage of 20 kV under high current was applied. The raw data was processed using the Inca 7.2 software package. The SEM overview area highlights the surface constitution of **{(CoNi)$_5$}-MOF**/FTO and **{(CoNi)$_5$}-MOF**/CC in addition to surface mapping.

In the case of **{(CoNi)$_5$}-MOF** on both FTO and CC electrodes, the metallic Co/Ni ratio was preserved with respect to the ratio of metal salts used in the direct synthesis step. For both, data collected shows a ratio of *approx*. 2:1 for Co/Ni when taking a spectrum area including (Figure 3.10.4). From this, it may be possible to control the metallic ratio by altering the amount of Co(II) nitrate and Ni(II) nitrate used in the deposition solution.

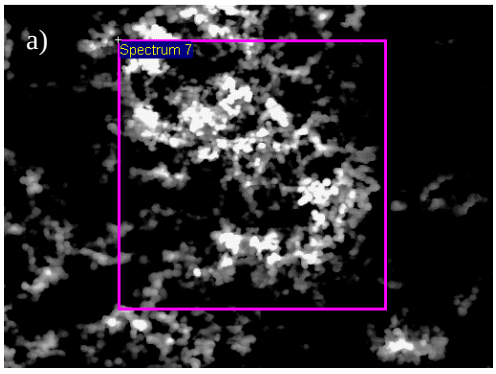

Element	*Weight %*	*Atomic (%)*
Co Kα	61.40	61.48
Ni Kα	38.60	38.51

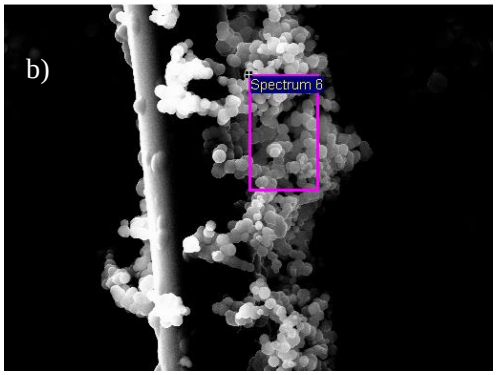

Element	Weight (%)	Atomic (%)
Co Kα	63.26	62.90
Ni Kα	36.73	37.09

***Figure 3.10.4**: SEM images of the polycrystalline Co/Ni film produced by electrodeposition on FTO (a) and CC (b) as described in section 2.7. The corresponding tables shows the results from the EDX analysis.*

To confirm that a MM-MOF could be synthesised through direct deposition, EDX mapping was employed. A cluster of particles with two distinct sizes was located on the film

surface to compare the homogeneous composition of each particle and identifying any differences between particles of different sizes. The results of the elemental mapping prove that both Co and Ni atoms are dispersed evenly within individual particles (Figure 3.10.5). In addition to this the particles appear to maintain the same 2:1 Co:Ni atom ratio.

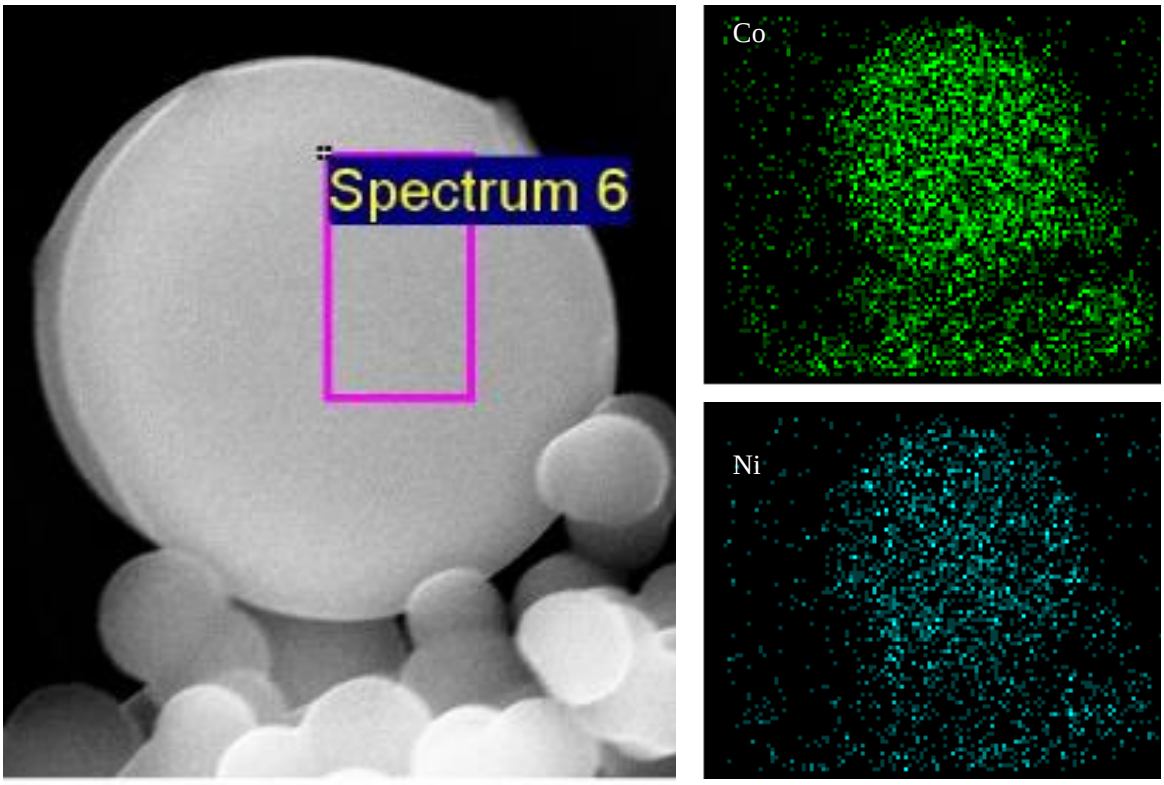

***Figure 3.10.5**: EDX mapping of the **{(NiCo)$_5$}-MOF**/CC electrode. The mapping demonstrates the material has Co and Ni evenly dispersed throughout. Colour code: Co Kα, green; Ni Kα, cyan.*

3.10.3 Powder X-ray diffraction

The powder X-ray diffraction patterns of the films were recoded as detailed before. The **{Co$_5$}-MOF**/FTO film was analysed by removing the deposited material from the FTO slide and grinding it to a fine powder, while the **{(NiCo)$_5$}-MOF**/FTO film was measured *in situ* on the FTO slide. The measured powder pattern from the solvothermal synthesised **{(NiCo)$_5$}**-MOF was used for comparison. The comparison of the patterns demonstrates the similarities between each of the powder patterns, however, it is notable that the pattern of the **{(NiCo)$_5$}**-film has a very broad first signal at approximately $2\theta = 5°$. It is likely that this is caused by a degree of amorphousness of the material deposited on the FTO slide. In addition, the particle size adds to the broadness of the signals.

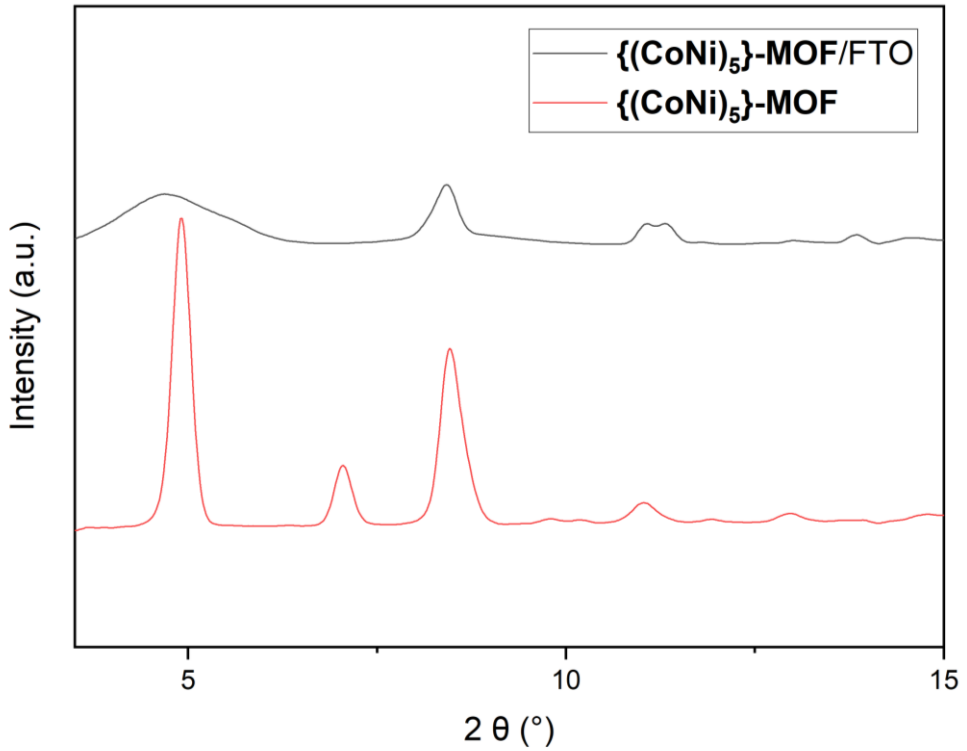

***Figure 3.10.6**: X-ray diffraction measurement of **{(NiCo)$_5$}-MOF**/FTO (black) and crystalline **{(NiCo)$_5$}-MOF** (red).*

3.10.4 Raman and FT-IR spectroscopy

Raman spectroscopy was used to compare the synthesised thin-films to the bulk crystalline sample of **{(NiCo)$_5$}-MOF**. The Raman spectra of **{(NiCo)$_5$}-MOF** crystals and the thin-films closely match confirming the presence of the ligand on the electrode surfaces. The signals at 993 cm^{-1} in the spectra derive from CH_2 rocking vibrations. Bands in the spectra at 1127, 1137 and 1171 cm^{-1} derive from C-C vibrations. A signal is found at 2216 cm^{-1} and derives from the alkyne C≡C vibration in the spectra of **{(NiCo)$_5$}-MOF**/electrode and **{(NiCo)$_5$}-MOF** crystals.

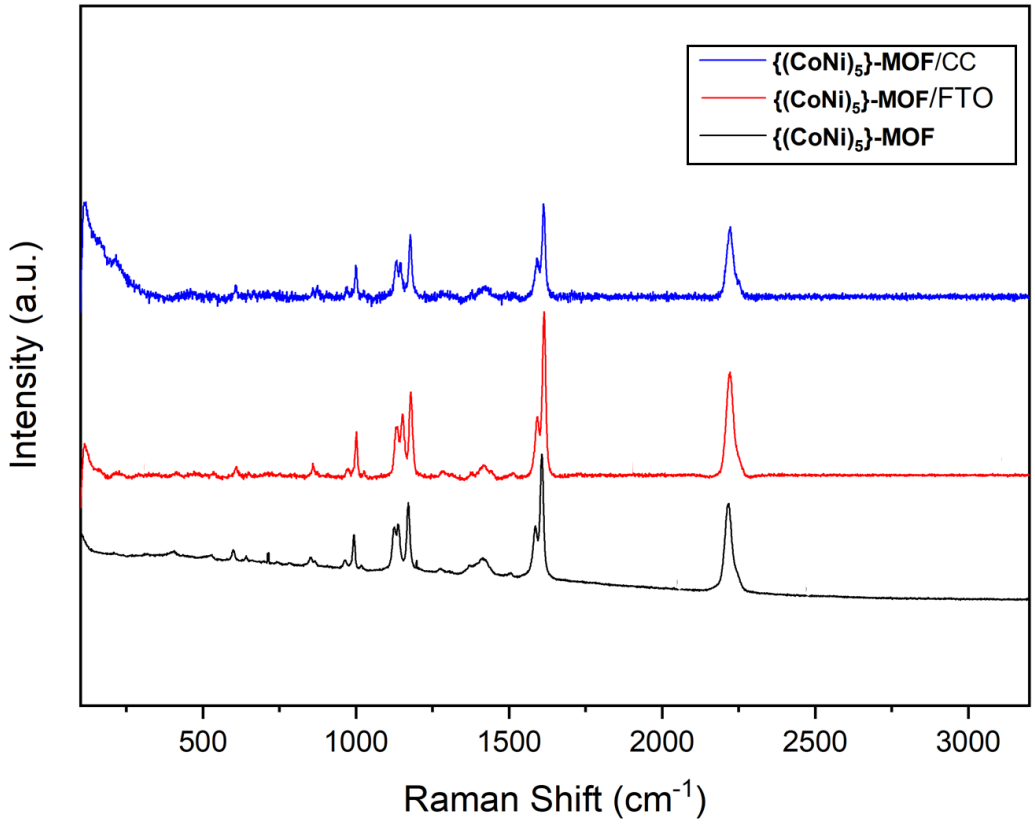

***Figure 3.10.7**: Raman spectra of **{(NiCo)$_5$}-MOF**/CC (blue), **{(NiCo)$_5$}-MOF**/FTO (red) and crystalline **{(NiCo)$_5$}-MOF** (black).*

FT-IR spectroscopic methods were employed to analyse **{(NiCo)$_5$}-MOF**/electrode in comparison to the isostructural **{Co$_5$}-MOF**/electrode. Resonances corresponding to **H$_3$BETB**, previously assigned for bulk **{(NiCo)$_5$}-MOF** crystals were previously assigned in detail in Section 3.7.3 and match closely to the electrodeposited samples, with bands appearing at 1537 and 1385 cm^{-1} assigned to the ν_{as}(COO) and ν_s(COO), respectively, yielding a Deacon-Phillips Δ value of 152 cm^{-1}. In addition to this, the FT-IR spectra for **{(NiCo)$_5$}-MOF** synthesised on FTO and carbon cloth show a high degree of similarities in the fingerprint region to electrodeposited **{Co$_5$}-MOF** (Figure 3.10.8).

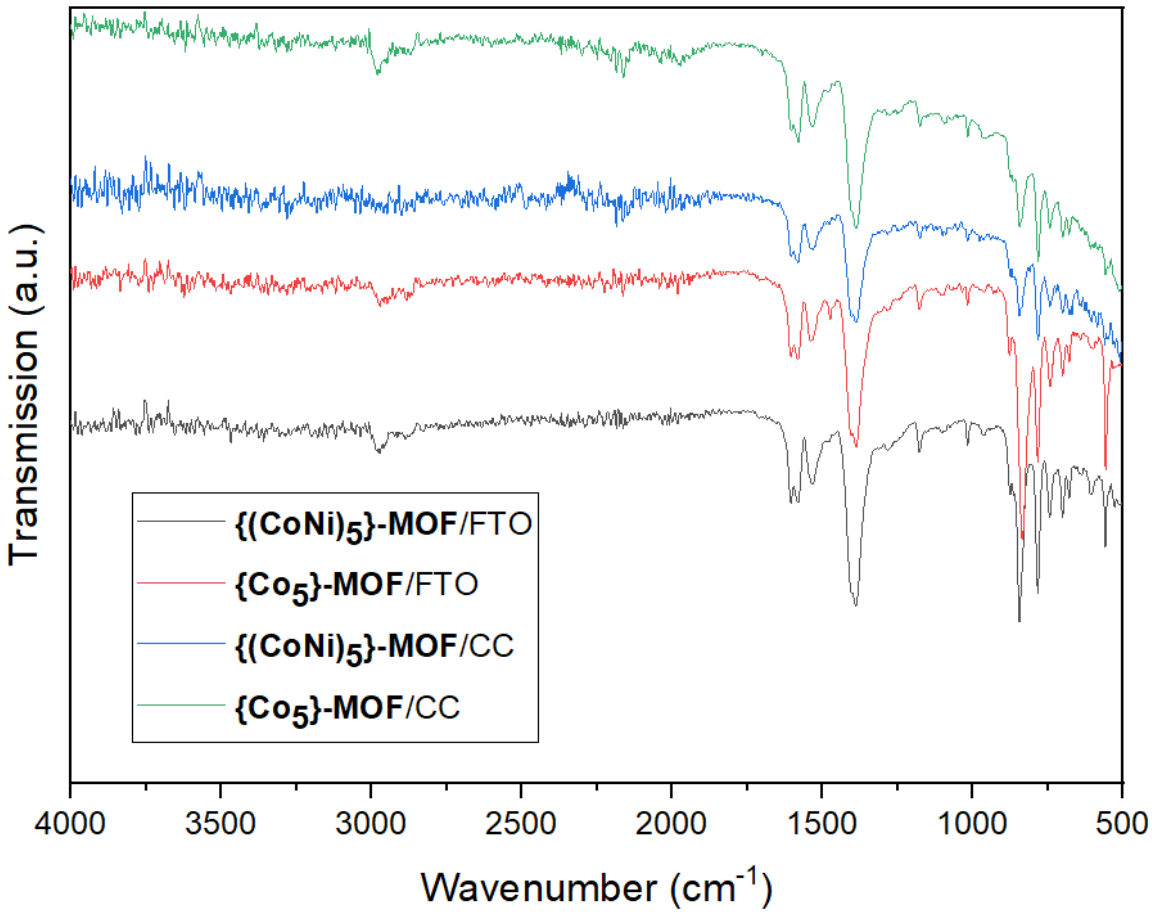

***Figure 3.10.8**: FT-IR spectra of **{(NiCo)$_5$}-MOF**/FTO (black), **{Co$_5$}-MOF**/FTO (red), **{(NiCo)$_5$}-MOF**/CC (blue) and **{Co$_5$}-MOF**/CC (green).*

3.11 Heat-Treatment

In addition to **{(CoNi)$_5$}-MOF** deposited on both FTO and CC, samples of each type of electrode were annealed. This process, described in detail in Section 2.5. was carried out under a N_2 atmosphere at 500 °C for 4 hours to obtain **CoNi@C-500**/FTO and **CoNi@C-500**/CC. After the heat-treatment step, the resulting opaque black films were washed with DMF. The electrodes were rinsed with MilliQ water and dried in air.

3.11.1 Transmission electron microscopy and scanning-transmission electron microscopy

The structural characteristics of **CoNi@C-500** were further investigated by TEM and STEM to observe the microstructure of the heat-treated material. The top layers of the thin film were removed from the FTO electrode using a scalpel before the material was sonicated

in isopropanol. Dispersed particles were drop cast onto a lacey carbon support film on a copper TEM grid. The grid was loaded into a FEI Titan 80 – 300kV FEG S/TEM for analysis. Images were obtained under an operating acceleration voltage of 300 kV with an informational resolution limit of 0.1 nm and processed using the Image J 2.0 software package.

As seen with **Co@C-500**, TEM imaging highlights the core@shell structure of **CoNi@C-500** with the interior structure composed of spherical Co/Ni nanoparticles imbedded within a carbon shell material. Using HR-TEM to investigate the lattice fringes in the area, the core material is indicative to that of $NiCo_2O_2$ which is in-line with the elemental composition of **{(CoNi)$_5$}-MOF** before heat-treatment having a 2:1 Co/Ni elemental composition. By observing the selected area of individual hierarchical nanostructure, structural information on the shell materials can be obtained by examining lattice spacing, determined using an average of lattice spacing distances calculated using Image J. Although it was difficult to locate clear areas of crystallinity within the carbon shell, it is noted that the lattice fringes with a spacing of *ca*. 0.21 and 0.25 nm, indexed to the (200) and (311) planes, respectively, of cubic $NiCo_2O_4$ (Figure 3.11.1). This is in agreement with spinel Co/Ni oxides synthesised through a variety of methods such as microwave assisted deposition[25] and most notably, Co/Ni core@shell arrays produced *via* solution deposition.[26]

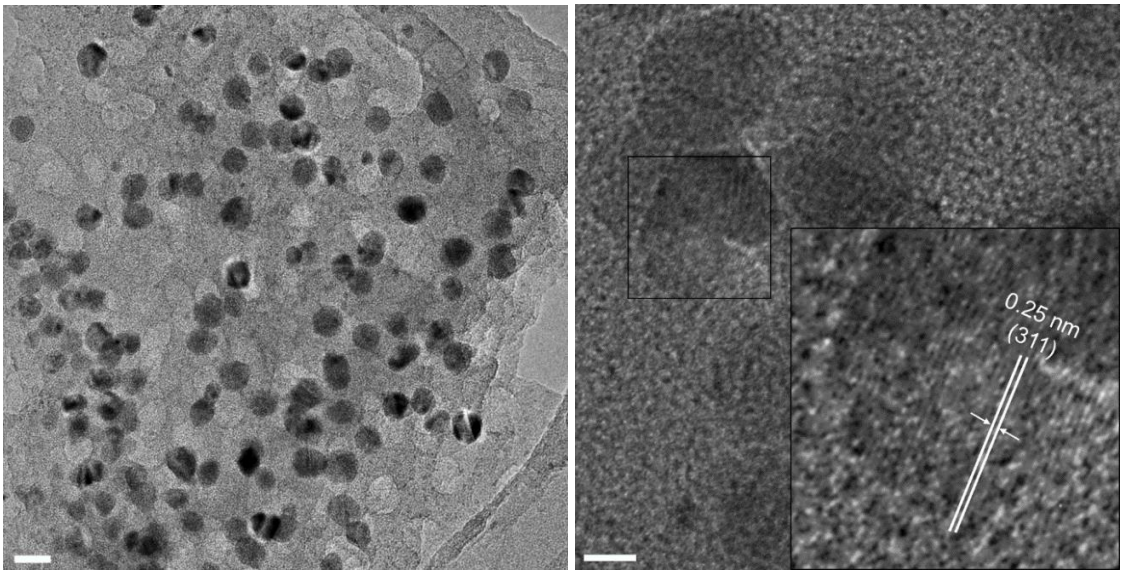

***Figure 3.11.1**: TEM image of **CoNi@C-500** highlighting the dispersed oxide cores within carbon matrices (left) Scale bar: 20 nm. Lattice spacing corresponding to that of the (311) edge (right). Scale bar: 5 nm.*

A small (*ca.* 6 nm) singular oxide particle could be isolated, protruding from the matrix on the edge of the carbon capsule (Figure 3.11.2). In addition to being able to easily determine the lattice spacing, this particle is of particular interest as it conforms the notion that during the annealing step, the amorphous carbon produced from the organic ligands of **{(CoNi)$_5$}-MOF** forms around the Co/Ni oxide centers, shielding the potential catalytic centers from the external environment and preventing Co(II)/Ni(II) leaching into the solution during catalytic experiments. The presence of a clear, porous carbon coating on this particle, attaching it to the internal cluster, confirms this hypothesis.

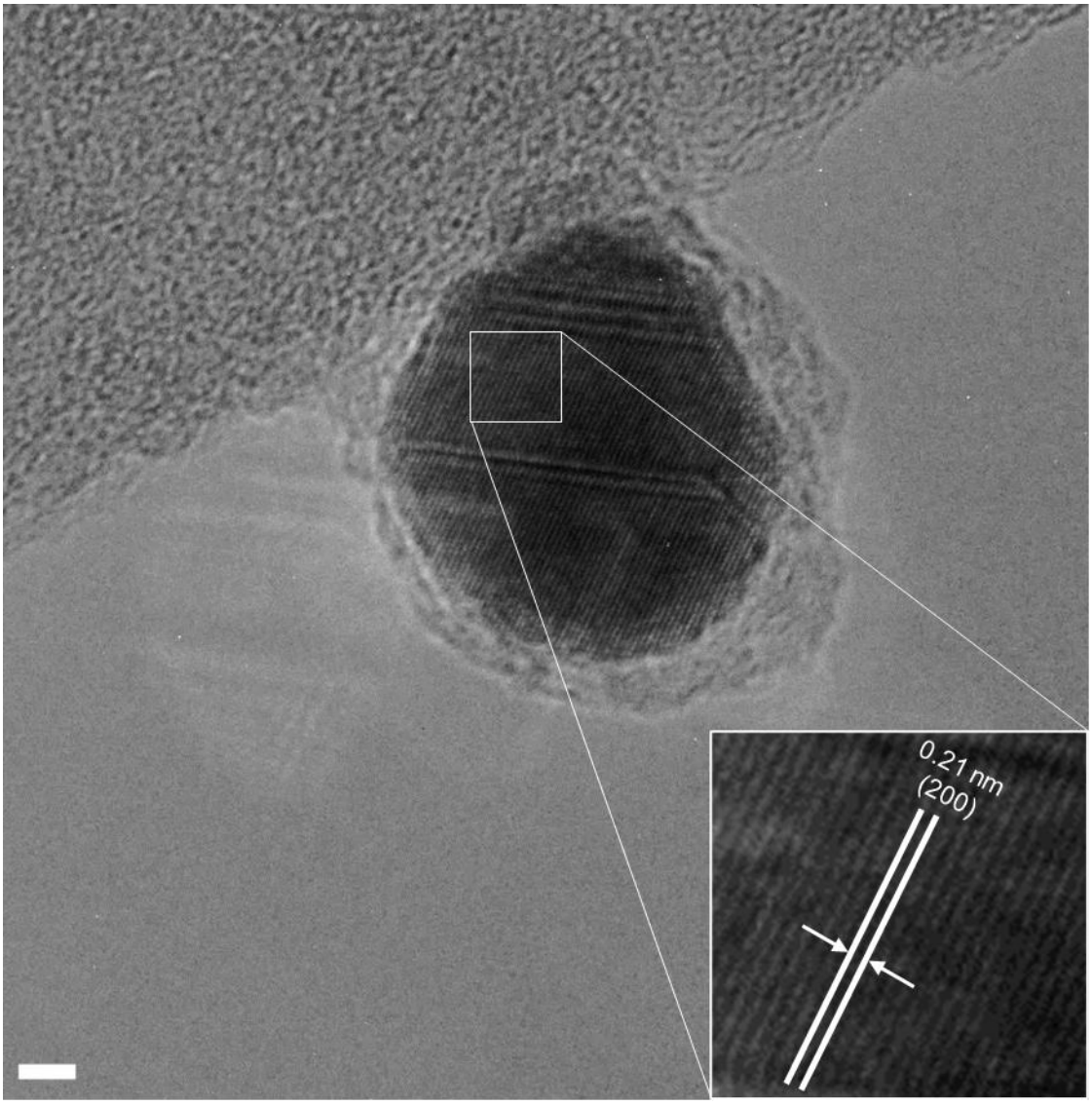

Figure 3.11.2*: TEM image highlighting a single Co/Ni particle and carbon shell, confirming the core@shell structure of the material. Lattice fringe showing the (200) plane (insert). Scale bar: 2 nm.*

STEM provides a facile analytical method to differentiate the oxide nanoparticles within the assembly of the material when using dark field imaging. Atomic-resolution HAADF imaging distinguishes bright atomic particles pertaining to the Ni and Co atoms. Conversely, the contrast from carbon-material is weaker in the HAADF image due to the relatively lower zeta potential. The $NiCo_2O_4$ particle sizes are in the range of 4 – 9 nm, similar to those of **Co@C-500** (Figure 3.11.3). The relative uniform distribution of the $NiCo_2O_4$ particle means that a high specific surface area can be maintained, creating a sufficiently active interface between the metal oxide and carbon support, which may translate to catalytic activity.[27]

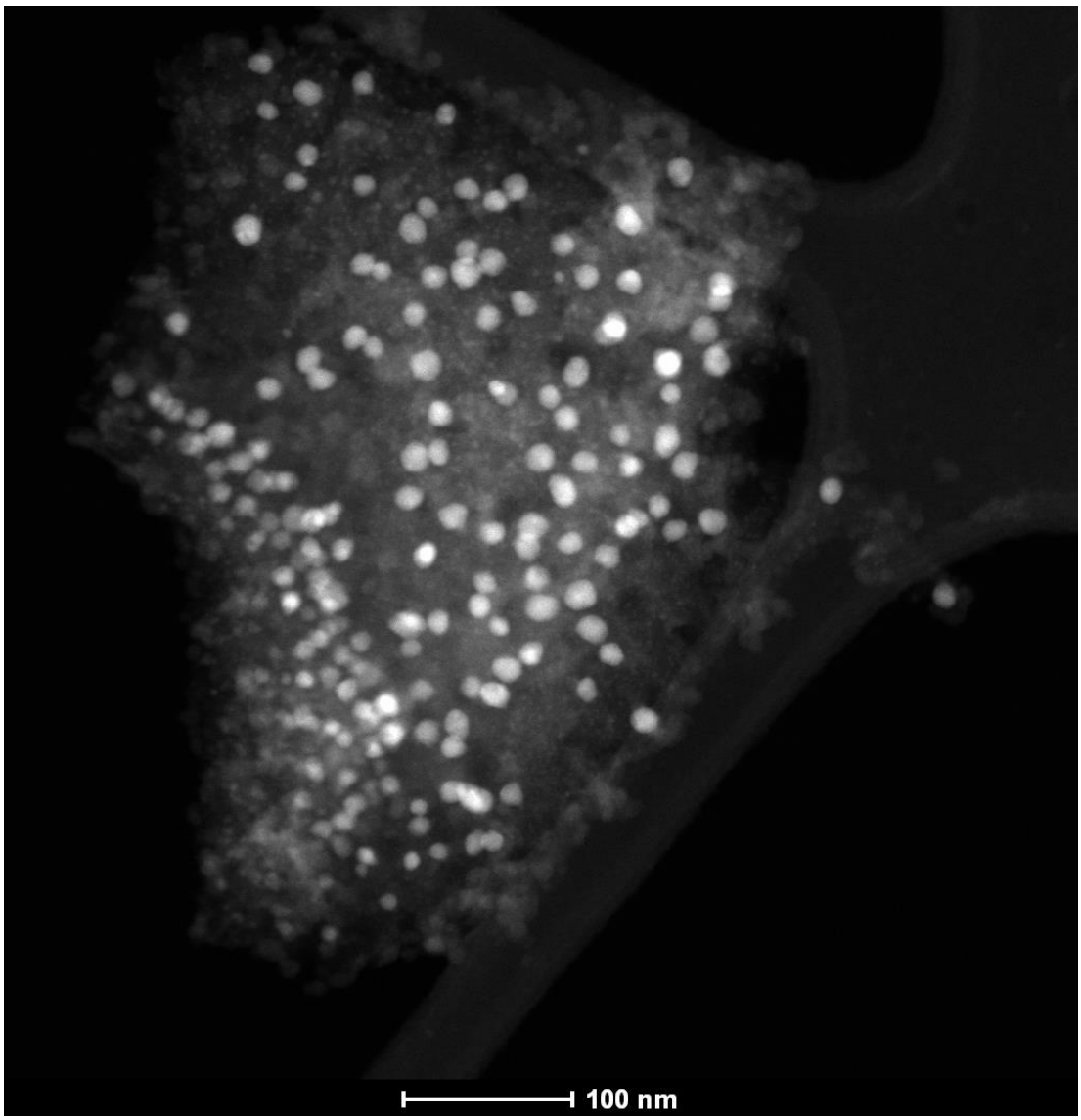

***Figure 3.11.3**: HAADF-STEM overview of a **CoNi@C-500** aggregate with lacy carbon from the TEM grid visible. This area was suitable for EDX analysis as both metallic nodes and porous carbon can be identified.*

3.11.2 Energy dispersive X-ray spectroscopy

EDX analyses was also performed under HAADF-STEM conditions to demonstrate the core@shell structure of the material and allowing distinction between the carbon matrix and metallic core. The exact atomic ratios were not able to be deduced due to the limitations of the EDAX EDX detector. Firstly, a number of oxide nanoparticles were identified and analysed. The presence of both cobalt and nickel atoms was confirmed by the resulting spectra (Figure 3.11.4).

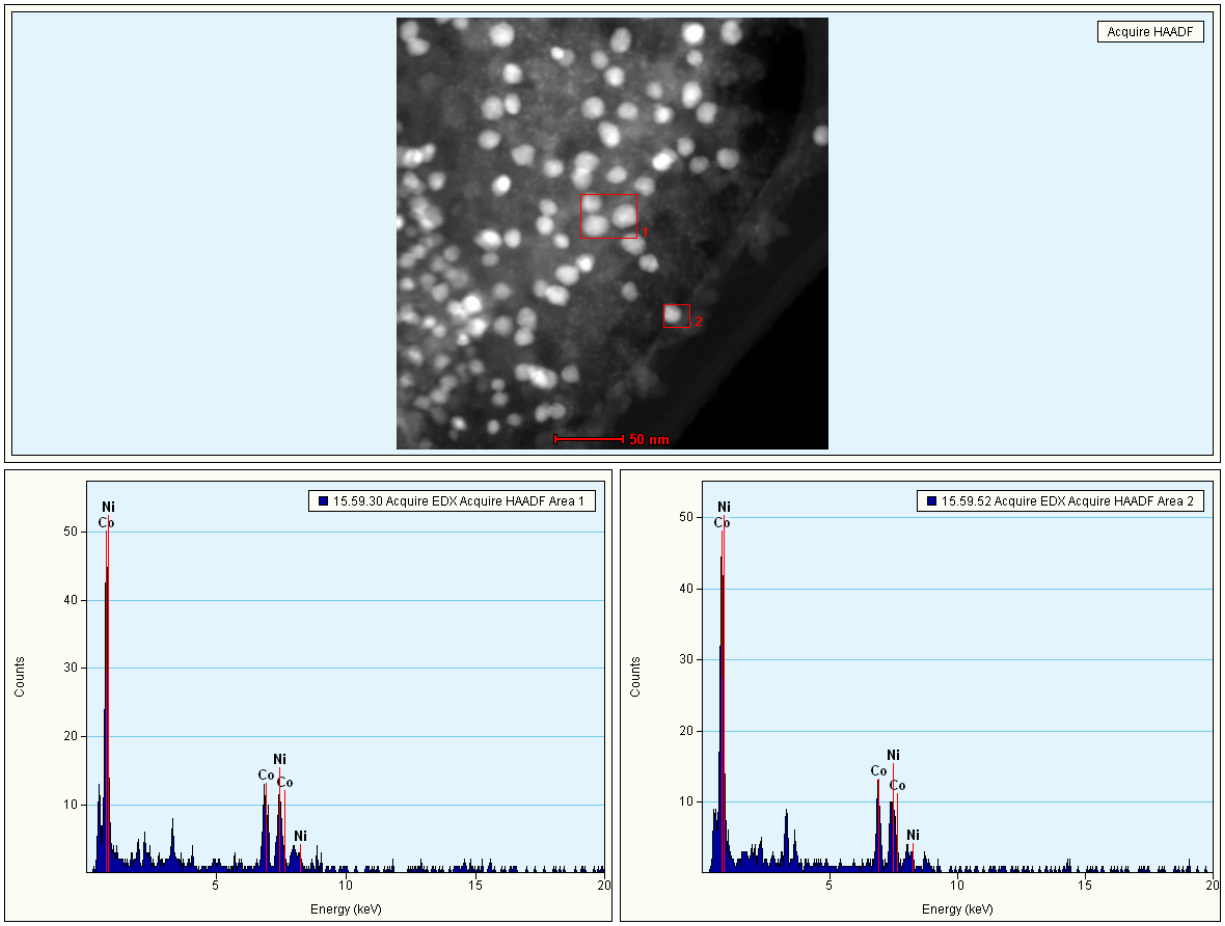

***Figure 3.11.4**: EDX analysis of areas highlighted using dark field imaging, showing the presence of cobalt and nickel atoms.*

The areas of the oxide were compared to the areas identified as containing porous carbon. This is useful in determining if all of the oxide cores are contained in the nanoparticle structures or if small components are dispersed within the matrix. This is not desirable as smaller structures could be physically removed from the matrix under electrocatalytic conditions. Two areas were selected for EDX analysis based on their Z-contrast (Figure 3.11.5). The spectra reveal a significant lack of Co- and Ni-derived signals within spectrum

2 furthering the notion that the $NiCo_2O_4$ nanoparticles are discreet entities within the quoted size range. In addition, it can be assumed that no other oxides (i.e. NiO) formed during the annealing process. Cu Kα and K Kα-derived signals can be identified in the spectra. These derive from the copper sample grid and potassium phosphate buffer that was used during the electrochemical synthesis of the MOFs, respectively.

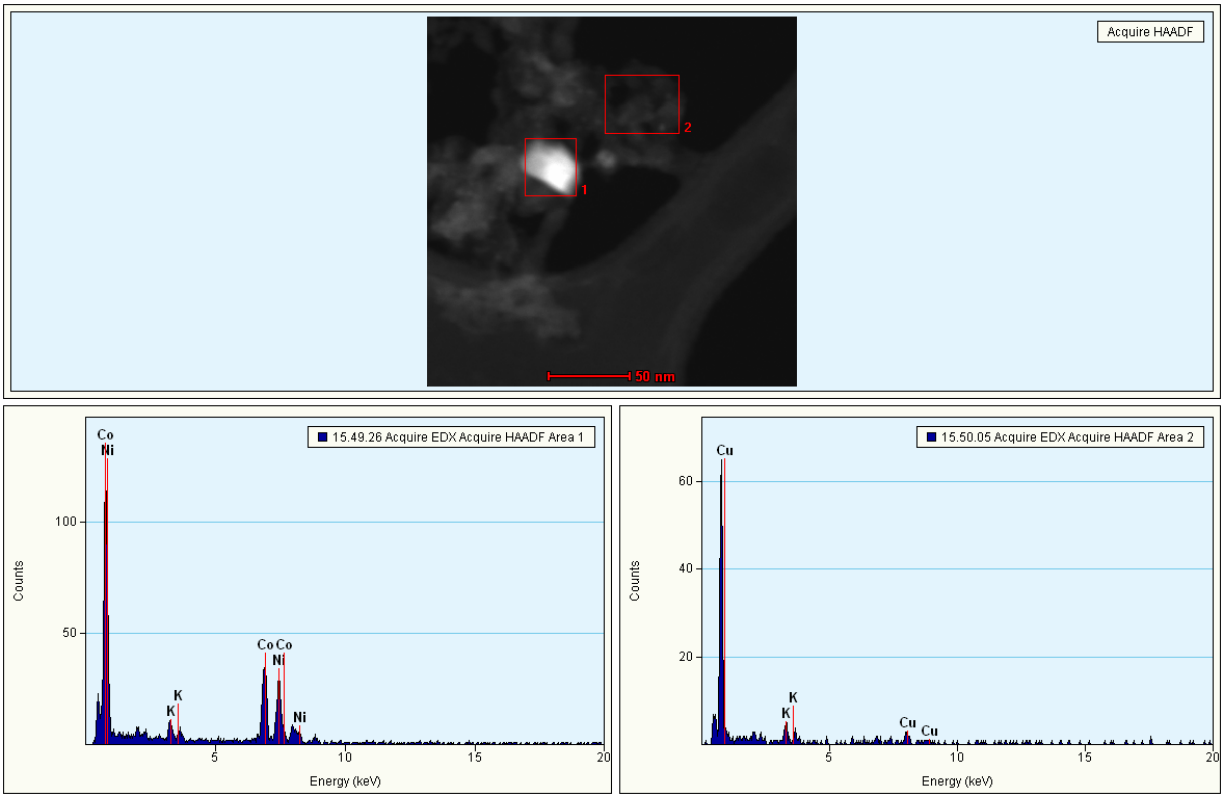

***Figure 3.11.5**: EDX analysis of areas 1 and 2 highlighted using dark field imaging, showing the contrast between the carbon matrix and the Co/Ni nanoparticles.*

3.11.3 Powder X-ray diffraction

Bulk characterisation of **CoNi@C-500** was caried *via* PXRD. A diffraction pattern was recorded on a Bruker D2 Phaser powder X-ray diffractometer on the FTO film to confirm the presence and structure of a Co/Ni oxide species. The PXRD pattern was measured in a zero-background sample holder plate with a powder well. Characterisation of the FTO electrode shows signals characteristic of spinel nickel cobalt oxide in the PXRD spectra in addition to peaks indicative to porous carbon (Figure 3.11.6). The peak positions (2θ = 19.0 º, 36.8 º, 38.7 º, 44.5 º and 56.2 º) obtained for the sample are indicative of $NiCo_2O_4$, indexed as (111), (311), (222), (400) and (442), respectively.[28,29] The signals at *approx*. 27 º and 46 º correspond to the (002) and (004) planes of porous carbon synthesised *via* the heat-treatment of a MOF parent template.[30] In addition to signals deriving from

CoNi@C-500, signals at *approx.* 29 º, 53 º and 62 º corresponding to the FTO coating are also present in the spectrum,[31] denoted in the spectrum under the '▽' symbol.

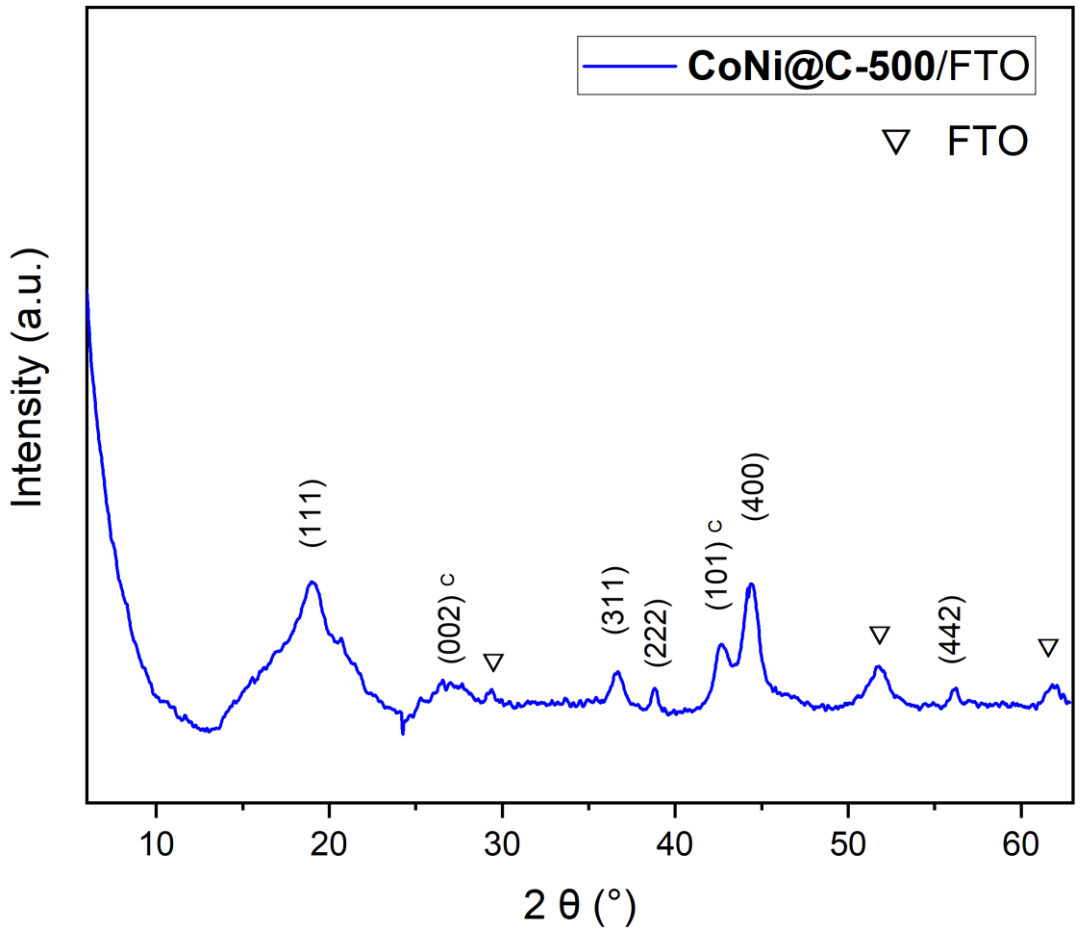

***Figure 3.11.6**: PXRD spectrum of **CoNi@C-500**/FTO showing the presence of crystalline $NiCo_2O_4$, porous carbon and the FTO electrode.*

3.11.4 Raman and FT-IR spectroscopy

The Raman spectra of **CoNi@C-500**/FTO and **CoNi@C-500**/CC were obtained from the electrode surface using a Renishaw-1000 micro-Raman spectrometer. The two samples appear to possess identical signals which, as seen with thin films of **Co@C-500** prepared using the standard synthesis, verifies that **CoNi@C-500** can be synthesised on a variety of electrode surfaces. The overview spectra in the range of 150 – 2000 cm^{-1} displays the D- and G-bands at 1320 and 1590 cm^{-1}, respectively (Figure 3.11.7). These signals are typical for porous carbon-based materials. The D-band is slightly red-shifted in comparison to typical porous carbon with D-band signals reported at *approx.* 1345 cm^{-1}. This band (the disorder-band) corresponds to the breathing mode of A1g symmetry in aromatic carbon. Porous structures such as carbon foam exhibit a D-band at 1320 cm^{-1}.

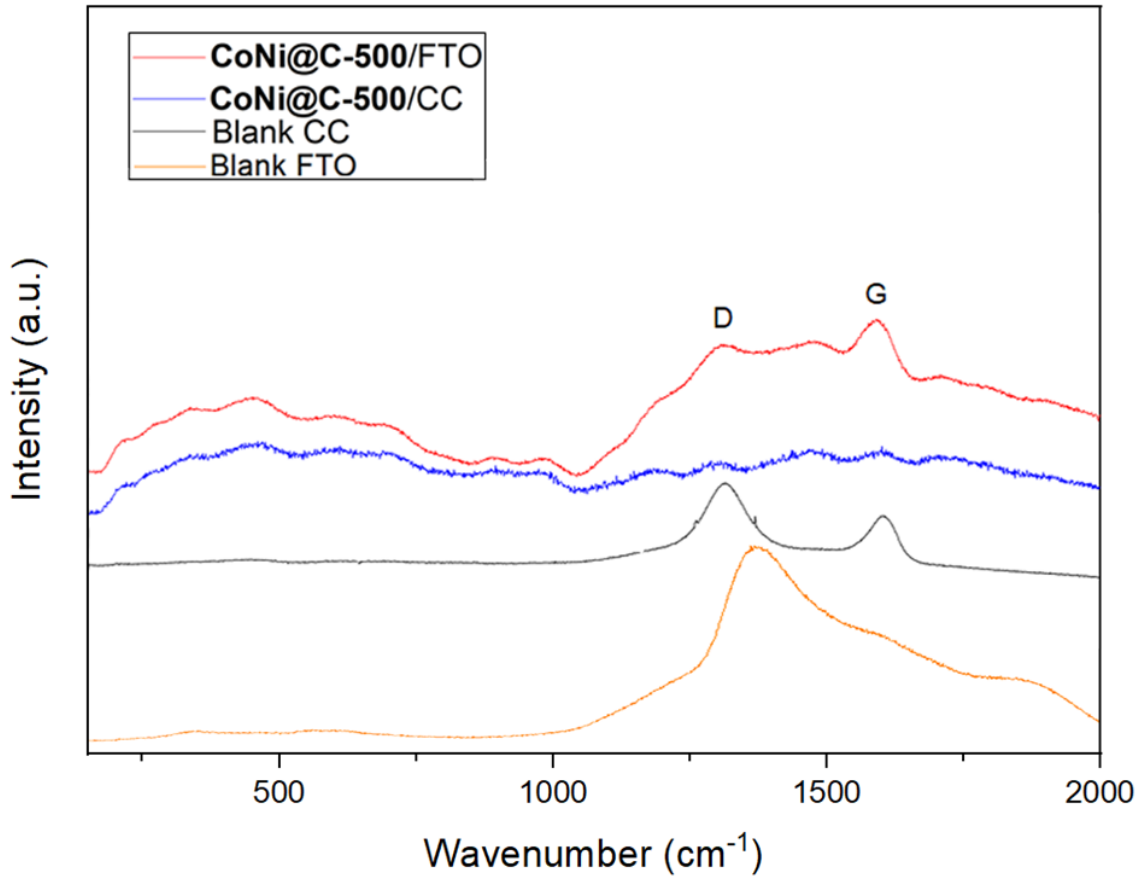

***Figure 3.11.7**: The overview Raman spectra of **NiCo@C**-500/FTO (red), **NiCo@C**-500/CC (blue), a black CC electrode (grey) and a blank FTO electrode (orange).*

The region 150 – 850 cm^{-1} is enlarged to investigate signals corresponding to the Ni/Co oxide centres within the carbon material (Figure 3.11.8). Signals can be identified at 251, 460, 604, 685 cm^{-1}. These peaks correspond to the *Eg* (460 cm^{-1}), *F2g* (212 and 604 cm^{-1}), *A1g* (685 cm^{-1}) modes of the spinel $NiCo_2O_4$ crystalline phase. It is noted that the intensity of the signals decreases despite the data being collected over 100 accumulations of each of the samples. Previous literature reports note that the crystallinity of spinel cobalt nickel oxide decreases with annealing temperatures in excess of 300 °C, coupled with broad, undefined signals, to which **CoNi@C-500** in is agreement with.

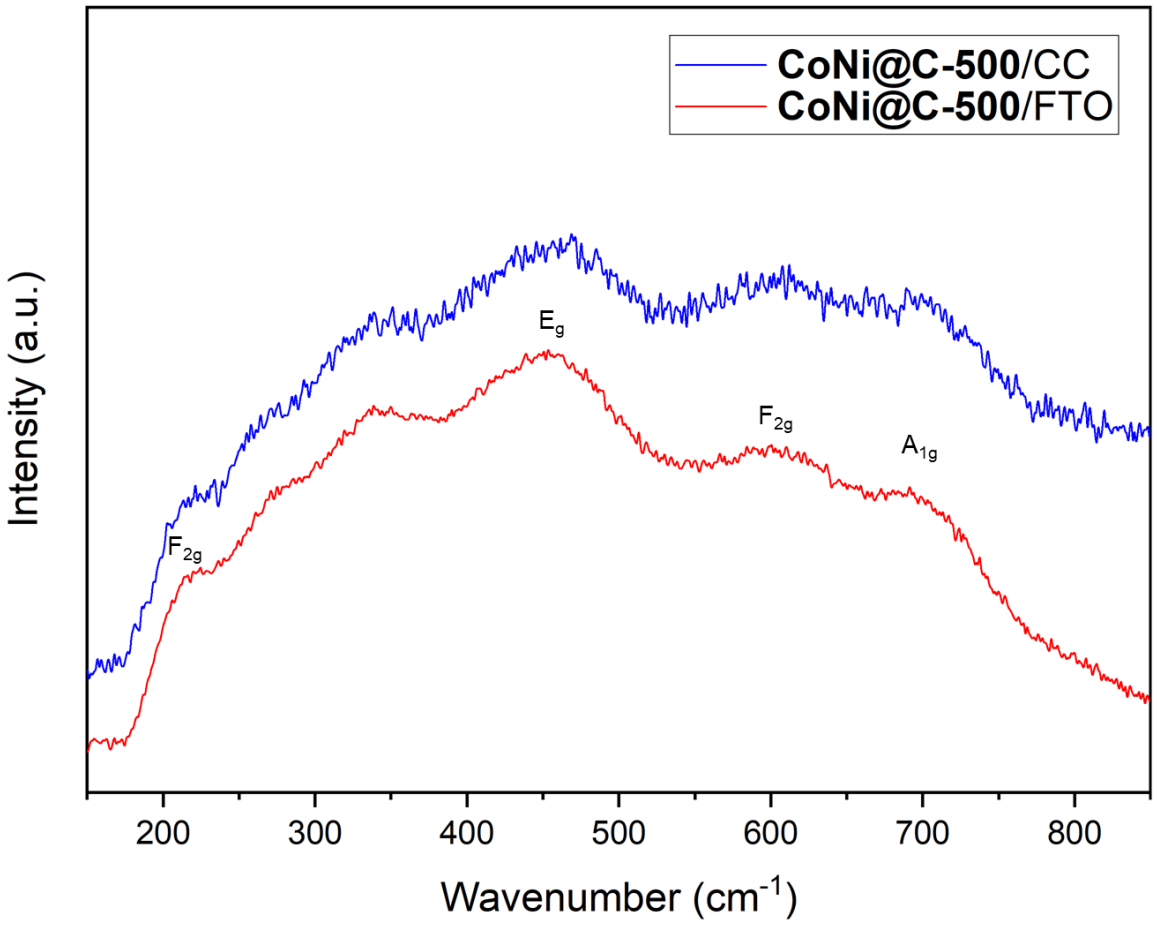

***Figure 3.11.8**: The Raman spectra of **NiCo@C**-500/FTO (red), **NiCo@C**-500/CC and (blue) in the 150 – 850 cm^{-1} region.*

Fourier transform infrared (FT-IR) spectra of the thin film surfaces were recorded on a PerkinElmer Spectrum One FT-IR spectrometer using a universal ATR sampling accessory. The experimental data was collected and processed using Spectrum v5.0.1 (2002 PerkinElmer Instrument LLC) software. A scan rate of 16 scans per minute with a resolution of 6 scans in the range 4000 - 500 cm^{-1} was recorded for both species. The resonance at 115 cm^{-1} indicates a C–O stretching region. The bands at 1251 and 1152 cm^{-1} are due to C–C skeletal vibration. The strongest signal recorded at 955 cm^{-1} is attributed to the distributed C=C bending mode. The carbon-derived resonances are in line with annealed porous carbon materials.[32] The FT-IR spectra for **CoNi@C-500** synthesised on FTO and carbon cloth show a high degree of similarities in the fingerprint region, as to the spectra of **Co@C-500** indicating that a carbon material and oxides are produced. The weak stretch at 647 and 549 cm^{-1} are consistent with metal–oxide vibrations in spinel $NiCo_2O_4$, Ni – O (647 cm^{-1}) and Co – O (549 cm^{-1}), respectively.[33,34] It is noted that the resonances are weak due to the layer of carbon encapsulating the Co/Ni oxide particles as seen with other CoNi@shell materials.[35]

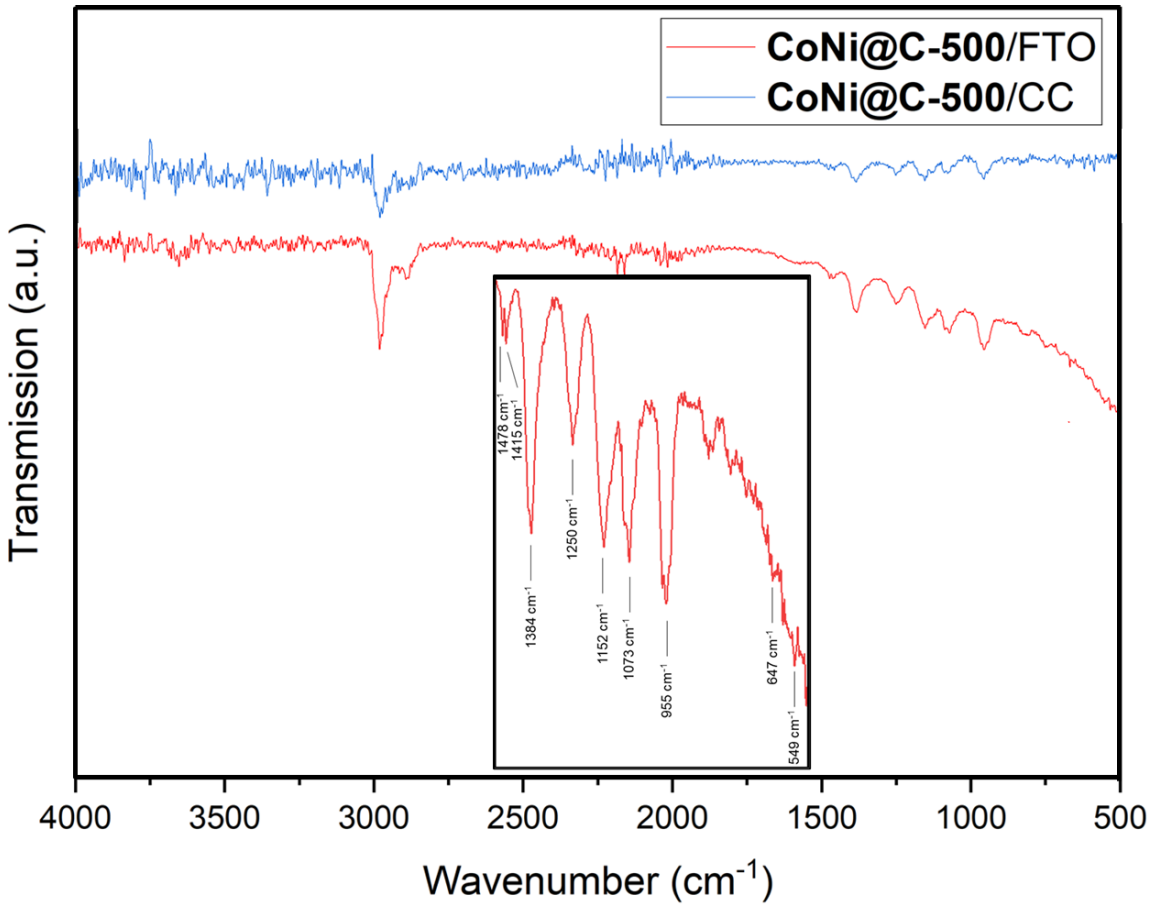

***Figure 3.11.9**: The FT-IR spectra of **NiCo@C**-500/FTO (blue) and **NiCo@C**-500/CC (red) with the fingerprint region expanded in the insert.*

3.12 Electrocatalytic experiments

3.12.1 Neutral pH conditions

Electrochemical experiments were first conducted on **CoNi@C-500**/FTO and **Co@C-500**/CC at pH 7.2. Measurements were conducted using the standard three-electrode setup in an electrochemical cell using the MOF film working electrode, Pt-wire as the counter electrode and an Ag/AgCl reference electrode in 50 mM KPi buffer and 1M KNO_3 electrolyte. LSV curves were recorded between 0.5 V and 1.2 V vs Ag/AgCl under continuous stirring. The responses of annealed Co/Ni thin-film electrodes were compared with those of with unannealed FTO and CC electrodes. It can be seen that the electrode support also influences the current densities reached within the identical testing window.

All electrodes give rise to OER activity at moderate overpotentials. The **NiCo@C-500**/CC electrode demonstrated the highest electrocatalytic ability, with **{(NiCo)$_5$}-MOF**/FTO demonstrating the lowest. The disparity between the unannealed FTO and unannealed CC can be explained in part by the difference in intrinsic surface areas of the electrodes, as discussed in Section 3.11.10, while the difference in catalytic ability between the annealed and unannealed CC electrodes is likely due to the increased conductivity of the porous carbon network produced upon heat treating the MOF. This data and the OER analysis collected in Chapter 3, demonstrates that at all substrates, the Co-only MOFs or oxide material perform superiorly, compared to the mixed Co/Ni materials at this pH value.

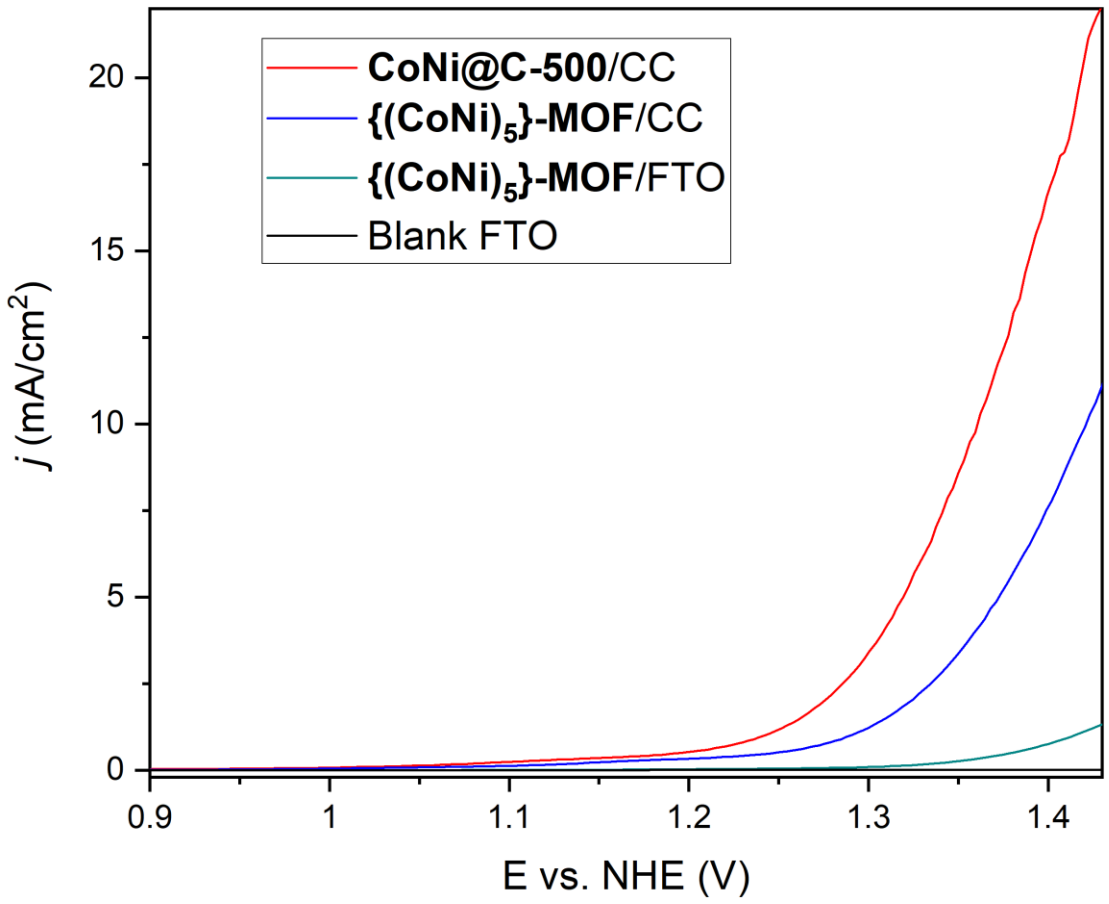

***Figure 3.11.10**: LSV conducted at pH 7.2 for **NiCo@C-500**/CC (red), **{(NiCo)$_5$}-MOF**/CC (blue), **{(NiCo)$_5$}-MOF**/FTO, and a blank FTO (black).*

***Table 3.11.1**: Summary of results obtained from the LSV data for **{(NiCo)$_5$}-MOF**/FTO, **{(NiCo)$_5$}-MOF**/CC and **NiCo@C-500**/CC at pH 7.2.*

Electrode	η_{onset} *(mV)*	*Tafel slope (mV/dec)*	η *@ j = 1 m A/cm^2 (mV)*	η *@ j = 10 m A/cm^2 (mV)*
{(NiCo)$_5$}-MOF/FTO	545	105	585	-
{(NiCo)$_5$}-MOF/CC	440	110	455	590
NiCo@C-500/CC	390	120	410	545

3.12.2 Alkaline conditions

Due to the hydrolytic instability of the coordination bonds of the MOF, the unannealed **{(NiCo)$_5$}-MOF** films are unstable at pH 13.5. Therefore, tests at pH 13.5 were carried out using the heat-treated films as working electrodes in conjunction with a Pt-wire counter electrode and an Ag/AgCl reference electrode in 0.1M KOH. LSV was carried out on these electrodes at pH 13.5, however the resulting current density plot was relatively noisy due to excessive O_2 bubbles produced during the electrocatalytic reaction. To obtain a more accurate result, steady-state voltammetry (SSV) was carried out.

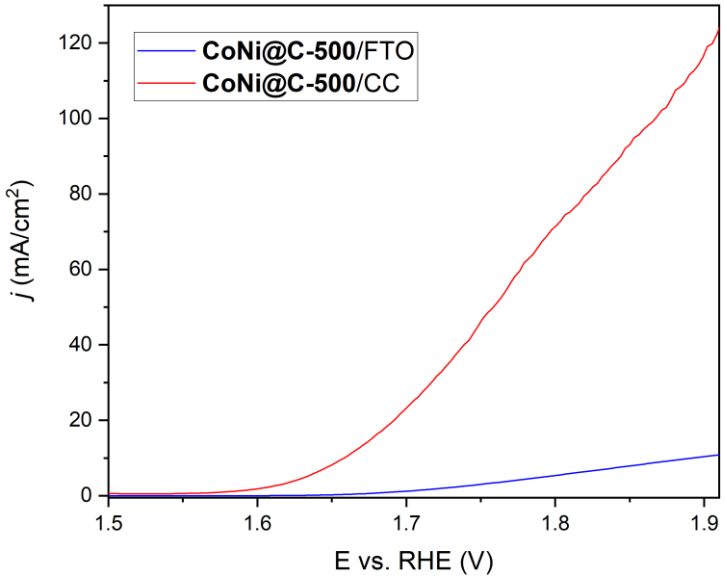

***Figure 3.11.11**: Results of LSV experiments conducted at pH 13.5 for **NiCo@C-500**/CC (red), **{(NiCo)$_5$}-MOF**/FTO (blue).*

As previously encountered, excessive O_2 bubble formation caused as issue under normal LSV conditions despite stirring, bubbles adhered to the electrode surface. Gas formation on the surface was unavoidable. Diffusion of the O_2 gas into the solution *via* stirring could not be efficiently facilitated as O_2 production occurred more rapidly than it could be removed. This resulted in spikes in current densities as not all of the electrode surface was in contact with the solution (Figure 3.11.12, b)). SSV was employed to overcome this problem and the values reported from this experiment likely provide a more accurate Tafel slope for the material. The SSV curves were used to determine the onset overpotential and Tafel slope for **CoNi@C-500**.

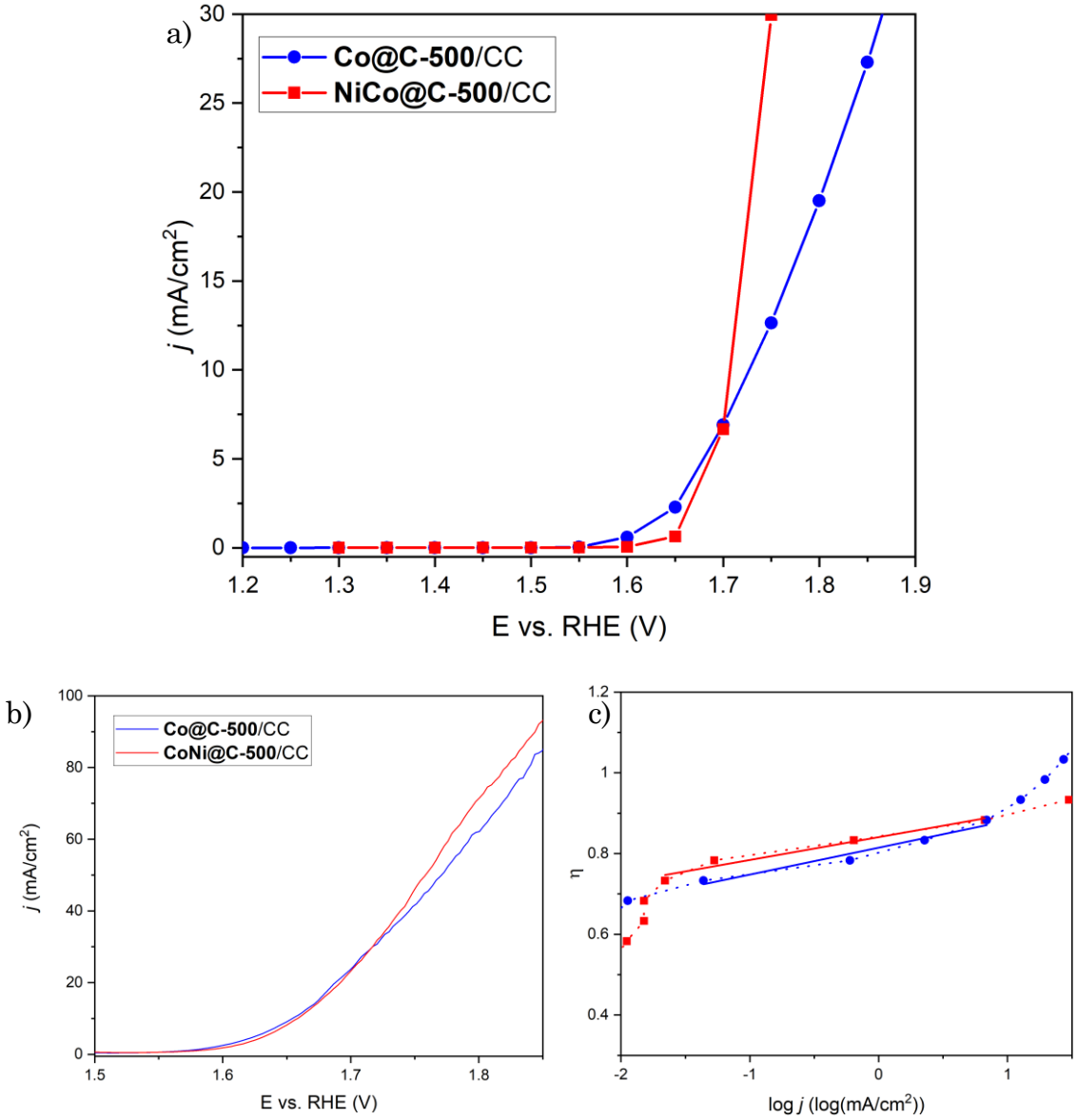

***Figure 3.11.12**: a) SSV experiments conducted at pH 13.5 carried out between 0.5 V and approx. 0.9 V vs Ag/AgCl. b) LSV experiments conducted at pH 13.5 .**c)** Tafel slopes of* **CoNi@C-500**/CC and **Co@C-500**/CC *obtained from the SSV data.*

***Table 3.11.2**: Results of electrochemical testing at pH 13.5.*

Electrode	η_{onset} *(mV)*	*Tafel slope (mV/dec)*	*η @ j = 10 mA/cm²* *(mV)*	*η @ j = 1 mA/cm²* *(mV)*
Co@C-500/CC	440	67	497	388
NiCo@C-500/CC	460	57	477	372

The **CoNi@C-500**/CC electrode performed the best electrochemically, and has a very comparable overpotential at 1 mA/cm^2 to electrodeposited $Ni_xCo_{3-x}O_4$ reported by Lambert *et al.*,[36] however, the current densities for the electrode reported here exceed those of reported comparable structures with that **CoNi@C-500**/CC reaching 15 mA/cm^2 at 1.8 V vs RHE. The **Co@C-500** activity is comparable to a similar cobalt oxide electrode reported by Surendranath *et al.*,[37] which has a Tafel slope of 60 mV/dec and an overpotential at 1 mA/cm^2 of 390 mV.

The reported data demonstrate the superiority of the **NiCo@C-500** as a water oxidation catalyst, in alkaline conditions. This result relates to previous studies on heat treated NiCo-MOF-74 materials reported by Feng *et al.*, which were used for water splitting and reported excellent stability.[38] Overall, the onset overpotentials are within the desired range, and indicate that the water oxidation mechanism is similar at both electrodes. The charge transport at the electrodes is excellent, yielding low Tafel slopes and very high current densities, particularly for the Ni/Co electrode which exhibited higher catalytic activity than **Co@C-500** at current densities > 25 mA/cm^2.

3.13 Conclusion

The direct synthesis of MM-MOFs was successfully employed in the formation of the trinuclear **{(Mn,Zn)$_3$}-MOF**, a doubly interpenetrated structure containing trinuclear metallic units stabilised by six ligands from **H$_3$BTEB** ligands and two axial-bound solvent molecules. The physical and structural attributes of the MOFs were studied using a number of analytical techniques including power X-ray diffraction, Raman spectroscopy and thermogravimetric analysis. The assignment of the relative positions of Mn(II) and Zn(II) in the inorganic SBUs was investigated using elemental techniques including EDX and XPS spectroscopy, in addition to computational modelling with good agreement to suggest Mn(II) in the octahedral sites and Zn(II) in the tetrahedral sites. However, the possibility of some deviation from order in alternative positions in some SBUs cannot be completely excluded.

The electrocatalyst activity of **{(MnZn)$_3$}-MOF** and previously reported {M$_3$} MM-MOFs was investigated and compared. **{(MnCo)$_3$}-MOF** showed superior catalytic performance but none of the three MM-MOFs were stable under bulk catalysis conditions, highlighting instability of the {M$_3$} inorganic unit. Although **{(MnZn)$_3$}-MOF** possessed the lowest catalytic activity, it was seen as another confirmation that catalytic inactive Zn(II) occupies the tetrahedral sites with labile solvent molecules.

Previous successes were recorded when using a pentanuclear MOF and **H$_3$BTEB**. Following on from this, the mixed metal variant, **{(NiCo)$_5$}-MOF**, was synthesised under direct syntheses both solvothermally but also *via* electrodeposition synthesis to produce both **{(NiCo)$_5$}-MOF**/FTO and **{(NiCo)$_5$}-MOF**/CC electrodes. Bulk crystalline and thin-film samples were fully characterised and tested for their OER activity.

Thin-film samples were annealed at 500 °C to synthesise core@shell materials containing nanoparticles indicative of $NiCo_2O_4$. As with **Co@C-500** investigated in Chapter 2, these electrodes demonstrated competitive electrocatalytic ability at pH 7.2, likely due to increased conductivity of the carbon porous network, compared to the ligand. These annealed samples were also used to carry out water oxidation at pH 13.5, which resulted in very high current densities, low overpotentials and small Tafel slopes. At pH 13.5, the mixed metal **NiCo@C-500**/CC electrode reached higher current densities than the monometallic **Co@C-500**/CC.

The methodology of direct synthesis *via* electrodeposition to prepare thin-film electrodes has many applications outside of water oxidation catalysis. Future work employing the electrodeposition/annealing strategy is currently being explored with the successful deposition of **{Co_5}-MOF** and **{$(CoNi)_5$}-MOF**, and formation of **Co@C-500** and **CoNi@C-500** on thin-film graphite electrodes in the hope that these materials can be utilised in battery technologies.

3.15 Bibliography

1 M. Y. Masoomi, A. Morsali, A. Dhakshinamoorthy and H. Garcia, *Angew. Chemie*, 2019, **131**, 15330–15347.

2 L. Martins, L. K. Macreadie, D. Sensharma, S. Vaesen, X. Zhang, J. J. Gough, M. O'Doherty, N. Y. Zhu, M. Rüther, J. E. O'Brien, A. L. Bradley and W. Schmitt, *Chem. Commun.*, 2019, **55**, 5013–5016.

3 N. Zhu, G. Tobin and W. Schmitt, *Chem. Commun.*, 2012, **48**, 3638–3640.

4 N. Zhu, D. Sensharma, P. Wix, M. J. Lennox, T. Düren, W. Y. Wong and W. Schmitt, *Eur. J. Inorg. Chem.*, 2016, **2016**, 1939–1943.

5 N. Zhu, G. Tobin and W. Schmitt, *Chem. Commun.*, 2012, **48**, 3638–3640.

6 M. O. Sinnokrot and C. D. Sherrill, *J. Phys. Chem. A*, 2004, **108**, 10200–10207.

7 K. I. Hadjiivanov, D. A. Panayotov, M. Y. Mihaylov, E. Z. Ivanova, K. K. Chakarova, S. M. Andonova and N. L. Drenchev, *Chem. Rev.*, 2021, **121**, 1286–1424.

8 H. G. M. Edwards, *J. Raman Spectrosc.*, 2005, **36**, 835–835.

9 M. J. Frisch, G. W. Trucks, H. B. Schlegel, G. E. Scuseria, M. A. Robb, J. R. Cheeseman, G. Scalmani, V. Barone, G. A. Petersson, H. Nakatsuji, X. Li, M. Caricato, A. Marenich, J. Bloino, B. G. Janesko, R. Gomperts, B. Mennucci, H. P. Hratchian, J. V. Ortiz, A. F. Izmaylov, J. L. Sonnenberg, D. Williams-Young, F. Ding, F. Lipparini, F. Egidi, J. Goings, B. Peng, A. Petrone, T. Henderson, D. Ranasinghe, V. G. Zakrzewski, J. Gao, N. Rega, G. Zheng, W. Liang, M. Hada, M. Ehara, K. Toyota, R. Fukuda, J. Hasegawa, M. Ishida, T. Nakajima, Y. Honda, O. Kitao, H. Nakai, T. Vreven, K. Throssell, J. A. Montgomery, J. E. P. Jr., F. Ogliaro,

M. Bearpark, J. J. Heyd, E. Brothers, K. N. Kudin, V. N. Staroverov, T. Keith, R. Kobayashi, J. Normand, K. Raghavachari, A. Rendell, J. C. Burant, S. S. Iyengar, J. Tomasi, M. Cossi, J. M. Millam, M. Klene, C. Adamo, R. Cammi, J. W. Ochterski, R. L. Martin, K. Morokuma, O. Farkas, J. B. Foresman and D. J. Fox, Gaussian, Inc., Wallingford CT, 2016.

10 J. P. Perdew, K. Burke and M. Ernzerhof, *Phys. Rev. Lett.*, 1996, **77**, 3865–3868.

11 C. Adamo and V. Barone, *J. Chem. Phys.*, 1999, **110**, 6158–6170.

12 M. Dolg, U. Wedig, H. Stoll and H. Preuss, *J. Chem. Phys.*, 1987, **86**, 866–872.

13 M. M. Francl, W. J. Pietro, W. J. Hehre, J. S. Binkley, M. S. Gordon, D. J. DeFrees and J. A. Pople, *J. Chem. Phys.*, 1982, **77**, 3654–3665.

14 M. J. Frisch, J. A. Pople and J. S. Binkley, *J. Chem. Phys.*, 1984, **80**, 3265–3269.

15 J. Lee, O. K. Farha, J. Roberts, K. A. Scheidt, S. T. Nguyen and J. T. Hupp, *Chem. Soc. Rev.*, 2009, **38**, 1450–1459.

16 J. Q. Shen, P. Q. Liao, D. D. Zhou, C. T. He, J. X. Wu, W. X. Zhang, J. P. Zhang and X. M. Chen, *J. Am. Chem. Soc.*, 2017, **139**, 1778–1781.

17 S. Bommakanti and S. K. Das, *Front. Mater.*, 2019, **6**, 170.

18 E. Pullicino, W. Zou, M. Gresil and C. Soutis, *Appl. Compos. Mater.*, 2017, **24**, 301–311.

19 K. I. Hadjiivanov, D. A. Panayotov, M. Y. Mihaylov, E. Z. Ivanova, K. K. Chakarova, S. M. Andonova and N. L. Drenchev, *Chem. Rev.*, 2021, **121**, 1286–1424.

20 H. Furukawa, N. Ko, Y. B. Go, N. Aratani, S. B. Choi, E. Choi, A. O. Yazaydin, R.

Q. Snurr, M. O'Keeffe, J. Kim and O. M. Yaghi, *Science*, 2010, **329**, 424–8.

21 G. B. Deacon and R. J. Phillips, *Coord. Chem. Rev.*, 1980, **33**, 227–250.

22 J. Rouquerol, P. Llewellyn and F. Rouquerol, *Stud. Surf. Sci. Catal.*, 2007, **160**, 49–56.

23 C. A. Downes and S. C. Marinescu, *ChemSusChem*, 2017, **10**, 4374–4392.

24 B. M. Quinn, C. Dekker and S. G. Lemay, *J. Am. Chem. Soc.*, 2005, **127**, 6146–6147.

25 C. Chen, W. Chen, B. Zong, X. Ding and H. Dong, *J. Mater. Sci. Mater. Electron.*, 2020, **31**, 20285–20294.

26 W. Zhou, D. Kong, X. Jia, C. Ding, C. Cheng and G. Wen, *J. Mater. Chem. A*, 2014, **2**, 6310–6315.

27 Q. Huang, W. Li, Y. Lei, S. Guan, X. Zheng, Y. Pan, W. Wen, J. Zhu, H. Zhang and Q. Lin, *Catal. Letters*, 2018, **148**, 2799–2811.

28 J. Zhan, M. Cai, C. Zhang and C. Wang, *Electrochim. Acta*, 2015, **154**, 70–76.

29 J. Li, N. Jiang, J. Liao, Y. Feng, Q. Liu and H. Li, *Nanomaterials*, 2020, **10**, 191.

30 H. J. Peng, G. X. Hao, Z. H. Chu, Y. W. Lin, X. M. Lin and Y. P. Cai, *RSC Adv.*, 2017, **7**, 34104–34109.

31 Y. Yue, H. Li, K. Li, J. Wang, H. Wang, Q. Zhang, Y. Li and P. Chen, *J. Phys. Chem. Solids*, 2017, **110**, 284–289.

32 H. Shang, Y. Lu, F. Zhao, C. Chao, B. Zhang and H. Zhang, *RSC Adv.*, 2015, **5**, 75728–75734.

33 H. Zhang, H. Li, H. Wang, K. He, S. Wang, Y. Tang and J. Chen, *J. Power Sources*,

2015, **280**, 640–648.

34 J. Hu, M. Li, F. Lv, M. Yang, P. Tao, Y. Tang, H. Liu and Z. Lu, *J. Power Sources*, 2015, **294**, 120–127.

35 X. Wei, Z. Zhang, L. Zhang and X. Xu, *J. Mater. Sci.*, 2019, **54**, 2066–2078.

36 T. N. Lambert, J. A. Vigil, S. E. White, D. J. Davis, S. J. Limmer, P. D. Burton, E. N. Coker, T. E. Beechem and M. T. Brumbach, *Chem. Commun.*, 2015, **51**, 9511–9514.

37 Y. Surendranath, M. Dincă and D. G. Nocera, *J. Am. Chem. Soc.*, 2009, **131**, 2615–2620.

38 X. Feng, H. Wang, X. Bo and L. Guo, *ACS Appl. Mater. Interfaces*, 2019, **11**, 8018–8024.

Chapter 4

Triazine-Functionalised Metal-Organic Frameworks

4.0 Introduction

Chapters 2 and 3 dealt with the electrodeposition of MOFs and MM-MOFs featuring a facilely synthesised tritopic ligand to fabricate thin-film electrodes. Following this success, focus was shifted to replicating these results using a tailor-made ligand to synthesise stable, layered MOF materials with high porosity. The synthesis of novel, large and ridged tritopic ligands extending from a 1,3,5-triazine core as planar struts for incorporation into interpenetrated MOFs and metal-organic layered materials (MOLs) is detailed in this chapter.

The triazine-based ligands trimethyl-4,4',4''-(((1,3,5-triazine-2,4,6-triyl)tris(benzene-4,1-diyl))tris(ethyne-2,1-diyl))tribenzoate (**H_3TAP**), trimethyl-3,3',3''-(((1,3,5-triazine-2,4,6-triyl) tris (benzene-4,1-diyl)) tris(ethyne-2,1-diyl))tribenzoate (**H_3TAM**) were synthesised and characterised to assess their physiochemical and photophysical properties to assess their potential as luminescent linkers. Solvothermal reactions with **H_3TAP** lead to the formation of four novel interweaving MOFs (**{Cu_2}-MOF-1**, **{Cu_2}-MOF-2**, **{Zn}-MOF** and **{Cd}-MOF**). The potential applications of these MOFs are explored by characterising their photophysical properties, and stability for gas sorption and water splitting catalysis.

4.1 General synthesis of triazine-based ligands

Triazine units enjoy a 'one-upmanship' over the traditionally used 1,3,5-benzene core, in that it is a more electron withdrawing group, has a high luminescence at room-temperature and possesses a larger nucleophilic susceptibility.[1,2] In the field of supramolecular chemistry, triazine derivatives are commonly used as ligands as they are well-known to form hydrogen bonds, favour π···π interactions and were shown to be involved in attractive anion···π-interactions.[3,4] Selective gas adsorption requires pore sizes that are comparable to the diameter of the target gas molecules. Triazine ligands are currently being exploited for their ability to induce network interpenetration to tailor MOFs with selective gas absorption properties for H_2 and favourable thermal stabilities.[5] The three nitrogen atoms in the triazine ring of the common ligand 1,3,5-triazine-2,4,6-tribenzoic acid (**H_3TATB**) allow the peripheral phenyl rings to be coplanar with the central triazine with an average dihedral angle of *ca*. 4.5°. This ensures delocalisation of π-electrons and strong inter-ligand π···π interactions, leading to the formation of metal-organic layers (MOLs) or interweaving MOFs, depending on the synthetic conditions.[6] Possible modification of these ligands include the synthesis of linearly extended triazine-based linkers. These struts have the potential to synthesise 2D layered materials and interpenetrated MOFs, with large voids and increased stability. Thus, frameworks constructed from these ligands are promising candidates for the electrodeposition of layered MOF materials, selective gas sorption and catalysis.

Polycarboxylates are the most readily employed organic struts in MOF synthesis, with the effects of position and extension having well-studied influences on the topology of the resulting MOFs.[7] Typically, ligands embodying triangular SBUs are built on a phenyl core. Triphenyl-substituted triazines have potential applications in MOF synthesis, due to their planar cores and high π-electrons delocalisation, allowing for strong inter-ligand π-π interaction, giving the potential to synthesise catenated MOFs and 2D-stacked structures with enhanced luminescence properties. Herein, two tritopic ligands incorporating both a carboxylate functionality and a 1,2,3-triazine planar core were synthesised in order to investigate their coordination to transition metal ions to form MOFs in the case of **H_3TAP**, and MOPs for **H_3TAM**. These ligands were synthesised by a series of catalytic Sonogashira cross-coupling reactions between 2,4,6-tris(4-ethynylphenyl)-1,3,5-triazine and an aryl halide with a carboxylic acid functionality substituted in either the meta or the *para* arene

position to yield **H$_3$TAP** or **H$_3$TAM**, respectively. The successful synthetic route to the ligands **H$_3$TAP** and **H$_3$TAM** is presented in Scheme 4.1.2.

4.1.1 Synthetic approach

Both **H$_3$TAP** and **H$_3$TAM** contain the same 2,4,6-tris(phenyl)-1,3,5-triazine core, synthesised from the trimerisation of commercially available 4-bromobenzonitrile. The tribromo-substituted triazine core subsequently underwent two Sonogashira cross-coupling reactions. Following this, two ester-hydrolysis reactions were employed to linearly extend the ligand, first with the addition of the alkyne spacer before adding the appropriate head-group containing the desired carboxylic acid functionality.

The first step of the synthesis generally proceeds *via* a nitrile trimerisation reaction. It is prepared according to Ranganathan *et al.* using trifluoromethanesulfonic acid at 0 °C.[8] However, the trimerisation steps for **1** was prepared according to Hanan *et al.*[9] using a modified procedure. LiN(CH$_3$)$_2$ was synthesised *in situ* from *n*-butyllithium and HN(CH$_3$)$_2$, as LiN(CH$_3$)$_2$ degrades more rapidly over time compared to *n*-butyllithium. The proposed mechanism for the reaction proceeds through the formation of a lithium ((4-bromophenyl)(dimethylamino)methylene)amide template with the addition of one equivalent of nitrile before the addition of the last two equivalents of the aryl-nitrile. The reaction proceeds at room temperature and resulted in an improved yield for **1** (86 %) compared to Ranganathan *et al.*[8]

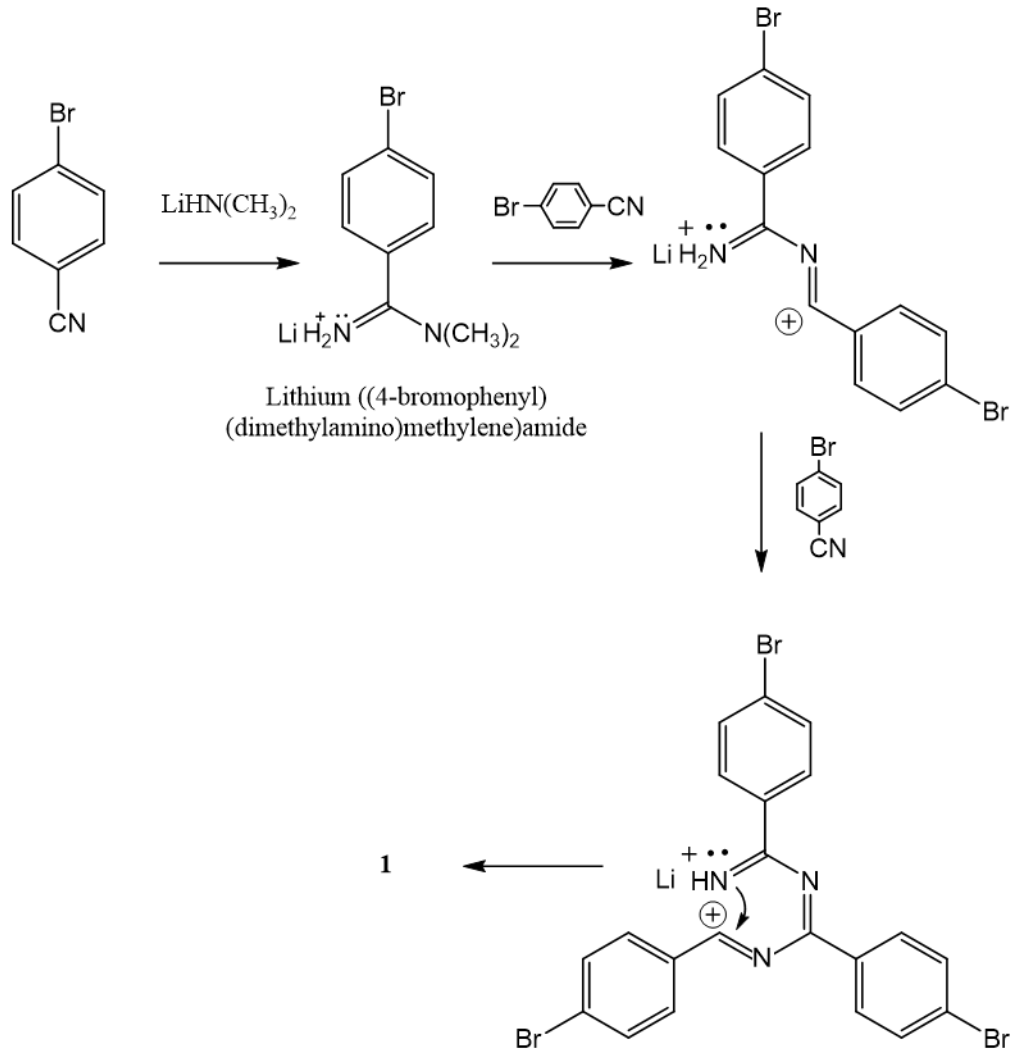

Scheme 4.1.1*: The synthesis of* ***1*** *using a nitrile trimerisation reaction via a lithium ((4-bromophenyl)(dimethylamino)methylene)amide intermediate.*

Two synthetic routes were investigated to attach the carboxylic acid moieties to the triazine core. Sonogashira cross-coupling reactions involve sp^2-sp C-C bond formation between an aryl-halide and a terminal alkyne.[10] Originally, the coupling reaction was attempted between **1** and 4-ethynylbenzoate based on a modified procedure from Jiménez-Sánchez *et al.*[11] The starting material, 4-ethynylbenzoate is commercially available, but poor yields were obtained, even with higher loading of the palladium catalyst and longer reaction times. In addition to this, the synthesis of **7** requires 3-ethynylbenzoate, which must be synthesised from 3-iodobenzoate *via* an additional Sonagashira cross-coupling reaction. So, to minimise reaction steps the synthesis of **3** was optimised for the final Sonogashira coupling reaction (Scheme 4.1.2) with 4-iodobenzoate to produce **4** with an average yield of 82 % and 3-iodobenzoate to yield **5** with an average yield of 69 %. Both were subjected to

base-catalysed ester hydrolysis with *aq.* KOH and subsequently acidified to yield the final ligands **H_3TAP** and **H_3TAM**.

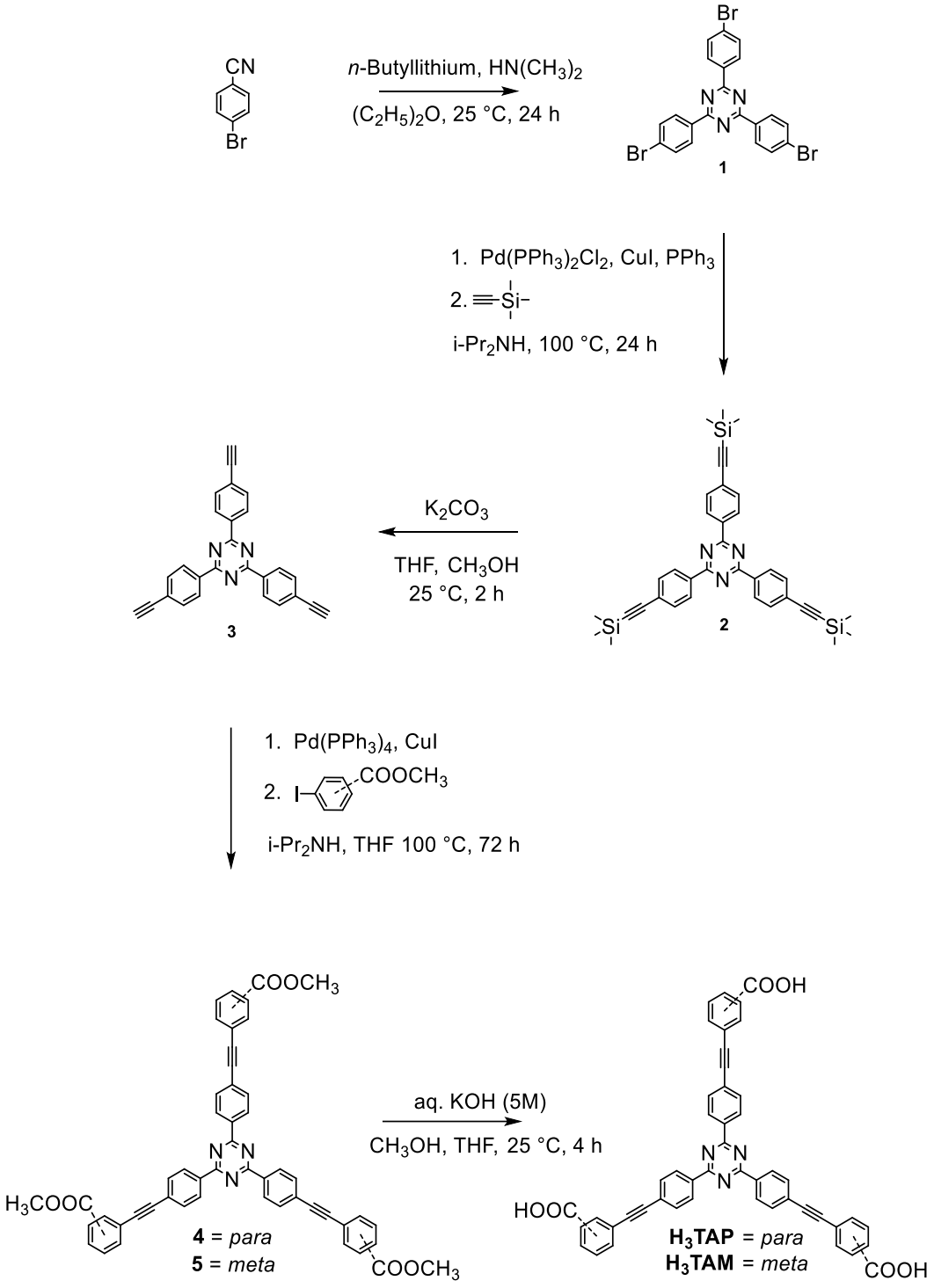

***Scheme 4.1.2**: Synthetic approach towards the ligands trimethyl-4,4',4''-(((1,3,5-triazine-2,4,6-triyl)tris(benzene-4,1-diyl))tris(ethyne-2,1-diyl))tribenzoate (**H_3TAP**) and trimethyl-3,3',3''-(((1,3,5-triazine-2,4,6-triyl)tris(benzene-4,1-diyl))tris(ethyne-2,1-diyl))tribenzoate (**H_3TAM**) for use in the synthesis of MOFs and MOPs.*

The ^{1}H-NMR spectra of the resulting products confirmed the formation of **H_3TAP** and **H_3TAM**. For both spectra, residual solvent peaks assigned to H_2O and DMSO are found below 4 ppm. For **H_3TAP**, a broad signal at 13.19 ppm that integrates to 3 H-atoms is evidence for the carboxylic acid -COOH functional group. Four multiplet signals found at 8.71, 7.89, 7.82 and 7.72 ppm, all of which integrate to six H-atoms can be attributed to the 24 H-atoms on the phenyl rings. For the *meta*-substituted analogue **H_3TAM**, two signals at 8.81 and 7.88 ppm, both integrating to 6 H, correspond to the H-atoms associated with the phenyl ring adjacent to the triazine core. Four unique signals are observed for the 3-substituted phenyl headgroup. The singlet located at 8.14 ppm corresponds to the H-atom at the 2-position of the ring. The doublet located at 7.78 and the multiplet located at 7.71 ppm, correspond to the H-atoms at the 4- and 6-position, respectively. The multiplet found at 7.55 ppm is attributed to the H-atom located on the 5-position of the phenyl ring.

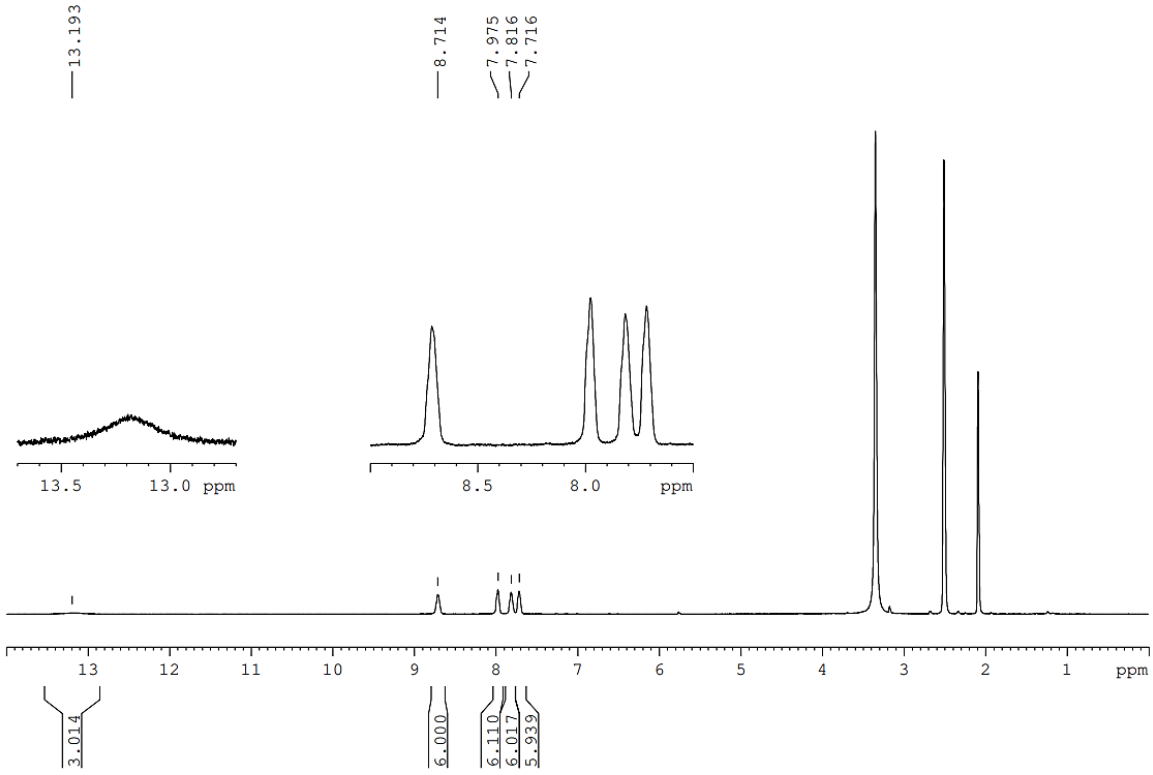

***Figure 4.1.3**: ^{1}H NMR spectrum of trimethyl-4,4',4''-(((1,3,5-triazine-2,4,6-triyl)tris(benzene-4,1-diyl))tris(ethyne-2,1-diyl))tribenzoate (**H_3TAP**)*

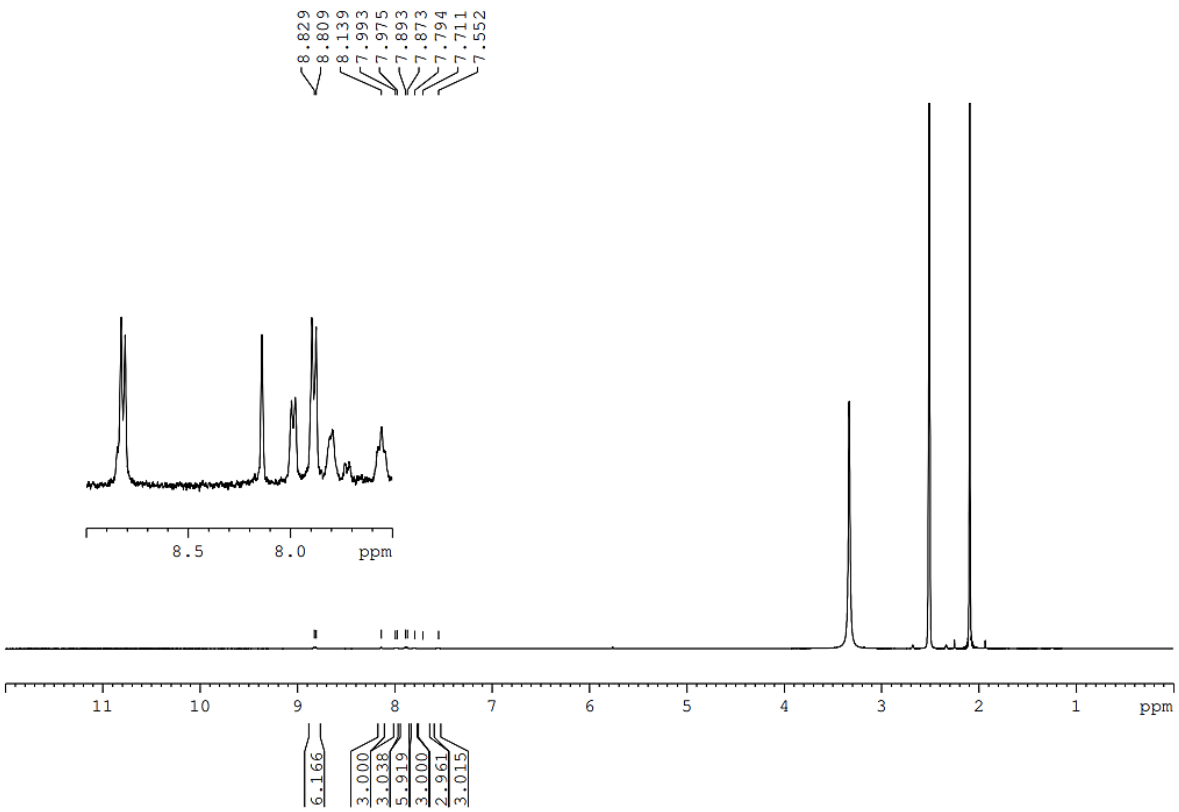

***Figure 4.1.4**: [1]H NMR spectrum of trimethyl-3,3',3''-(((1,3,5-triazine-2,4,6-triyl)tris(benzene-4,1-diyl))tris(ethyne-2,1-diyl))tribenzoate (**H₃TAM**)*

4.1.2 Crystal structure description of compound 4

The ester-protected precursor to **H₃TAP** was successfully crystallised from DMF *via* solvent evaporation. **4** forms yellow needle-shaped crystals which were suitable for analysis using single-crystal X-ray diffraction. It crystallises in the monoclinic space group *C*2/*c*, with one molecule comprising the asymmetric unit. C-C and N-C bond lengths are in the range of 1.118(4) – 1.206(4) Å and 1.329(4) – 1.346(5) Å, respectively, which are typical of triazine rings substituted with aromatic groups.[12,13] The three nitrogen atoms in the triazine ring of **4** allow the peripheral benzene rings to be coplanar with the central ring with torsion angles that range between 1.7 – 16.4° with respect to the central triazine ring. Individual torsion angles can be viewed in Table 4.1.1.

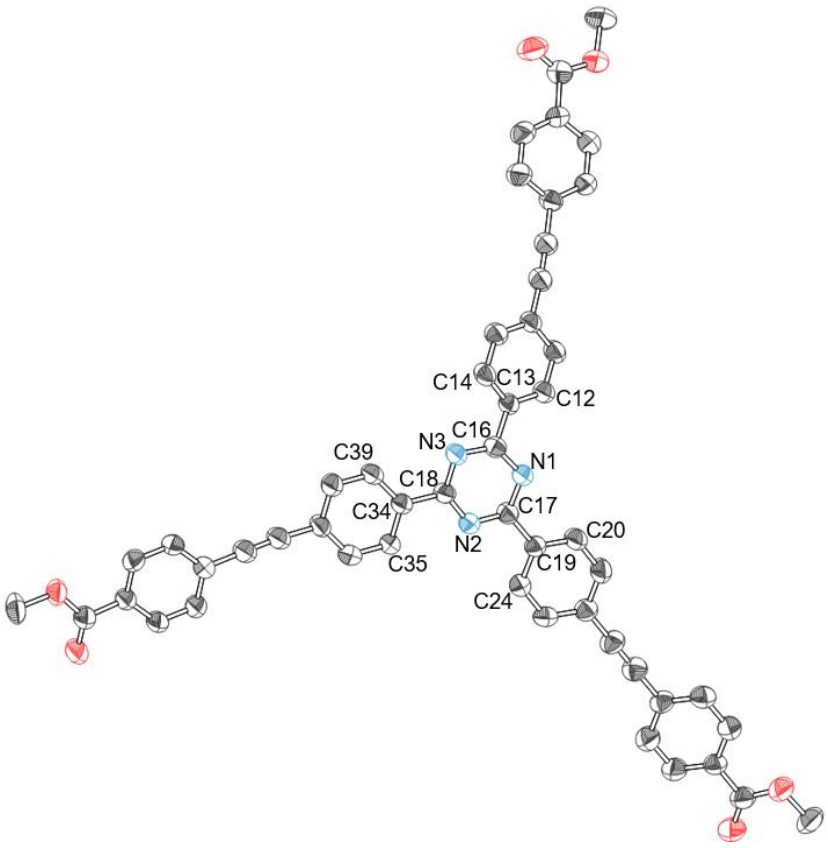

***Figure 4.1.5**: The asymmetric unit of **4** with thermal displacement ellipsoids shown at 50 % probability. Hydrogen atoms were omitted for clarity. Colour scheme: C, grey; O, red; N, blue. H-atoms omitted for clarity.*

***Table 4.1.1**: Selected plane torsion angles for the planer phenyl-substituted triazine core of compound **4**.*

Plane Torsions	°
N1-C16-C13-C12	1.7(4)
N1-C17-C19-C20	7.3(4)
N2-C17-C19-C24	5.6(4)
N2-C18-C34-C35	14.7(4)
N3-C18-C34-C39	16.4(4)
N3-C16-C13-C14	3.9(4)

With respect to the packing of **4**, the extended arms bend the structure so that the molecules form *zig-zag* layers when viewed down the crystallographic *c*-axis (Figure 4.1, a)). Weak π-π stacking is identified through rings phenyl C(2) – C(7) and C(34) – C(39) when adjacent molecules traverse, and through the central triazine ring to ring C(27) – C(32) with centroid to centroid distances of *ca.* 3.9 Å for both stacking of both phenyl rings and *ca.* 2.7 Å for the triazine (Figure 4.1.6, b)). The molecules also form parallel rows along the *b*-axis *via* moderate C-H···O hydrogen bonding to the three carboxylate groups, bonding with an average distance of *ca.* 2.6 Å (Figure 4.1.6, c)). This distance is consistent with that of hydrogen bonds reported by T. Steiner *et al.*.[14]

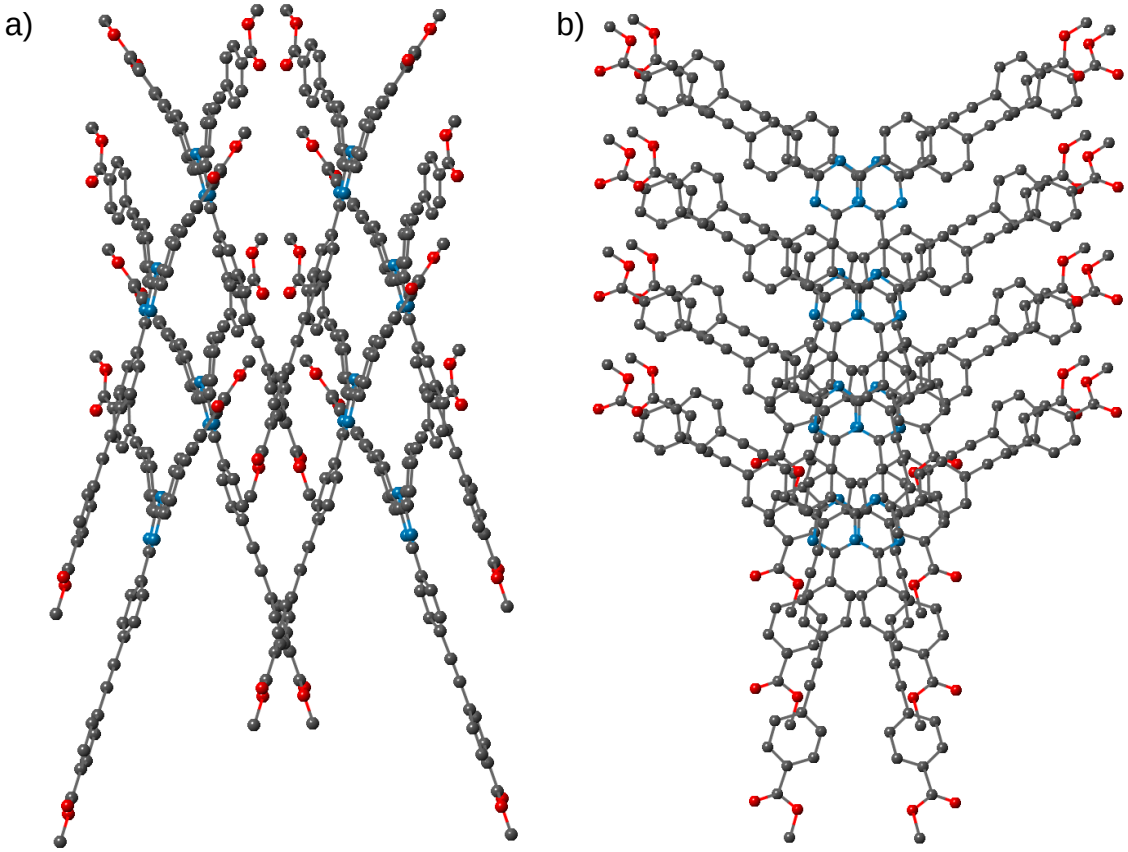

c)

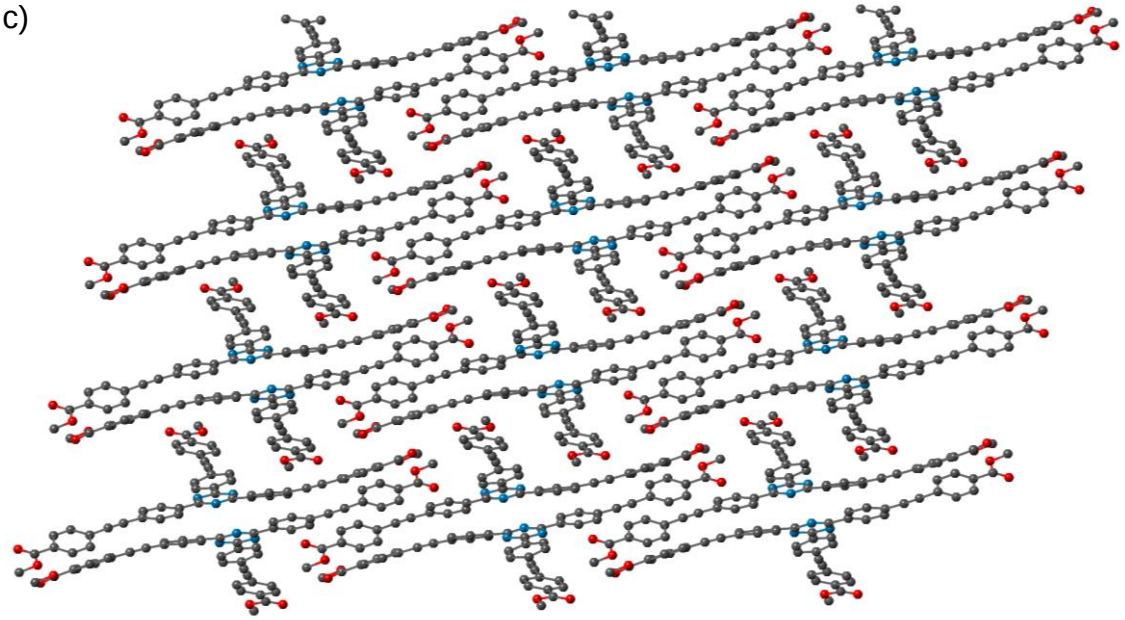

Figure 4.1.6*: Packing diagram of* ***4*** *viewed down the crystallographic a- (a), b- (b) and c-axis (c). Colour scheme: C, grey; O, red; N, blue. H-atoms omitted for clarity.*

Table 4.1.2*: Crystallographic table for compound* ***4****.*

Identification code	Compound **4**
Empirical formula	$C_{51}H_{33}N_3O_6$
Formula weight	783.80 g mol^{-1}
Temperature	214(2) K
Wavelength	1.54178 Å
Crystal system	Monoclinic
Space group	C 2/*c*
Unit cell dimensions	*a* = 19.5482(7) Å
	α = 90°
	b = 11.0277(4) Å
	β = 104.698(2)°
	c = 37.9909(13) Å
	γ = 90°
Volume	7921.8(5) $Å^3$
Z	8
Density (calculated)	1.314 Mg/m^3
Absorption coefficient	0.702 mm^{-1}
F(000)	3264
Crystal size	0.55 x 0.11 x 0.06 mm^3
Theta range for data collection	2.405 to 51.729°

Index ranges	$-17 \leq h \leq 19$, $-10 \leq k \leq 11$, $-24 \leq l \leq 38$
Reflections collected	10018
Independent reflections	4274
Completeness to theta = 51.729°	97.3 %
Max. and min. transmission	0.7502 and 0.0833
R_{int}	0.0442
Goodness-of-fit on F^2	1.014
Final R indices [I>2sigma(I)]	R1 = 0.0445, wR2 = 0.1185
R indices (all data)	R1 = 0.0717, wR2 = 0.1356
Largest diff. peak and hole	0.199 and -0.206 e.$Å^{-3}$

4.1.3 Photophysical properties of H_3TAP and H_3TAM

Triazine-based linkers are known for both their ability to form stable MOFs and their luminosity properties. Photophysical characterisation of **H_3TAM** and **H_3TAM** were performed at room temperature in degassed DMF. UV-visible absorption and emission spectra for the ligands were obtained as seen in Figure 4.1.7 and summarised in Table 4.1.4. The sample solutions were placed in 3 mL quartz cuvettes with optical path lengths of 1 cm. Absorption spectra were recorded using a Lambda 35 UV-vis spectrometer with a wavelength range of 250-700 nm and a scan rate of 600 nm min^{-1}. The photoluminescence spectra were recorded with an excitation wavelength of 300 nm. The absorption spectra and photoluminescence spectra of the samples were measured using a solution of the ligand in DMF (**H_3TAM**: 63 μM; **H_3TAP**: 14 μM) and were measured using a Horiba FluoroMax 4 spectrometer.

The UV-visible absorption of **H_3TAM** and **H_3TAM** show strong $\pi \rightarrow \pi^*$ transitions (**H_3TAP**: λ_{max} = 301 nm, ε = 14,900 M^{-1} cm^{-1}; **H_3TAM**: λ_{max} = 319 nm, ε = 57,700 M^{-1} cm^{-1}) and are red-shifted from that of 1,3,5-triazine (λ_{max} = 272 nm) due to the expansion of the π-conjugation system.[15] **H_3TAM** shows a lower energy absorption and emission due to the closer proximity of the *meta*-substituted heteroatoms leading to a more effective transmission.[16] Broad emissions are observed for both ligands after excitation at their respective λ_{max} absorbance value (**H_3TAP**: λ_{max} = 422 nm; **H_3TAM**: λ_{max} = 480 nm). These are shifted to lower energy compared to ligand 2,4,6-tris(4-(4-ethynylbenzonitrile)phenyl)-1,3,5-triazine (**CN_3TAP**) (λ_{max} = 386 nm) which has a very similar degree of electron conjugation (nitrile groups replacing the carboxylic acid moieties) and has a comparable

absorption spectra.[8] **CN_3TAP** has been employed with Zn(II) centres to produce a luminescent, layered MOF with large 1D void channels. Both **H_3TAP** and **H_3TAM** show promising preliminary results as potential luminescent linkers for use in the synthesis of MOFs, MOLs and MOPs.

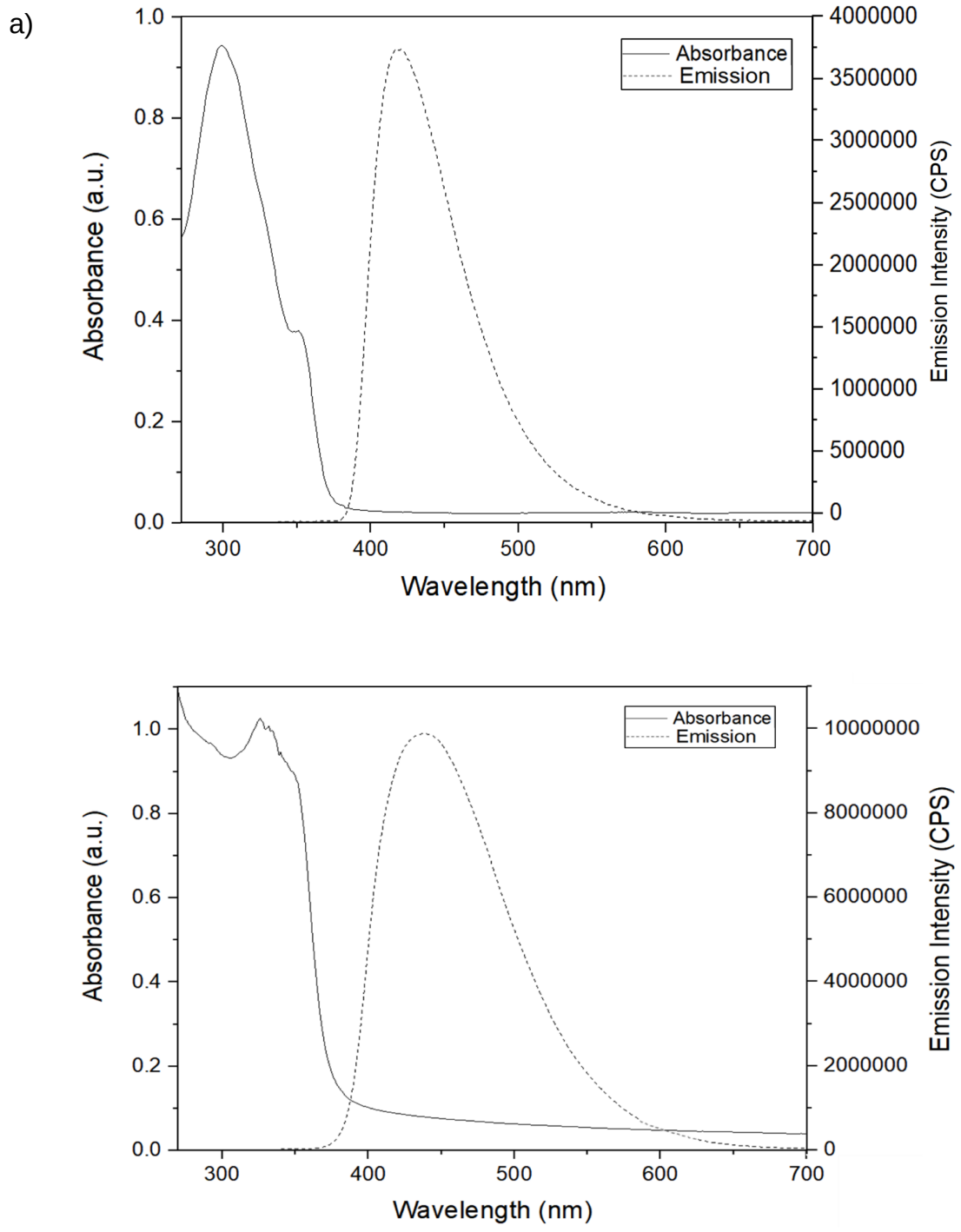

***Figure 4.1.7**: Solution state UV-visible absorption and emission spectra for **H_3TAP** (63 μM) (a) and **H_3TAM** (14 μM) (b) in DMF.*

***Table 4.1.4**: UV-visible absorption and emission data of **H_3TAP** and **H_3TAM** in DMF.*

Ligand	Absorption λ_{max} (nm)	Molar Extinction Coefficient (L mol^{-1} cm^{-1})	Emission in DMF solution λ_{max} (nm)	Stokes Shift (nm)
H_3TAP	301	14,900	422	121
H_3TAM	319	57,700	480	161

4.2 Triazine-Incorporated MOFs

Several crystalline compounds were grown using the ligand **H_3TAP** and a number of metal salts. Single-crystal X-ray diffraction data were collected for four novel MOFs incorporating this ligand. The proligand **H_3TAP** was fully deprotonated during MOF synthesis to form **TAP^{3-}**. Powder X-ray diffraction patterns were also obtained for analysis of the bulk crystalline material and compared with simulated powder patterns calculated from the appropriate single-crystal X-ray diffraction data. Elemental analysis was performed using energy-dispersive X-ray analysis (EDX) and structural stability was determined using thermogravimetric analysis (TGA) to indicate this MOF's suitability for gas absorption.

4.3 $[Cu_2(TAP)_3(H2O)_2]$ ({Cu_2}-MOF-1)

Heating a solution of **H_3TAP** and $Cu(NO_2)_2 \cdot 3H_2O$ in DMF at 70 °C for 48 hours resulted in the formation of green, block-like crystals of $[Cu_2(TAP)_3(H_2O)_2]$ (**{Cu_2}-MOF-1**) with a yield of ca. 45 % that were of suitable quality for analysis using single-crystal X-ray diffraction. This analysis revealed that **{Cu_2}-MOF-1** is a quadruply interpenetrated MOF that crystallises in the tetragonal space group $I\bar{4}$. The asymmetric unit of **{Cu_2}-MOF-1** features four dicopper paddlewheel SBUs linked by four coordinated **TAP^{3-}** ligands. Each carboxylic acid site of the ligand is deprotonated and linked to three paddlewheel building units *via* a bidentate binding mode. Each paddlewheel building unit is connected to four **TAP^{3-}** ligands. Such organisation gives rise to augmented (3,4)-nets and results in augmented (3,4)-**pto** nets, a well-known structure arising from the combination of the vertices of square-shaped and triangular SBUs.[17] This crystal structure is comprised of four structurally identical, interpenetrated (3,4)-coordinated nets (Figure 4.3.1).

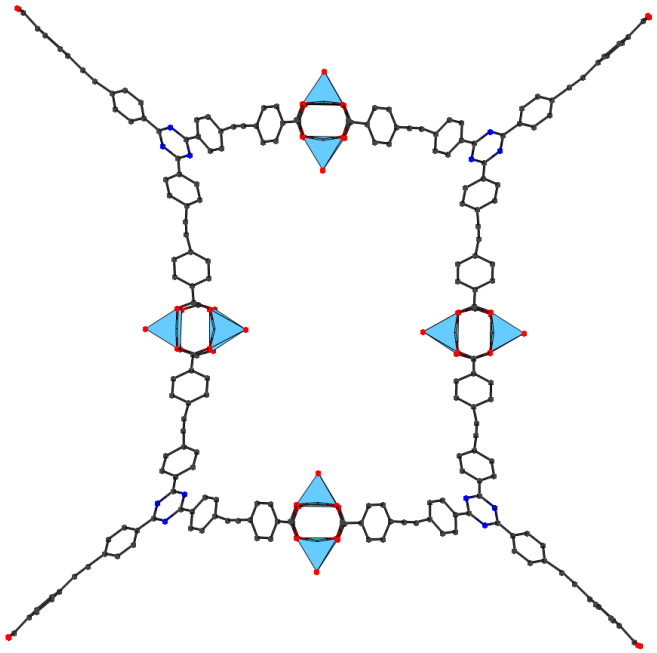

***Figure 4.3.1**: (3,4)-coordinated net of **{Cu$_2$}-MOF-1** viewed in the direction of the crystallographic c-axis. Colour scheme: C, grey; O, red; Cu represented as blue polyhedra. H-atoms omitted for clarity.*

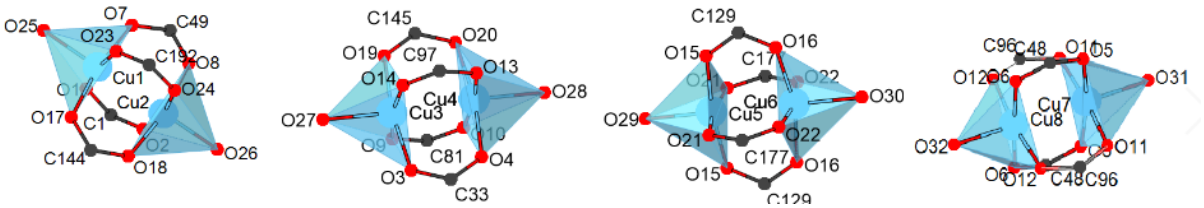

***Figure 4.3.2**: The four dicopper paddlewheels of nets 1-4. Colour scheme: C, grey; O, red; Cu represented as blue polyhedra.*

***Table 4.3.1**: The selected bond lengths (Å) and angles (°) for {**Cu$_2$}-MOF-1** concerning the Cu paddlewheels of nets 1-4.*

Bond Lengths	**Å**	**Bond angles**	**°**
Cu(1)-Cu(2)	2.626(4)	O(7)-Cu(1)-O(1)	88.7(5)
Cu(3)-Cu(4)	2.631(4)	O(7)-Cu(1)-O(25)	94.4(5)
Cu(5)-Cu(6)	2.622(5)	O(1)-Cu(1)-O(25)	93.2(4)
Cu(7)-Cu(8)	2.586(7)	O(8)-Cu(2)-O(2)	91.1(5)
Cu(1)-O(25)	2.122(9)	O(8)-Cu(2)-O(26)	96.0(5)

Cu(1)-O(7)	1.932(12)	O(2)-Cu(2)-O(26)	96.3(5)
Cu(2)-O(8)	1.962(13)	O(19)-Cu(3)-O(14)	88.8(4)
Cu(2)-O(2)	1.969(12)	O(19)-Cu(3)-O(9)	90.1(4)
Cu(2)-O(26)	2.101(12)	O(14)-Cu(3)-O(9)	169.1(5)
Cu(3)-O(19)	1.931(10)	O(19)-Cu(3)-O(27)	92.4(4)
Cu(3)-O(14)	1.950(10)	O(14)-Cu(3)-O(27)	92.9(4)
Cu(3)-O(9)	2.033(11)	O(9)-Cu(3)-O(27)	98.0(4)
Cu(3)-O(27)	2.185(10)	O(10)-Cu(4)-O(20)	90.4(4)
Cu(1)-O(1)	1.969(12)	O(10)-Cu(4)-O(13)	170.8(5)
Cu(4)-O(10)	1.982(11)	O(20)-Cu(4)-O(13)	90.8(4)
Cu(4)-O(20)	2.013(10)	O(10)-Cu(4)-O(28)	92.4(4)
Cu(4)-O(13)	2.014(11)	O(20)-Cu(4)-O(28)	97.5(4)
Cu(4)-O(28)	2.213(8)	O(13)-Cu(4)-O(28)	96.5(4)
Cu(5)-O(14)	1.920(12)	O(14)-Cu(5)-O(29)	94.6(4)
Cu(5)-O(29)	2.112(12)	O(16)-Cu(6)-O(30)	97.8(4)
Cu(1)-O(25)	2.122(9)	O(11)-Cu(7)-O(31)	93.2(4)
Cu(6)-O(16)	1.975(11)	O(12)-Cu(8)-O(32)	94.2(5)
Cu(6)-O(30)	2.143(14)	O(2)-C(1)-O(1)	127.5(16)
Cu(7)-O(11)	1.912(13)	O(4)-C(33)-O(3)	127.3(14)
Cu(7)-O(31)	2.18(2)	O(6)-C(48)-O(5)	138.7(18)
Cu(8)-O(12)	1.908(14)	O(8)-C(49)-O(7)	124.7(16)
Cu(8)-O(32)	2.10(2)	O(10)-C(81)-O(9)	126.3(16)

The three nitrogen atoms in the triazine ring of **TAP^{3-}** allow the peripheral phenyl rings to be coplanar with the triazine core. The average dihedral angle between the three peripheral phenyl rings of the ligand is 7.0°, as opposed to 36.2° seen in the triphenyl-substituted benzene based ligand, **H$_3$BTB**, used in interwoven MOF-14.[18] This ensures delocalisation of π-electrons and strong inter-ligand π-π interaction, leading to an interpenetrated MOF, seen previously in MOF-338.[19] The extension of the ligand from the triazine-based ligand, **TAPB**, in MOF-338 to **H$_3$TAP**, leads to both the enlargement of the cage size in each net from 27.1 Å to *ca.* 31.3 Å in **{Cu$_2$}-MOF-1** but also allows for a higher degree of interpenetration, from two-fold to four-fold. The unit cell of **{Cu$_2$}-MOF-1** with topological representation of the (3,4)-nets can be seen in Figure 4.3.3.

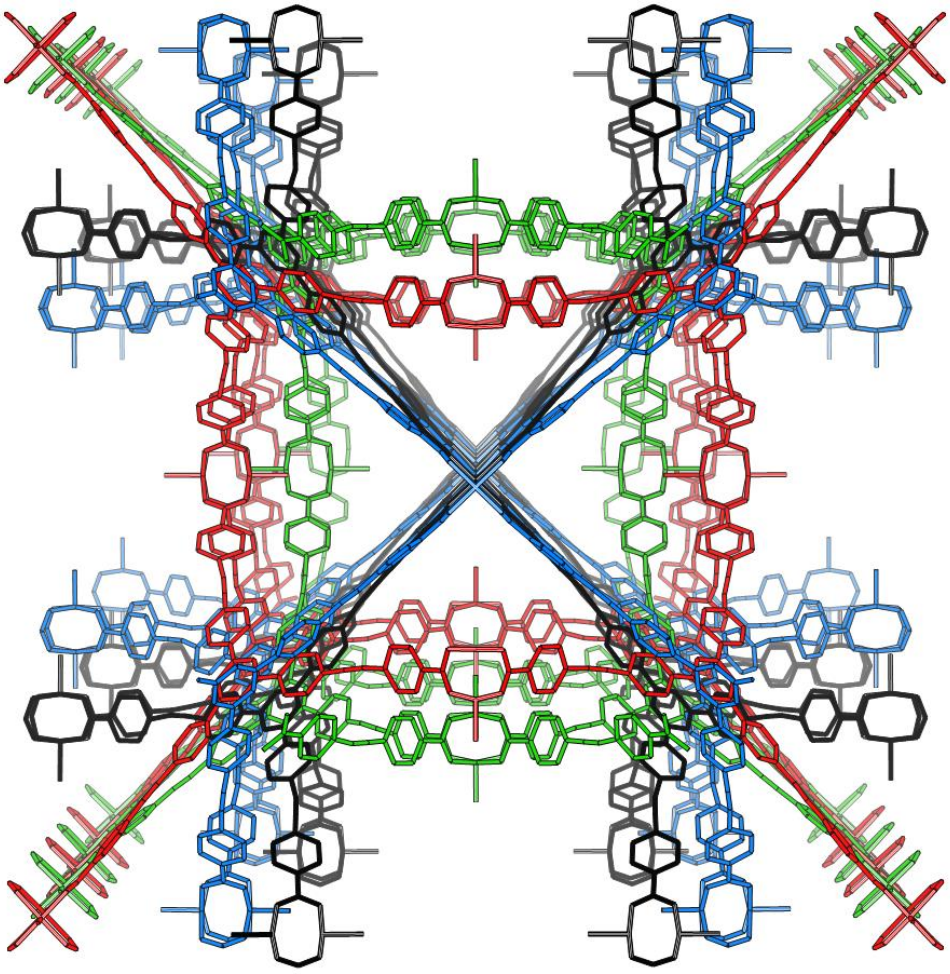

***Figure 4.3.3**: **{Cu$_2$}-MOF-1** viewed down the c-axis showing depth-fading, with each net coloured; Net 1 (blue), Net 2 (green), Net 3 (black), Net 4 (red).*

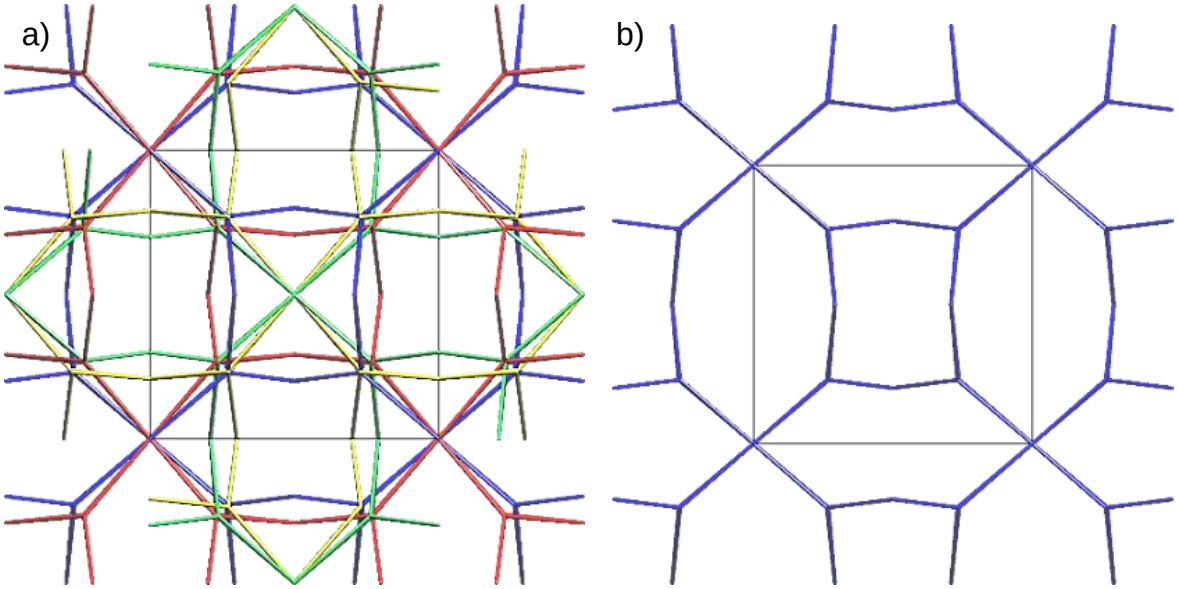

***Figure 4.3.4**: a) Schematic representation of **{Cu$_2$}-MOF-1** represented by (3,4) nets viewed down the c-axis. b) Single net showing cage size typical to **pto** structures.*

The triazine rings from different nets that overlap with slight displacement, destroying the 3-fold rotational symmetry. Inter-net displacement of triazine rings of two ligands was found to be *ca.* 3.46 Å seen along the [111] direction in Figure 4.3.4. Such interaction is typical of triazine-based MOFs and facilitates close packing of the structure.[20] The distances between paddlewheel centres facing each other within a net did not vary between different nets (19.4 and 26.4 Å), not seen in dual-interpenetrated structures. **{Cu$_2$}-MOF-1** has a maximum cavity diameter of 10.4 Å, with smaller channels of 8.4 Å, a theoretical void volume of 80.17% and a crystal density of 0.47 g/cm^3. The structure contains larger cavities and a bigger void volume than that MOF-14 (67 %, 0.53 g/cm^3) but smaller than MOF-388 (84 %, 0.34 g/cm^3) despite the extensions of the ligand, due to the higher degree of self-catination.[21]

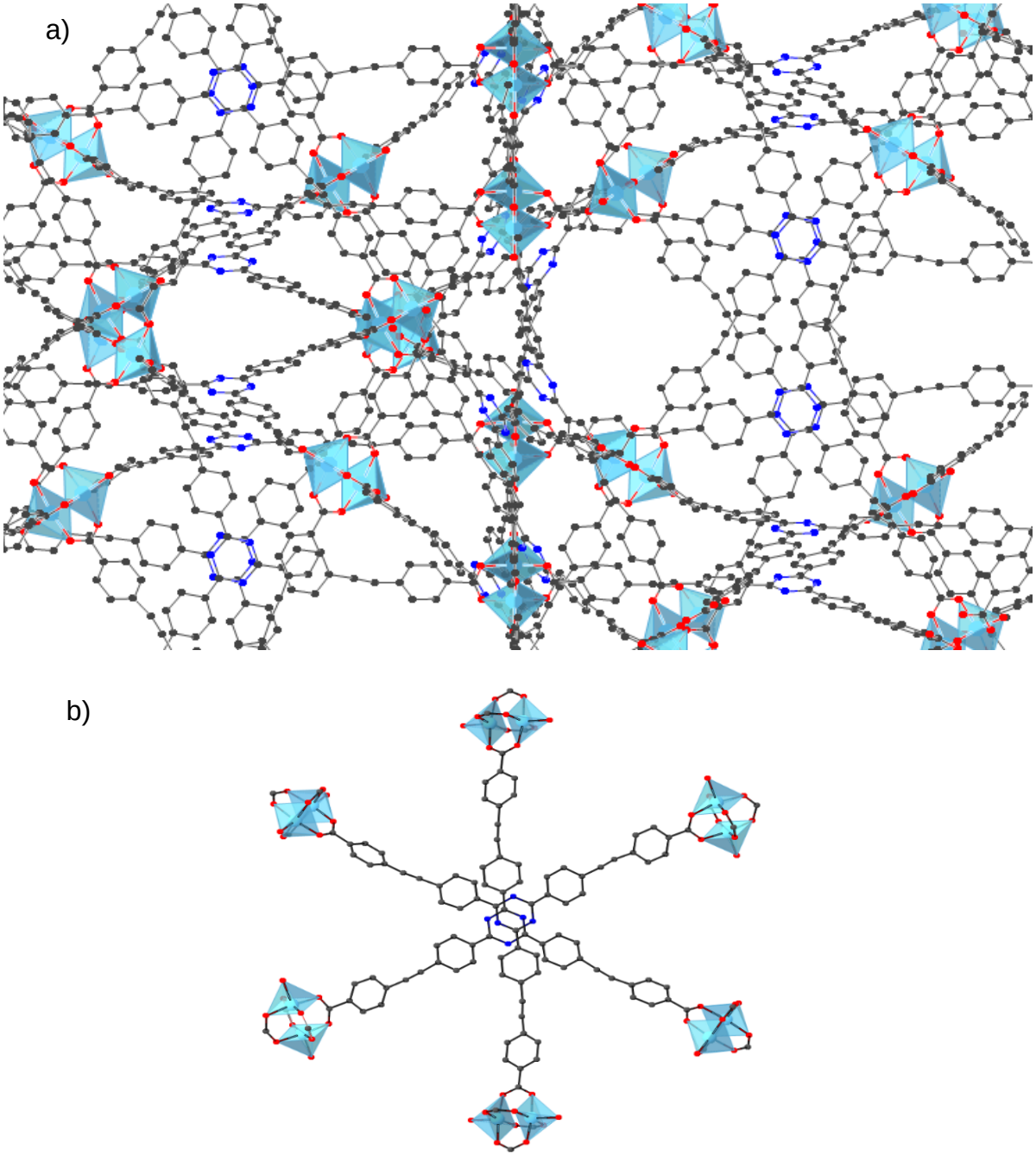

***Figure 4.3.5**: a) {**Cu₂**}-**MOF-1** viewed in the [111] direction. b) π-stacking of **TAP**$^{3-}$ through triazine rings (between net 1 and 2) can be seen with centroid-centroid distances of ca. 3.46 Å. Net 3, net 4 and hydrogen atoms were omitted for clarity. Colour scheme: C, grey; O, red; Cu represented as blue polyhedra. H-atoms omitted for clarity.*

***Table 4.2.2**: Crystallographic table for {**Cu₂**}-**MOF-1**.*

Identification code	**{Cu₂}-MOF-1**
Empirical formula	$C_{12.33}H_{12}Cu_{0.67}N_{1.33}O_{3.33}$
Formula weight	382.68 g mol^{-1}

Temperature	214(2) K
Wavelength	1.54178 Å
Crystal system	Tetragonal
Space group	I -4
Unit cell dimensions	a = 46.521(10) Å
	α = 90°
	b = 46.521(10) Å
	β = 90°
	c = 45.299(11) Å
	γ = 90°
Volume	98033(50) $Å^3$
Z	72
Density (calculated)	0.467 Mg/m^3
Absorption coefficient	0.501 mm^{-1}
F(000)	14064
Crystal size	0.17 x 0.10 x 0.05 mm^3
Theta range for data collection	4.031 to 38.106°.
Index ranges	$-10 \leq h \leq 37$, $-28 \leq k \leq 37$, $-36 \leq l \leq 36$
Reflections collected	56484
Independent reflections	25460
Completeness to theta = 38.106°	97.9 %
Max. and min. transmission	0.7475 and 0.2730
R_{int}	0.0655
Data / restraints / parameters	25460 / 164 / 657
Goodness-of-fit on F^2	0.909
Final R indices [I>2sigma(I)]	R1 = 0.0718, wR2 = 0.1866
R indices (all data)	R1 = 0.1193, wR2 = 0.2067
Absolute structure parameter	0.45(6)

4.3.1.1. Powder X-ray diffraction

In order to confirm the phase-purity of the bulk synthesis of {**Cu_2}-MOF-1**, the MOF was synthesised in bulk and ground into a powder to characterise using PXRD. The PXRD pattern was measured in a quartz capillary in DMF at 220 K to obtain low angle peaks and to avoid loss of crystallinity associated with solvent evaporation from the sample, as the framework was found to collapse when dry. The measurement reveals that the peak positions closely match the simulated pattern generated using the SCXD data, indicative of a phase-pure product (Figure 4.3.6). A large number signals are visible in the measured pattern

between 2θ = 5 and 15° due the interpenetrating nature of the structure as seen with other quadruple-interpenetrated dicopper-based MOFs.[22] Variations in peak intensity between the experimental and simulated patterns can be attributed to the morphology and preferred crystallographic orientation of the sample in the capillary.[23]

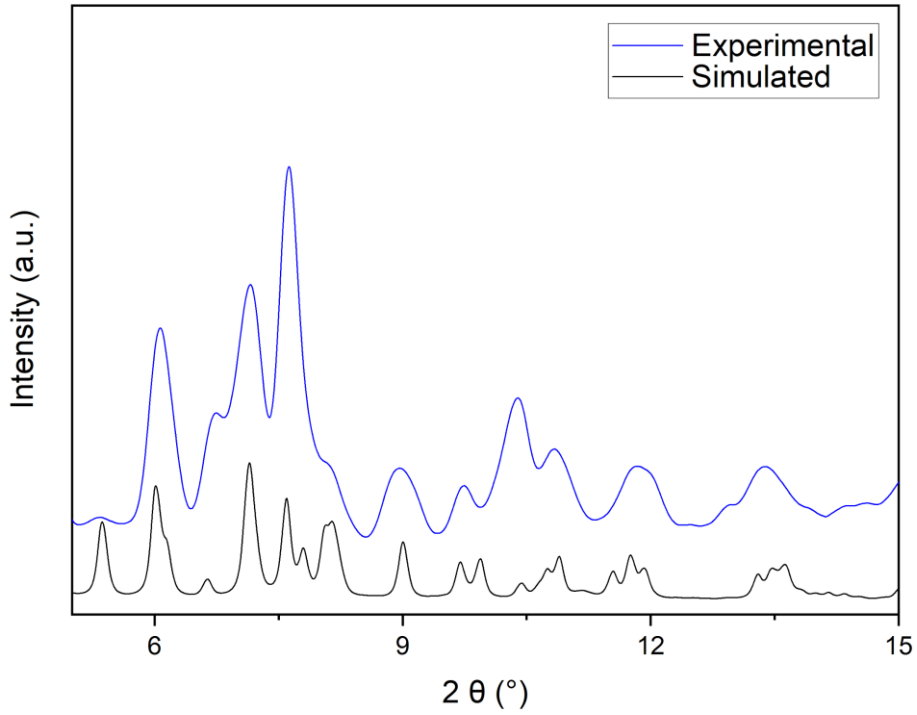

***Figure 4.3.6**: Experimental PXRD pattern of crystals of **{Cu₂}-MOF-1** measured in a capillary (blue) compared with the simulated diffraction pattern from the single crystal data of this MOF (black).*

4.3.1.2. FT-IR and Raman spectroscopy

FT-IR spectroscopy was employed to confirm the existence of functional groups within a sample of **{Cu₂}-MOF-1**. Figure 4.3.7 shows the FT-IR spectra of **{Cu₂}-MOF-1**. The FT-IR spectrum of **{Cu₂}-MOF-1** was recorded and compared to the FT-IR spectrum of **H₃TAP**. The data reveals a strong correlation between the MOF and the ligand. A weak band at 2900 cm^{-1} in the spectrum of **{Cu₂}-MOF-1** corresponds to C-H stretches predominantly deriving from the DMF molecules within the pores of the MOF. Thus, this stretch is not visible in the spectrum of **H₃TAP**. At 1602 and 1572 cm^{-1} in **{Cu₂}-MOF-1** and 1603 and 1566 cm^{-1} in **H₃TAP**, vibrations corresponding to C=C bond vibrations of aromatic moieties are observed.[24] Weak bands are observed at 1014 and 777 cm^{-1}, in the FT-IR spectrum of **{Cu₂}-MOF-1** which are attributed to δ(C–H) and γ(C–H) vibrations of the aromatic rings, respectively. The spectrum of **H₃TAP** confirms the presence of carboxylic

acid groups, with in/out of plane C=O, C-O and O-H stretches, appearing at 1661, 1263 and 1014 cm^{-1}, respectively. In the spectrum of **{Cu₂}-MOF-1**, asymmetric and symmetric carboxylate COO^- stretches can be seen at 1513 and 1360 cm^{-1}, respectively, yield a Deacon-Phillips Δ value of 153 cm^{-1}, which agrees with the observed bidentate bridging binding mode found in the dicopper paddlewheel SBU.[25,26]

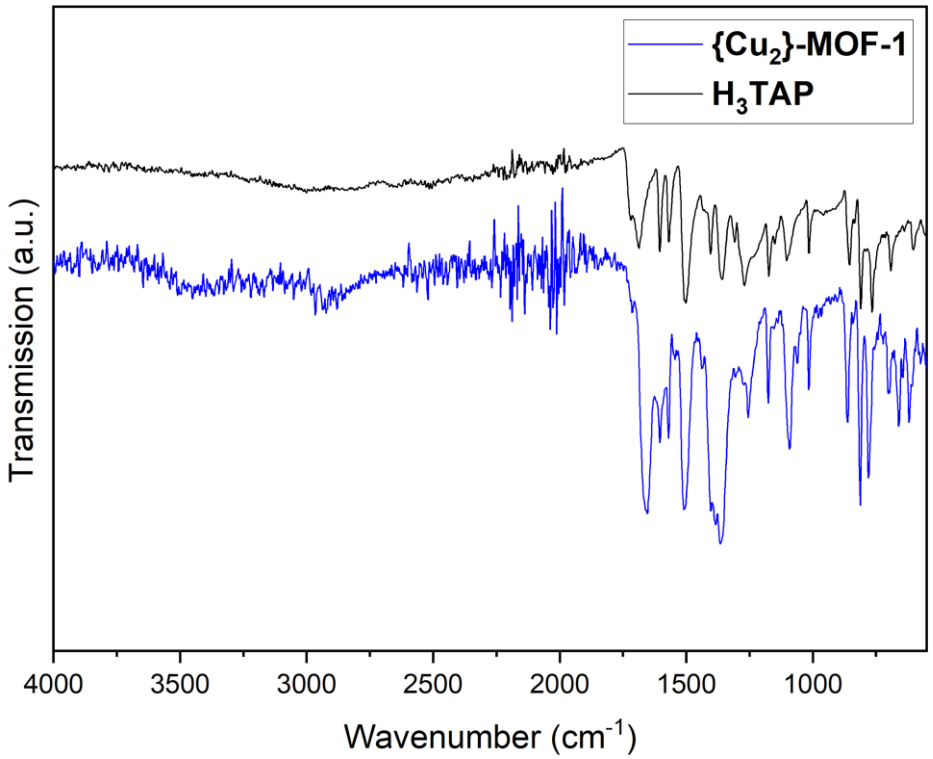

***Figure 4.3.7**: FT-IR spectra of **{Cu₂}-MOF-1** (blue) and **H₃TAP** (black).*

The Raman spectrum of **{Cu₂}-MOF-1** is dominated by ligand-derived stretches, further confirming the presence of the ligand in the MOF (Figure 4.3.8). The signal found at 2218 cm^{-1} derives from the alkyne C≡C vibration in the spectrum of **{Cu₂}-MOF-1** and **H₃TAP**. In the ligand spectrum**,** the most intense signals in the spectra derive from the aromatic C=C bond vibrations and appear at 1605 and 1512 cm^{-1}. The signals at 990 cm^{-1} for both the MOF and the ligand derive from CH_2 rocking vibrations. The signal at 987 cm^{-1} is indicative of the C=N bond vibrations associated with the central triazine ring of **H₃TAP**. There is no detectable shift for the signals of $\mathbf{TAP^{3-}}$ in relation to the ligand's incorporation into **{Cu₂}-MOF-1**.

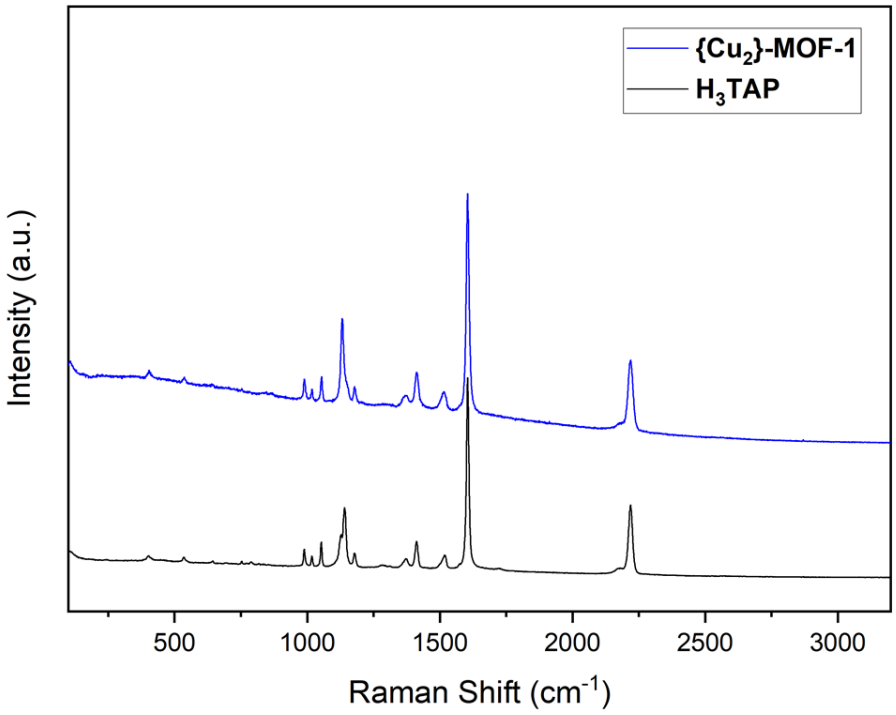

***Figure 4.3.8**: Raman spectra of **{Cu₂}-MOF-1** (blue) and **H₃TAP** (black).*

4.3.1.3. Scanning electron microscopy and energy dispersive spectroscopy

Crystals of **{Cu₂}-MOF-1** were drop casted from DMF onto a silicon wafer attached to an aluminium stub mount and dried in air for 24 hours. The use of a silicon wafer instead of the standard carbon adhesive tab allowed for the Cu:C:O ratio to be examined. The sample was examined using scanning electron microscopy (SEM) and energy-dispersive X-ray (EDX) spectroscopy using a Zeiss ULTRA Plus scanning microscope (Figure 4.3.9). The EDX analysis was carried out using a 20 mm^2 Oxford Inca detector with an acceleration voltage of 20 kV. The obtained atomic ratio was 1:33:6, is in reasonable agreement with the expected value 1:35:5 for **{Cu₂}-MOF-1**, corresponding to the molecular formula $[Cu_2(\mathbf{TAP})_3(H_2O)_2] = C_{70}H_{46}Cu_2N_6O_{10}$. The N Kα could not be resolved from the EDX spectra as it overlaps with the C Kα and O Kα.

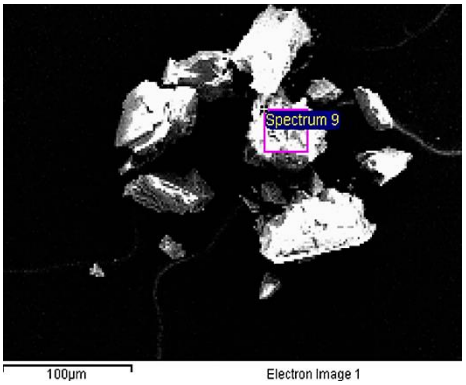

Element	*Weight %*	*Atomic (%)*
C Kα	74.47	83.26
O Kα	18.21	15.24
Cu L	7.12	1.51

***Figure 4.3.9**: SEM image (left) and EDX analysis (right) of **{Cu$_2$}-MOF-1**.*

4.3.1.4. UV-vis and photoluminescence spectroscopy

Due to the luminescent properties demonstrated by **H$_3$TAP**, UV-vis absorption and spectral photoluminescence studies were performed on **{Cu$_2$}-MOF-1**. The absorption spectra were recorded on Lambda 35 UV-vis spectrometer with a wavelength range of 250-700 nm and a scan rate of 600 nm min^{-1} The photoluminescence spectra were measured using a Horiba FluoroMax 4 spectrometer with an excitation wavelength of 350 nm. The absorption spectra and photoluminescence spectra of {**Cu$_2$}-MOF-1** was measured using a suspension of the MOF in DMF. As the concentration cannot be quantified, the absorbance units are normalised and only the λ_{max} values are considered.

The UV-visible absorption spectrum of **H$_3$TAP** shows strong $\pi \rightarrow \pi^*$ transitions with a λ_{max} = 301 nm (Section 4.1.3). For **{Cu$_2$}-MOF-1**, this excitation is red-shifted, with a λ_{max} = 335 nm. Photoluminescence studies of **{Cu$_2$}-MOF-1** showed that the excitation of the sample produces the same luminescence band at 420 nm. The intense blue luminescence signal is noted in previously reported MOFs with triazine ligands, and results from ligand $\pi \rightarrow \pi^*$ transitions as seen in the photoluminescence spectrum of **H$_3$TAP**.[8]

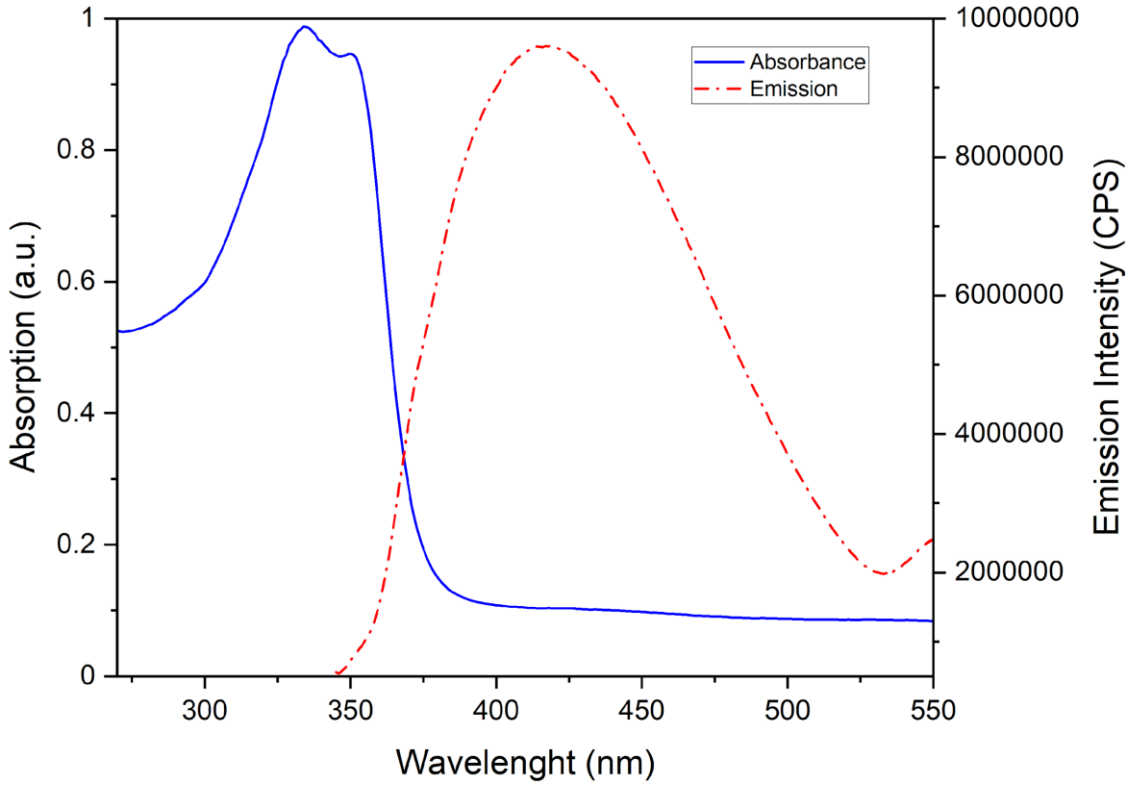

***Figure 4.3.10**: UV-vis (blue) and* photoluminescence *(red) spectra of **{Cu$_2$}-MOF-1**.*

4.3.1.5. Thermogravimetric analysis

Thermogravimetric analysis of **{Cu$_2$}-MOF-1** was performed under an N_2 atmosphere at a heating rate of 3 °C per minute (Figure 4.3.11) between 25 and 900 °C. The resulting TGA trace reveals an initial weight loss of *ca.* 61 % between 25 and 110 °C which can be attributed to the loss of the coordinated H_2O molecules and DMF solvent molecules in the pores. Two-step decomposition of triazine based ligands has been previously reported.[27] The thermogravimetric step of *ca.* 20 % is observed between 300 to 350 °C which derives from the initial decomposition step of the **TAP^{3-}** ligands. There is a further weight loss of *ca.* 26.5% between 350 and 800 °C that results from a gradual decomposition of the organic ligand.

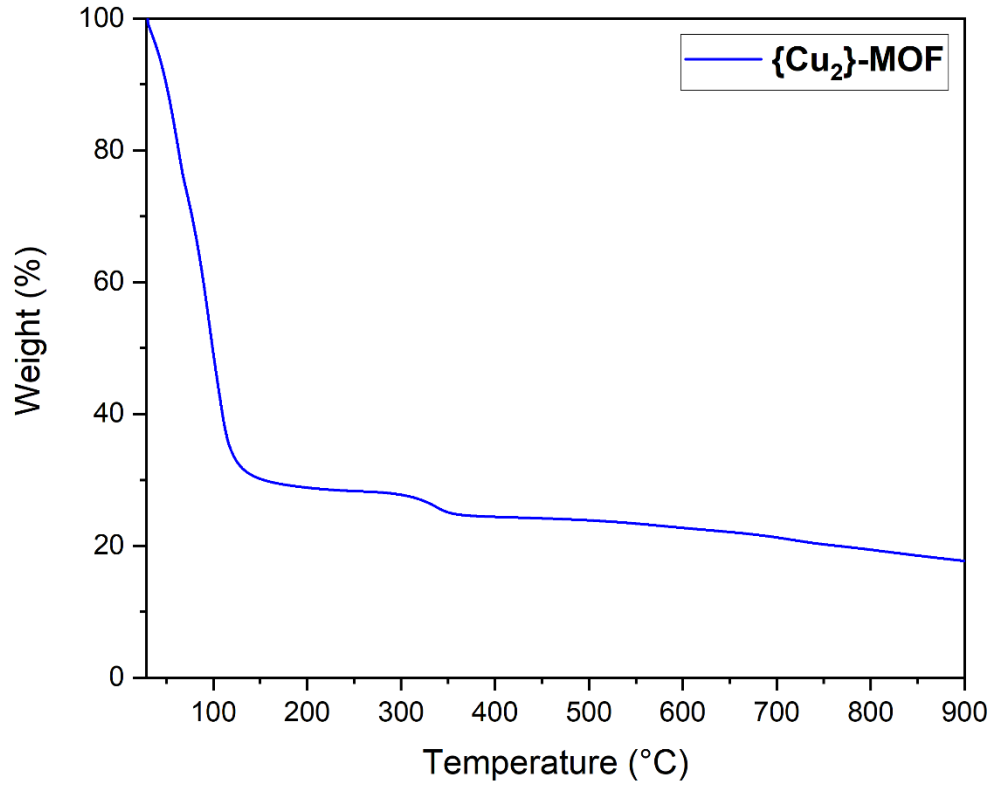

***Figure 4.3.11**: TGA analysis of **{Cu₂}-MOF-1**.*

4.4 [Cu₂(TAP)₃(DMF)₂] ({Cu₂}-MOF-2)

{Cu₂}-MOF-2 forms green needles from **H₃TAP** and $Cu(NO_3)_2 \cdot 3H_2O$ in DMF at 90 °C, with the empirical formula [Cu_2(**TAP**)$_3$(DMF)$_2$]. A yield of *ca.* 5 % was obtained. **{Cu₂}-MOF-2** crystallises in the trigonal space group $R\bar{3}c$. One third of the formula unit comprises the asymmetric unit and the remainder was generated by symmetry operations, about 2- and 3-fold symmetry axes. The crystal structure contains (3,4)-coordinated nets incorporating dicopper paddlewheels and **TAP**$^{3-}$ ligands, structurally identical to **{Cu₂}-MOF-1**, but here contains five distinct nets leading to quintuple-fold interpenetration. The higher temperature used in this synthesis may result in a higher degree of interpenetration. Coordinated DMF molecules locate at the apical positions of the dicopper paddlewheels in **{Cu₂}-MOF-2**.

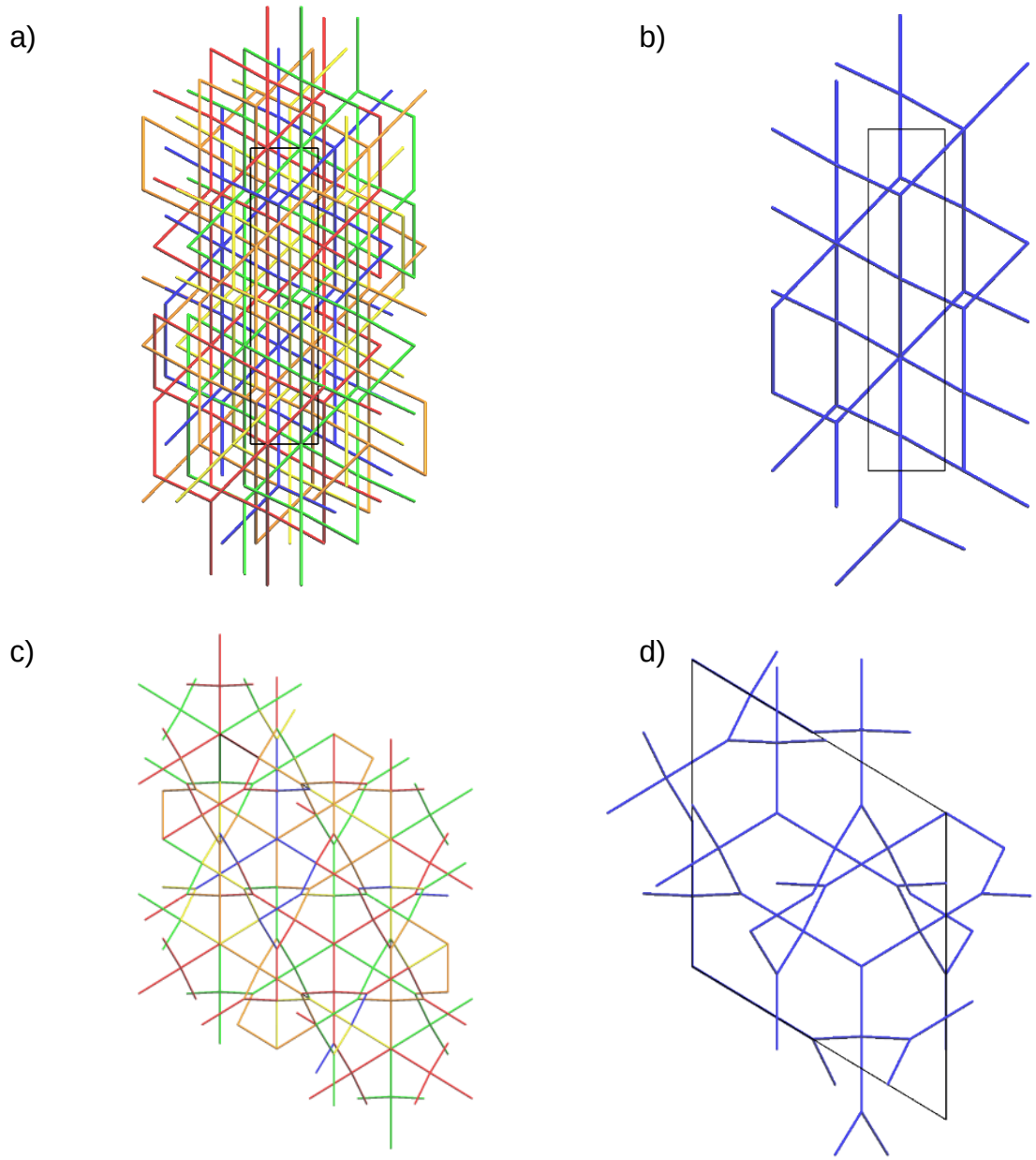

***Figure 4.4.1**: a) Schematic representing the five (3,4)-coordinated nets in {**Cu$_2$**}-MOF-2 down the crystallographic b-axis. b) A single net is represented adjacent in blue. **c)** The schematic representing the five (3,4) nets in {**Cu$_2$**}-MOF-2 down the crystallographic c-axis. d) A single net is represented in blue.*

Interestingly, the triazine rings align along the crystallographic *c*-axis but the average centroid-centroid distance between neighbouring rings was found to be *ca.* 6.8 Å. This lies outside the normal bounds of π-π-stacking interactions for triazine rings, for which maximum distances of *approx.* 4 Å are considered.[28] Instead, crystal assembly occurs through π-π interactions between phenyl rings peripheral to the central triazine rings (Figure

4.4.2, a)), with centroid-centroid distances of *ca.* 3.7 Å. This results in the formation of pseudo-1D organic chains extending in the [111] direction (Figure 4.4.2. b)) and rationalises the dense packing of the crystal structure as inter-net point of contacts are found at this site and not at triazine stacking channels. **{Cu_2}-MOF-2** forms as a mixture with **{Cu_2}-MOF-1** at elevated temperatures and could not be isolated for bulk analysis.

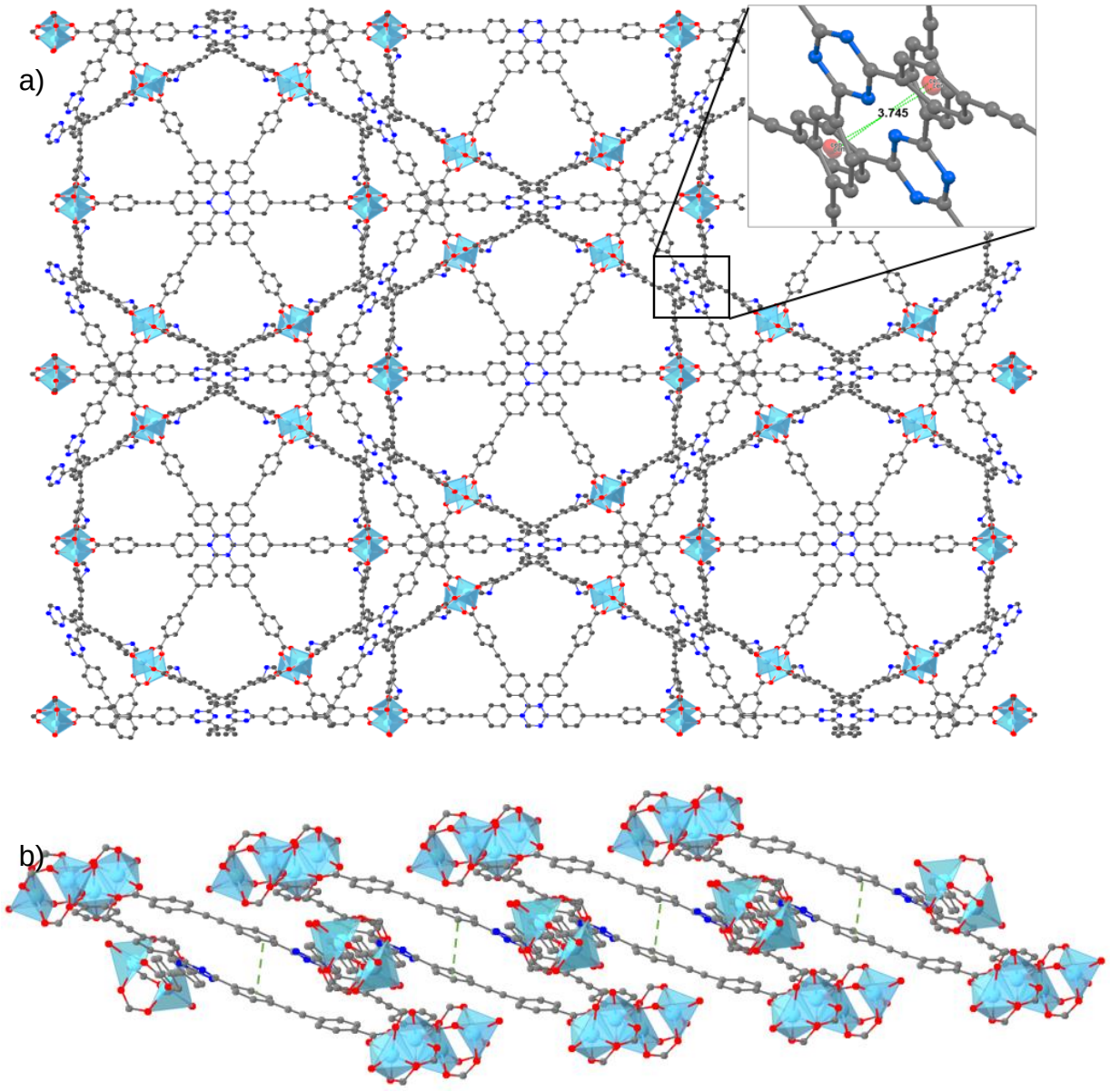

***Figure 4.4.2**: a) {Cu_2}-MOF-2 packing diagram viewed down the c-axis. π-π stacking is highlighted with calculated centroid to centroid distance of 3.745 Å. b) 1D packing along the [111] direction due to π-π interactions. Hydrogen atoms and coordinated DMF molecules were removed for clarity. Colour scheme: C, grey; O, red; Cu represented as blue polyhedra. H-atoms omitted for clarity.*

***Table 4.4.1**: Crystallographic table for {**Cu$_2$**}-MOF-2.*

Identification code	**{Cu$_2$}-MOF-2**
Empirical formula	$C_{70}H_{46}Cu_2N_6O_{10}$
Formula weight	1108.04 g mol^{-1}
Temperature	214(2) K
Wavelength	1.54178 Å
Crystal system	Trigonal
Space group	R -3 c :H
Unit cell dimensions	*a* = 69.823(3) Å
	α = 90°
	b = 69.823(3) Å
	β = 90°
	c = 13.528(4) Å
	γ = 120°
Volume	57116(19) Å^3
Z	42
Density (calculated)	1.353 Mg/m^3
Absorption coefficient	1.334 mm^{-1}
F(000)	23436
Crystal size	0.370 x 0.090 x 0.090 mm^3
Theta range for data collection	12.146 to 45.730°.
Index ranges	$-64 \leq h \leq 41$, $-27 \leq k \leq 64$, $-12 \leq l \leq 12$
Reflections collected	38742
Independent reflections	5186
Completeness to theta = 45.730°	96.9 %
Max. and min. transmission	0.7491 and 0.2806
R_{int}	0.0950
Data / restraints / parameters	5186 / 30 / 406
Goodness-of-fit on F^2	1.041
Final R indices [I>2sigma(I)]	R_1 = 0.0729, wR_2 = 0.1983
R indices (all data)	R_1 = 0.0911, wR_2 = 0.2084
Largest diff. peak and hole	0.311 and -0.309 e.Å^{-3}

4.5 [Zn(TAP)$_3$(H$_2$O)] ({Zn}-MOF)

{Zn}-MOF forms colourless pin-like crystals from **H$_3$TAP** and Zn(NO$_3$)$_2$·3H$_2$O in DMF at 70 °C, with the general formula [Zn(**TAP**)$_3$(H$_2$O)]. It crystallises with a yield of *ca.* 19% in the monoclinic space group *C*2/*c* and possesses two independent zinc ions, coordinated with **TAP^{3-}** and water molecules in the asymmetric unit. The crystal structure features two mononuclear zinc units, each bound by 3 carboxylates of **TAP** *via* a monodentate coordination, resulting in two honeycomb **hcb** nets. The Zn^{2+} centres Zn(1) and Zn(2) display distorted tetrahedral arrangements (Figure 4.5.1). The Zn-O distances range from 1.93(1) to 2.26(2) Å for Zn(1) and 1.97(3) to 2.44(2) Å for Zn(2), in the order Zn – O$_{water}$ < Zn – O$_{ligand}$, with the O-Zn-O bond angles varying from 95.5(7)° to 117.4(7)° for Zn(1) and 94(1)° to 123(1)° for Zn(2). These bond distances and angles are comparable to those of reported for Zn^{2+} coordination polymers containing triangular SBUs and confirms the assignment of the oxidation state.[29,30]

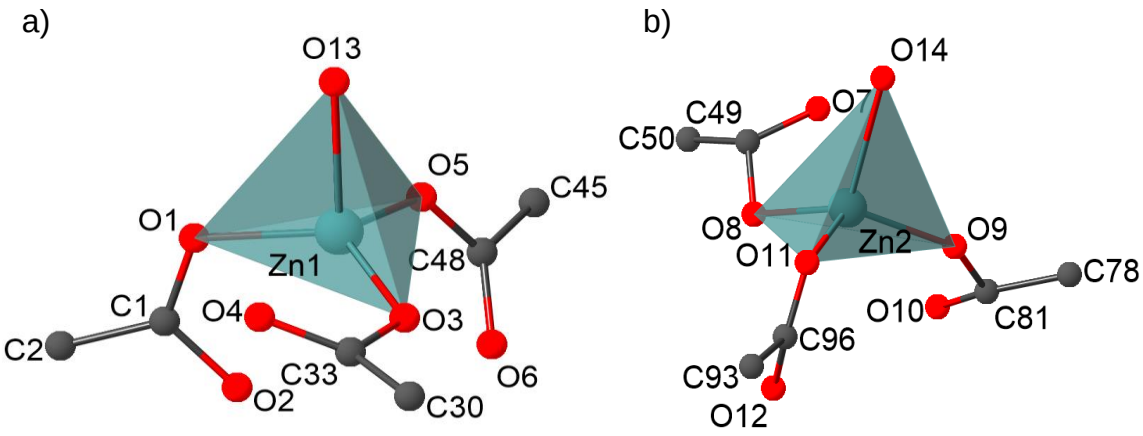

***Figure 4.5.1**: a) Coordination environment for Zn(1) in net 1. b) Zn(2) in net 2. C, grey; O, red; Zn (turquoise, polyhedra bound by {Zn-O} points of extension).*

The structure is composed of two 2D, 3-c, uni-nodal layers giving rise to a **hcb** topology. The monolayers interpenetrate, seen in Figure 4.5.2, at *approx.* 60° with respect to each other. 2D-MOLs are often synthesised from **hcb** nets with stacked layers,[31,32] but tend to form interpenetrated structures with extended ligand systems.[33]

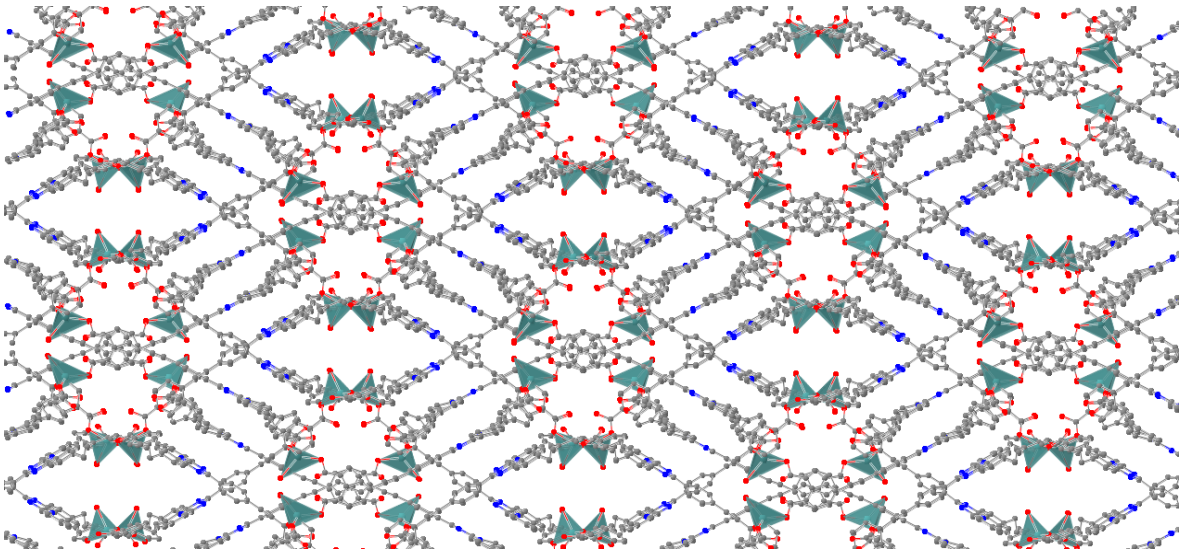

***Figure 4.5.2**: Interpenetration of hexagonal nets along the [111] direction. Hydrogen atoms were removed for clarity. Zn(2) in net 2. Colour scheme: C, grey; O, red; Zn (turquoise, polyhedra bound by {Zn-O} points of extension). H-atoms omitted for clarity.*

In **{Zn}-MOF** interpenetration occurs from extensive π-π stacking and C-H···O bonding arising due to the delocalisation of π-electrons in **H_3TAP** allowing for strong inter-ligand π-π interaction. Triazine rings arrange down the *c*-axis shown in Figure 4.5.3, to allow parallel displacement π-π stacking with centroid-centroid distances of *ca.* 4.2 Å, seen in Zn(II)-based MOFs composed of triazine-containing linkers.[29] Additionally, C-H···O bonding occurs between phenyl rings peripheral to triazines and carboxylate. Hydrogen bond distances range from *ca.* 2.2 Å with a non-coordinated carboxylate oxygen atom to *ca.* 2.5 Å with an oxygen atom directly bound to a zinc node. **{Zn}-MOF** has a large void channel with a diameter of 22.4 Å along the *c*-axis (Figure 4.5.3) and with smaller channels with diameter 6.2 Å which extend in the direction of the *b*-axis.

The structure occupies 33.3% of the unit cell volume and has a crystal density of 0.75 g/cm^3. Bulk analysis of **{Zn}-MOF** was carried out using PXRD, FT-IR and Raman spectroscopy, and EDX mapping which confirmed that the MOF was the only product in the sample. TGA was performed on the bulk sample and showed solvent loss from void channels and ligand stability to *approx.* 360 °C. N_2 gas absorption was attempted on **{Zn}-MOF** after activation at 140 °C but the structure was found to be non-porous after the activation process.

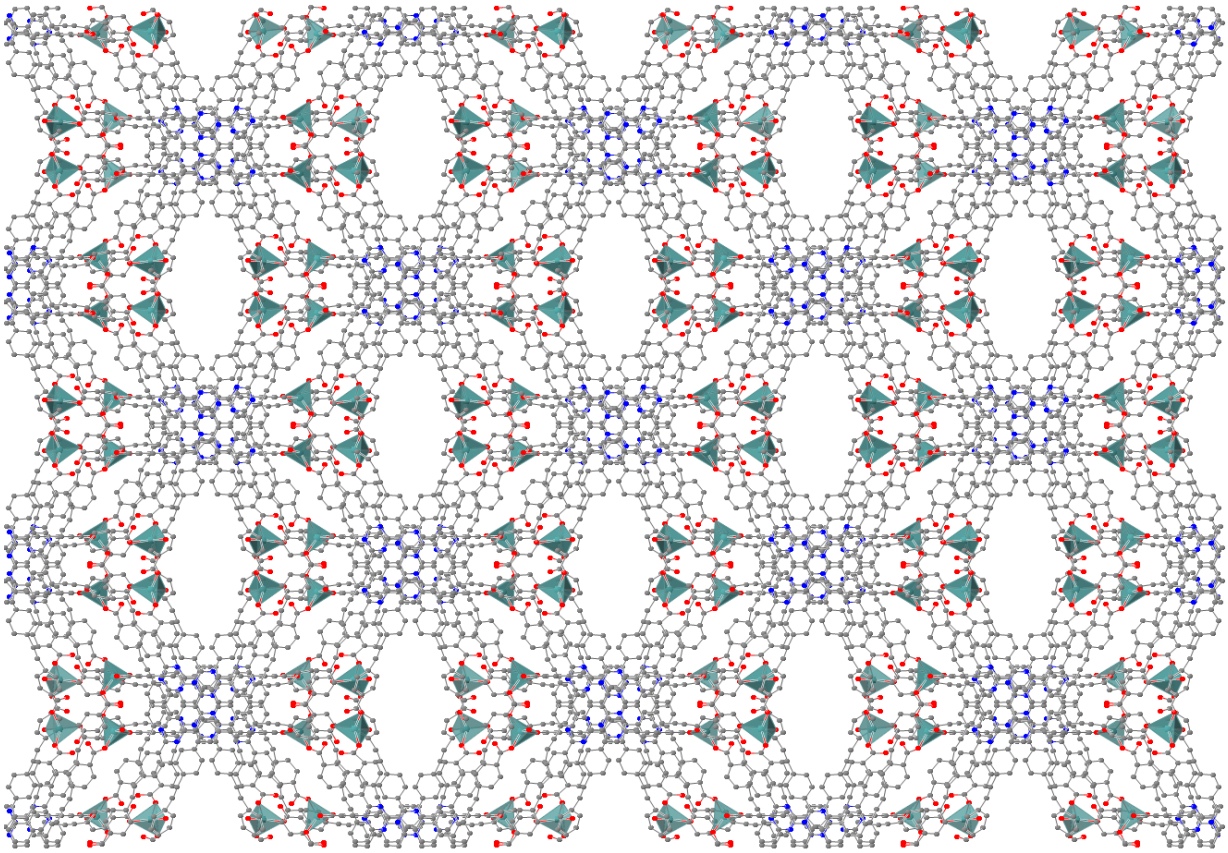

Figure 4.5.3*: Void channels of* ***{Zn}-MOF*** *with diameter of 22.4* Å*, viewed down the crystallographic c-axis. Hydrogen atoms were removed for clarity. H-atoms omitted for clarity.*

Table 4.5.1*: Crystallographic table for {****Zn}-MOF****.*

Identification code	**{Zn}-MOF**
Empirical formula	$C_{32}H_{17.33}N_2O_{4.67}Zn_{0.67}$
Formula weight	548.06 g mol^{-1}
Temperature	214(2) K
Wavelength	1.54184 Å
Crystal system	Monoclinic
Space group	C 2/*c*
Unit cell dimensions	*a* = 36.358(5) Å
	α = 90°
	b = 41.399(5) Å
	β = 128.59(2)°
	c = 24.665(3) Å
	γ = 90°
Volume	29020(9) $Å^3$

Z	24
Density (calculated)	0.753 Mg/m^3
Absorption coefficient	0.732 mm^{-1}
F(000)	6736
Crystal size	0.30 x 0.14 x 0.10 mm^3
Theta range for data collection	1.885 to 36.505°.
Index ranges	$-27 \leq h \leq 28$, $-31 \leq k \leq 31$, $-18 \leq l \leq 19$
Reflections collected	32036
Independent reflections	6944
Completeness to theta = 36.505°	99.6 %
Max. and min. transmission	0.7479 and 0.2567
R_{int}	0.0766
Data / restraints / parameters	6944 / 50 / 314
Goodness-of-fit on F^2	1.897
Final R indices [I>2sigma(I)]	R1 = 0.1789, wR2 = 0.4710
R indices (all data)	R1 = 0.2063, wR2 = 0.4964
Largest diff. peak and hole	0.651 and -0.565 $e.Å^{-3}$

4.5.1.1. Powder X-ray diffraction

The PXRD pattern of **{Zn}-MOF** was measured in a quartz capillary in DMF at 220 K to obtain low angle peaks and to avoid loss of crystallinity associated with solvent evaporation from the sample, as the framework was found to collapse when dry. The measurement reveals that the peak positions in the experimental spectrum aligns with the simulated pattern generated from the single crystal data (Figure 4.5.5). The amount of **{Zn}-MOF** that could be synthesised affected the detail seen in the PXRD spectrum by in conjunction with using a quartz capillary, broadening the signals.

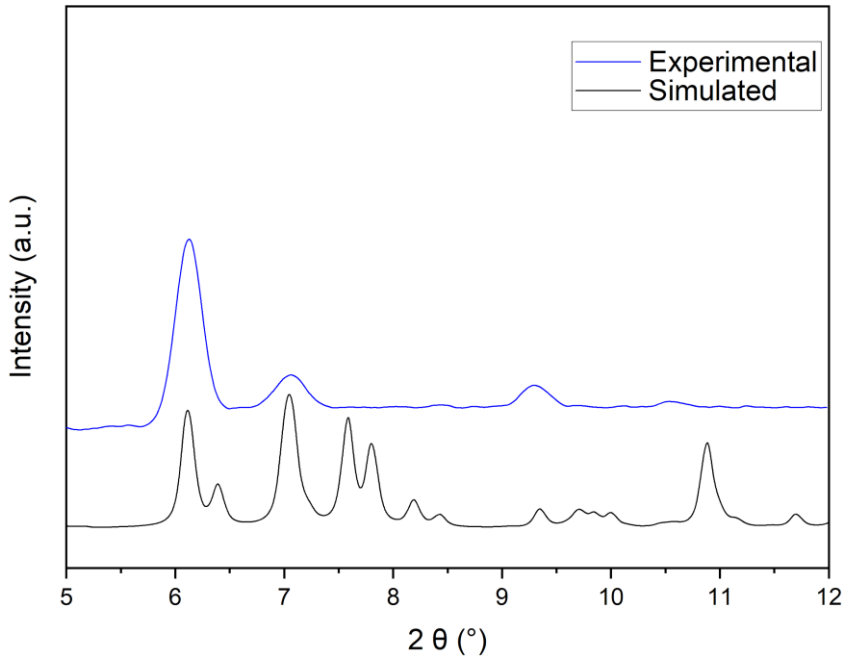

Figure 4.5.5*: PXRD results for the experimental results recorded for* ***{Zn}-MOF*** *(blue) and the simulated powder pattern obtained from the SCXD structure (black).*

4.5.1.2. FT-IR and Raman spectroscopy

FT-IR spectroscopy was performed on **{Zn}-MOF** and the resulting spectrum was compared to the spectrum of **H_3TAP**. The data reveals a strong correlation between the MOF and the ligand. **{Zn}-MOF** gives rise to sharp intensive bands at 1550 and 1386 cm^{-1} which relate to asymmetric and symmetric stretching modes of the coordinated carboxylate moiety, respectively. Weak and narrow signals seen at 1015 and 770 cm^{-1} can be attributed to δ(C–H) and γ(C–H) vibrations of the aromatic rings, respectively. The corresponding resonances in **H_3TAP** at 1014 and 771 cm^{-1} derive from the aromatic ring confirms that the organic ligand is present in the final product. The vibrations at 1608 and 1570 cm^{-1} correspond to C=C bond vibrations in the aromatic groups of **{Zn}-MOF**. The broad band at *approx.* 2930 cm^{-1} is attributed to aliphatic (C–H) stretching vibrations of DMF molecules located within the pores of the MOF.[24]

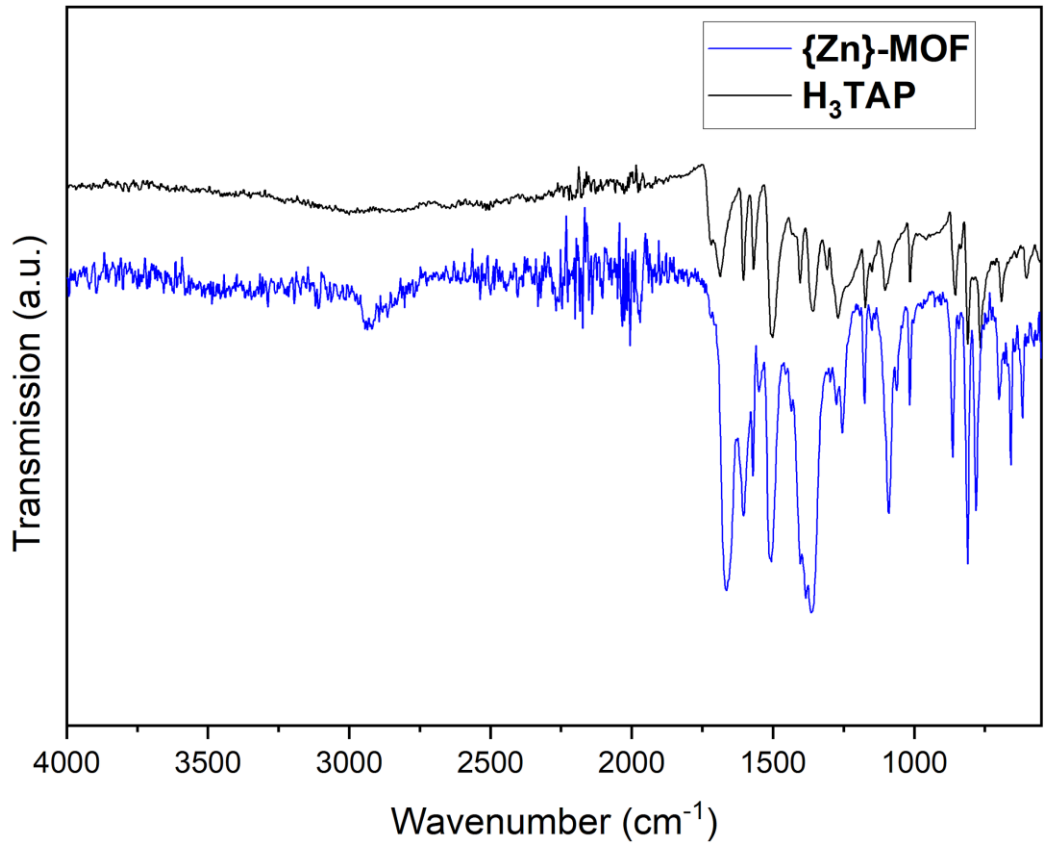

***Figure 4.5.6**: FT-IR spectra of **{Zn}-MOF** (blue) and **H₃TAP** (black).*

As seen for **{Cu₂}-MOF-1**, the signals seen in the Raman spectrum of **{Zn}-MOF** are dominated by ligand-derived stretches without any significant change in the signal positions or intensities when compared to the spectrum of **H₃TAP** (Figure 4.5.7). The resonance at 2219 cm^{-1} corresponds to the alkyne C≡C vibration. Signals arising from the aromatic C=C bond vibrations appear at 1604 and 1514 cm^{-1}, the former of which may also correspond to C=N bonds, appearing in a similar range. The signals at 1112 cm^{-1} for both the MOF and the ligand derive from CH rocking vibrations. Three signals in the range 990 – 1100 cm^{-1} are due to C-C, vibrations.[34]

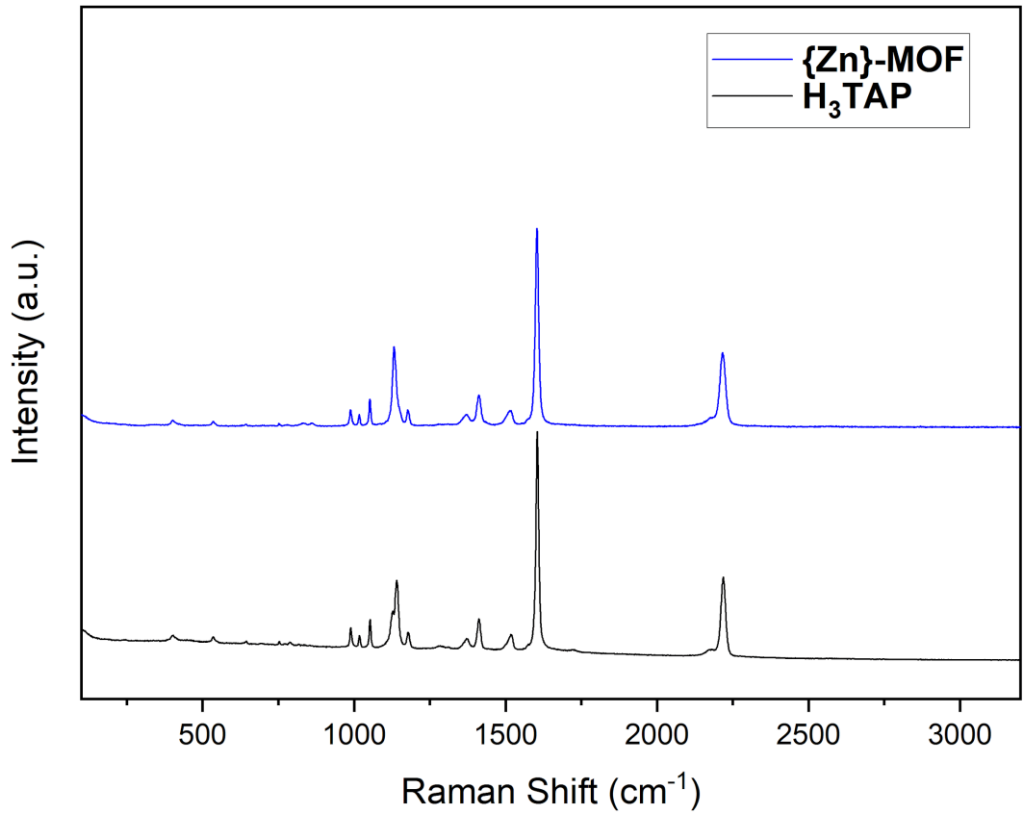

***Figure 4.5.7**: Raman spectra of **{Zn}-MOF** (blue) and **H_3TAP** (black).*

4.5.1.3. Scanning electron microscopy and energy dispersive spectroscopy

{Zn}-MOF was examined using scanning electron microscopy (SEM) and energy-dispersive X-ray (EDX) spectroscopy using a Zeiss ULTRA Plus scanning microscope (Figure 4.5.8). The EDX analysis was carried out using a 20 mm^2 Oxford Inca detector with an acceleration voltage of 20 kV. **{Zn}-MOF** has the molecular formula $C_{48}H_{26}N_3O_7Zn$. The obtained Zn:C:O atomic ratio was 1:53:8, in comparison to the theoretical ratio of 1:48:7 for **{Zn}-MOF**. The N Kα could not be individually resolved from the EDX spectra as it overlaps with the C Kα and O Kα.

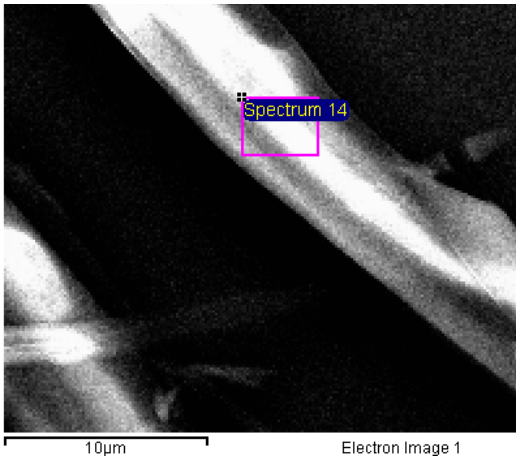

Element	*Weight %*	*Atomic (%)*
C Kα	77.19	86.55
O Kα	9.42	11.84
Zn Kα	2.89	1.61

***Figure 4.5.8**: SEM image (left) and EDX analysis (right) of **{Zn}-MOF**.*

4.5.1.4. UV-vis and emission spectroscopy

The absorption spectra of **{Zn}-MOF** were recorded on a Lambda 35 UV-vis spectrometer at a wavelength range of 250-700 nm and a scan rate of 600 nm min^{-1}. The photoluminescence spectra were measured using a Horiba FluoroMax 4 spectrometer at an excitation wavelength of 350 nm. The absorption spectra and photoluminescence spectra of **{Zn}-MOF** was measured using a suspension of the MOF in DMF and the normalised intensities are reported. **{Zn}-MOF** shows a broad absorbance maximum at λ_{max} = 315 nm. Photoluminescence studies of **{Zn}-MOF** showed that the excitation of the sample produces the same luminescence band at 420 nm and a weaker signal centred at 521 nm resulting from the $\pi \rightarrow \pi^*$ transition in **H_3TAP**, as seen in the ligand photoluminescence spectrum.

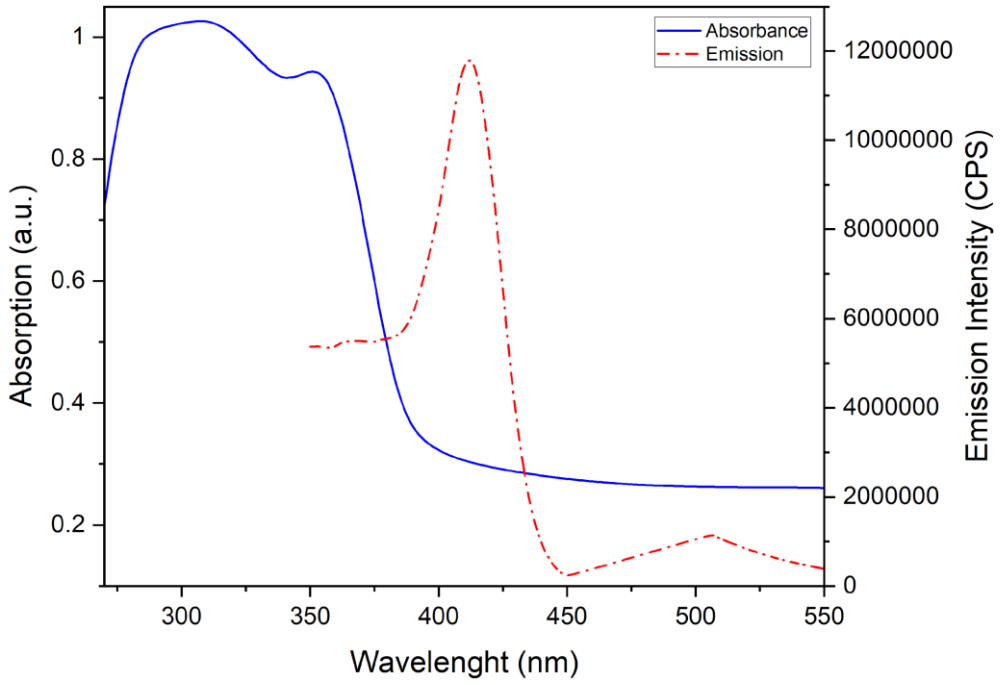

***Figure 4.5.9**: UV-Vis (blue) and photoluminescent spectra (red) of **{Zn}-MOF**.*

2.1.1.1. Thermogravimetric analysis

Thermogravimetric analysis of **{Zn}-MOF** was performed in an N_2 atmosphere at a heating rate of 3 °C per minute (Figure 4.5.10). It reveals an initial weight loss of *ca.* 78% between 25 and 110 °C due to the loss of the constitutional H_2O molecules and DMF solvent molecules in the pores. The thermogravimetric step of *ca.* 20% is observed between 400 – 500 °C which can be attributed to the initial decomposition step of the **TAP**$^{3-}$ ligands. There is a further weight loss of 26.5% between 450 and 800 °C that likely results from the full decomposition of the organic ligand.

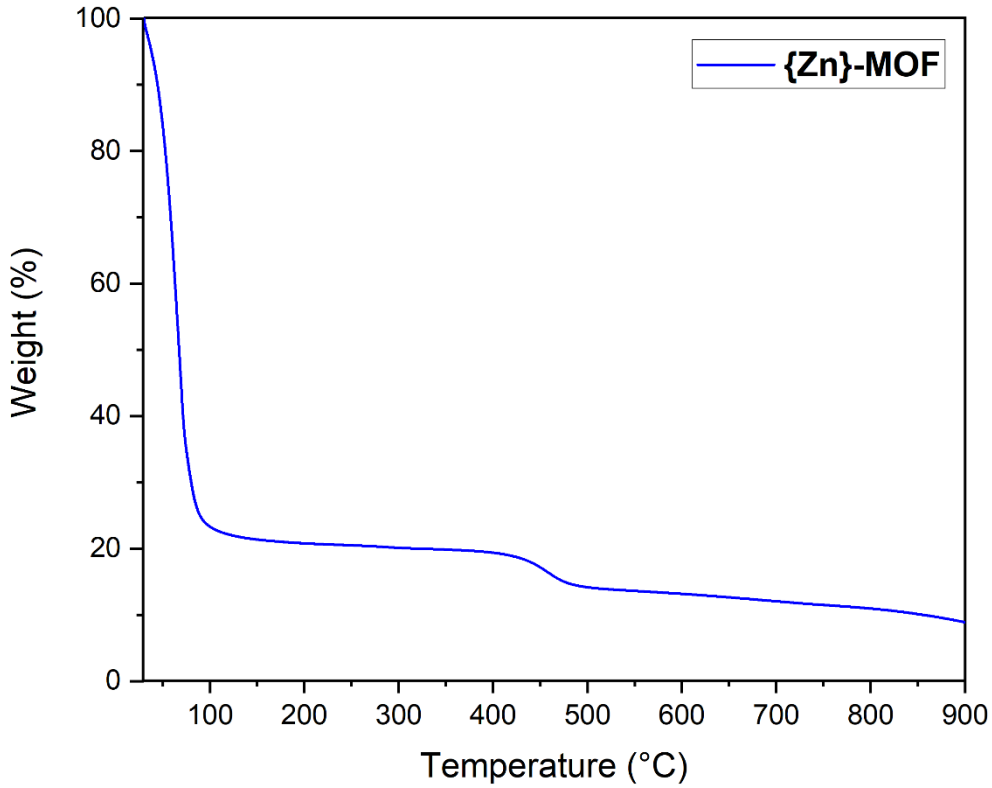

***Figure 4.5.10**: Thermogravimetric analysis of **{Zn}-MOF** from 25 to 900 °C.*

4.6 $[Cd(TAP)_3(H_2O)]$ {Cd}-MOF

The reaction between **H_3TAP** and $Cd(NO_3)_2 \cdot 3H_2O$ in DMF (1.5 mL) at 70 °C resulted in the formation of colourless needle-shaped crystals of **{Cd}-MOF** after 48 hours which were suitable for analysis using single crystal X-ray analysis. This analysis reveals that **{Cd}-MOF** crystallises in the monoclinic space group *C*2/*c* at a yield of 15 %. The MOF was found to be a structural analogue of **{Zn}-MOF** with the empirical formula $[Cd(\mathbf{TAP})_3(H_2O)]$. EDX analysis was also carried out for **{Cd}-MOF** and results were found to be within the error of the expected elemental composition. The full crystallographic refinement could not be completed but from the preliminary data is in line with the crystallographic data obtained for **{Zn}-MOF** and the PXRD of the two structures are identically, suggesting that they are isostructural. Due to limited access to analytical methods, compete bulk TGA characterisation could not be carried out.

***Table 4.6.1**: Crystallographic table for {**Cd}-MOF**.*

Identification code	**{Cd}-MOF**
Empirical formula	$C_{32}H_{17.33}Cd_{0.67}N_2O_{4.67}$
Formula weight	579.41 g mol^{-1}
Temperature	214(2) K
Crystal system	monoclinic
Space group	*C*2/*c*
	a = 36.016(3) Å
	b = 42.053(4) Å
	c = 23.937(2) Å
	α = 90°
	β = 126.230(5)°
	γ = 90°
Volume/$Å^3$	29244(5)
Z	24
ρ_{calc}g/cm^3	0.790
μ/mm^{-1}	2.652
F(000)	7024.0
Radiation	CuKα (λ = 1.54178)
2Θ range for data collection/°	3.696 to 93.676
Index ranges	$-33 \leq h \leq 33$, $-39 \leq k \leq 39$, $-18 \leq l \leq 22$
Reflections collected	73272
Independent reflections	12561 [R_{int} = 0.1090, R_{sigma} = 0.1039]

Data/restraints/parameters	12561/50/305
Goodness-of-fit on F^2	2.337
Final R indexes [I>=2σ (I)]	R_1 = 0.3257, wR_2 = 0.6762
Final R indexes [all data]	R_1 = 0.3675, wR_2 = 0.7049
Largest diff. peak/hole / e $Å^{-3}$	2.48/-1.97

4.6.1.1. Powder X-ray diffraction

The PXRD pattern of **{Cd}-MOF** was measured in a quartz capillary in DMF at 220 K and compared to the experimental powder pattern of the isostructural **{Zn}-MOF**. The measurement reveals that the peak positions and intensities are in agreement with the Zn-analogue (Figure 4.6.1). The major signals for both MOFs were found at 2 θ = 3.8 and 6.1°.

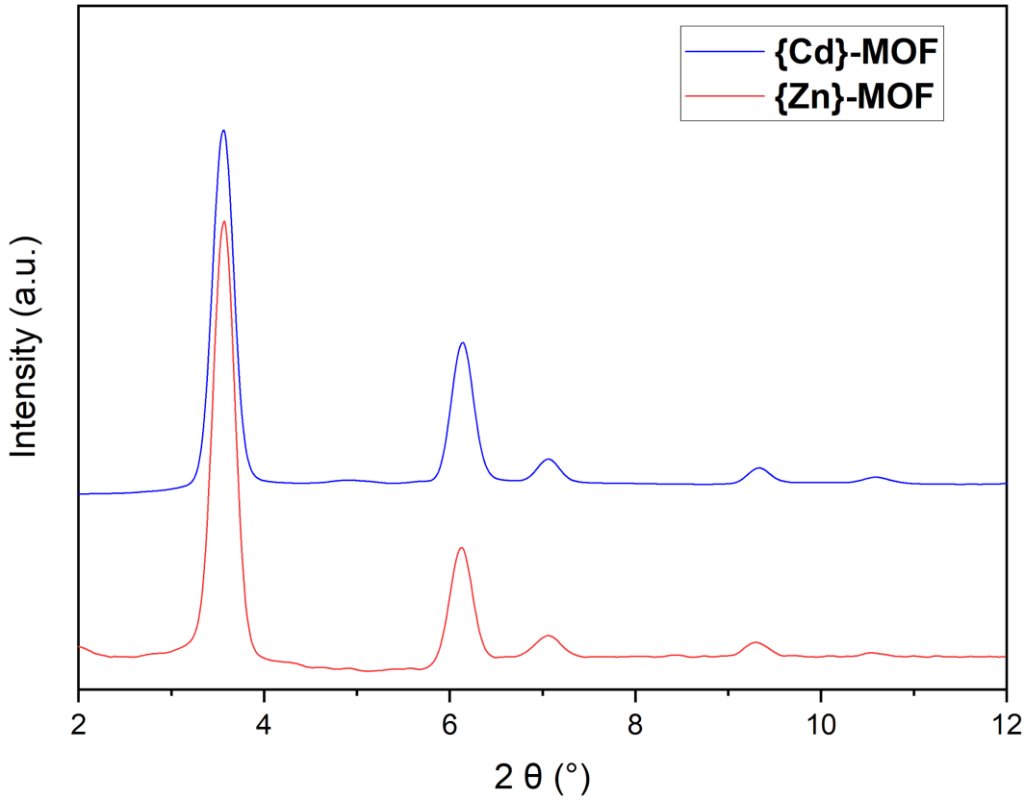

***Figure 4.6.1**: PXRD patterns of experimentally measured crystals of **{Cd}-MOF** (blue) and the PXRD pattern obtained of **{Zn}-MOF** (red). Both samples were measured in a quartz capillary.*

4.6.1.2. FT-IR and Raman spectroscopy

The FT-IR spectrum data was obtained for **{Cd}-MOF** and compared with the spectra of both **{Zn}-MOF** and **H_3TAP**. The data further confirms the correlation between **{Cd}-MOF** and **{Zn}-MOF**. **{Cd}-MOF** gives rise to intensive signals at 1550 and 1386

cm^{-1} which can be attributed to the asymmetric and symmetric stretching modes of coordinated carboxylate moieties, respectively. Weak, sharp signals seen at 1015 and 770 cm^{-1} are attributed to δ(C–H) and γ(C–H) vibrations of the aromatic rings, respectively. The corresponding resonances in **H_3TAP** at 1014 and 771 cm^{-1} deriving form the aromatic rings confirms that the organic ligand is present in the final product. The vibrations at 1608 and 1570 cm^{-1}, correspond to C=C bond vibrations of aromatic groups in **{Cd}-MOF**. The broad band at *approx.* 2930 cm^{-1} is attributed to aliphatic (C–H) asymmetric stretching vibrations of DMF within the pores of the MOF. This signal is not present in the spectrum of **H_3TAP**.[24]

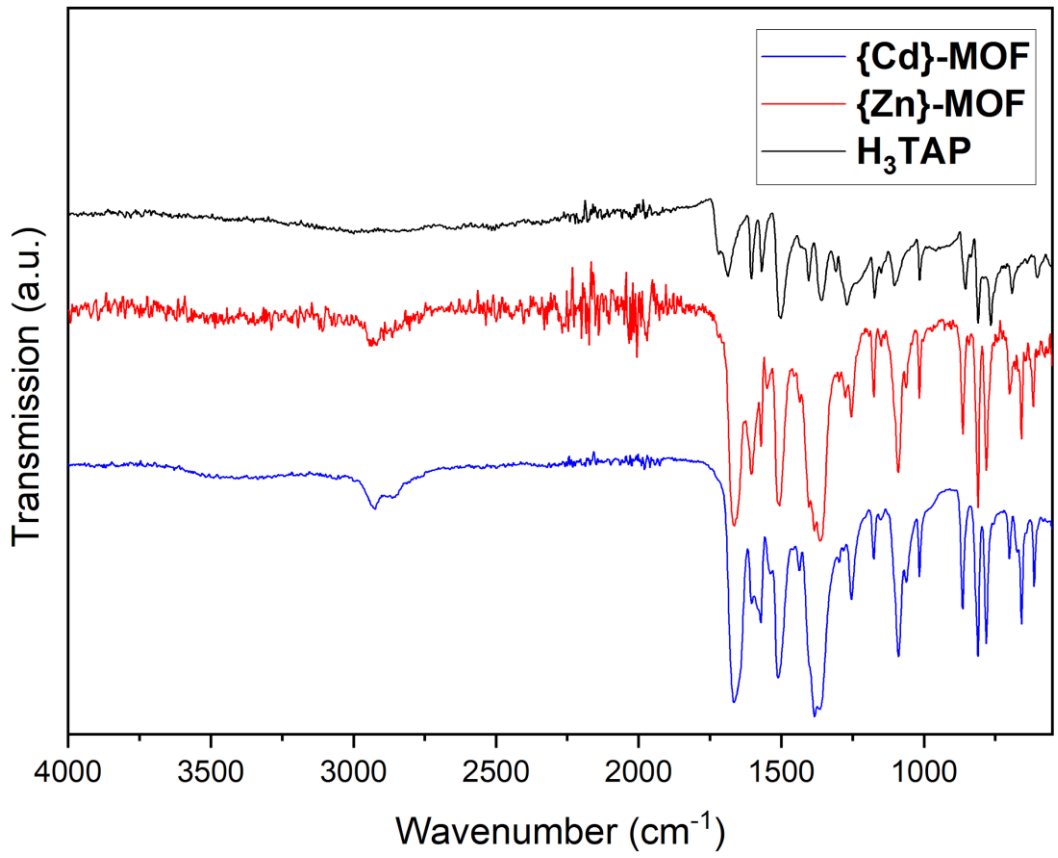

***Figure 4.6.2**: FT-IR spectra of **{Cd}-MOF** (blue), **{Zn}-MOF** (red) and **H_3TAP** (black)*

4.6.1.3. UV-vis and emission spectroscopy

The absorption spectra and photoluminescence spectra of **{Cd}-MOF** were measured using a suspension of the MOF in DMF under the conditions reported for **{Zn}-MOF**. **{Cd}-MOF** shows a broad absorbance signal at λ_{max} = 320 nm. The photoluminescence spectrum recorded upon excitation at 350 nm of **{Cd}-MOF** exhibits emission bands at 385 and 480 nm resulting from the $\pi \rightarrow \pi^*$ transition of the **H_3TAP** ligand, consistent with the photoluminescence spectrum of the ligand.

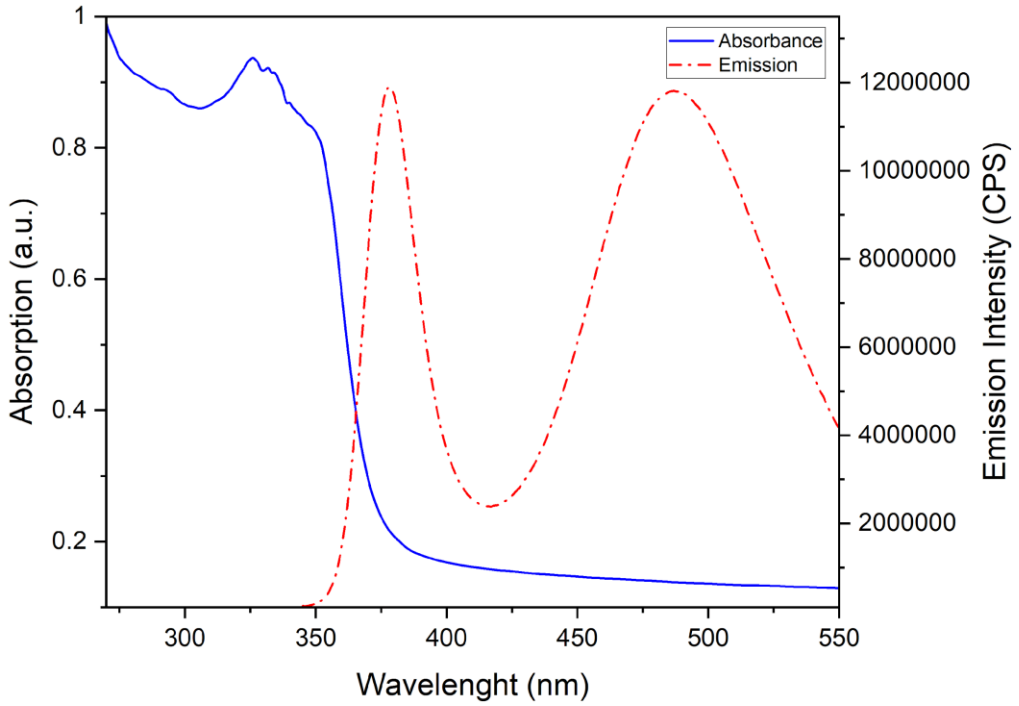

***Figure 4.6.3**: UV-Vis (blue) and photoluminescent spectra (red) of **{Cd}-MOF**.*

4.7 Future work

The key characteristics of linearly extended, tritopic, trazine-based ligands stem from their photochemical properties and their ability to induce network interpenetration or layering of materials through π-bonding. These struts have the potential to synthesise 2D layered materials and MOFs with interpenetration, while still retaining large voids in frameworks with increased stability, making promising candidates for the electrodeposition of layered MOF materials, selective gas sorption and catalysis.

The photoluminescence properties of the MOFs were explored, proving that the incorporation of the luminescent linker **H_3TAP** into **{Cu_2}-MOF-1**, **{Zn}-MOF** and **{Cd}-MOF** results in a red-shift of the emission in comparison to that of **H_3TAP**. These results indicate that these MOFs pose as ideal candidates for solution-based sensing of metal ions and organic molecules with the triazine core acting as abundant exposed Lewis basic sites.[35] This process shifts the π→π* transition of organic ligands and MLCT and results in a shift in the emission spectra.

The structural characteristics of the MOFs were explored by conducting N_2 gas sorption experiments on **{Cu$_2$}-MOF-1** and **{Zn}-MOF**. After the initial activation step, both MOFs failed to uptake N_2. PXRD analysis was conducted on air-dried samples of MOF but the structures underwent framework collapse and were not found to be stable outside of solution. In addition to this, they were found to be unstable in water, thus deeming them unsuitable for water oxidation experiments. This is likely due to the weak, monodentate coordination of **TAP^{3-}** to the Zn atoms in the case of **{Zn}-MOF**. A cobalt analogue of {**Zn}-MOF** and {**Cd}-MOF** was synthesised but the SCXD data was poor due to the polycrystalline nature of the sample. Modification of the solvothermal synthesis of this and was not discussed further. Preliminary OER experiments were carried out on this MOF but, as for **{Zn}-MOF** and **{Cd}-MOF**, the Co MOF degraded in aqueous solution, seen by subsequent cyclic voltammetry cycles. As a result, the deposition of the **H$_3$TAP** MOF series onto FTO and CC electrodes, as outlined in Chapters 1 and 2, was not investigated. A future application combines the MOFs discussed in this chapter with thermal-treated processes with graphite to investigate the influence of their carbonised analogue as modifiers on the electrochemical performance as electrodes in lithium-ion batteries, with focus given to the kinetics at the electrode-electrolyte interface. Initial experiments conducted by Marina Bauer at Karlsruher Institut für Technologie show that the cycling stability of graphite electrodes was enhanced with **{Zn}-MOF** in a composite with graphite.

Lastly, the trimerisation reaction *via* a lithium ((4-bromophenyl)-(dimethylamino)methylene)amide intermediate to form the **1** in the synthesis of **H$_3$TAP** and **H$_3$TAM** was identified as a potential step to introduce a terpyridine-triazine moiety into the ligand synthesis as a binding site for photoactive metals that would couple well with the extended luminescent linkers. In particular, Ruthenium terpyridine-based complexes do not have a sufficiently long-lived ^{3}MLCT excited state to transfer an electron or energy to a suitable acceptor.[36] Adding π-accepting ligands can reduce the energy of the ^{1}MLCT and consequently the energy of the ^{3}MLCT. A central triazine ring can be substituted to maintain the tridentate coordination mode but increasing the excited state lifetime. The synthesis of such a complex was started using the nitrile trimerisation reaction and general Sonogashira coupling and deprotection reactions but due to issues with isolation of the desired intermediate complex, coupled with time constraints, at present, this work is still ongoing.

4.8 Conclusion

Alkyne-extended ligands were synthesised from a central 2,4,6-triphenyl-1,3,5-triazine core, incorporating carboxylic acid functionalities in the 3- and 4-positions of the terminal phenyl ring for incorporation into novel MOFs. The previously unreported ligands **H_3TAP** and **H_3TAM** were synthesised *via* Sonogashira cross-coupling reactions in good yields.

Single crystal data was obtained for four new MOFs incorporating 4-functionalised ligand **H_3TAP**, namely **{Cu_2}-MOF-1**, **{Cu_2}-MOF -2**, **{Zn}-MOF** and **{Cd}-MOF**. Both **{Cu_2}-MOF-1** and **{Cu_2}-MOF-2** contain dicopper paddlewheel SBUs and form interwoven (3,4)-coordination nets with an overall **pto** topology. **{Zn}-MOF** and **{Cd}-MOF** were found to be structural isomers, containing triangular metal ion SBUs, linked with **H_3TAP** to form two-fold interpenetrated uninodal layers giving rise to hexagonal nets. Reactions with ligand the **H_3TAM** and various metal salts were performed under solvothermal and non-solvothermal conditions, but crystalline material was not obtained. **H_3TAM** was found to have poor solubility in DMF in comparison to **H_3TAP**, which may have inhibited MOP formation. Reactions with altered pH were conducted to improve the solubility of **H_3TAM**, as it boasted noteworthy luminescent properties, but crystals suitable for X-ray diffraction could not be obtained.

TGA analysis of **{Cu_2}-MOF-1** and **{Zn}-MOF** showed that ligand **TAP^{3-}** is stable to *approx*. 360 °C. Void channel diameters of **{Zn}-MOF** were large enough to investigate gas sorption studies. N_2 uptake of **{Zn}-MOF** was investigated with activation at 100 and 140 °C but underwent framework collapse during both activation conditions. The emission spectra were obtained for **{Cu_2}-MOF-1**, **{Zn}-MOF** and **{Cd}-MOF** showing moderate room-temperature luminescence upon excitation at 350 nm.

4.9 Bibliography

1 A. Ranganathan, B. C. Heisen, I. Dix and F. Meyer, *Chem. Commun.*, 2007, 3637–3639.

2 S. Ren, Q. Fang, F. Yu and D. Bu, *J. Polym. Sci. Part A Polym. Chem.*, 2005, **43**, 6554–6561.

3 P. Gamez and J. Reedijk, *Eur. J. Inorg. Chem.*, 2006, **2006**, 29–42.

4 M. Giese, M. Albrecht and K. Rissanen, *Chem. Commun.*, 2016, **52**, 1778–1795.

5 D. Zhao, D. J. Timmons, D. Yuan and H. C. Zhou, *Acc. Chem. Res.*, 2011, **44**, 123–133.

6 A. Klinkebiel, O. Beyer, B. Malawko and U. Lüning, *Beilstein J. Org. Chem.*, 2016, **12**, 2267–2273.

7 O. M. Yaghi, M. O'Keeffe, N. W. Ockwig, H. K. Chae, M. Eddaoudi and J. Kim, *Nature*, 2003, **423**, 705–714.

8 A. Ranganathan, B. C. Heisen, I. Dix and F. Meyer, *Chem. Commun.*, 2007, 3637–3639.

9 M. I. J. Polson, N. J. Taylor and G. S. Hanan, *Chem. Commun.*, 2002, **2**, 1356–1357.

10 R. Chinchilla and C. Nájera, *Chem. Soc. Rev.*, 2011, **40**, 5084–5121.

11 A. Jiménez-Sánchez, I. Isunza-Manrique, G. Ramos-Ortiz, J. Rodríguez-Romero, N. Farfán and R. Santillan, *J. Phys. Chem. A*, 2016, **120**, 4314–4324.

12 D. A. Safin, N. A. Tumanov, A. A. Leitch, J. L. Brusso, Y. Filinchuk and M. Murugesu, *CrystEngComm*, 2015, **17**, 2190–2195.

13 K. Stanley Cameron, Mannan, *Z. Naturforsch.*, 1975, **30**, 973–974.

14 T. Steiner, *Angew. Chemie-International Ed.*, 2002, **41**, 48.

15 N. Zhang, Q. L. Guan, C. H. Liu, Y. Sun, B. Li, Y. H. Xing and F. Y. Bai, *Appl. Organomet. Chem.*, 2020, **34**, 5506–5516.

16 R. C. Hirt and R. G. Schmitt, *Spectrochim. Acta.*, 1958, **12**, 127–138.

17 W. F. Forbes and M. B. Sheratte, *Can. J. Chem.*, 1955, **33**, 1829–1839.

18 O. Delgado-Friedrichs, M. O'Keeffe and O. M. Yaghi, *Acta Crystallogr. Sect. A Found. Crystallogr.*, 2006, **62**, 350–355.

19 V. Vergadou, G. Pistolis, A. Michaelides, G. Varvounis, M. Siskos, N. Boukos and S. Skoulika, *Cryst. Growth Des.*, 2006, **6**, 2486–2492.

20 H. Furukawa, Y. B. Go, N. Ko, Y. K. Park, F. J. Uribe-Romo, J. Kim, M. O'Keeffe and O. M. Yaghi, *Inorg. Chem.*, 2011, **50**, 9147–9152.

21 D. Sun, Shengqian Ma, Y. Ke, D. J. Collins and H.-C. Zhou, *J. Am. Chem. Soc.*, 2006, **128**, 3869–3897.

22 B. Chen, M. Eddaoudi, S. T. Hyde, M. O'keeffe and O. M. Yaghi, *Science*, 2001, **291**, 1021–1023.

23 S. Pappuru, K. B. Idrees, Z. Chen, D. Shpasser and O. M. Gazit, *Dalt. Trans.*, 2021, **50**, 6631–6636.

24 B. H. Stuart, *Infrared Spectroscopy: Fundamentals and Applications*, J. Wiley, 2005.

25 G. B. Deacon and R. J. Phillips, *Coord. Chem. Rev.*, 1980, **33**, 227–250.

26 K. I. Hadjiivanov, D. A. Panayotov, M. Y. Mihaylov, E. Z. Ivanova, K. K. Chakarova, S. M. Andonova and N. L. Drenchev, *Chem. Rev.*, 2021, **121**, 1286–1424.

27 F. X. Gao, Y. J. Ye, L. T. Zhao, D. H. Liu and Y. Li, *Inorg. Chem. Commun.*, 2018, **94**, 39–42.

28 C. A. Hunter and J. K. M. Sanders, *J. Am. Chem. Soc.*, 1990, **112**, 5525–5534.

29 X.-B. Liu, Z.-Y. Xiao, M.-H. Zhang, L.-L. Zhang, R.-M. Wang and D.-F. Sun, *Zeitschrift für Anorg. und Allg. Chemie*, 2015, **641**, 1781–1785.

30 J.-X. Chen, W.-E. Lin, M. Chen, F.-C. Que, L. Tao, X.-L. Cen, Y.-M. Zhou and W.-H. Chen, *Inorganica Chim. Acta*, 2014, **409**, 195–201.

31 L. Cao, Z. Lin, W. Shi, Z. Wang, C. Zhang, X. Hu, C. Wang and W. Lin, *J. Am. Chem. Soc*, 2017, **139**, 38.

32 J. P. Dong, Z. Z. Shi, B. Li and L. Y. Wang, *Dalt. Trans.*, 2019, **48**, 17626–17632.

33 R. Medishetty, V. Nalla, L. Nemec, S. Henke, D. Mayer, H. Sun, K. Reuter and R. A. Fischer, *Adv. Mater.*, 2017, **29**, 1605637–1605642.

34 A. Modak, M. Pramanik, S. Inagaki and A. Bhaumik, *J. Mater. Chem. A*, 2014, **2**, 11642–11650.

35 T. Fan, T. Xia, Q. Zhang, Y. Cui, Y. Yang and G. Qian, *Microporous Mesoporous Mater.*, 2018, **266**, 1–6.

36 Y. Sun, M. El Ojaimi, R. Hammitt, R. P. Thummel and C. Turro, *J. Phys. Chem. B*, 2010, **114**, 14664–14670.

Chapter 5

Experimental

5.0 Experimental

5.1 Materials and methods

Reagents: All chemicals and solvents were purchased from Sigma-Aldrich Chem. Co. Ltd. and Flurochem Ltd. and were used without further purification. Water was deionised before use.

NMR spectroscopy: ^{1}H and ^{13}C NMR spectra were recorded on a Bruker DPX 400 machine operating at 400.13 MHz and a Bruker 600 machine operating at 600 MHz by Dr John O'Brien and Dr Manuel Rüther, Trinity College Dublin. Samples were prepared in deuterated solvents. Standard abbreviations for spectra*: s*, singlet; d, doublet; t, triplet; m, multiplet; *J*, coupling constant.

Infrared spectroscopy: Fourier-transform infrared spectroscopy was recorded on a PerkinElmer Spectrum One FT-IR spectrometer using a universal ATR sampling accessory. Data was collected and processed using Spectrum v5.0.1 (2002 PerkinElmer Instrument LLC) software. The scan rate was 16 scans per minute with a resolution of 4 scans in the range 4000-550 cm^{-1}.

Mass spectrometry: Mass spectrometry was carried out on a Micromass LCT Electrospray mass spectrometer by Dr Gary Hessman.

Thermogravimetric analysis: Thermogravimetric analysis (TGA) was carried out using a Perkin Elmer Pyris-1 Thermogravimetric analyser under air. Measurements were carried out between 25 °C and 900 °C at a heating rate of 5 °C per minute.

X-ray diffraction analysis: All diffraction data was collected by Dr Nian-Yong Zhu and Dr Amal Cherian Kathalikkattil, Trinity College Dublin, using a Bruker APEX-II Duo dual-source instrument using graphite-monochromated Mo Kα (λ =0.71073 Å) or microfocus Cu Kα (λ = 1.54178 Å) radiation. Datasets were collected using ω and φ scans with the samples immersed in oil and maintained at a constant temperature of 100 K using a Cobra cryostream. The data were reduced and processed using the Bruker APEX suite of programs. Multi-scan absorption corrections were applied using SADABS. The diffraction data were solved using SHELXT and refined by fullmatrix least squares

procedures using SHELXL-2014 within the OLEX-2 GUI. All nonhydrogen atoms were refined anisotropically.

Scanning electron microscopy: SEM images were taken on the Zeiss ULTRA Plus. The acceleration voltage was in the range 2 kV – 30 kV with InLens, EsB, SE2, detectors used.

Energy-dispersive X-ray spectroscopy: EDX spectroscopy measurements were performed on the Zeiss ULTRA Plus scanning electron microscope with the 20mm² Oxford Inca EDX detector. The raw data was processed *via* the Inca 7.2 software package.

Scanning/transmission electron microscopy: TEM imaging were generated using an FEI Titan 80 FEG S/TEM equipped with a high-brightness Schottky-field emission electron source, a Gatan Imaging Filter, and with third-order spectrometer aberration correctors. An acceleration voltage of 300 kV was applied to all samples with an information limit of 0.1 nm.

X-ray photoelectron spectroscopy: XPS analysis was performed by Dr Cian Bartlam, Universität der Bundeswehr München. Sample data was collected under ultra-high vacuum conditions on a Phi Versa Probe III analyser equipped with a 1487 eV Rowland circle monochromatic Al Kα X-ray source. Samples were adhered to background-corrected adhesive tabs and imaged before analysis using scanning X-ray imaging (SXI) to identify good measurement positions. The survey scan was conducted using a 200 µm spot size with a 224 eV pass energy in 0.4 eV increments. Individual orbitals were analysed on the same sample area at 26 eV for the O 1s and the C 1s and 55 eV for the Co 2p. All orbital scans used with 0.05 eV increment steps.

Raman spectroscopy: Raman measurements were obtained using a Renishaw Raman spectrometer with a 785 nm laser source. Data was processed using the Renishaw WiRE 3.2 software package and OriginPro 9.1 SR0 (214).

UV-visible absorption: UV-visible absorption measurements were performed in DMF and CH_3CN in an optical path 1 cm quartz cuvette (3mL) at room temperature. Absorption spectra were recorded on Lambda35 UV-visible spectrometer with a wavelength range of 270-700 nm and a scan rate of 600 nm min-1. Baseline correction measurements were used for all spectra and all data was processed *via* OriginPro 9.1 SR0 (214).

Fluorescence spectrometry: Emission measurements were performed on a Horiba FluoroMax 4 spectrometer between 290 – 850 nm. Baseline correction measurements were used for all spectra and all data was processed *via* OriginPro 9.1 SR0 (214). All solution state measurements were performed in an optical path 1 cm quartz cuvette (3mL) at room temperature in dry DMF and CH_3CN. Solid state analysis was performed on a quartz slide.

Electrochemical measurements: were performed using a Biologic VSP potentiostat. Measurements were carried out in a 50 mM potassium phosphate (KPi) buffer solution using a KNO_3 (1 M) solution as an electrolyte at pH 7.2 and in 1 M KOH solution at pH 13.5. Ohmic drop compensations (85%) were applied before each experiment using the positive feedback compensation method as implemented in the instrumental setup. A three-electrode set-up was used for all experiments with Ag/AgCl (KCl 3M) as the reference electrode and a Pt-mesh as the counter electrode. A carbon paste (CP), fluorine-doped tin oxide (FTO) or carbon cloth (CC) electrode was used as the working electrode. Linear sweep voltammetry (LSV) for CP electrodes were conducted using an ALS RDE set-up additional to the Biologic VSP potentiostat with a 1 mV s^{-1} scan rate, and at 1,600 rpm LSV data was used for calculating the onset overpotential and Tafel plot. Chronopotentiometric and chronoamperometric measurements were performed at a constant temperature of 25 °C in an H-tube with the working and reference electrodes separated from the counter electrode by a glass frit.

The thermodynamic water oxidation potential ($E^0_{H_2O/O_2}$) is calculated using the Nernst equation at pH 7.2:

$$E^0_{H_2O/O_2} = 1.229 - (0.059 \times 7.2)\ (V) \text{ vs NHE at } 25\ ℃$$

All applied potentials (E_{app}) were converted to the NHE reference scale as:

$$E_{NHE} = E_{Ag/AgCl} + 0.210\ (V).$$

Overpotentials were calculated by subtracting the thermodynamic H_2O oxidation potential ($E^0_{H_2O/O_2}$) from E_{app} as:

$$\eta = E_{app} - E^{0}_{H_2O/O_2}$$

Current densities were calculated based on the geometrical surface area of the electrodes, 0.07 cm^2 and 1 cm^2 for CP and FTO electrodes, respectively. The onset potentials were calculated from the intersection point between the tangent lines of the Faradaic current at 0.2 mA cm^{-2} and the non-Faradic current.

Computational modelling: was performed by Dr. Swetanchu Tandon, Trinity College Dublin. The SBUs for the $\{M_3\}$ and $\{M_5\}$ mixed metal complexes were modelled in a non-periodic environment using density function theory (DFT). The calculations were carried out with the cluster code gaussian09[1] using PBE0[2,3] functional in conjunction with SDDALL[4] basis set with and effective core potential for Co, Zn and Mn, and 6-31g(d)[5] basis set for C, O and N, and 6-31g(p)[6] basis set for H. The default convergence criteria consisted of a large integration grid containing 225 radial shells with each shell containing 974 angular points were used. For each system, only the ferromagnetic configuration was modelled. To capture the proper electronic picture, the SBU was simplified by replacing the **BTEB^{3-}** ligand with benzoate ligand.

5.2 Synthetic procedures

5.2.1 Synthesis of 4,4',4''-(benzene-1,3,5-triyltris(ethyne-2,1-diyl))tribenzoic acid, (H_3BTEB)

Synthesis of 4,4',4''-(benzene-1,3,5-triyltris(ethyne-2,1-diyl))tribenzoic acid (**H_3BTEB**) was carried out in four steps using a modified literature procedure. The final product and all intermediates have been previously reported in the work of Yao *et al.*.[7]

1,3,5-Tris((trimethylsilyl)ethynyl)benzene: 1,3,5-Tribromobenzene (10 g, 0.032 mol) was added to Ethynyltrimethylsilane (15.56 mL, 0.112 mol) in triethylamine solvent (243 mL) in a three neck round bottom flask under an inert atmosphere. Bis(triphenylphosphine)palladium(II) dichloride (0.45 g, 0.641 mmol) and copper(I) iodide (0.05 g, 0.262 mmol) were subsequently added to the mixture. The mixture was heated to 80 ˚C for 24 hours. The solvent was removed using rotary evaporation and the crude product was washed thrice with a 1:1 ratio of dichloromethane and aqueous

ammonia solution to remove the catalysts. The brown product was subjected to column chromatography with hexane yielding pure 1,3,5-tris((trimethylsilyl)ethynyl)benzene. Yield: 9.15 g (0.025 mol, 78%). ^{1}H-NMR ($CDCl_3$, 400 MHz): δ (ppm) = 7.51 (3H, s, H^1), 0.25 (27H, s, H^2).

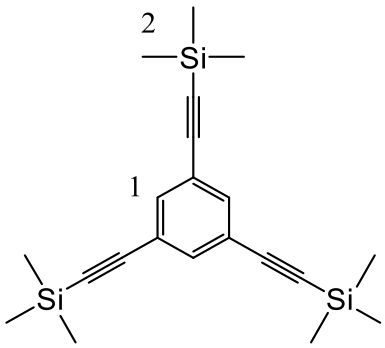

Figure 5.2.1*: 1,3,5-Tris((trimethylsilyl)ethynyl)benzene.*

1,3,5-Triethynylbenzene: 1,3,5-Tris((trimethylsilyl)ethynyl)benzene (9.15 g ,0.025 mol) was added to K_2CO_3 (19.22, 0.139 mol) in 35 mL of dichloromethane, and 300 mL of methanol, and stirred for 4 hours at room temperature. The filtrate was dissolved in dichloromethane and passed through a silica plug to obtain pure 1,3,5-triethynylbenzene as off-white crystals. Yield: 3.8 g (19.7 mmol, 79%). ^{1}H-NMR ($CDCl_3$, 400 MHz) δ (ppm): 7.58 (3H, s, H^1), 3.12 (3H, sm H^2).

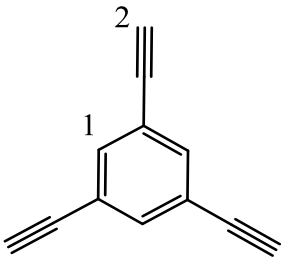

Figure 5.2.2*: 1,3,5-Triethynylbenzene.*

Trimethyl 4,4',4''-(benzene-1,3,5-triyltris(ethyne-2,1-diyl))tribenzoate: 1,3,5-Triethynylbenzene (3.8 g, 19.78 mmol), 4-methyliodobenzoate (21.21 g 80.94 mmol), copper(I) iodide (1.44 g, 7.561 mmol) and bis(triphenylphosphine)palladium(II) dichloride (5.32 g 7.57 mmol) were stirred in 250 mL of trimethylamine at 80° C for 24 hours under a nitrogen atmosphere. The solvent was removed from the product mixture and the crude product was redissolved in dichloromethane. This solution was filtered and

purified by column chromatography (hexane/THF, 1:2) yielding a yellow powder. Yield: 10.68 g (19.32 mmol, 61%). ^{1}H-NMR ($CDCl_3$, 400 MHz) δ (ppm): 8.08 (6H, d, J_1 = 8.32Hz, H^3), 7.73 (3H, s, H^1), 7.61 (6H, d, J_1 = 8.34Hz, H^2), 3.96 (9H, s, H^4).

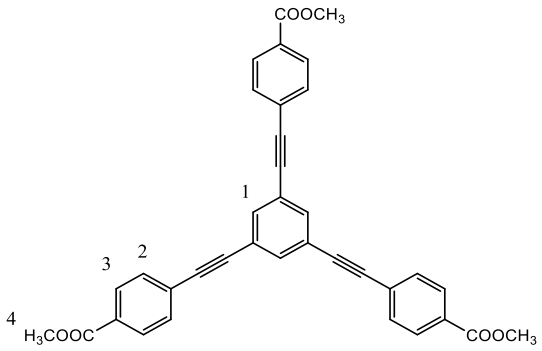

Figure 5.2.3*: Trimethyl 4,4',4''-(benzene-1,3,5-triyltris(ethyne-2,1-diyl))tribenzoate.*

4,4',4''-(benzene-1,3,5-triyltris(ethyne-2,1-diyl))tribenzoic acid **(H_3BTEB)**: A saturated LiOH solution (5.405g, 0.129 mol) in 25 mL of deionised water was added to a solution of trimethyl 4,4',4''-(benzene-1,3,5-triyltris(ethyne-2,1-diyl))tribenzoate (10.68 g, 19.32 mmol) in 100 mL of THF and stirred overnight. The mixture was stirred at room temperature for 3 hours. The mixture was acidified using 2M HCl and the product precipitated out of the solution. The precipitate was washed with methanol and purified by column chromatography using tetrahydrofuran as eluent. **H_3BTEB** was further washed and filtered with diethyl ether to yield the pure product as an off-white powder. Yield 4.63 g (9.06 mmol, 48%). ^{1}H-NMR (DMSO-d_6,400 MHz) δ (ppm): 13.22 (3H, s, H^4), 8.00 (6H, d, *J*=8 Hz, H^4), 7.89 (3H, s, H^2), 7.72 (6H, d, J=8 Hz, H^2); ^{13}C-NMR (DMSO-d_6, 100 MHz) ^{13}C-NMR (DMSO-d_6,400 MHz) δ (ppm): 167.1, 134.9, 132.2, 131.4, 130.1, 126.4, 123.8,90.7, 90.2.

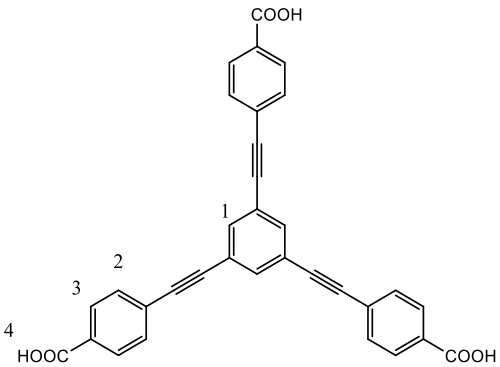

***Figure 5.2.4**: 4,4',4''-(benzene-1,3,5-triyltris(ethyne-2,1-diyl))tribenzoic acid (**H_3BTEB**).*

5.2.2 General Synthesis of Trimethyl-4,4',4''-(((1,3,5-triazine-2,4,6-triyl)tris(benzene-4,1-diyl))tris(ethyne-2,1-diyl))tribenzoate (H_3TAP) and Trimethyl-3,3',3''-(((1,3,5-triazine-2,4,6-triyl)tris(benzene-4,1-diyl)) tris(ethyne-2,1-diyl))tribenzoate (H_3TAM):

2,4,6-Tris(4-bromophenyl)-1,3,5-triazine (**1**): *n*-Buthyllithium (1.6 M in hexane, 5.80 mL, 9.28 mmol) was added dropwise to a stirring solution of $HNMe_2$ (2 M in THF, 4.64 mL, 9.28 mmol) in dry $(C_2H_5)_2O$ (120 mL) under N_2. The mixture was stirred for 30 mins before the addition 4-bromo-benzonitrile (8.44 mmol). The mixture was stirred for 1 h, followed by two additional equivalents of 4-bromo-benzonitrile (16.92 mmol). The reaction was stirred under N_2 for 24 h and in air for a further 1 h. The brown solid was collected by filtration, recrystallised from EtOH/H_2O (2:1) and washed with Et_2O to afford the product **1** as a white powder (4.02 g, 86 % yield). ^{1}H NMR (400 MHz, $CDCl_3$): δ (ppm) = 8.63 (2H, d, J_1 = 8.4), 7.74 (2H, d, J_1 = 8.4). ^{1}H NMR in agreement with the literature.[8]

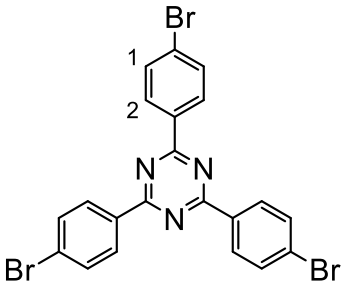

***Figure 5.2.5**: 2,4,6-Tris(4-bromophenyl)-1,3,5-triazine.*

2,4,6-Tris(4-((trimethylsilyl)ethynyl)phenyl)-1,3,5-triazine (**2**): To a stirred solution of 2,4,6-Tris(4-bromophenyl)-1,3,5-triazine (6.5 mmol), $PdCl_2(PPh_3)_2$ (6 mol %) and CuI (2 mol %) in anhydrous diisopropylamine (80 mL) was added under Ar. The reaction mixture was stirred for a further 5 mins before the addition of ethynyltrimethylsilane (3.6 mL, 25.9 mmol). The reaction mixture was refluxed for 24 h. Upon complete conversion of the starting material, the crude reaction mixture was concentrated under vacuum and was purified by column chromatography (CH_2Cl_2) to afford the desired product as a white crystalline solid (3.19 g, 82 % yield). ^{1}H NMR (400

MHz, $CDCl_3$): δ (ppm) = 8.71 (6H, d, J_1 = 8.4), 7.68 (6H, d, J_1 = 8.4), 0.32 (27H, s); ^{1}H NMR in agreement with the literature.[9]

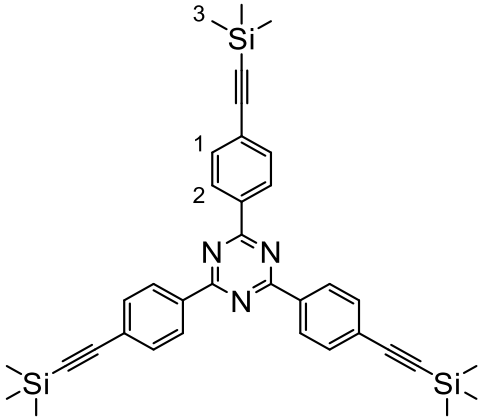

Figure 5.2.6*: 2,4,6-Tris(4-((trimethylsilyl)ethynyl)phenyl)-1,3,5-triazine.*

2,4,6-Tris(4-ethynylphenyl)-1,3,5-triazine (**3**): To a stirred solution of 2,4,6-Tris(4-((trimethylsilyl)ethynyl)phenyl)-1,3,5-triazine (5.0 mmol) in CH_2Cl_2 (20 mL), K_2CO_3 (14.5 mmol) in CH_3OH (20 mL) was added at room temperature. The reaction mixture was stirred at room temperature for 3 h, until complete conversion of the starting material. H_2O (50 mL) was added to the crude reaction mixture. The product was extracted with CH_2Cl_2 (2x20 mL) and was purified by column chromatography (CH_2Cl_2/C_6H_{14}) to afford the desired product as a white solid (1.86 g, 95 % yield). ^{1}H NMR (400 MHz, $CDCl_3$): δ (ppm) = 8.74 (6H, d, J_1 = 8.4), 7.71 (6H, d, J_1 = 8.4), 3.31 (3H, s); ^{1}H NMR in agreement with the literature.[10]

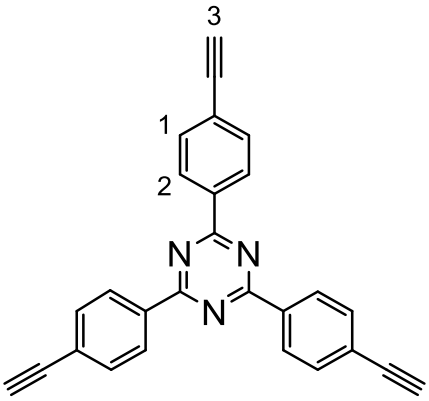

Figure 5.2.7*: 2,4,6-Tris(4-ethynylphenyl)-1,3,5-triazine.*

5.2.3 General Procedure for Sonogashira Cross-Coupling (A):

To a stirred solution of the deprotected aryl-alkyne (2.6 mmol), $Pd(PPh_3)_4$ (6 mol %) and CuI (2 mol %) in anhydrous diisopropylamine (100 mL) and tetrahydrofuran (30 mL), the aryl-bromide was added under Ar. The reaction mixture was refluxed for 48 h. The crude reaction mixture was concentrated under vacuum and was purified by column chromatography (CH_2Cl_2) and recrystallised from CH_3OH/CH_2Cl_2 to afford the product.

Trimethyl-4,4',4''-(((1,3,5-triazine-2,4,6-triyl)tris(benzene-4,1-diyl))tris(ethyne-2,1-diyl))tribenzoate (**4**): Following the general procedure **A** from **3** and methyl 4-iodobenzoate, **4** was recovered as a white solid (3.19 g, 82 % yield). ^{1}H NMR (400 MHz, $CDCl_3$): δ (ppm) = 8.78 (6H, d, J_1 = 9.6, H^2), 8.08 (6H, d, J_1 = 7.2, H^3), 7.75 (6H, d, J_1 = 9.6, H^1) 7.67 (6H, d, J_1 = 8.0, H^7), 3.98 (9H, s, H^5); ^{13}C NMR (400 MHz, $CDCl_3$): δ (ppm) = 170.8, 167.2, 135.9, 132.6, 132.2, 130.1, 129.4, 126.8, 92.0, 91.9, 79.4, 79.2; FT-IR (ATR) $\bar{\nu}$/cm^{-1} 1417 s (C=O st), 1383 w, 1352 w (ar C=N), 1088 (C-O st), 814 s, 632 m; ESI$^+$ MS (CH_2Cl_2): 786.2353 $[M+Na]^+$

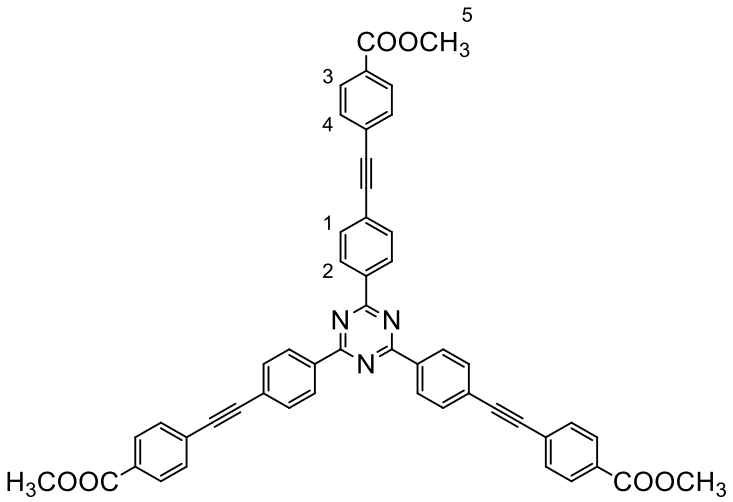

***Figure 5.2.8**: Trimethyl-4,4',4''-(((1,3,5-triazine-2,4,6-triyl)tris(benzene-4,1-diyl))tris(ethyne-2,1-diyl))tribenzoate.*

Trimethyl-3,3',3''-(((1,3,5-triazine-2,4,6-triyl)tris(benzene-4,1-diyl))tris(ethyne-2,1-diyl))tribenzoate (**5**): Following the general procedure **A** from **3** and methyl 3-iodobenzoate, **5** was recovered as a white solid (2.68 g, 69 % yield). ^{1}H NMR (400 MHz, $CDCl_3$): δ (ppm) = 8.81 (6H, d, J_1 = 9.6, H^2), 8.30 (3H, s, H^3), 7.80 (3H, d, J_1 = 7.1, H^4),

7.78 (9H, m, $H^{2,6}$), 7.50 (3H, t, J_1 = 7.6, H^5), 3.99 (3H, s, H^7); ESI^+ MS (CH_2Cl_2): 784.2357 [M].

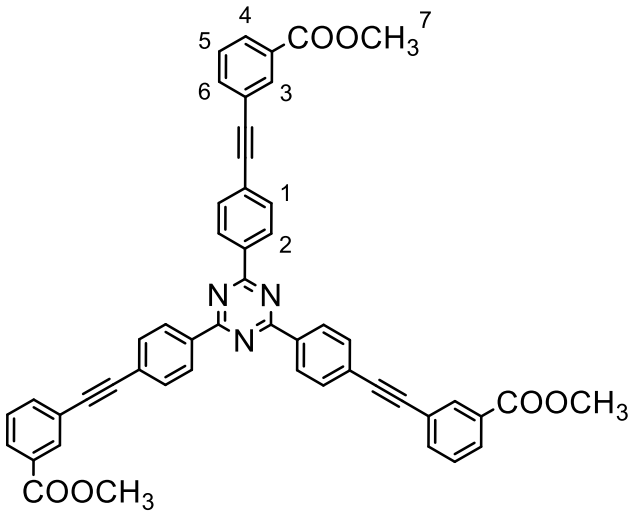

***Figure 5.2.9**: Trimethyl-3,3',3''-(((1,3,5-triazine-2,4,6-triyl)tris(benzene-4,1-diyl))tris(ethyne-2,1-diyl))tribenzoate.*

5.2.4 General Procedure for Ester-Hydrolysis (B):

To a stirred solution of the protected aryl-alkyne (5.0 mmol) in tetrahydrofuran (9 mL) and CH_3OH (9 mL), KOH (4 mL, 5 M in CH_3OH, 14.5 mmol) was added. The reaction mixture was stirred at room temperature for 24 h. The reaction solution was diluted with H_2O (10 mL) and HCl (5 M) was added dropwise until a pH of 3 was reached. This resulted in the precipitation of the product, which was isolated by filtration and recrystallised from tetrahydrofuran to yield the product.

Trimethyl-4,4',4''-(((1,3,5-triazine-2,4,6-triyl)tris(benzene-4,1-diyl))tris(ethyne-2,1-diyl))tribenzoate (**H_3TAP**): Following the general procedure **B**, **H_3TAP** was recovered as a bright yellow solid (2.71 g, 74 % yield). ^{1}H NMR (400 MHz, $CDCl_3$): δ (ppm) = 13.19 (3H, broad, H^5), 8.83 (4H, m, H^2), 8.07 (8H, m, H^3), 7.76 (2H, m, H^2), 7.67 (6H, m, H^1); ^{13}C NMR (600 MHz, DMSO-D_6): δ (ppm) = 170.8, 167.2, 135.9, 132.6, 132.2, 130.1, 129.4, 126.8, 92.0, 79.4; FT-IR (ATR) $\bar{\nu}$/cm^{-1} 1686 s (C=O st), 1604 s, 1401 s (ar C=C st), 1359 (ar C=N), 1270 w, 1173 m (C-O st) 765 s, 691 m, 602; UV-visible λ_{max} (DMF) = 301 nm, ε = 39,148 M^{-1} cm^{-1}; Emission (DMF) λ_{max} = 422 nm; MALDI-TOF-MS (CH_2Cl_2): 808.2217 $[M+Na]^+$.

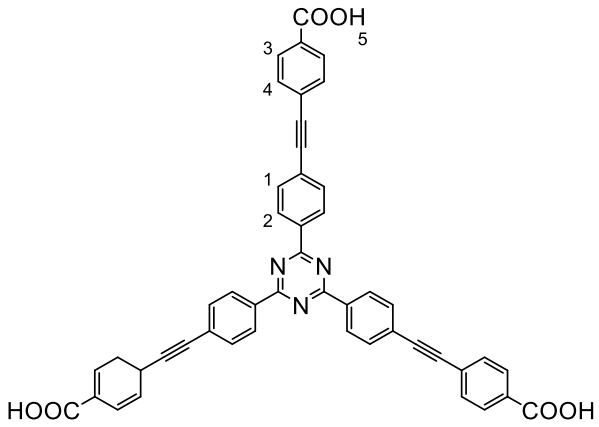

***Figure 5.2.10**: Trimethyl-4,4',4''-(((1,3,5-triazine-2,4,6-triyl)tris(benzene-4,1-diyl))tris(ethyne-2,1-diyl))tribenzoate (**H₃TAP**).*

Trimethyl-3,3',3''-(((1,3,5-triazine-2,4,6-triyl)tris(benzene-4,1-diyl)) tris(ethyne-2,1-diyl))tribenzoate (**H₃TAM**): Following the general procedure **B**, **H₃TAM** was recovered as an off-white solid (3.33 g, 90 % yield). ^{1}H NMR (400 MHz, DMSO-D$_6$): δ (ppm) = 8.81 (6H, d, J_1 = 9.4, H^2), 8.14 (3H, s, H^3), 7.78 (3H, d, J_1 = 9.2, H^4), 7.88 (6H, J_1 = 9.0, H^1), 7.71 (3H, m, H^6), 7.55 (3H, m, H^5); ^{13}C NMR (600 MHz, DMSO-D$_6$): δ (ppm) = 170.8, 166.9, 136.0, 135.7, 132.7, 132.5, 131.9, 130.3, 129.4, 127.0, 122.8, 91.8, 90.2; UV-visible λ_{max} (DMF) = 319 nm, ε = 59,582 M^{-1} cm^{-1}; Emission (DMF) λ_{max} = 480 nm.

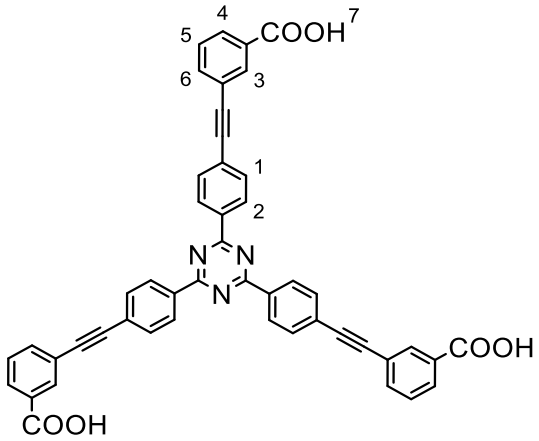

***Figure 5.2.11**: Trimethyl-3,3',3''-(((1,3,5-triazine-2,4,6-triyl)tris(benzene-4,1-diyl)) tris(ethyne-2,1-diyl))tribenzoate (**H₃TAM**).*

5.2.5 Synthesis of {Co_5}-MOF

The self-assembly of **{Co_5}-MOF** was previously reported by Dr. Kevin Byrne. **H_3BTEB** (9.13 mg, 1.78x10^{-2} mmol) was added to a solution of $Co(NO_3)_2 \cdot 6H_2O$ (17.0 mg, 5.8x10^{-2} mmol) in DMF (1 mL) and sonicated for 10 mins. The reaction vial was placed in an aluminium heating block for 48 h at 90 °C. The solution was cooled to room temperature during 4 h. The product was obtained as dark purple crystals and were suitable for X-ray diffraction.

5.2.6 Synthesis of {$(CoNi)_5$}-MOF

H_3BTEB (13.16 mg, 25.79 mmol), $Co(NO_3)_2.6H_2O$ (5.0 mg, 17.19 mmol) and $Ni(NO_3)_2.6H_2O$ (2.5 mg, 8.59 mmol) were dissolved in 1 mL of DMF and sonicated for 30 minutes. The solution was then heated to 85 ˚C for 48 hours, before allowing it to cool slowly to ambient temperature. Following this, violet rod shaped crystals formed suitable for analysis by single crystal X-ray diffraction. A yield of 25% was obtained. FT-IR (ATR) $\bar{\nu}$/cm^{-1} 1650 s (C=C st), 1582 s (C=C st), 1538 s (ν_{as}COO), 1380 (ν_sCOO); Raman, 2216 cm^{-1} (C≡C), 1605 cm^{-1} (C=C), 1582 cm^{-1} (C=C), 1171 cm^{-1}, 1137 cm^{-1}, 1126 cm^{-1} (C-C).

5.2.7 Synthesis of {$(CoMn)_3$}-MOF

The self-assembly of {Co_5}-MOF was previously reported by Dr. Kevin Byrne. **H_3BTEB** (8.77 mg, 17.18 mmol), $Co(NO_3)_2.6H_2O$ (1.66 mg, 5.72 mmol) and $Zn(NO_3)_2.6H_2O$ (3.41 mg, 11.5 mmol) were dissolved in 1 mL of DMF and sonicated for 30 minutes. The solution was then heated to 90 ˚C for 72 hours, before allowing it to cool slowly to ambient temperature. Following this, violet rod-shaped crystals formed which were suitable for analysis by single crystal X-ray diffraction with a yield of 45%.

5.2.8 Synthesis of {$(CoZn_3$}-MOF

The self-assembly of {Co_5}-MOF was previously reported by Dr. Kevin Byrne. **H_3BTEB** (8.77 mg, 17.18 mmol), $Co(NO_3)_2.6H_2O$ (1.66 mg, 5.72 mmol) and $Zn(NO_3)_2.6H_2O$ (3.41 mg, 11.5 mmol) were dissolved in 1 mL of DMF and sonicated for 30 minutes. The solution was then heated to 90 ˚C for 72 hours, before allowing it to cool slowly to ambient temperature. Following this, violet rod-shaped crystals formed which were suitable for analysis by single crystal X-ray diffraction.

5.2.9 Synthesis of {(MnZn)$_3$}-MOF

H$_3$BTEB (12.89 mg, 25.26 mmol), Zn(NO$_3$)$_2$.6H$_2$O (5.01 mg, 16.84 mmol) and MnCl$_2$.4H$_2$O (1.66 mg, 8.42 mmol) were dissolved in 1 mL of DMF and sonicated for 30 minutes. The solution was then heated to 90 ˚C for 72 hours, before allowing it to cool slowly to ambient temperature. Following this, colourless rod-shaped crystals formed suitable for analysis by single crystal X-ray diffraction. A yield of 32% was obtained. Raman, 2217 cm^{-1} (C≡C), 1605 cm^{-1} (C=C), 1582 cm^{-1} (C=C), 1173 cm^{-1}, 1142 cm^{-1}, 1121 cm^{-1} (C-C).

5.2.10 Synthesis of {Cu$_2$}-MOF-1

H$_3$TAP (5 mg, 6.7x10^{-3} mmol) was added to a solution of Cu(NO$_3$)$_2$·3H$_2$O (17.2 mg, 4.6x10^{-2} mmol) in DMF (1 mL) and sonicated for 10 mins. The reaction vial was placed in an aluminium heating block for 48 h at 70 °C. The solution was cooled to room temperature during 4 h. The product was obtained as green, tetragonal crystals and were suitable for X-ray diffraction. FT-IR (ATR) $\bar{\nu}$/cm^{-1} 1657 s (C=O st), 1406 s (ar C=N st), 1362 s, 1092 m (C-O st), 812 m, 778 m, 658 w; Elemental analysis (%) Found (Calculated): C/N 75.21 (85.00), O 17.82 (12.50), Cu 6.97 (2.50).

5.2.11 Synthesis of {Cu$_2$}-MOF-2

H$_3$TAP (5 mg, 6.7x10^{-3} mmol) was added to a solution of Cu(NO$_3$)$_2$·3H$_2$O (17.2 mg, 4.6x10^{-2} mmol) in DMF (1 mL) and sonicated for 10 mins. The reaction vial was placed in an aluminium heating block for 24 h at 90 °C. The solution was cooled to room temperature during 4 h. The product was isolated as pin-needle green crystals in co-existence with block-like green crystals. The resulting needle crystals were suitable for X-ray diffraction. The crystals were not able to be isolated for further characterisation.

5.2.12 Synthesis of {Zn}-MOF

H$_3$TAP (5 mg, 6.7x10^{-3} mmol) was added to a solution of Zn(NO$_3$)$_2$·3H$_2$O (17.2 mg, 4.6x10^{-2} mmol) in DMF (1 mL) and sonicated for 10 mins. The reaction vial was placed in an aluminium heating block for 48 h at 75 °C. The solution was cooled to room temperature during 4 h. The product was obtained as colourless, pin-needle crystals and were suitable for X-ray diffraction. FT-IR (ATR) $\bar{\nu}$/cm^{-1} 1664 s (C=O st), 1406 s (ar C=N

st), 1384 s, 1091 m (C-O st), 810 m, 781 m; Elemental analysis (%) Found (Calculated): C 88.70 (86.43), O 9.43 (11.86), Cu 1.89 (1.70).

5.2.13 Synthesis of {Cd}-MOF

H_3TAP (5 mg, $6.7x10^{-3}$ mmol) was added to a solution of $Cd(NO_3)_2 \cdot 6H_2O$ (17.2 mg, $4.6x10^{-2}$ mmol) in DMF (1 mL) and sonicated for 10 mins. The reaction vial was placed in an aluminium heating block for 48 h at 75 °C. The solution was cooled to room temperature during 4 h. The product was obtained as colourless, pin-needle crystals of which preliminary X-ray diffraction data was obtained. FT-IR (ATR) $\bar{\nu}/cm^{-1}$ 1666 s (C=O st), 1411 s (ar C=N st), 1383 s, 1089 m (C-O st), 811 m, 781 m, 613 w; Elemental analysis (%) Found (Calculated): C 86.62 (86.43), O 11.85 (11.86), Cu 1.53 (1.70).

5.3 Bibliography

1 J. R. . S. Frisch, M. J. T., G. W.; Schlegel, H. B.; Scuseria, G. E.; Robb, M. A.; Cheeseman, H. G.; Barone, V.; Mennucci, B.; Petersson, G. A.; Nakatsuji, H.; Caricato, M.; Li, X.; Hratchian, K. . P.; Izmaylov, A. F.; Bloino, J.; Zheng, G.; Sonnenberg, J. L.; Hada, M.; Ehara, M.; Toyota, T. . Fukuda, R.; Hasegawa, J.; Ishida, M.; Nakajima, T.; Honda, Y.; Kitao, O.; Nakai, H.; Vreven, E. . K. Montgomery, J. A., Jr.; Peralta, J. E.; Ogliaro, F.; Bearpark, M.; Heyd, J. J.; Brothers, J. K. N.; Staroverov, V. N.; Kobayashi, R.; Normand, J.; Raghavachari, K.; Rendell, A.; Burant, J. C.; Iyengar, S. S.; Tomasi, J.; Cossi, M.; Rega, N.; Millam, J. M.; Klene, M.; Knox, J. E.; Cross, A. B.; Bakken, V.; Adamo, C.; Jaramillo, J.; Gomperts, R.; Stratmann, R. E.; Yazyev, O.; Austin, V. G. . J.; Cammi, R.; Pomelli, C.; Ochterski, J. W.; Martin, R. L.; Morokuma, K.; Zakrzewski, Ö. . F. Voth, G. A.; Salvador, P.; Dannenberg, J. J.; Dapprich, S.; Daniels, A. D.; Farkas and D. J. J. B.; Ortiz, J. V.; Cioslowski, J.; Fox, Gaussian, Inc., Wallingford CT, 2009.

2 J. P. Perdew, K. Burke and M. Ernzerhof, *Phys. Rev. Lett.*, 1996, **77**, 3865–3868.

3 C. Adamo and V. Barone, *J. Chem. Phys.*, 1999, **110**, 6158–6170.

4 M. Dolg, U. Wedig, H. Stoll and H. Preuss, *J. Chem. Phys.*, 1986, **86**, 866–872.

5 M. M. Francl, W. J. Pietro, W. J. Hehre, J. S. Binkley, M. S. Gordon, D. J. DeFrees and J. A. Pople, *J. Chem. Phys.*, 1982, **77**, 3654–3665.

6 M. J. Frisch, J. A. Pople and J. S. Binkley, *J. Chem. Phys.*, 1984, **80**, 3265–3269.

7 Q. Yao, A. Bermejo Gómez, J. Su, V. Pascanu, Y. Yun, H. Zheng, H. Chen, L. Liu, H. N. Abdelhamid, B. Martín-Matute and X. Zou, *Chem. Mater.*, 2015, **27**, 5332–5339.

8 H. Tanaka, K. Shizu, H. Nakanotani and C. Adachi, *Chem. Mater.*, 2013, **25**, 3766–3771.

9 Q. Y. Hu, W. X. Lu, H. D. Tang, H. H. Y. Sung, T. Bin Wen, I. D. Williams, G. K. L. Wong, Z. Lin and G. Jia, *Organometallics*, 2005, **24**, 3966–3973.

10 P. Das, A. Kumar, A. Chowdhury and P. S. Mukherjee, *ACS Omega*, 2018, **3**, 13757–13771.

Chapter 6

Conclusion and future work

6.0 Conclusion and future work

This research project aimed to develop synthetic pathways to produce novel, catalytic MOFs and MOF-derived materials. To achieve this aim, a robust direct method was explored to synthesise MOFs and mixed-metal MOF systems, both in pristine crystalline form and as thin-films on conductive electrodes. This was achieved while utilising the established, tritopic linker **H_3BTEB**, and **H_3TAP** linker and a set of earth-abundant transition metals, namely a combination Co(II), Mn(II), Zn(II), Cd(II) Cu(II) and Ni(II) metal ions. The direct synthesis method also detailed the post-synthetic heat-treatment of the MOF and MM-MOF structures to afford porous carbon-based metal oxide systems. X-ray diffraction techniques were employed as the primary characterisation technique to determine the MOF framework structures, and the resulting materials were thoroughly characterised by analytical techniques. These physiochemical techniques include gas sorption, catalytic OER activity and photochemical properties.

An initial synthetic strategy was developed using **{Co_5}-MOF**, compromised of pentanuclear {Co_5} clusters connected by nine 4,4',4''-(benzene-1,3,5-triyltris(ethyne-2,1-diyl))tribenzoate (**$BTEB^{3-}$**) linkers and containing two metal-bound labile DMF molecules. This MOF was an ideal template to synthesis a cobalt based nanomaterial with an affinity for stable water oxidation at high pH. This was due to the material having the ability to be synthesised both solvothermally to produce crystalline material, and electrochemically to afford a MOF thin film. **Co@C-500** was produced *via* the thermal-treatment of **{Co_5}-MOF** materials under an inert atmosphere. The resulting carbonised materials were extensively characterised to conform the structural change to a Co_3O_4-carbon material *via* PXRD, Raman, XPS and FT-IR spectroscopy. The method of electrodeposition and post synthetic heat-treatment afforded homogeneous, monodispersed catalytic site within a porous carbon framework on both FTO coated glass and carbon cloth electrodes. Imaging techniques such as TEM, STEM and SEM were used to confirm the existence of a core@shell structure with cobalt oxide nanoparticles encapsulated within a carbon matrix and suggested a close structural and constitutional relationship between **Co@C-500** from solvothermally synthesised MOF crystals and the electrochemically synthesised materials.

Gas sorption analysis confirmed the stability of the materials and that a degree of porosity was retained from the precursor MOF template. The N_2 gas uptake yielded a reversible type-I isotherm at 77 K with a BET surface area of 348 m^2/g. It was surmised that

as the annealing process was undertaken stepwise *via* a gradual temperature ramp, a partial framework collapse was avoided during the change in structure. The electrochemical performance of **Co@C-500**/FTO materials were investigated under neutral pH conditions and compared to the activity of **{Co5}-MOF**/FTO, yielding a noticeable decrease of the Tafel slope, 98 and 175 mV dec^{-1}, respectively. In addition to this, **Co@C-500**/FTO catalysed the OER under basic conditions with an onset overpotential of 454 mV and a Tafel slope of 40 mV dec^{-1}. Post-catalytic characterisation of thin-film **Co@C-500** after chronopotentiometry experiments at 1 mA cm^{-2} at pH 13.5 for 24 h, highlighted the structural stability of the material under basic conditions over **{Co5}-MOF**.

The direct synthesis of MM-MOFs was achieved by the addition of a second metal salt in the MOF formation step. Firstly, **{(MnZn)$_3$}-MOF** was synthesised, a doubly interpenetrated structure containing trinuclear metallic units stabilised by six ligands from **BTEB^{3-}** ligands and two axial-bound solvent molecules. The physical and structural attributes of the MOFs were studied using a number of analytical techniques including powder X-ray diffraction, Raman spectroscopy and thermogravimetric analysis. The assignment of the relative positions of Mn(II) and Zn(II) in the inorganic SBUs was investigated using elemental techniques including EDX and XPS spectroscopy, in addition to computational modelling to suggest Mn(II) occupies the octahedral sites and Zn(II) in the tetrahedral sites.

Previous successes were recorded when using a pentanuclear MOF SBU and **H$_3$BTEB**. Following on from this, the mixed metal variant, **{(NiCo)$_5$}-MOF**, was synthesised under direct synthesis both solvothermal but also *via* rapid electrodeposition synthesis to produce both **{(NiCo)$_5$}-MOF**/FTO and **{(NiCo)$_5$}-MOF**/CC materials. Bulk crystalline and thin-film samples were fully characterised and tested for their OER activity. The thin-film samples were annealed at 500 °C to synthesise core@shell materials containing nanoparticles indicative of $NiCo_2O_4$. These electrodes demonstrated competitive electrocatalytic ability at pH 7.2. The systems were also used to carry out water oxidation at pH 13.5, which resulted in very high current densities, low overpotentials and small Tafel slopes. At pH 13.5, the mixed metal **NiCo@C-500**/CC electrode reached higher current densities than the monometallic **Co@C-500**/CC, showing that the addition of a second metal centre can have an additive effect on the catalytic activity of the overall material.

The catalytic activity of MOFs and MOF-derived systems present in Chapters 2 and 3 were directly compared under alkaline and neutral conditions. As of submission of this thesis, highest performing pristine MOF-based catalysts (such as those noted in Table 1.6.2) achieve overpotentials below 230 A cm^{-2} in alkaline media. This is in comparison to overpotential of 457 A cm^{-2} and above, reported in this thesis. However, the activity of MOFs are seldom reported under neutral conditions due to unfavourable kinetics at this pH, whereas cobalt-containing MOFs (such as **{(NiCo)$_5$}-MOF**) appear to have long-term activity. This could prove useful in green-chem catalytic applications as a catalyst with activity in the absence of a caustic electrolyte. The unique aspect of these materials is their robust ability to be synthesised from both solvothermal means and by using electrodeposition techniques on a multitude of surfaces. The deposition of MOFs on thin films is a relatively new and rapidly expanding field and this general synthesis could be used as a template to synthesise a wide variety of mono- and mixed- metallic MOFs incorporating catalytically active metal centres. In addition to this, the stepwise approach of initial electrodeposition and heat treatment to form thin-film nanomaterials has not been reported to date.

Preliminary investigations were carried out to incorporate highly extended ligands into the direct synthesis method with phenyl-alkyne-extended ligands. These were synthesised from a central 2,4,6-triphenyl-1,3,5-triazine core, incorporating carboxylic acid functionalities in the 3- and 4-positions of the terminal phenyl ring for incorporation into novel MOFs. The previously unreported ligands **H$_3$TAP** and **H$_3$TAM** were synthesised *via* 1,3,5-triazine trimerisation from cyano-group reagents and Sonogashira cross-coupling reactions. Single crystal data was obtained for four new MOFs incorporating 4-functionalised ligand **H$_3$TAP**, namely **{Cu$_2$}-MOF-1**, **{Cu$_2$}-MOF -2**, **{Zn}-MOF** and **{Cd}-MOF**. Both **{Cu$_2$}-MOF-1** and **{Cu$_2$}-MOF-2** contain dicopper paddlewheel SBUs and form interwoven (3,4)-coordination nets with an overall **pto** topology. **{Zn}-MOF** and **{Cd}-MOF** were found to be structural isomers, containing single tetrahedral metal ion SBUs, linked with **H$_3$TAP** to form two-fold interpenetrated uninodal layers giving rise to hexagonal nets.

An added characteristic of this ligand set stems from their photochemical properties and their ability to induce network interpenetration or layering of materials through π-bonding. The photoluminescence properties of the MOFs were explored, proving that the incorporation of the luminescent linker **H$_3$TAP** into **{Cu$_2$}-MOF-1**, **{Zn}-MOF** and **{Cd}-**

MOF results in a red-shift of the emission in comparison to that of **H_3TAP**. A future application combines these MOFs and heat-treated MOFs with graphite to investigate the influence of modifiers on the electrochemical performance as electrodes in lithium-ion batteries, especially to learn about the electrode-electrolyte interface. Initial experiments conducted by Marina Bauer at Karlsruher Institut für Technologie showed that the cycling stability of graphite electrodes was enhanced with **{Zn}-MOF** in a composite with graphite.

In conclusion, a general synthetic pathway to generate crystalline and thin-film MOF analogues, and MOF-derived metal oxide-based system was demonstrated. Synthetic, structural and analytical challenges associated with the synthesis extended organic ligands, MOF structures and core@shell systems were overcome. The presented materials reveal interesting structural attributes and unique physicochemical properties that derive from the large ligands employed. Additionally, the design of carbonised MOF derivatives reveals a promising strategy to afford thin-film materials with long-term durability to alkaline conditions, with high OER activity.

In work described in chapters 2 and 3 showed the development of a robust process including MOF synthesis, electrodeposition and heat treatment using cheap, earth-abundant metals and a relatively simple and studied ligand. Chapter 4 begins to expand on this process by utilising extended, trazine-based ligands known for their photochemical properties and their preference to generate structures with network interpenetration or layering/stacking effects. 2D layered materials and MOFs with interpenetration aid to improve conductivity in the overall structure and provide enhanced catalytic activity. Building from this, future work in this area would be to advance the standard method of cathodic electrodeposition of MOFs onto thin-films developed in this thesis and employ this technique for high-conjugation, light-active ligands such as those characterised in chapter 4. Such materials would possess photocatalytic properties and improved stability, in addition to electrochemical properties, of which have not been reported to date. Specifically, focusing on the synthesis of MOFs incorporating cobalt or nickel oxo-clusters bound by multiple tritopic **H_3TAP**-based ligands to improve framework stability in comparison to the unimodal MOFs reported with these linkers to date. Following on from this, an advanced avenue of exploration would be the inclusion of a photoactive metal into the **H_3TAP**-based motif *via* the introduction of a terpyridine-triazine moiety during the trimerisation step. This provides a binding site for photoactive metals within the linker while allowing the metalloligand to participate in MOF formation and deposition without major influence. In particular, Ruthenium terpyridine-

triazine-based complexes. The synthesis of such a complex was confirmed during the work undertaken in this thesis, but the potential of the ligand was not investigated for MOF formation, thin-film deposition, or catalysis.

7.0 Appendix

^{1}H NMR

2,4,6-Tris(4-bromophenyl)-1,3,5-triazine (**1**)

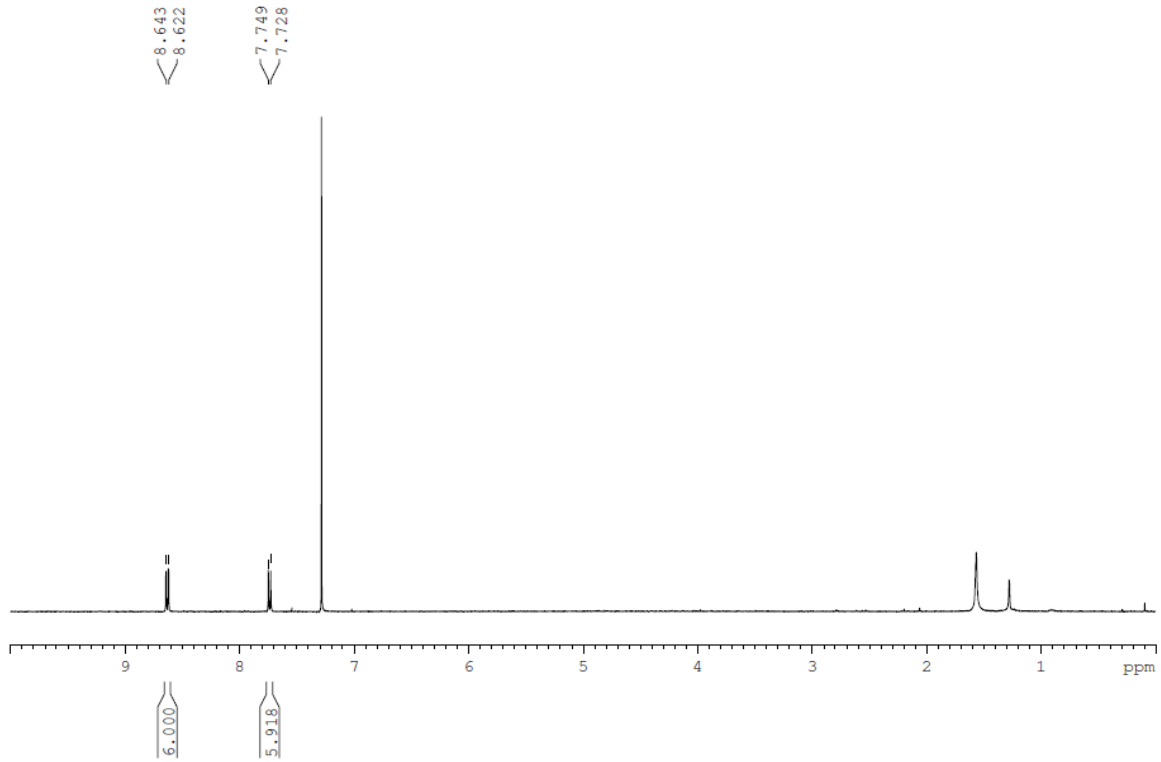

2,4,6-Tris(4-((trimethylsilyl)ethynyl)phenyl)-1,3,5-triazine (**2**)

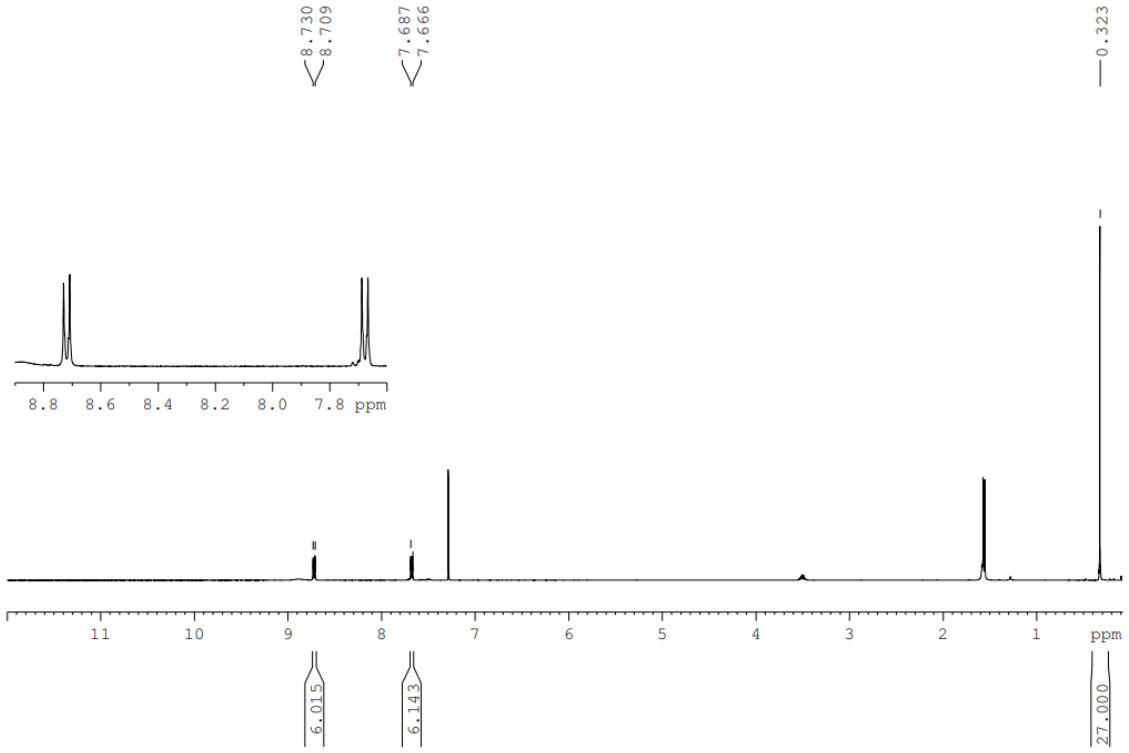

2,4,6-Tris(4-ethynylphenyl)-1,3,5-triazine (**3**)

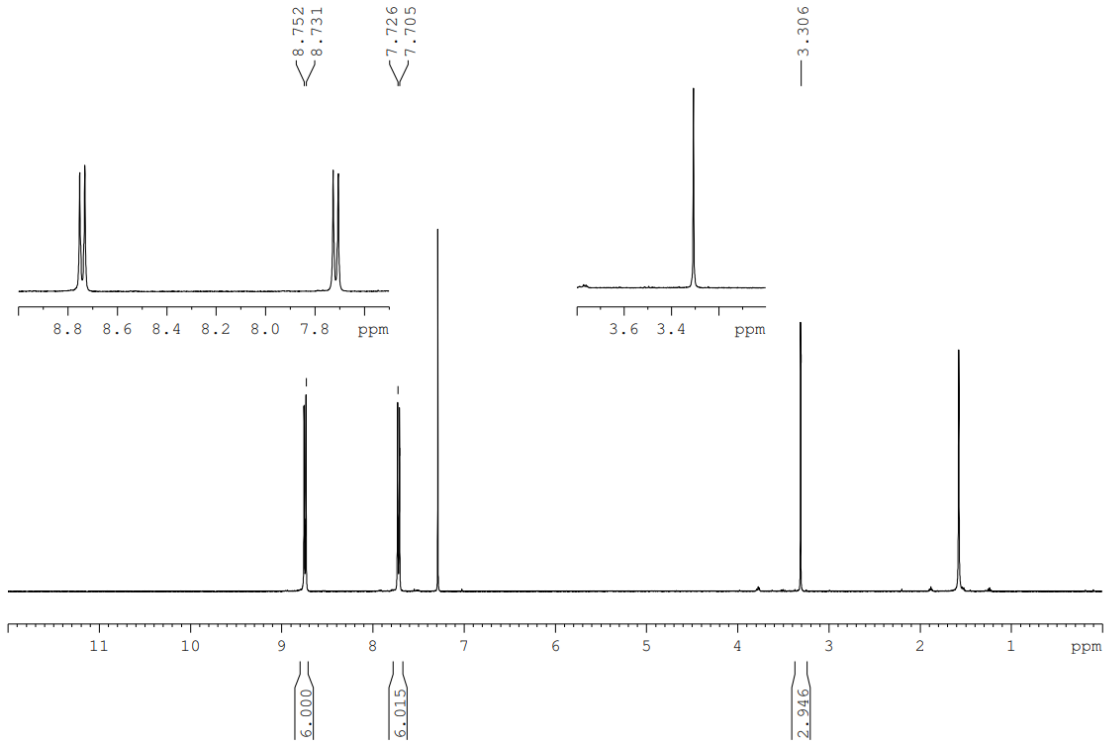

Trimethyl-4,4',4''-(((1,3,5-triazine-2,4,6-triyl)tris(benzene-4,1-diyl))tris(ethyne-2,1-diyl))tribenzoate (**4**)

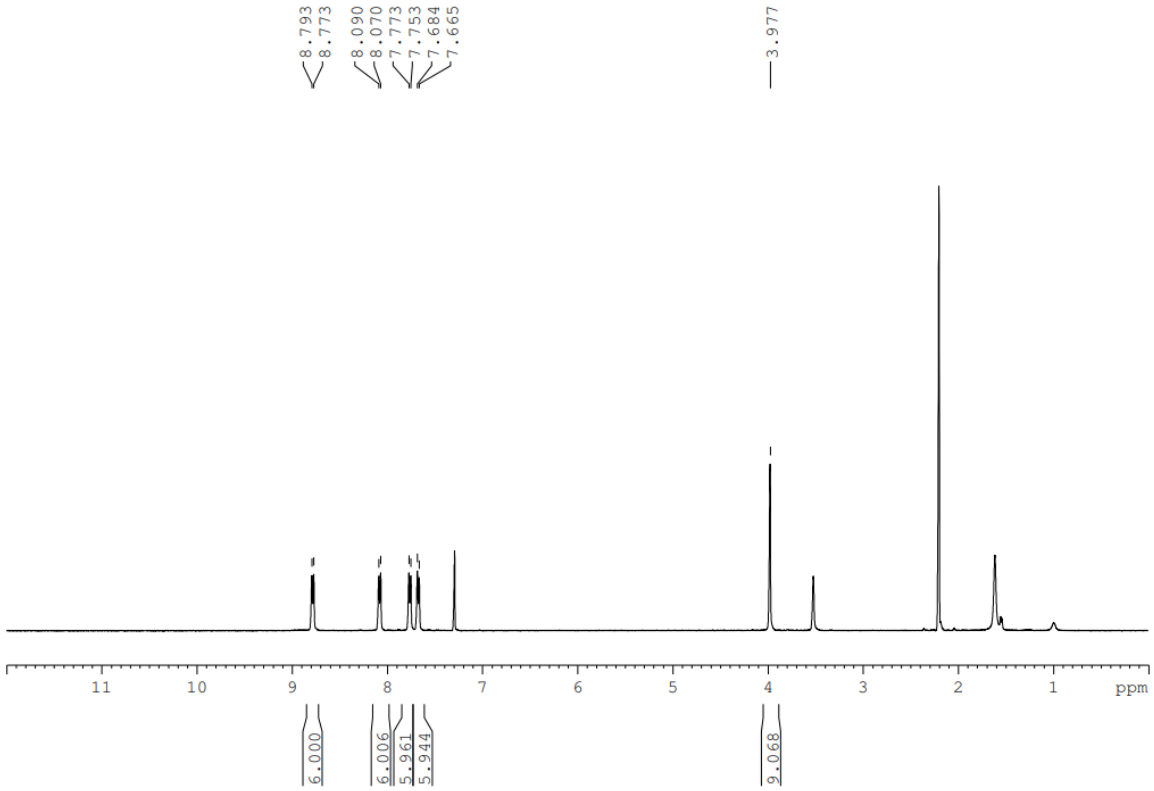

Trimethyl-3,3',3''-(((1,3,5-triazine-2,4,6-triyl)tris(benzene-4,1-diyl))tris(ethyne-2,1-diyl))tribenzoate (**5**)

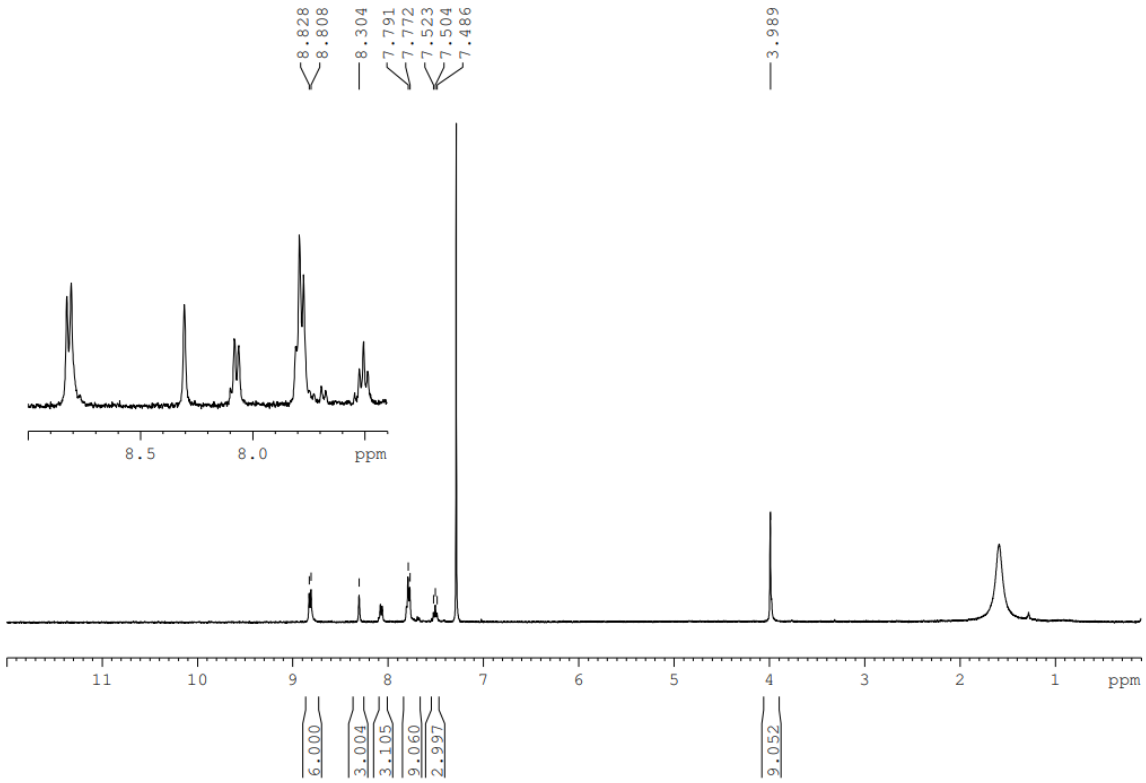

Trimethyl-4,4',4''-(((1,3,5-triazine-2,4,6-triyl)tris(benzene-4,1-diyl))tris(ethyne-2,1-diyl))tribenzoate (**H$_3$TAP**)

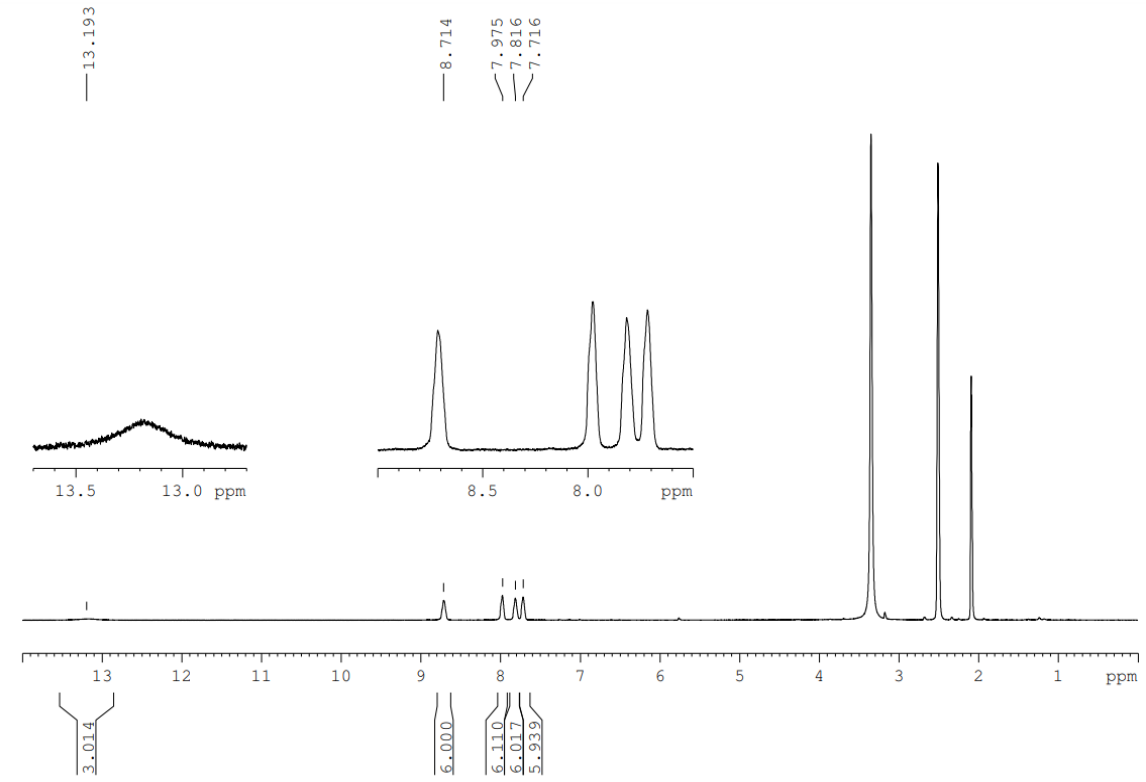

Trimethyl-3,3',3"-(((1,3,5-triazine-2,4,6-triyl)tris(benzene-4,1-diyl))tris(ethyne-2,1-diyl))tribenzoate (**H_3TAM**)

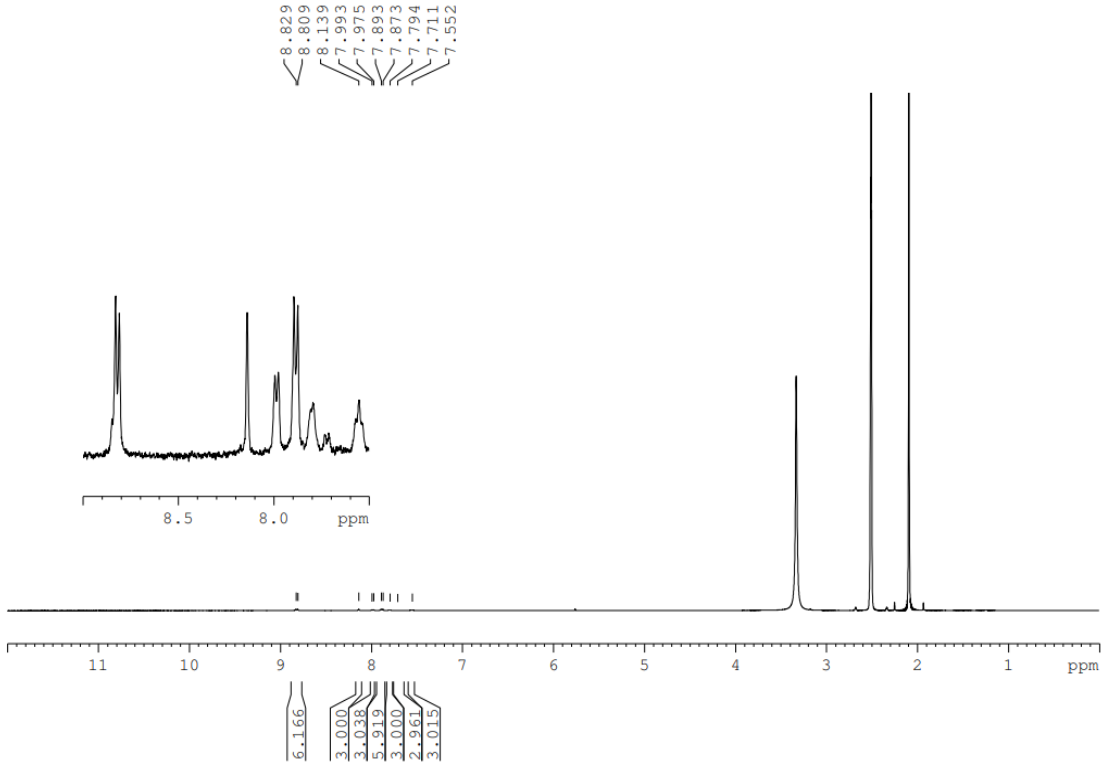

1,3,5-Tris((trimethylsilyl)ethynyl)benzene

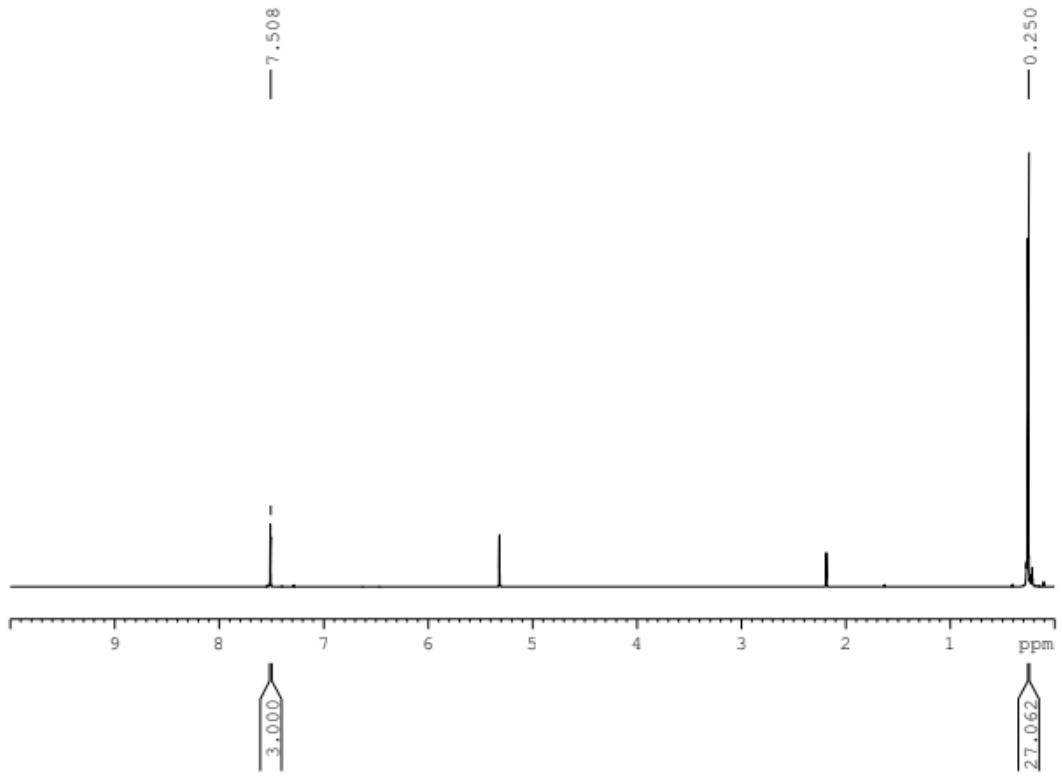

1,3,5-Triethynylbenzene

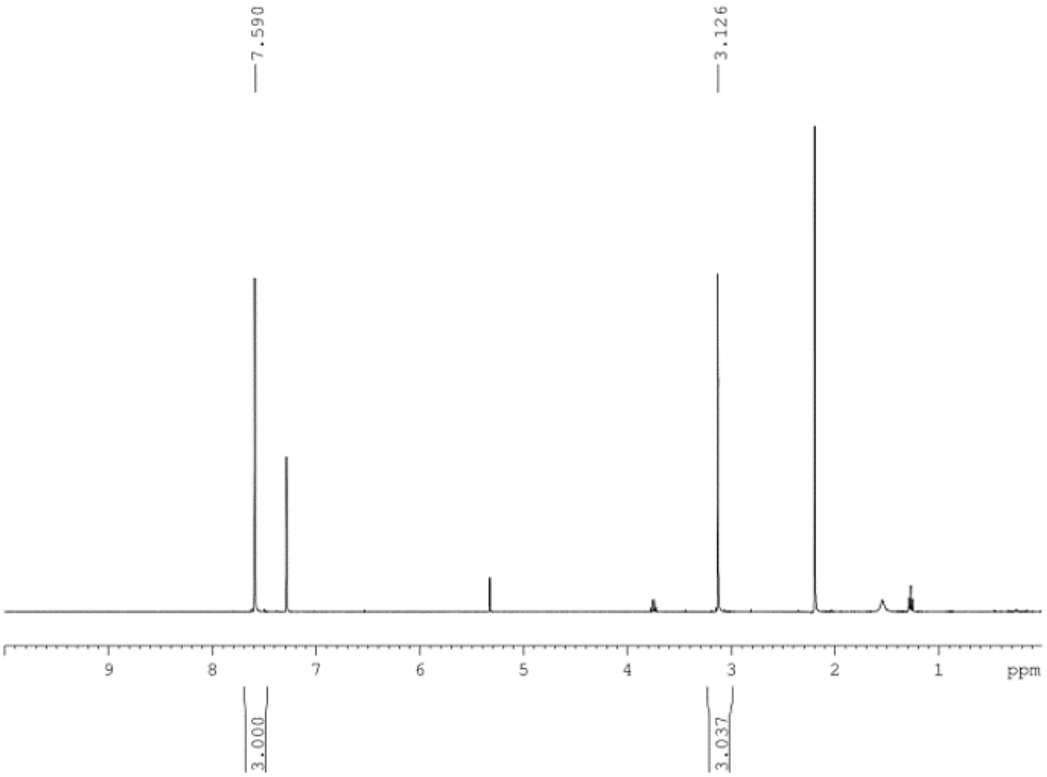

Trimethyl 4,4',4''-(benzene-1,3,5-triyltris(ethyne-2,1-diyl))tribenzoate

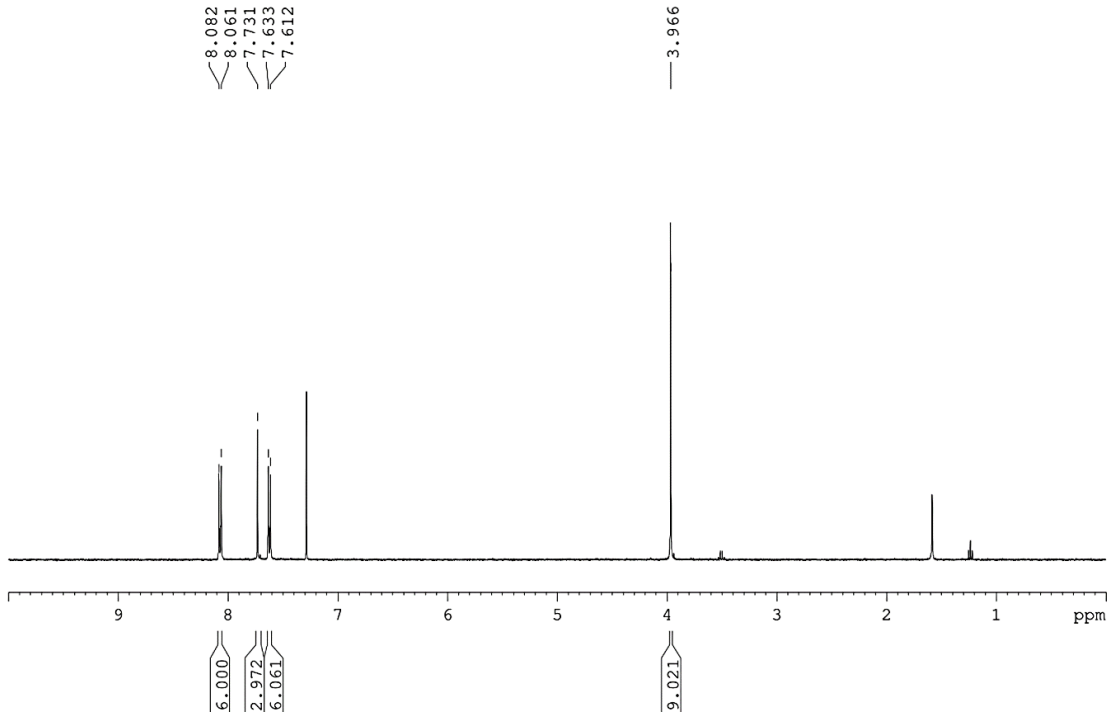

4,4',4"-(*benzene-1,3,5-triyltris(ethyne-2,1-diyl))tribenzoic acid* **(H_3BTEB)**

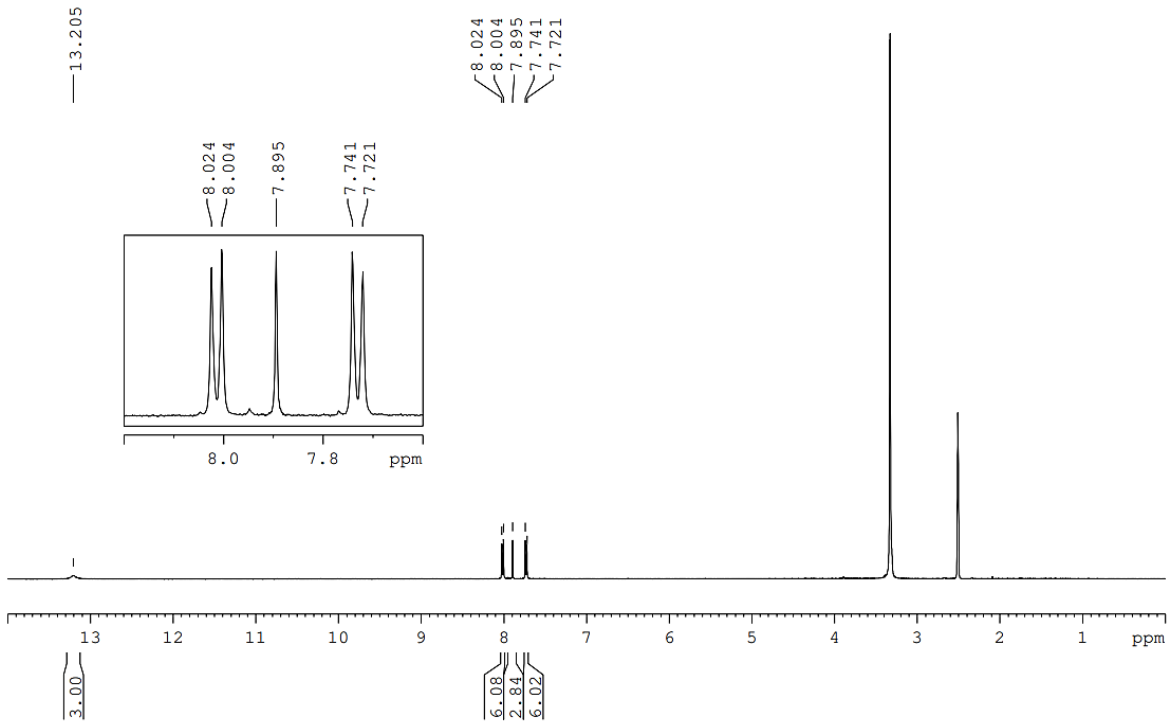

^{13}C NMR

2,4,6-Tris(4-bromophenyl)-1,3,5-triazine (**1**)

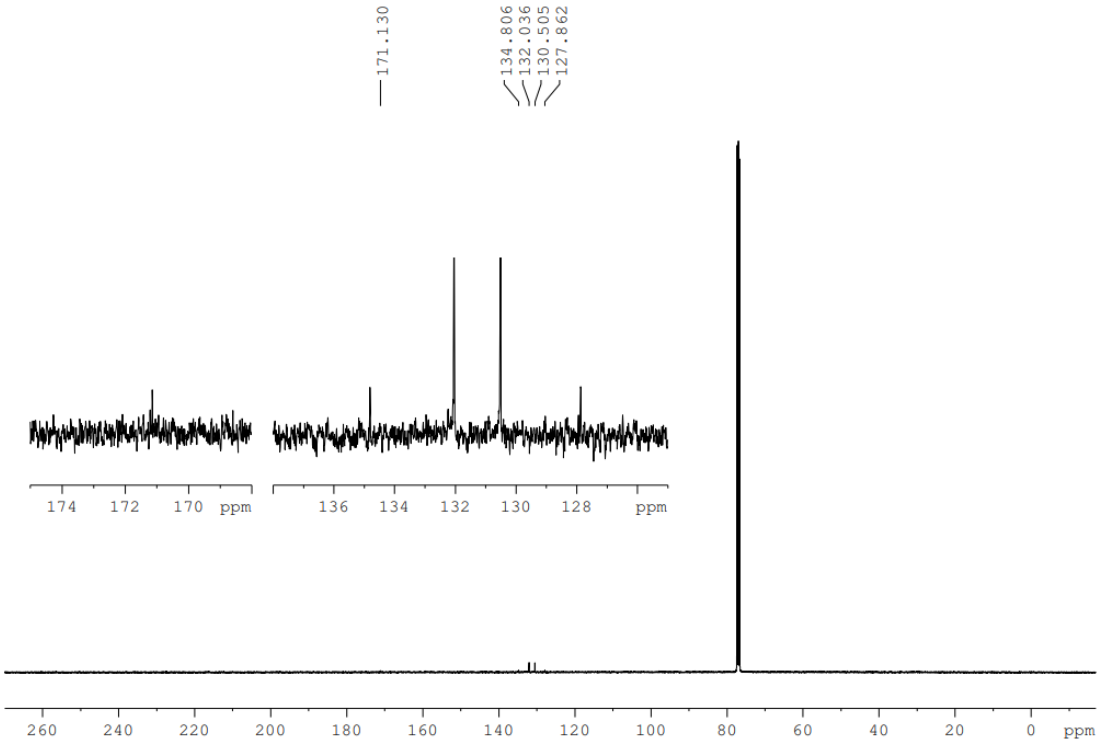

Trimethyl-4,4',4''-(((1,3,5-triazine-2,4,6-triyl)tris(benzene-4,1-diyl))tris(ethyne-2,1-diyl))tribenzoate (**H_3TAP**)

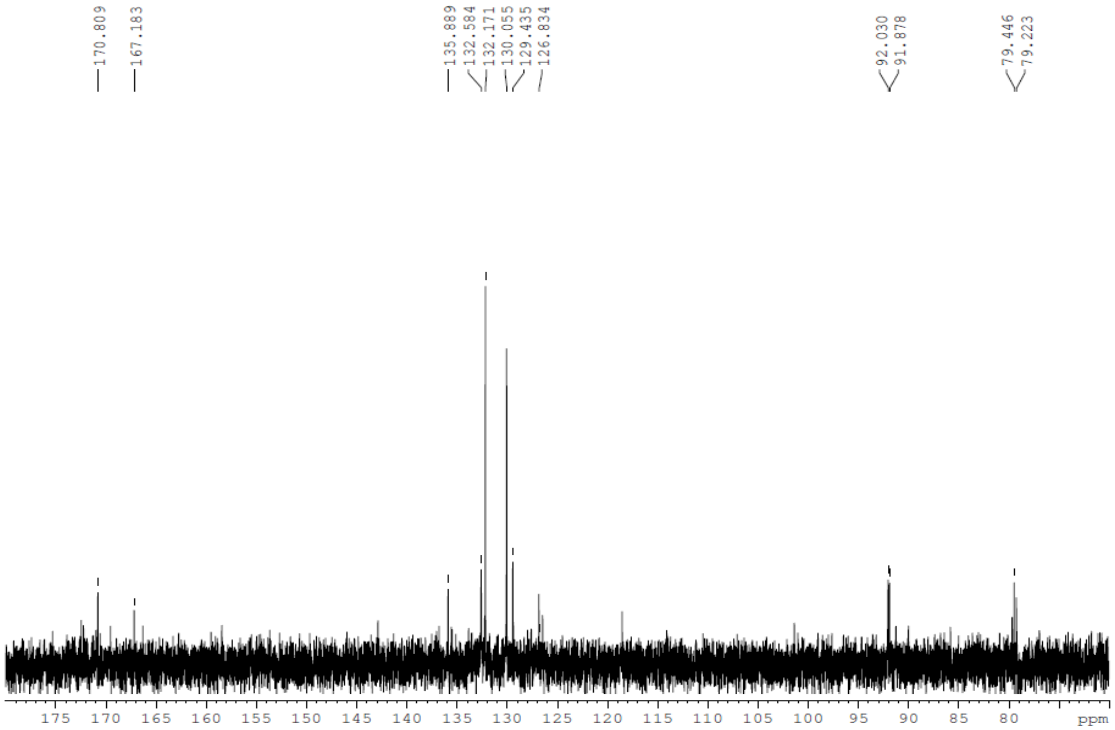

Trimethyl-4,4',4''-(((1,3,5-triazine-2,4,6-triyl)tris(benzene-4,1-diyl))tris(ethyne-2,1-diyl))tribenzoate (**6**)

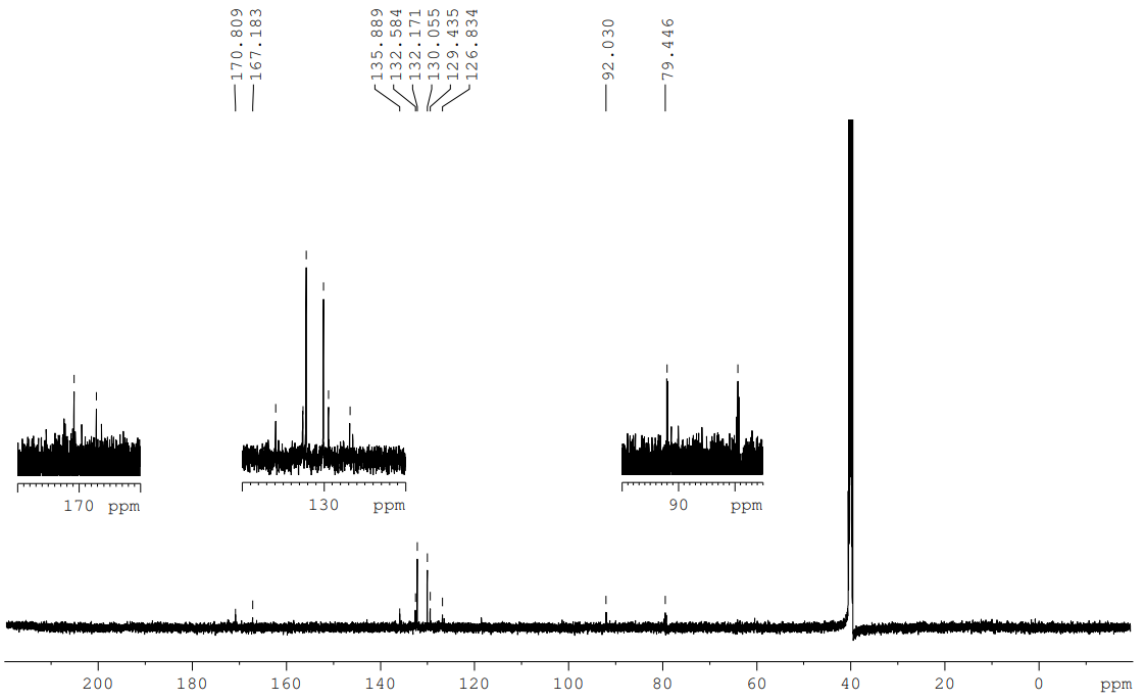

Trimethyl-3,3',3"-(((1,3,5-triazine-2,4,6-triyl)tris(benzene-4,1-diyl))tris(ethyne-2,1-diyl))tribenzoate (**H_3TAM**)

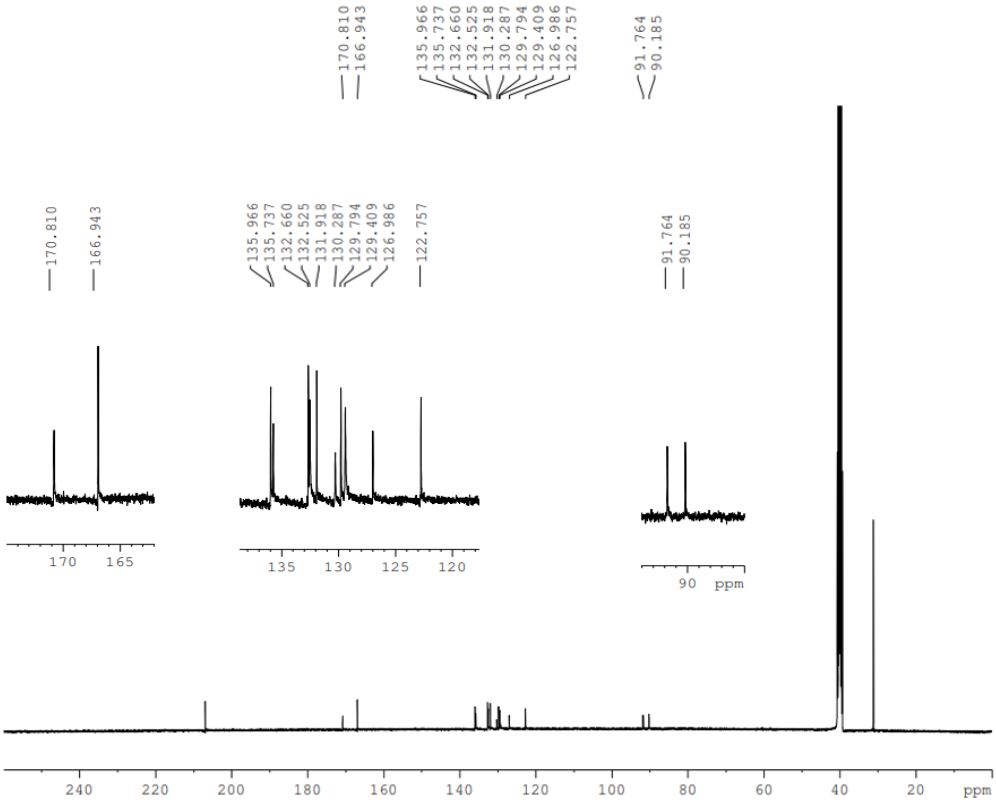

4',4''-(benzene-1,3,5-triyltris(ethyne-2,1-diyl))tribenzoic acid **(H_3BTEB**)

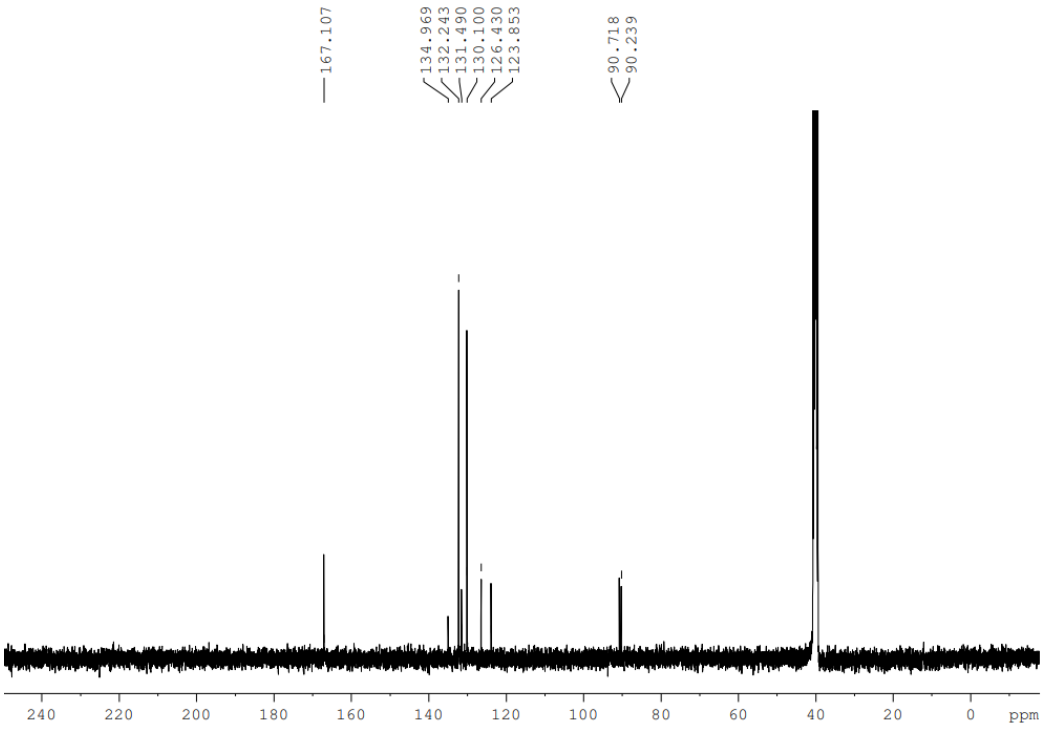

FT-IR Spectra

Trimethyl-4,4',4''-(((1,3,5-triazine-2,4,6-triyl)tris(benzene-4,1-diyl))tris(ethyne-2,1-diyl))tribenzoate
(**H_3TAP**)

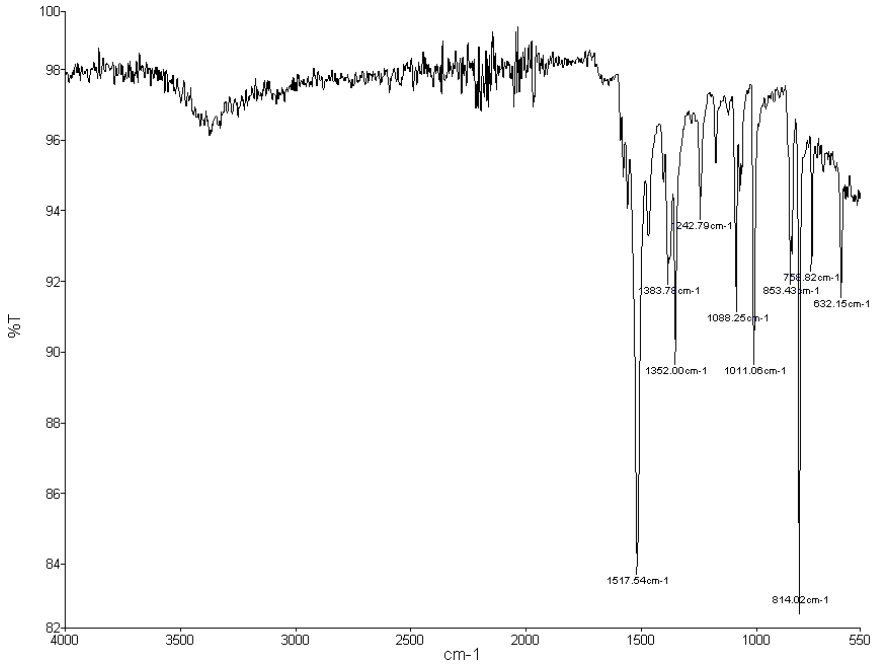

Trimethyl-3,3',3''-(((1,3,5-triazine-2,4,6-triyl)tris(benzene-4,1-diyl))tris(ethyne-2,1-diyl))tribenzoate (**H_3TAM**)

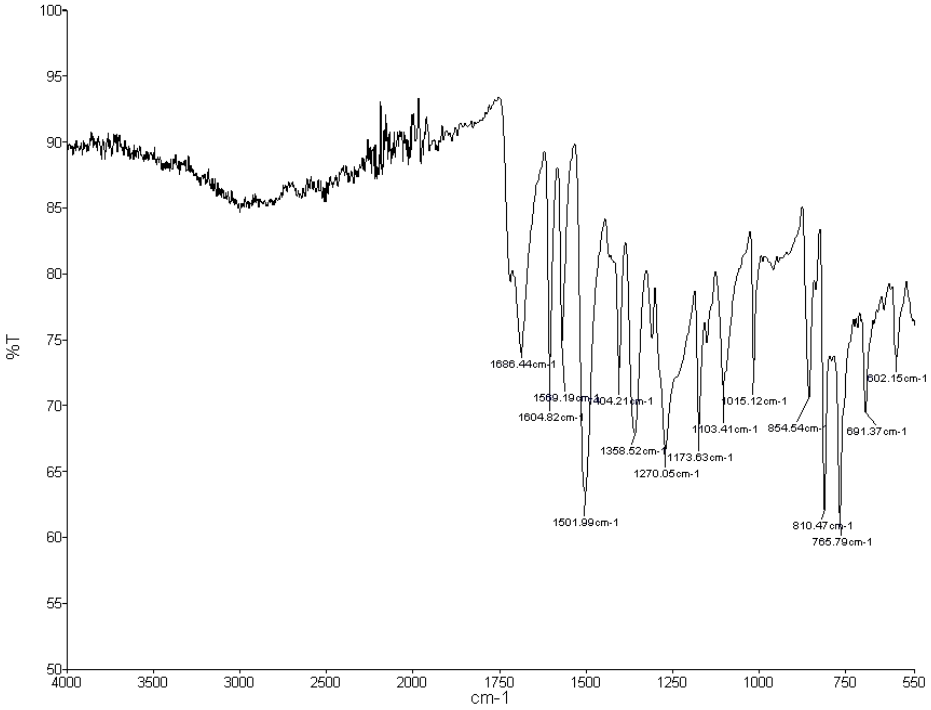

Mass spectrometry

2,4,6-Tris(4-bromophenyl)-1,3,5-triazine (**1**)

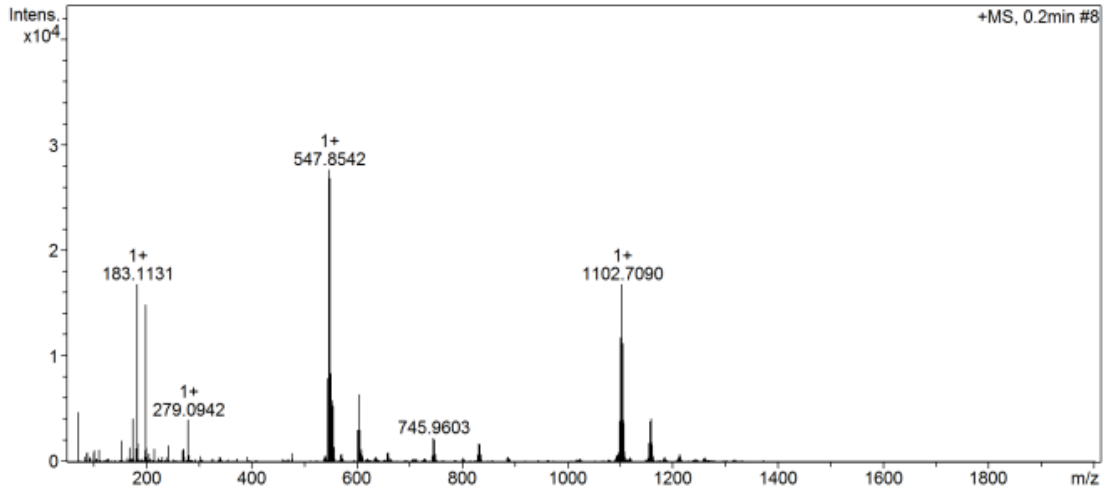

2,4,6-Tris(4-((trimethylsilyl)ethynyl)phenyl)-1,3,5-triazine (**2**)

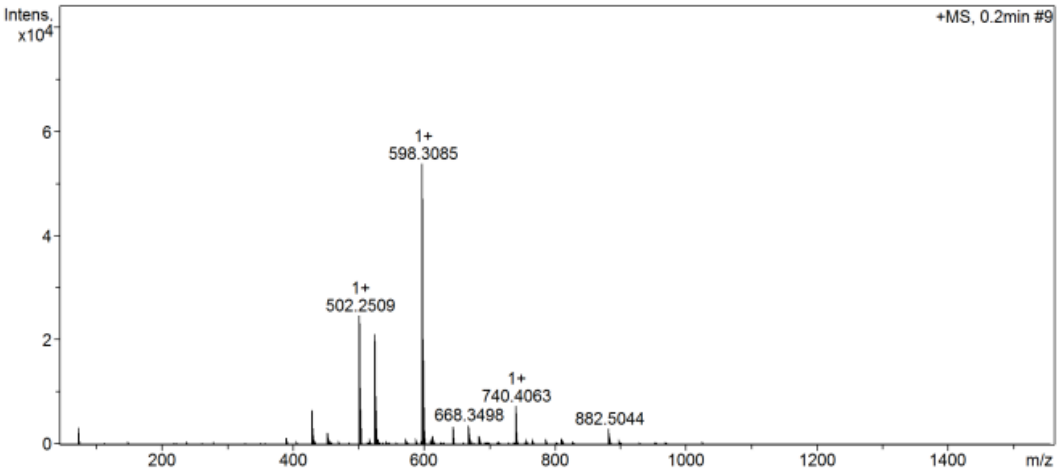

2,4,6-Tris(4-ethynylphenyl)-1,3,5-triazine (**3**):

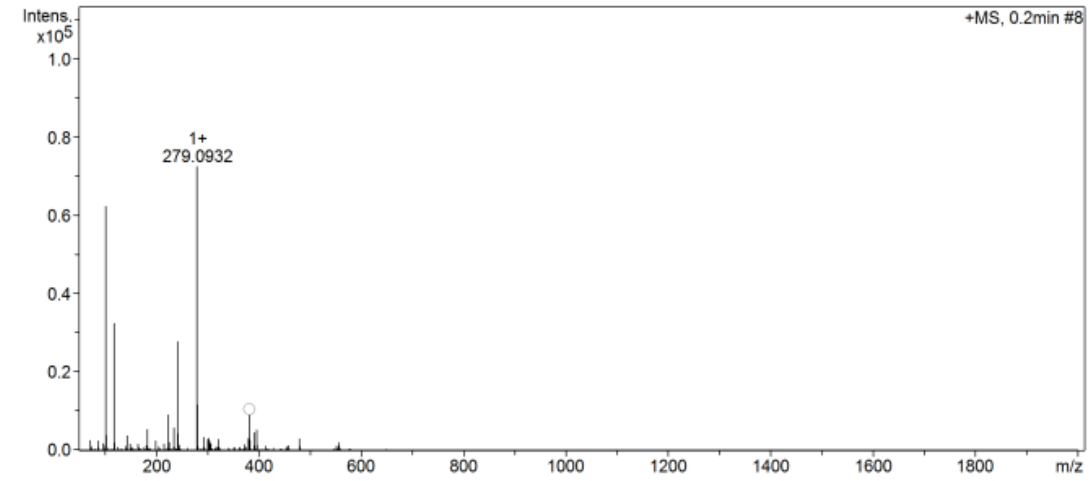

Meas. m/z	#	Ion Formula	m/z	err [mDa]	err [ppm]	rdb	N-Rule	e¯ Conf	mSigma
382.133162	1	C27H16N3	382.133874	-0.7	-1.9	21.5	ok	even	14.3

Trimethyl-4,4',4''-(((1,3,5-triazine-2,4,6-triyl)tris(benzene-4,1-diyl))tris(ethyne-2,1-diyl))tribenzoate (**H$_3$TAP**)

Elemental Composition Report **Page 1**

Single Mass Analysis
Tolerance = 10.0 PPM / DBE: min = -1.5, max = 200.0
Element prediction: Off
Number of isotope peaks used for i-FIT = 5

Monoisotopic Mass, Odd and Even Electron Ions
11 formula(e) evaluated with 1 results within limits (up to 10 best isotopic matches for each mass)
Elements Used:
C: 0-51 H: 0-35 N: 0-3 O: 0-6
Mariah O Doherty (WS), MOD-116
Q-TOF20180509MF005 48 (0.890) AM (Cen,6, 80.00, Ht,10000.0,1570.68,0.70); Sm (SG, 2x3.00); Sb (15,10.00); Cm (2:114-(46:51+94:101)) TOF MS LD+
1.06e+003

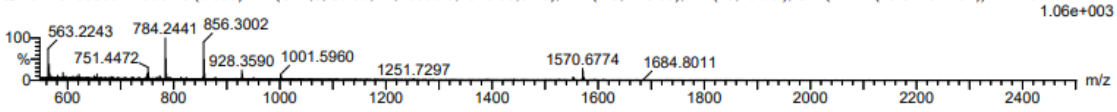

Minimum:				-1.5				
Maximum:		5.0	10.0	200.0				
Mass	Calc. Mass	mDa	PPM	DBE	i-FIT	i-FIT (Norm)	Formula	
784.2441	784.2448	-0.7	-0.9	36.5	144.6	0.0	C51 H34 N3 O6	

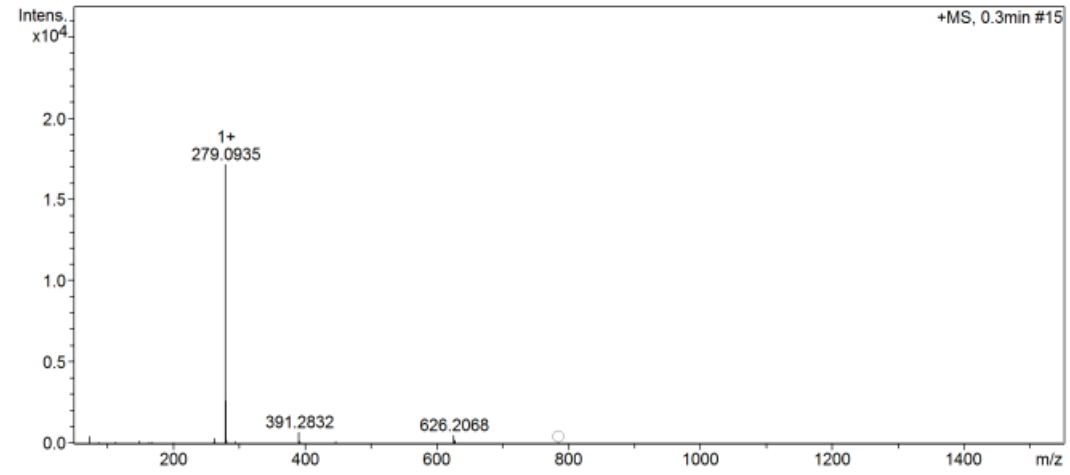

Meas. m/z	#	Ion Formula	m/z	err [mDa]	err [ppm]	rdb	N-Rule	e¯ Conf	mSigma
784.245450	1	C51H34N3O6	784.244212	1.2	1.6	36.5	ok	even	83.6

Trimethyl-3,3',3''-(((1,3,5-triazine-2,4,6-triyl)tris(benzene-4,1-diyl)) tris(ethyne-2,1-diyl))tribenzoate (**H_3TAM**)

Elemental Composition Report **Page 1**

Single Mass Analysis
Tolerance = 10.0 PPM / DBE: min = -1.5, max = 200.0
Element prediction: Off
Number of isotope peaks used for i-FIT = 5

Monoisotopic Mass, Odd and Even Electron Ions
37 formula(e) evaluated with 1 results within limits (up to 10 best isotopic matches for each mass)
Elements Used:
C: 0-51 H: 0-35 N: 0-3 O: 0-6 Ni: 0-1
Mariah O Doherty (WS), MOD-129-B-ii
Q-TOF20180530MF010 43 (0.933) AM (Cen,6, 80.00, Ht,10000.0,1570.68,0.70); Sm (SG, 2x3.00); Sb (15,10.00); Cm (9:77-(40:47+51)) TOF MS LD+
6.76e+002

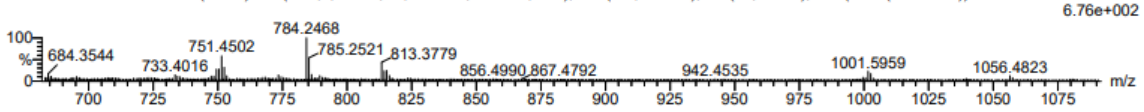

Minimum:				-1.5				
Maximum:		5.0	10.0	200.0				
Mass	Calc. Mass	mDa	PPM	DBE	i-FIT	i-FIT (Norm)	Formula	
784.2468	784.2448	2.0	2.6	36.5	131.3	0.0	C51 H34 N3 O6	

EDX Mapping of {Zn}-TAP on carbon tab